FACULTY OF ENGINEERING
AND ARCHITECTURE

CO_2-Assisted Propane Dehydrogenation over Pt-Based Catalysts: Looking inside via In Situ X-Ray Absorption Spectroscopy

Nadadur Veeraraghavan Srinath

Doctoral dissertation submitted to obtain the academic degree of
Doctor of Chemical Engineering

Supervisors

Prof. Vladimir Galvita, PhD* - Prof. Jolien Dendooven, PhD**

* Department of Materials, Textiles and Chemical Engineering
Faculty of Engineering and Architecture, Ghent University

** Department of Solid State Sciences
Faculty of Sciences, Ghent University

March 2022

GHENT
UNIVERSITY

FACULTY OF ENGINEERING
AND ARCHITECTURE

CO_2-Assisted Propane Dehydrogenation over Pt-Based Catalysts: Looking inside via In Situ X-Ray Absorption Spectroscopy

Nadadur Veeraraghavan Srinath

Doctoral dissertation submitted to obtain the academic degree of
Doctor of Chemical Engineering

Supervisors
Prof. Vladimir Galvita, PhD* - Prof. Jolien Dendooven, PhD**

* Department of Materials, Textiles and Chemical Engineering
Faculty of Engineering and Architecture, Ghent University

** Department of Solid State Sciences
Faculty of Sciences, Ghent University

March 2022

GHENT
UNIVERSITY

ISBN 978-94-6355-580-7
NUR 952, 971
Wettelijk depot: D/2022/10.500/21

Members of the Examination Board

Chair

Prof. Patrick De Baets, PhD, Ghent University

Other members entitled to vote

Valérie Briois, PhD, Synchrotron SOLEIL, France
Prof. Michiel Dusselier, PhD, KU Leuven
Matthias Filez, PhD, Ghent University
Prof. Marie-Françoise Reyniers, PhD, Ghent University
Prof. Joris Thybaut, PhD, Ghent University

Supervisors

Prof. Vladimir Galvita, PhD, Ghent University
Prof. Jolien Dendooven, PhD, Ghent University

Acknowledgements

As this long journey full of gaining knowledge, memories and experiences comes to an end, I realize that this PhD is a result of the combined efforts of a number of people. I would like to take this opportunity to show my appreciation to many of these individuals.

First, I'll start off by thanking my main Promoter, Prof. Vladimir V. Galvita. I realized quite early on that I was a lucky individual to be working with you, considering the vast breadth of knowledge that you possess. You are one of the kindest individuals that one can possibly meet, providing guidance when necessary and always open for discussions with your students. I enjoyed our discussions on a variety of topics ranging from research to sleight of hand card tricks, to watching and discussing sports (Basketball, Ice Hockey) during the night shifts of XAS beamtimes. That is another aspect which is really admirable, the fact that you are performing experiments at beamlines through the night with the student while always remaining curious about the results. All PhD students across the world will be hard-pressed to find any other professor that would do the same.

Next, I have to thank my main mentor/coach for the PhD: Dr Hilde Poelman. She is an unbelievably compassionate, calm and helpful individual. Thank you for going through my manuscripts, helping run experiments during beamtimes, checking on me from time to time to make sure that I am fine and not just in a work sense, making a Dutch translation of this thesis, and many more aspects that cannot be put into words. I have learned a lot from you and also appreciate the conversations we had during the lockdown period in 2020 while taking a walk around Zwijnaarde. Also, thank you for showing me around the area, as I was too lazy to look around by myself and only realized how beautiful the area really is once you showed it to me.

I would like to thank my 2nd promoter: Prof. Jolien Dendooven for the smooth collaboration with your department, as this work wouldn't have been possible without it. Thank you for providing insights as it pertains to atomic layer deposition and also for the general discussions during the progress meetings. Prof. Reyniers, you were originally my promoter and I thank you for being very kind to me and always testing my hypothesis at all times during our progress meetings. I did manage to pick up a few ideas from these which helped expand my knowledge.

I extend my gratitude to the doctoral committee of my thesis and the reviewers of my manuscripts whose numerous suggestions and questions improved the overall quality of the work.

Dr Alessandro Longo, without your insights and guidance into XAS and SAXS data processing, I would not have been able to perform the level of analysis that I have and for that, you have my sincerest gratitude. I hope that I was a good teacher when it comes to playing pool and I enjoyed the times when you were in Ghent and when I met you at the beamline.

Valentijn and Lennert, I feel delighted to have been the coach for your Master thesis, as I got to learn something from you also. Working with the two of you improved my understanding of the subject. Thank you for being such good students and not causing me any stress.

The next piece of appreciation goes out to all the technicians: Michael, Wim, Lambert, Erwin, Hans for keeping the setups running, ordering chemicals and providing support where necessary. Special thanks to the beamline scientists and technicians at ROCK (Camille, Valérie, Laurent) and DUBBLE (Alessandro, Marcus) for your assistance during the experiments as it forms a big part of this thesis.

Thanks to all the regular step-response users over the years for the smooth collaboration towards the use of the setup: Mostafa, Varun, Marian & Vladimir, and for helping me on the setup when required. Special mention goes to Mostafa for having maintained the Step-response for most of the years. Thanks, Lukas for showing me how to use the TEM setup and for measuring some of my samples when I first joined. Varun, I appreciate your efforts to keep the Autochem and Tristar running over the years.

There are administrative matters that have to be taken care of from time to time, and it was not as smooth as you would hope when I first joined the lab. However, once Paulien & Heidi joined the secretary’s office it became plain sailing and for this, you have my appreciation.

There is an LCT badminton team that has existed and this was a great way to cool off after work. I have to acknowledge the people with whom I played badminton over the years: Hilde, Sashwath, Shekhar, Pedro, Paulien, Dries, Reza, Nebojsa, Zinat, Mostafa, Lies, Eli, Arno, Tom, Sribala, Chanakya, Ana Rita, Laura. I enjoyed myself through a lot of those evenings by beating you regularly. I am not a professional badminton player by any means and nowhere close to it, but playing with all of you certainly made me feel like one and the least I could do is to thank you for that.

At this point, I must mention my Indian friends at LCT: Sashwath, Shekhar, Rakesh, Sribala, Anoop. Thank you as I could rely on you to get any form of help and that certainly made matters easier.

I would also like to acknowledge my office mates over the years: Farhan, Yonggang, Sebastien, Alireza, Fernando. Also, Prof. Maarten Sabbe with whom I shared the office at the beginning of this journey, for being open to having discussions regarding a variety of topics.

Over the years I have been able to get acquainted with a lot of PhD students and postdocs and would like to thank them all for the memories. Just to name a few: Lennert, Tom, Parviz, Mostafa, Paulien, Yaoyuan, Bo Jin, Hao Wang, Eli, Evangelos, Marco, Fernando, Manuel, Lukas, Juan, Varun, Bert, Reza, Beruk, Guillermo, Vaios, Pedro, Valentijn, Thobani, Ana Rita, Marian, Laura, Zinat, Arezoo and many others.

I would like to mention the following set of people: Sashwath, Shekhar, Aleksandar, Robert, Arno, Nebojsa, Olivier and Jeroen for being wonderful friends who are like brothers. I had a lot of fun in your company and hope to remain in touch in the future.

Finally, I must thank the most important people in my life without whom nothing is possible. Amma, Appa and Srikanth. Your continued strength and support is what keeps me going and gives me purpose in life. No words can ever describe your importance. Thank you for always being there when needed.

Nadadur Veeraraghavan Srinath

February 2022

Table of Contents

List of Figures

a function of the phase angle ΦPhSD. Instead of appearing at a certain time delay Δt, in the phase domain, the absolute phase delay φ contains information about the dynamics and kinetics of the studied system.[65]

Figure 2.12: *Schematic representation of SAXS measurement.*

Figure 2.13: *Data treatment procedure for SAXS. The steps indicated in the picture are the data treatment steps described in § 2.4.2.*

Figure 2.14: *Overview of the step-response setup showing the* ***a:*** *reactor,* ***b:*** *feed and* ***c:*** *analysis sections. The image b also has an analysis section with the MS situated below the feed MFC's.*

Figure 3.1: *Experimental scheme employed for in situ QXAS measurements.*

Figure 3.2: *STEM DF images of* ***a:*** *Pt:Sn/HSA (scale 20 nm) and* ***b:*** *Pt:Sn/LSA after one H_2-TPR step at 923 K (scale 50 nm). Insets: histograms of particle size image; extra inset in* ***a:*** *image at higher magnification to show the small Pt particles (scale 10 nm).*

Figure 3.3: *XANES spectra at the Pt L_{III}-edge during H_2-TPR from room temperature (RT) to 923 K under a flow of 2 Nml/min H_2 mixed with 5 Nml/min Ar (total flow 7 Nml/min), for Pt:Sn samples supported on* ***a:*** *HSA and* ***b:*** *LSA. The insets for the two plots show the maximum values taken as average at each energy position. The arrows within the inset graphs provide a guide-to the-eye as to how the maxima positions shift with temperature and time.* ■, ●*: negative, positive position difference with respect to the previous data point.*

Figure 3.4: *XANES spectra at Pt L_{III}-edge during CO_2-TPO from RT to 923 K at a flow rate of 2 Nml/min of CO_2 mixed with 5 Nml/min of Ar (7 Nml/min total flow), for Pt:Sn samples supported on* ***a:*** *HSA and* ***b:*** *LSA. The inset for the two plots shows the maximum values taken as average at each energy position. The arrows within the inset graphs provide a guide-to the-eye as to how the maxima positions shift with temperature and time.*

Figure 3.5: *MCR-ALS determination of* ***a:*** *XANES spectra at the Pt L_{III}-edge. It was found that 2 distinct components were present, which likely correspond to the Pt-Sn alloy and the monometallic Pt state* ***b:*** *Concentration profiles of the 2 components with time during H_2/Ar/CO_2 /Ar 1 min cycles. There were 10 H_2/CO_2 redox cycles that the catalyst sample was exposed to leading 10 oscillatory peaks.*

Figure 3.6: *All RT XANES spectra collected at the Sn K-edge subsequent to each treatment (H_2-TPR, CO_2-TPO, H_2/CO_2 redox cycles) for Pt:Sn supported on a: HSA and b: LSA. The plot also contains the Sn foil and SnO_2 XANES spectra.*

Figure 3.7: *MCR-ALS determination of* ***a:*** *XANES spectra at the Sn K-edge. It was found that 2 distinct components could be extracted, which likely correspond to the Pt-Sn alloy or SnO and the SnO_2 oxidised state;* ***b:*** *Concentration profiles of the 2 components with time during cycles of H_2/Ar/CO_2/Ar for 1 min each. There were 10 H_2/CO_2 redox cycles at 923 K to which the catalyst sample was exposed leading to 10 oscillatory peaks.*

Figure 3.8: *Experimental k^3-weighted Fourier transformed EXAFS signals at RT at the Pt L_{III}-edge subsequent to each treatment (H_2-TPR, CO_2-TPO, H_2/CO_2 redox cycles) for Pt:Sn supported on* ***a:*** *HSA and* ***b:*** *LSA. The dashed lines depict the fits for each of the signals.*

Figure 3.9: *Experimental k^3-weighted Fourier transformed EXAFS signals at RT at the Sn K-edge subsequent to each treatment (H_2-TPR, CO_2-TPO, H_2/CO_2 redox cycles) for Pt:Sn supported on* ***a:*** *HSA and* ***b:*** *LSA. The dashed lines depict the fits for each of the signals.*

***Figure 3.10:** Scheme depicting the evolution of the calcined Pt:Sn/HSA sample over different treatments based on the XAS data.*

***Figure 3.11:** **a:** Conversion and **b:** selectivity plots for CO_2-assisted PDH at different ratios of CO_2:C_3H_8 for the Pt:Sn/HSA catalyst (T=873 K and 1.2 bar, with flow of C_3H_8 being set at 60 Nml/min and a total flow set at 200 Nml/min). Plots for STY and C_3H_8 consumption rates are in Appendix B, Figure B13a, b, and c.*

***Figure 3.12:** C_3H_8/CO_2 cycles performed to determine the effect of CO_2 flow on the Pt:Sn/HSA catalyst after 5 redox cycles. The temporary increments in conversion follow upon exposure to a 15 Nml/min flow of CO_2 for 2 min (indicated by blue arrows). The time scale on the x-axis only shows the duration of sequential propane exposures. Temperature = 873 K, C_3H_8 flow = 40 Nml/min.*

***Figure 3.13:** Schematic representation of all reactions occurring on the catalyst during CO_2-assisted PDH. Part I of the scheme represents all the reactions taking place on the catalyst by the Langmuir-Hinshelwood mechanism, while part II represents the reactions occurring by Mars-van Krevelen mechanism. All reactions occur simultaneously. The catalyst goes from part I to part II in presence of CO_2, which would oxidise Sn to SnO, thereby segregating Sn from the Pt_3Sn alloy and then go back to part I through reduction by H_2 generated from PDH. (—) reduction, (—) oxidation, (—) PDH reaction, (—) RWGS reaction.*

***Figure 4.1:** Complete experimental scheme employed for in situ QXAS measurements. Sequence 2 started with an "As prepared" catalyst. ME scheme refers to the modulation excitation experiments. It is represented in sequence 1 as the 60 H_2:CO_2 redox cycles.*

***Figure 4.2:** XANES spectra at Pt L_{III} during H_2-TPR up to 873 K for **a:** Pt:In and **b:** Pt:Sn. Inset of graphs shows the WL intensity evolution with temperature. H_2 = 1 Nml/min, He=9 Nml/min (total flow = 10 Nml/min).*

***Figure 4.3:** XANES profiles at Pt L_{III} during isothermal CO_2-oxidation at 873 K for **a:** Pt:In and **b:** Pt:Sn. Insets show the evolution of the WL maxima during the oxidation. CO_2 = 1 Nml/min, He = 9 Nml/min (total flow = 10 Nml/min).*

***Figure 4.4:** white lines for Pt L_{III} during isothermal H_2/O_2 redox cycles at 873 K in **a:** Pt:In, **b:** Pt:Sn. Values within the graphs depict the WL height reached at the end of a 20 min half-cycle. Each half-cycle of (-) H_2 cycle for 20 min (1 Nml/min of H_2 + 9 Nml/min He) and (-) O_2 cycle for 20min (2 Nml/min 20% O_2/He + 8 Nml/min He). 5 total H_2/O_2 cycles were performed finishing with a H_2 half-cycle at the end (not all half-cycles shown).*

***Figure 4.5:** **a:** Pt:In, **b:** Pt:Sn. All RT XANES spectra collected at the (a) In & (b) Sn K-edge subsequent to each treatment (H_2-TPR, CO_2-TPO, Isothermal CO_2-oxidation, H_2/O_2 & H_2:CO_2 redox cycles). The plots contain the reference spectra of In foil and In_2O_3 (in a), and Sn foil and SnO_2 (in b)*

***Figure 4.6:** XANES profiles during H_2-TPR up to 873 K for **a:** Pt:In (In K-edge) and **b:** Pt:Sn (Sn K-edge). H_2 = 1 Nml/min, He = 9 Nml/min (total flow = 10 Nml/min), T_{max} = 873 K. Insets show the evolution of WL intensity with temperature.*

***Figure 4.7:** WL intensity evolution for Pt L_{III}- (black), In K- or Sn K-edge (blue) during CO_2-TPO up to 873 K. **a:** Pt:In, **b:** Pt:Sn. graphs vs. temperature.*

***Figure 4.8:** white lines for In or Sn K-edge during isothermal H_2/O_2 redox cycles at 873 K in **a:** Pt:In, **b:** Pt:Sn. Values within the graphs depict the WL height reached at the end of a 20 min half-cycle. (-) H_2 half-cycle (1 Nml/min of H_2 + 9 Nml/min He) and (-) O_2 half-cycle (2 Nml/min 20% O_2/He + 8 Nml/min He). 5 H_2/O_2 cycles were performed in total, finishing with a H_2 half-cycle (not all half-cycles shown).*

Figure C18: *Picture of the capillary after the in situ XAS experiments for the Pt:In sample. The yellow colouration of the inner wall of the capillary stems from In that was lost from the catalyst.*

Figure D1: *Ellingham diagrams for Ga, In and Sn under* ***a:*** O_2*,* ***b:*** CO_2 *and* ***c:*** H_2 *atmospheres.*

Figure D2: H_2*-TPR signal for* ***a:*** *Pt/*$MgAl_2O_4$*,* ***b:*** *Pt:Ga/*$MgAl_2O_4$*,* ***c:*** *Pt:In/*$MgAl_2O_4$*,* ***d:*** *Pt:Sn/*$MgAl_2O_4$*. One main peak appears for the monometallic sample, two major peaks are observed for all three bimetallic samples.*

Figure D3: *DF STEM images for the bimetallic catalysts.* ***a1:*** *Pt:Ga/*$MgAl_2O_4$ *reduced,* ***a2:*** *Pt:Ga/*$MgAl_2O_4$ *after 20 redox cycles/spent,* ***b1:*** *Pt:In/*$MgAl_2O_4$ *reduced,* ***b2:*** *Pt:In/*$MgAl_2O_4$ *after 20 redox cycles/spent,* ***c1:*** *Pt:Sn/*$MgAl_2O_4$ *reduced and* ***c2:*** *Pt:Sn/*$MgAl_2O_4$ *after 20 redox cycles/spent.*

Figure D4: *Activity plots during PDH for* ***a:*** *Pt:Ga,* ***b:*** *Pt:In and* ***c:*** *Pt:Sn.* ***1:*** *Propylene selectivity &* ***2:*** *propylene yield. Flows for PDH:* C_3H_8 *= 40 Nml/min,* H_2 *= 40 Nml/min, Ar = 70 Nml/min. Total flow = 150 Nml/min. Catalyst amount = 0.1 g. T = 873 K. P = 1.2 bar.*

Figure D5: *All activity plots for ratio studies for* CO_2*-PDH for* ***a:*** *Pt/*$MgAl_2O_4$*,* ***b:*** *Pt:Ga,* ***c:*** *Pt:In and* ***d:*** *Pt:Sn.* ***1:*** *Space time yield (STY)* C_3H_6*,* ***2:*** *STY* C_3H_8*,* ***3:*** CO_2 *conversion,* ***4:*** *m/z = 18 signal (for* H_2O *outlet). For information on flow rates please refer to §5.2.3 in chapter 5.*

Figure D6: *Chromatogram obtained for the Pt:Sn catalyst during* CO_2*-PDH at 0.125:1 -* CO_2*:*C_3H_8 *ratio flow.* ***Top:*** *from FID showing* CH_4*,* C_2H_6*,* C_2H_4*,* C_3H_8 *and* C_3H_6 *peaks.* ***Bottom:*** *TCD showing* CO_2*,* C_2H_6*,* C_2H_4*, Ar, CO and* CH_4 *peaks.*

Figure D7: *All activity plots* CO_2*-PDH after redox activation for* ***a:*** *Pt:Ga,* ***b:*** *Pt:In and* ***c:*** *Pt:Sn.* ***1:*** *Space time yield (STY) of* C_3H_6*,* ***2:*** *STY for* C_3H_8*,* ***3:*** CO_2 *conversion,* ***4:*** *m/z = 18 signal (for* H_2O *outlet),* ***5:*** *m/z = 44 signal during* O_2 *flow after each reaction step to quantify outlet* CO_2 *and thereby the carbon formed during reaction (integrated values show total* CO_2*). For information on flow rates please refer to §5.2.3 in chapter 5.*

Figure D8: *Activity plots for RWGS experiments at 3 different ratios of* H_2*:*CO_2 *for* ***a:*** *Pt:Ga,* ***b:*** *Pt:In and* ***c:*** *Pt:Sn.* ***1:*** CO_2 *conversion,* ***2:*** H_2 *conversion, 3: m/z = 18 signal (*H_2O *outlet). Flows:* CO_2 *= 10 Nml/min,* H_2 *= 10-30 Nml/min, Ar = 110-130 Nml/min, Total flow = 150 Nml/min. Mass of catalyst = 0.1 g.*

Figure D9: *Thermodynamic calculation of the equilibrium conversion of* ***a:*** CO_2 *&* ***b:*** H_2 *with respect to relative flow of* H_2 *to* CO_2 *at different temperatures.*

Figure E1: *All SAXS fits for the Pt:Ga/* $MgAl_2O_4$ ***(1)*** *and* $10Al_2O_3$*/Pt:Ga/*$MgAl_2O_4$ ***(2)*** *catalysts.* ***a:*** *As prepared state,* ***b:*** *After TPR,* ***c:*** *After TPO and* ***d:*** *After* H_2*/*O_2 *cycles. All black lines are the original SAXS signals (not normalized), while the dashed red lines are the fits.*

Figure E2: *All SAXS fits for the Pt/ MgGaAlO* ***(1)*** *and* $10Al_2O_3$*/Pt/MgGaAlO* ***(2)*** *catalysts.* ***a:*** *As prepared state,* ***b:*** *After TPR,* ***c:*** *After* H_2*/*O_2 *cycles. All black lines are the original SAXS signals (not normalized), while the dashed red lines are the fits.*

Figure E3: *XANES spectra for monometallic Pt/*$MgAl_2O_4$ *at Pt* L_{III}*-edge during* ***a:*** H_2*-TPR from room temperature (RT to 923 K) under a flow of 2 ml/min* H_2 *mixed with 5 ml/min Ar (total flow 7 ml/min) and* ***b:*** CO_2*-TPO (RT to 923 K) at a flow rate of 2 ml/min of* CO_2 *mixed with 5 ml/min of Ar (7 ml/min total flow).* ***The insets for the two plots show the WL maximum at each energy position****. The arrows within the inset graphs provide a guide-to the-eye as to how the maxima positions shift with temperature and time*[1]*.*

Figure E4: *Pt:Ga/$MgAl_2O_4$. Values within the graphs depict the WL height reached at the end of a 20 min half-cycle. Each half-cycle of (—) H_2-cycle for 20 min (5 ml/min of 5%H_2/He) and (—) O_2 cycle for 20min (2 ml/min 20% O_2/He+3 ml/min He). 5 total H_2/O_2 cycles were performed finishing with a H_2 half-cycle at the end (not all half-cycles shown).*

Figure E5: a: *Pt/MgGaAlO,* ***b:*** *10Al_2O_3/Pt/MgGaAlO. Values within the graphs depict the WL height reached at the end of a 20 min half-cycle. Each half-cycle of (—) H_2-cycle for 20 min (5 ml/min of 5% H_2/He) and (—) O_2 cycle for 20 min (2 ml/min 20% O_2/He+3 ml/min He). 5 total H_2/O_2 cycles were performed finishing with a H_2 half-cycle at the end (not all half-cycles shown).*

Figure E6: *k^3-weighted k-space EXAFS signal for (—) Pt/MgGaAlO and (—) 10Al_2O_3/Pt/MgGaAlO samples after 5 O_2/H_2 redox cycles with last H_2 exposure.*

Figure E7: *k^3-weighted k-space EXAFS signal for Pt/MgGaAlO reduced state. The signal has very low S/N ratio and is difficult to treat for EXAFS modelling adequately.*

Figure E8: *Experimental k^3-weighted Fourier transformed EXAFS signal and fit at RT at the Pt L_{III}-edge for 10Al_2O_3/Pt/MgGaAlO after CO_2-TPO.*

Figure E9: *Activity results for* ***Pt/$MgAl_2O_4$ (black)*** *and* ***10Al_2O_3/Pt/$MgAl_2O_4$ (red). a1:*** *C_3H_8 conversion for samples after 1 reduction step at 873 K for 30 min,* ***a2:*** *C_3H_8 conversion after 5 H_2/O_2 redox treatments with a H_2 reduction as the last step.;* ***b1:*** *STY C_3H_8 for reduced state,* ***b2:*** *STY C_3H_8 for cycled state,* ***c1:*** *STY C_3H_6 reduced state,* ***c2:*** *STY C_3H_6 for cycled state. Flows : C_3H_8 = 40 Nml/min, H_2 = 40 Nml/min Ar = 120 Nml/min. Ratio C_3H_8:H_2:Ar = 1:1:3, total flow = 200 Nml/min, catalyst amount = 0.1 g, T =873 K, P =1.2 bar.*

Figure E10: *Activity test results for the coated and uncoated Pt:Ga WI catalysts.* ***a:*** *STY C_3H_8,* ***b:*** *STY C_3H_6. Flows : C_3H_8 = 40 Nml/min, H_2 = 40 Nml/min Ar = 120 Nml/min. Ratio C_3H_8:H_2:Ar = 1:1:3, total flow = 200 Nml/min, catalyst amount = 0.1 g, T =873 K, P =1.2 bar.*

Figure E11: *All reaction plots for* ***a:*** *Pt/MgGaAlO* ***b:*** *10Al_2O_3/Pt/MgGaAlO* ***c:*** *40Al_2O_3/Pt/MgGaAlO. Flows : C_3H_8 = 40 Nml/min, H_2 = 40 Nml/min Ar = 120 Nml/min. Ratio C_3H_8:H_2:Ar = 1:1:3, total flow = 200 Nml/min, catalyst amount = 0.1 g, T =873 K, P =1.2 bar.*

Figure E12: *Comparison of STY for Pt:Ga/$MgAl_2O_4$ (wet impregnated) and Pt/MgGaAlO (Ga-incorporated) samples for* ***a:*** *propane and* ***b:*** *propylene.* ***1:*** *uncoated and* ***2:*** *coated samples. STY was calculated based on the Pt Wt% obtained from ICP. Flows : C_3H_8 = 40 Nml/min, H_2 = 40 Nml/min Ar = 120 Nml/min. Ratio C_3H_8:H_2:Ar = 1:1:3, total flow = 200 Nml/min, catalyst amount = 0.1 g, T =873 K, P =1.2 bar.*

List of Tables

List of Abbreviations and Acronyms

ALD	Atomic layer deposition
ALS	Alternating least squares
amu	Atomic mass unit
ASAXS	Anomalous small angle x-ray scattering
BET	Brunauer-Emmett-Teller
BJH	Barrett-Joyner-Halenda
CN	Coordination number
CO_2-PDH	CO_2-assisted propane dehydrogenation
CO-DRIFTS	Carbon monoxide diffuse reflectance FTIR spectroscopy
DFT	Density functional theory
DS	Difference spectrum
DUBBLE	Dutch Belgian beamline
EDH	Ethane dehydrogenation
EDX	Energy dispersive x-ray
ESRF	European synchrotron radiation facility
EXAFS	Extended x-ray absorption fine structure
fcc	Face centered cubic
FCC	Fluid catalytic cracking
FID	Flame ionization detector
FTIR	Fourier transformed infra-red spectroscopy
GB	Giga byte
GC	Gas Chromatograph
HSA	Higher surface area
HTL	Hydrotalcite
i.d.	Internal diameter
ICP-OES	Inductively coupled plasma optical emission spectroscopy
INC	Incorporated sample

LCF	Linear combination fitting
L-H	Langmuir-Hinshelwood
LSA	Lower surface area
MCR	Multivariate curve resolution
ME	Modulation excitation
MES	Modulation excitation spectroscopy
MS	Mass spectrometer
MTO	Methanol to olefins
MTP	Methanol to propylene
MvK	Mars-van Krevelen
NPs	Nanoparticles
NSR	Nox storage reduction
o.d.	Outer diameter
ODP	Oxidative dehydrogenation of propane
PCA	Principle component analysis
PDH	Propane dehydrogenation reaction
PhSD	Phase-sensitive detection
PSD	Particle size distribution
Pt-M	Platinum-Metal alloy
QXAS	Quick X-ray absorption spectroscopy
ROCK	Rocking Optics for Chemical Kinetics
ROI	Region of interest
RT	Room temperature
RWGS	Reverse water gas shift reaction
S/N	Signal-to-noise
SAXS	small angle x-ray scattering
SEM	Scanning electron microscope
SOLEIL	Source optimisée de lumière d’énergie intermédiaire du Laboratoire pour l’utilisation du rayonnement électromagnétique

SSITKA	Steady-state isotoic transient kinetic analysis
STAR	Steam active reforming
STEM-DF	Dark field scanning transmission electron microscopy
STY	Space time yield
TB	Tera byte
TCD	Thermal conductivity detector
TMA	Tri-methyl aluminum
TOS	Time-on-stream
TPO	Temperature programmed oxidation
TPR	Temperature programmed reduction
TWC	Three way catalyst
USAXS	Ultra small-angle x-ray scattering
WAXS	Wide angle x-ray scattering
WHSV	Weight hour space velocity
WI	Wet impregnated sample
WL	White line
XANES	X-ray absorption near edge spectroscopy
XAS	X-ray absorption spectroscopy
XRD	X-ray diffraction

List of Symbols

Symbol	**Description**	**Units**
E	X-ray energy	eV
E_0	Absorption edge energy	eV
F_{C3H6}	Outlet flow rate of propylene	$mol \cdot s^{-1}$
F_{C3H8}	Outlet flow rate of propane	$mol \cdot s^{-1}$
$F_{C3H8}{}^{0}$	Inlet flow rate of propane	$mol \cdot s^{-1}$
$F_j^{eff}(k)$	Photoelectron backscattering amplitude function of the scatterers in path j	Å
h	Planck's constant	eV·s
$\hbar$	Reduced Planck's constant	eV.s
I_0	Incoming x-ray intensity	s^{-1}
I_e	Electron yield	s^{-1}
I_f	X-ray fluorescence intensity of fluoresecence yield	s^{-1}
$i_{scat}(q)$	Scattering profile	$Å^{-1}$
I_t	Intensity transmitted through the sample	s^{-1}
k	Photoelectron wave number	$Å^{-1}$
Δk	k-space fitting range	$Å^{-1}$
m	Electron mass	Kg
m_{Pt}	Mass of Platinum loaded into catalyst bed	Kg
MSc	Multiple scattering	-
N_{idp}	Number of independent points	-
$N_{In\text{-}O}$	In-O coordination number	-
N_j	Number of equivalent scattering paths j (MSc), or coordination number j (SS)	-
N_{par}	Number of parameters employed for the fit	-
N_{pts}	Number of data points used for data fitting	-
$N_{Pt\text{-}Ga}$	Pt-Ga coordination number	-
$N_{Pt\text{-}In}$	Pt-In coordination number	-

$N_{Pt\text{-}O}$	Pt-O coordination number	-
$N_{Pt\text{-}Pt}$	Pt-Pt coordination number	-
$N_{Pt\text{-}Sn}$	Pt-Sn coordination number	-
$N_{Sn\text{-}O}$	Sn-O coordination number	-
$N_{Sn\text{-}Pt}$	Sn-Pt coordination number	-
q	Scattering vector	-
r	Coordinate vector of the electron	-
R	Radial distance from x-ray absorber	Å
ΔR	R-space fitting range	$Å^{-(z+1)}$
$R_{In\text{-}O}$	In-O interatomic distance	Å
R_j	Half path length of photoelectron scattering path j (MSc), or interatomic distance j (SS)	Å
$R_{Pt\text{-}Ga}$	Pt-Ga interatomic distance	Å
$R_{Pt\text{-}In}$	Pt-In interatomic distance	Å
$R_{Pt\text{-}O}$	Pt-O interatomic distance	Å
$R_{Pt\text{-}Pt}$	Pt-Pt interatomic distance	Å
$R_{Pt\text{-}Sn}$	Pt-Sn interatomic distance	Å
$R_{Sn\text{-}O}$	Sn-O interatomic distance	Å
$R_{Sn\text{-}Pt}$	Sn-Pt interatomic distance	Å
S_{C3H6}	Selectivity towards propylene	%
S_0^2	Amplitude reduction factor	-
SS	Single scattering	-
T_{melt}	Melting point	K
V(E)	Victoreen function	-
x	Sample thickness	mm
X_{C3H8}	Conversion of propane	%

Greek symbols

Symbol	Descrption	Units
$\mu(E)$	Linear absorption coefficient	m^{-1}
$\mu(E,t)$	Time resolved spectra	
$\mu(E,\Delta\varphi t)$	Phase-resolved spectra	
μ_0	Atomic background	m^{-1}
μx	Total absorption	-
$\Delta\mu(E)x$	Edge step	-
ΔH	Reaction Enthalpy	$kJ\cdot mol^{-1}$
ΔH_{298}	Standard reaction enthalpy at 298 K	$kJ\cdot mol^{-1}$
$\delta_j(k)$	Phase shift for photoelectron scattering path j	-
$\Delta\varphi$	Phase lag	°
ϵ	Measurement uncertainty	$Å^{-(z+1)}$
λ	Incoming X-ray wavelength	Å
$\lambda(k)$	Energy dependent mean-free path distance of the photoelectron	Å
v	Frequency	s^{-1}
σ^2_{In-O}	Debye-Waller disorder factor for In-O neigbours	$Å^2$
σ^2_{Pt-Ga}	Debye-Waller disorder factor for Pt-Ga neigbours	$Å^2$
σ^2_{Pt-In}	Debye-Waller disorder factor for Pt-In Neigbours	$Å^2$
σ^2_{Pt-O}	Debye-Waller disorder factor for Pt-O neigbours	$Å^2$
σ^2_{Pt-Pt}	Debye-Waller disorder factor for Pt-Pt neigbours	$Å^2$
σ^2_{Pt-Sn}	Debye-Waller disorder factor for Pt-Sn neigbours	$Å^2$
σ^2_{Sn-O}	Debye-Waller disorder factor for Sn-O neigbours	$Å^2$
σ^2_{Sn-Pt}	Debye-Waller disorder factor for Sn-Pt neigbours	$Å^2$
σ_j^2	Squared Debye-Waller (DW) bond length disorder factor for photoelectron scattering path j	$Å^2$
$\chi_j(k)$	j^{th} contribution to the total EXAFS signal	-
$\chi(k)$	EXAFS signal in k-space	-
$\chi(R)$	EXAFS signal in R-space	$Å^{-(z+1)}$

χ^2	Chi-squared objective function	-
$\chi(E)$	EXAFS signal in E-space	-
$\chi_e(R_i)$	Complex Fourier transformed experimental χ(k) signal	Å$^{-(z+1)}$
$\chi_t(R_i)$	Complex Fourier transformed theoretical χ(k) signal	Å$^{-(z+1)}$
χ_v^2	Reduced chi-squared $\chi 2/\boldsymbol{\nu}$ (-)	-

Glossary of terms

Alloy	A metal that is made by mixing two or more metals, or a metal and another substance. The structure of the alloy can vary depending on the environment.
Active site	The region of a catalyst where adsorbate molecules bind and undergo a chemical reaction
Adsorption	The preferential concentration of a species at the interface between two phases. Adherence of the atoms, ions or molecules of a gas or liquid to the surface of another substance
As prepared catalyst	The catalysts after the calcination step
After TPR	State of the catalyst following a cool down to room temperature subsequent, to a hydrogen - temperature programmed reduction experiment.
After TPO	State of the catalyst following a cool down to room temperature, subsequent to a carbon dioxide-temperature programmed oxidation experiment.
After redox or After cycles	State of the catalyst following a cool down to room temperature, subsequent to a H_2/O_2 or H_2/CO_2 redox treatment at high temperature.
After IsoOx	State of the catalyst following a cool down to room temperature, subsequent to a isothermal CO_2 oxidation experiment at high temperature.
Catalyst	Substance or material, which through repeated cycles of elementary steps, accelerates the conversion of reagents into products. Catalysts are classified into homogeneous, which are in the same phase with the reagents (e.g. acids and bases, metal complexes, etc.), and heterogeneous, which are separated from the reactants by an interface (e.g. metals, metal oxides, etc.).
C_3H_8 consumption rate	Normalized measure for the amount of propane that has been reacted. Calculated on the basis of a

	difference between the inlet and outlet flow molar rates, measured relative to an internal standard.
Coking	Build-up of carbon depositions during a reaction
Conversion	Measure for the amount of a reactant that has been transformed into products as a result of a chemical reaction
Deactivation	Loss in catalytic activity due to chemical, mechanical or thermal process.
Dehydrogenation	A chemical reaction that involves the removal of hydrogen from an organic molecule.
Dispersion	The level to which active sites are distributed over the catalyst surface
Langmuir-Hinshelwood mechanism	This is a theoretical model of bimolecular chemical reactions on solid surfaces in which two atoms or molecules are adsorbed on the surface and at least one diffuses on the surface until both are close enough to interact.
Mars-van Krevelen mechanism	A reaction between the oxide catalyst and a reducing agent (e.g. hydrogen, hydrocarbons, etc), in which the latter is oxidized and the former is reduced, followed by the reaction of reduced oxide with an oxidizing agent (O_2, CO_2) to restore the initial state.
Promoter	Substance added to a catalyst in order to improve its performance, such as activity, selectivity or stability, in a chemical reaction. By itself the promoter has little or no catalytic effect. It can interact with the active component of the catalyst and thereby alter its properties.
Reduction	The pre-treatment process performed prior to each activity or stability test in order to reduce the metal oxides to metals.
Regeneration	Regeneration is renewal through the internal processes of a body or system. Here, it refers to the

	application of a set of treatments on the catalyst to regain activity following a chemical reaction.
Sintering	Coalescence of separate metal particles to become one bigger particle.
Support	Material, typically of a high surface area, onto which the active catalyst material, present as the minor component, is dispersed. The support may be catalytically inert, but it may contribute to the overall catalytic activity.

Summary

Alkane dehydrogenation is an important synthesis route towards selective alkene production and one of the major alkane dehydrogenation processes is propane dehydrogenation (PDH) to form propylene. The global demand for propylene derivatives such as polypropylene is expected to rise, thereby creating a demand for high purity propylene. Today, there is an issue as it pertains to global climate change and the need to reduce the emission of greenhouse gases such as CO_2 or CH_4. One of these greenhouse gases, CO_2, can be employed in conjunction with propane in the feed to form a CO_2-assisted propane dehydrogenation process, which can help to consume some CO_2. This CO_2 consumption would be achieved through the reverse water gas shift (RWGS) reaction, where the H_2 formed through PDH reacts with the feed CO_2 to form CO and H_2O. This in turn can help to shift the equilibrium of the PDH reaction towards product formation, which would make the co-feed of CO_2 doubly beneficial, i.e. leading to higher propane conversion and CO_2 consumption. CO_2 can also assist towards mitigation of carbon formation through the reverse Boudouard reaction, thereby increasing catalyst lifetime. Most of the existing industrial dehydrogenation processes utilize Pt-based bimetallic catalysts (typically Pt:Sn or Pt:Ga supported on $ZnAl_2O_4$ or $MgAl_2O_4$). Therefore, the development of CO_2-assisted propane dehydrogenation necessitates to test the effect of CO_2 addition on such catalysts.

Next to CO_2 addition, there are other ways to improve the PDH process, e.g. through tailoring of the catalyst synthesis. One promising means is the application of a coating to the catalyst, which can assist towards prevention of sintering and therefore lead to a longer catalyst life span. Such a coating addition however could also lead to other effects and till date, it hasn't been applied to a bimetallic catalyst system. Hence, it requires careful investigation of the nanoparticles in presence of such a coating and its effect on the performance.

In this dissertation, both the effect of CO_2 addition in the feed and of coating addition on the integrity of Pt-based bimetallic alloys have been investigated. The main technique employed for this analysis is X-ray absorption spectroscopy (XAS), in part extended with small angle X-ray scattering (SAXS). These are supplemented with catalytic activity tests for PDH and CO_2-PDH to get to a complete understanding of the catalyst.

Initially, a Pt:Sn catalyst supported on $MgAl_2O_4$ is investigated for CO_2-PDH with support surface areas of ~127 m^2/g (higher surface area, HSA) or ~5 m^2/g (lower surface area, LSA), 3 wt% Pt and a Pt:Sn molar ratio of 3:1. The difference in available support surface area led to the deposition of different nanoparticle sizes, which upon reduction led to different levels of Sn content in the Pt-Sn alloy. In situ XAS was employed to track the dynamic changes occurring to the catalyst in presence of a reductive (H_2) or oxidative (CO_2) atmosphere. Pt-Sn alloy formation was detected upon reduction under H_2. Oxidation by CO_2 led to loss of the Pt-Sn alloy due to firstly oxidation of Sn to SnO and subsequent oxidation of SnO to SnO_2. Modelling of the acquired EXAFS data assisted in determining the electronic and structural properties.

A big data analysis method, Multivariate Curve Resolution-Alternating Least Squares (MCR-ALS, Figure 1), was employed in conjunction with the XAS data and proved to be valuable tool to determine the amount of Sn present in the Pt-Sn alloy phase and the phase of the Pt-Sn alloy itself: after a single step reduction, 42% of all Sn went into Pt_3Sn alloy, participating in the reaction, with the remainder being SnO_x. The percentage of Sn going into the Pt_3Sn alloy increased after 10 H_2/CO_2 redox cycles to 72%.

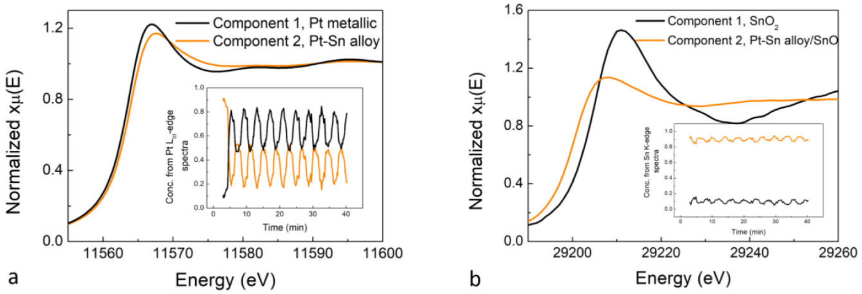

***Figure 5:** MCR-ALS determination at **a:** Pt L_{III}-edge & **b:** Sn K-edge for Pt:Sn/HSA.*

The catalyst was then tested for CO_2-PDH, covering CO_2:C_3H_8 ratios from 0.25:1 to 1:1. Lower ratios proved to work better due to the Pt-Sn alloy being more stable in such case, when compared with higher ratios. Higher CO_2 flows led to the oxidation of Sn to SnO_x and therefore the loss of the Pt-Sn alloy. Suppression of carbon accumulation was detected, which occurred by means of the reverse Boudouard reaction with the carbon formed during PDH. As possible reaction network for the entire CO_2-PDH reaction, a combination of Langmuir-Hinshelwood

(L-H) and Mars-van Krevelen mechanism (MvK) was proposed (Figure 2). The MvK steps comprise the oxidation by CO_2 of Sn to SnO, extracting the promoter from the alloy, which would then subsequently react with the H_2 and carbon generated from PDH taking place on Pt sites via the L-H mechanism, to go back to the Pt_3Sn alloy.

Since alloy segregation was detected for Pt:Sn, a new set of catalysts were prepared: Pt:Sn and Pt:In, the difference in this case being that the promoter loadings were much higher than in the first set of Pt:Sn catalysts (1:1.5 vs. 3:1 previously). Both these catalysts were supported on $MgAl_2O_4$ (107 m^2/g). The loading of Pt was kept consistent at 3 wt%. In was chosen as a second promoter as it has different oxidation/reduction potentials when compared to Sn and it had been used as a viable PDH catalyst. XAS measurements were performed during CO_2-TPO after reduction of both these catalysts and through these experiments it was concluded that the Sn and In present in the samples begin to undergo oxidation back to their respective oxides at low temperatures, i.e. <500 K.

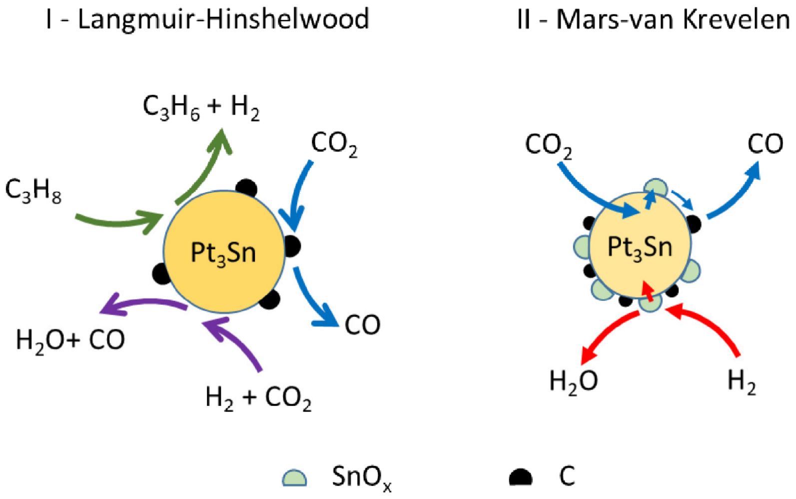

Figure 6: *Schematic representation of all reactions occurring on a Pt:Sn catalyst during CO_2-PDH. Part I of the scheme represents all the reactions taking place on the catalyst by the Langmuir-Hinshelwood mechanism, while part II represents the reactions occurring by Mars-van Krevelen mechanism. All reactions occur simultaneously. The catalyst goes from part I to part II in presence of CO_2, which will oxidise Sn to SnO_x, thereby segregating Sn from the Pt_3Sn alloy and then go back to part I through reduction by H_2 generated from PDH. (—) reduction, (—) oxidation, (—) PDH reaction, (—) RWGS reaction.*

Further detailed characterization of Pt:In and Pt:Sn catalysts was performed through in situ QXAS coupled with Modulation Excitation spectroscopy (MES, Figure 3a), based on flow perturbations. In this case, MCR-ALS did not prove to be as valuable as with the sample with lower Sn content, because the rate at which the alloy was lost under CO_2 was now drastically slower for the higher Sn content. As for Pt:In, this catalyst lost the alloy phase more quickly than Pt:Sn. Through MES analysis of the Pt L_{III}-edge, it was determined that the In content at the surface of the Pt:In nanoparticles (NPs) increased with time and became In-rich compared to the bulk, in contrast to Pt:Sn. In fact, a reversible process occurred for the Pt:In sample, wherein the sample oscillated between two different Pt-In alloy phases. It was quantified that about 11 atoms per 100 took actively part in this process. Pt:Sn by comparison showed a much lower sensitivity to the changes imposed, with only 1 atom out of 100 being responsive.

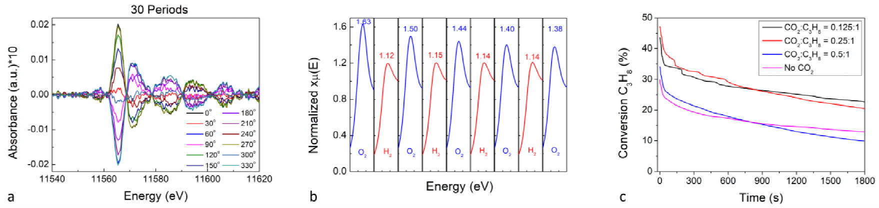

Figure 7: ***a:*** *Demodulated spectra consisting of 24 spectra averaged over 30 periods for Pt:In catalyst,* ***b:*** *data for Pt:Sn where values within the graphs depict the Pt L_{III} edge WL height reached at the end of a 20 min half-cycle of H_2 or O_2,* ***c:*** *C_3H_8 conversion plots with different feed ratios for CO_2-PDH on a Pt:Sn catalyst.*

As the main factor determining the alloy stability during CO_2-PDH is the ratio between H_2 and CO_2, with H_2 arising from the dehydrogenation of propane, RWGS was chosen as a model reaction to probe the stability of the Pt-In and Pt-Sn alloys. Three different CO_2:H_2 flow compositions were selected (1:1, 3:1 and 5:1) for the in situ QXAS measurements. Increasing ratios led to a larger number of surface species engaged in reaction, with the engagement being around 12% for Pt:In. The kinetics of change were slower for Pt:Sn as compared to Pt:In.

Another characteristic of the Pt-based bimetallic catalysts that hasn't been investigated in detail, is the evolution of the bimetallic catalysts with progressive H_2/O_2 redox cycles (Figure 3b). This is a critical aspect to research as a typical industrial process involves reaction/regeneration cycles, where the regeneration cycle entails removal of the formed coke with O_2 followed by an alloy regeneration step through reduction with H_2. In this dissertation, this was tracked for Pt:In and Pt:Sn through in situ QXAS. For Pt:In, increasing the number of redox cycles led to sintering of the NPs, while the In content in the Pt-In alloy remained quasi constant. Pt:Sn on the other hand behaved differently, in that the content of Sn in the Pt-Sn alloy increased with the redox cycles, while the NP size did not show major changes. Tracking the changes to the In K-edge edge jumps during all these in situ experiments revealed a loss of In taking place and the total In lost during these experiments was quantified to be at 24%. These losses only occurred under reductive atmosphere and at temperatures above 780 K. This behaviour of In is a possible reason for the ease with which the Pt:In NPs sinter, which is more readily than Pt:Sn. Such losses weren't detected at the Sn K-edge.

As such detailed insights were available for the Pt:In and Pt:Sn catalysts, they were then used for testing in PDH and CO_2-PDH, along with a monometallic Pt catalyst. A third catalyst, Pt:Ga (atomic ratio = 1:1.2, Pt = 3 wt%), was also included in these tests as the latter has also shown to be a viable candidate for PDH through literature review, and in addition it has a different CO_2 oxidation/reduction potential compared to In and Sn. All of these catalysts were supported on $MgAl_2O_4$ (107 m^2/g). The potential for oxidation by CO_2 is ordered as Ga > In > Sn, and corollary to this the performance for CO_2-PDH ordered as: Pt:Sn > Pt:In > Pt:Ga > Pt. In order to remove any doubt as to the inherent activity differences between the catalysts, they were tested for PDH with H_2 as a co-feed. All three catalysts (Pt:Ga, Pt:In and Pt:Sn) showed similar conversions of propane for PDH.

Changing the feed ratio of CO_2:C_3H_8 from 0 to 0.125 strongly improved the activity through combination of RWGS and reverse Boudouard reactions (Figure 3c). Higher ratios led to lower C_3H_8 conversion for all catalysts. In Pt:Ga and Pt:In, this loss was due to alloy segregation induced by CO_2, while for Pt:Sn it arose from lower availability of adsorption sites. Applying a number of H_2/O_2 redox cycles as pretreatment led to lower activity in CO_2-PDH due to an increase in promoter content in the Pt-M alloy for Pt:Ga and Pt:Sn. For Pt:In, redox cycles led to sintering of the catalyst as was found through XAS characterization and this led to a drop in activity. Equilibrium conversions were achieved for all catalysts for the RWGS reaction. Quantification of the total amount of carbon formed on unpromoted and promoted Pt for CO_2-PDH yielded the order: Pt > Pt:Ga > Pt:In > Pt:Sn, i.e. the reciprocal of the performance.

Finally, the effect of applying an alumina (Al_2O_3) coating by atomic layer deposition (ALD), with a thickness of about ~1 nm, on two Pt:Ga catalysts (Pt:Ga/$MgAl_2O_4$ & Pt/MgGaAlO) was explored for PDH. The Pt:Ga/$MgAl_2O_4$ is a sample prepared through incipient wetness impregnation of both Pt and Ga onto a spinel-type support $MgAl_2O_4$. Pt/MgGaAlO on the other hand has a hydrotalcite-type support with incorporated Ga, onto which Pt is impregnated. The 2 samples are expected to differ in the process by which the alloy formation between Pt and Ga takes place. For the Ga-incorporated sample, the Ga has to be delivered from within the support to form the Pt-Ga alloy (Figure 4), while for the sample with Pt and Ga impregnated, alloy formation should occur on the surface through mobile Pt and Ga nanoparticles.

In order to understand the effect of application of such a coating on catalyst stability, a combined experiment of SAXS and XAS was implemented. Through these techniques it has been established that the coating restricts the mobility of surface metal nanoparticles (NPs), thereby preventing sintering of the catalyst. However, for the Pt:Ga/$MgAl_2O_4$ catalyst, the presence of the coating also hindered the alloy formation between Pt and Ga. The same was not the case for the Pt/MgGaAlO catalyst, as the Ga is then delivered from the support (Figure 4). The SAXS and XAS findings were also reflected in the PDH activity tests.

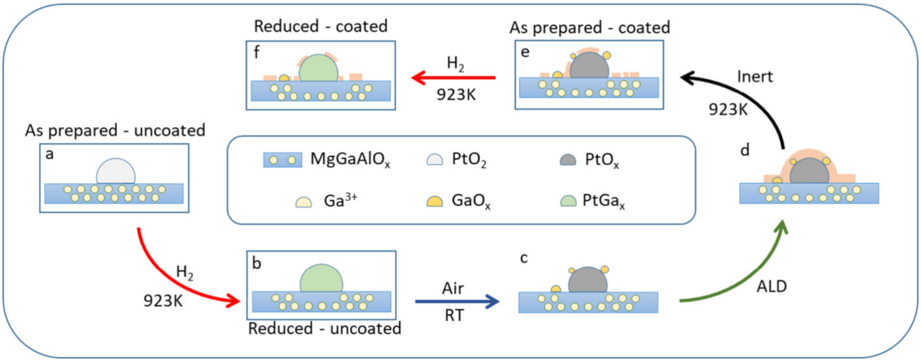

Figure 8: *Schematic for the coated and uncoated (1 nm coating) Ga-incorporated samples.* ***a:*** *as prepared state for uncoated sample.* ***b:*** *reduced state for uncoated sample. For this sample all the Pt participates in alloy formation.* ***c:*** *partial oxidation of Pt and Ga upon exposure to atmosphere leading to alloy segregation.* ***d:*** *coating with alumina by ALD leading to coated state.* ***e:*** *as prepared state for coated catalyst after inert calcination.* ***f:*** *reduced state for coated sample. Note: the fraction of Ga in Pt-Ga*$_x$ *alloy is unaffected. Whatever Ga is lost upon partial oxidation or because of hindrance of mobility due to coating on the surface, is regained through the support.*

The coated $10Al_2O_3$/Pt:Ga/$MgAl_2O_4$ performed worse than its uncoated counterpart due to the limited alloy formation in presence of the coating. Testing of the coated and uncoated Pt/MgGaAlO catalysts for PDH after 1, 5 and 10 H_2/O_2 redox cycles was performed in order to see the effect of the coating on activity and stability. The coating was found to reduce the total amount of carbon formed during PDH and the rate of deactivation for the coated sample proved slower than for the uncoated counterpart. Furthermore, a direct correlation between increasing coating thickness and a decreased activity for PDH was confirmed. However, when compared at similar conversions of propane, the increasing coating thickness led to lower carbon formation. Finally, the coated and uncoated Pt/MgGaAlO samples were subjected to 40 redox cycles in total and subsequently examined with scanning transmission electron microscopy (STEM DF). Through particle size distributions from STEM images, it was determined that the coating reduced the extent of sintering of the sample. The direct correlation between increased coating thickness and lower extent of sintering of the surface metal nanoparticles was established.

The major challenge for Pt-based bimetallic catalysts, determined through all these studies, is the ability to maintain a constant promoter content in the Pt-M alloy throughout the catalyst lifetime. The changes in promoter content in the alloy that occur during the regeneration steps affect the performance for CO_2-PDH and PDH. One means to circumvent this would be to prepare phase-pure nanoalloys, through e.g. colloidal synthesis, and then deposit them onto a support such as $MgAl_2O_4$. This can be followed by application of a coating such as alumina through ALD to stabilize the nanoparticles and prevent compositional changes to the alloy during the catalyst regeneration steps. Another possibility could be to prepare the catalyst through conventional impregnation techniques on a $MgAl_2O_4$ support and subject the catalyst to about 3 to 5 H_2/O_2 redox cycles followed by a coating application to prevent further major alloy compositional changes. In the case of a hydrotalcite-type support, the challenge would be the choice of loading of the promoter that has to be incorporated into the support. If the loading is too high, then with increased H_2/O_2 redox cycles, the promoter content in the alloy will continuously increase even in presence of a coating, as the promoter is delivered from within the support. Another aspect that could be investigated is the behaviour of a Pt:Sn catalyst that is coated for CO_2-PDH. Since the coating helps to suppress carbon formation, there is a possibility of longer activity lifetime for such a coated Pt:Sn catalyst in CO_2-PDH.

Samenvatting

Alkaan dehydrogenering is een belangrijke syntheseroute voor selectieve alkeenproductie en een van de belangrijkste alkaan dehydrogeneringsprocessen is propaan dehydrogenering (PDH), waarmee propyleen wordt gevormd. De wereldwijde vraag naar propyleenderivaten, zoals polypropyleen, zal naar verwachting toenemen, waardoor de vraag naar propyleen met een hoge zuiverheid navenant stijgt. Vandaag de dag is er een probleem met betrekking tot de wereldwijde klimaatverandering en de noodzaak om de uitstoot van broeikasgassen zoals CO_2 of CH_4 te verminderen. Een van deze broeikasgassen, CO_2, kan in combinatie met propaan in de voeding worden gebruikt om een door CO_2 ondersteund propaan dehydrogeneringsproces te ontwikkelen, wat kan helpen om wat CO_2 te verbruiken. Dit CO_2-verbruik zou volgen uit de omgekeerde watergasverschuivingsreactie (RWGS), waarbij de H_2 die door PDH wordt gevormd, reageert met CO_2 uit de voeding om CO en H_2O te vormen. Dit kan op zijn beurt helpen om het evenwicht van de PDH-reactie te verschuiven naar productvorming, wat de toevoeging van CO_2 dubbel voordelig zou maken, nl. leidend tot een hogere propaanomzetting én CO_2-verbruik. CO_2 kan ook bijdragen aan het mitigeren van de vorming van koolstof via de omgekeerde Boudouard reactie, waardoor de levensduur van de katalysator wordt verlengd. De meeste van de bestaande industriële dehydrogeneringsprocessen maken gebruik van op Pt gebaseerde bimetaalkatalysatoren (meestal Pt:Sn of Pt:Ga gedragen op $ZnAl_2O_4$ of $MgAl_2O_4$). Daarom is het voor de ontwikkeling van CO_2-geassisteerde propaan dehydrogenering noodzakelijk om het effect van CO_2-toevoeging op dergelijke katalysatoren te testen.

Naast CO_2-toevoeging zijn er nog andere manieren om het PDH-proces te verbeteren, b.v. door het aanpassen van de katalysatorsynthese. Een veelbelovend middel is het aanbrengen van een coating op de katalysator, die kan helpen bij het voorkomen van sinteren en daardoor tot een langere levensduur van de katalysator leidt. Een dergelijke toevoeging van coating kan echter ook tot andere effecten leiden en tot op heden is een coating niet toegepast op een bimetaalkatalysatorsysteem. Daarom is zorgvuldig onderzoek van de nanodeeltjes vereist in aanwezigheid van een dergelijke coating om het effect op de prestaties te bepalen.

In dit proefschrift is zowel het effect van CO_2-toevoeging in de voeding als van toevoeging van een coating op de integriteit van op Pt gebaseerde bimetaallegeringen onderzocht. De belangrijkste techniek die voor deze analyse wordt gebruikt, is röntgenabsorptiespectroscopie (XAS), gedeeltelijk uitgebreid met kleine hoek röntgenverstrooiing (SAXS). Deze worden aangevuld met katalytische activiteitstesten voor PDH en CO_2-PDH om de katalysator volledig te begrijpen.

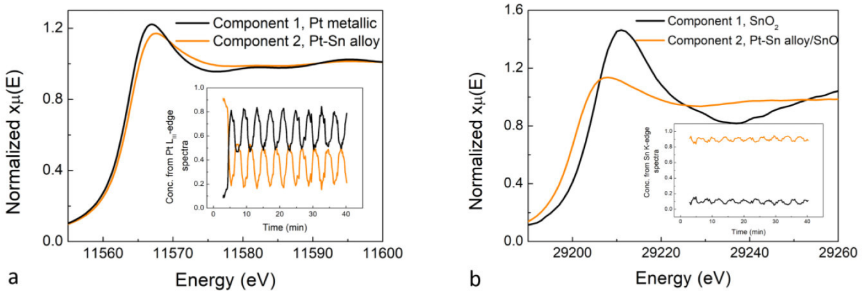

***Figuur 1:** MCR-ALS bepaling aan **a:** Pt L_{III}-rand & **b:** Sn K-rand voor Pt:Sn/HSA.*

In eerste instantie wordt voor CO_2-PDH een Pt:Sn-katalysator gedragen op $MgAl_2O_4$ onderzocht met een oppervlakte van ~127 m^2/g of ~5 m^2/g, 3 gew.% Pt en een Pt:Sn molverhouding van 3:1. Het verschil in beschikbare oppervlakte leidde bij impregnatie tot verschillende groottes aan nanodeeltjes, die bij reductie aanleiding gaven tot verschillende Sn-gehaltes in de Pt-Sn-legering. XAS werd In situ gebruikt om de dynamische veranderingen te volgen die optreden in de katalysator in aanwezigheid van een reductieve (H_2) of oxidatieve (CO_2) atmosfeer. Pt-Sn-legeringsvorming werd gedetecteerd na reductie onder H_2. Oxidatie door CO_2 leidde tot verlies van de Pt-Sn-legering door eerst oxidatie van Sn tot SnO en vervolgens oxidatie van SnO tot SnO_2. Modellering van de verkregen EXAFS-gegevens hielp bij het bepalen van de elektronische en structurele eigenschappen. Een big data-analysemethode, Multivariate Curve Resolution-Alternating Least Squares (MCR-ALS, figuur 1), werd gebruikt in combinatie met de XAS-gegevens en bleek een waardevol hulpmiddel te zijn om de hoeveelheid Sn te bepalen die aanwezig is in de Pt-Sn-legeringsfase evenals de fase van de Pt-Sn-legering zelf: na een reductie in één stap ging 42% van alle Sn in de Pt_3Sn-legering en nam deel aan de reactie, terwijl de rest als SnO_x aanwezig was. Het percentage Sn dat in de Pt_3Sn-legering terechtkwam, nam na 10 H_2/CO_2-redoxcycli toe tot 72%.

De katalysator werd vervolgens getest op CO_2-PDH, met een CO_2:C_3H_8-verhouding van 0,25:1 tot 1:1. Lagere verhoudingen bleken beter te werken omdat de Pt-Sn-legering in dergelijke gevallen stabieler is in vergelijking met hogere verhoudingen. Meer CO_2 leidde tot de oxidatie van Sn tot SnO_x en dus tot het verlies van de Pt-Sn-legering. Onderdrukking van koolstofaccumulatie werd gedetecteerd, wat optrad door middel van de omgekeerde Boudouard-reactie met de tijdens PDH gevormde koolstof. Als mogelijk reactienetwerk voor de gehele CO_2-PDH-reactie werd een combinatie van Langmuir-Hinshelwood (L-H) en Mars-van Krevelen-mechanisme (MvK) voorgesteld (Figuur 2). De MvK-stappen omvatten de oxidatie door CO_2 van Sn tot SnO, waarbij de promotor uit de legering wordt geëxtraheerd, die vervolgens zou reageren met de H_2 en koolstof gegenereerd uit PDH die plaatsvindt op Pt-plaatsen via het LH-mechanisme, om terug te gaan naar de Pt_3Sn-legering.

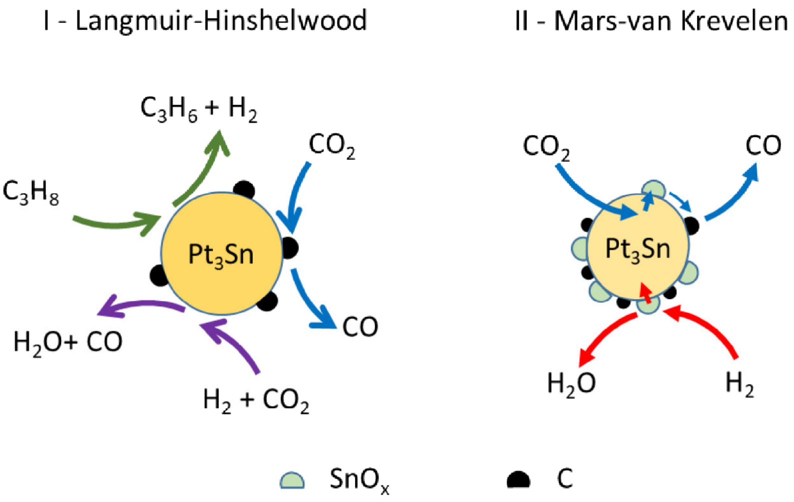

Figuur 2: *Schematische weergave van alle reacties die optreden op een Pt:Sn-katalysator tijdens CO_2-PDH. Deel I van het schema geeft alle reacties weer die plaatsvinden op de katalysator door het Langmuir-Hinshelwood-mechanisme, terwijl deel II de reacties weergeeft die plaatsvinden door het Mars-van Krevelen-mechanisme. Alle reacties vinden gelijktijdig plaats. De katalysator gaat van deel I naar deel II in aanwezigheid van CO_2, dat Sn tot SnO_x zal oxideren, waardoor Sn van de Pt_3Sn-legering zal worden gescheiden en dan terug gaat naar deel I via reductie door H_2 gegenereerd uit PDH. (—) reductie, (—) oxidatie, (—) PDH reactie, (—) RWGS reactie.*

Omdat legeringssegregatie werd gedetecteerd voor Pt:Sn, werd een nieuwe set katalysatoren bereid: Pt:Sn en Pt:In, met in dit geval hogere promotorbeladingen dan in de eerste set Pt:Sn-katalysatoren (1:1,5 versus 3:1 eerder). Deze beide katalysatoren werden gedragen op

$MgAl_2O_4$ (107 m^2/g). De belading van Pt werd constant gehouden op 3 gew.%. In werd gekozen als een tweede promotor omdat het verschillende oxidatie-/reductiepotentialen heeft in vergelijking met Sn en het zelf ook gebruikt wordt als PDH-katalysator. XAS-metingen werden uitgevoerd tijdens CO_2-TPO na reductie van beide katalysatoren en uit deze experimenten werd geconcludeerd dat Sn en In in die monsters bij lage temperatuur, d.w.z. <500 K, beginnen te oxideren naar hun respectieve oxides.

Verdere gedetailleerde karakterisering van Pt:In- en Pt:Sn-katalysatoren werd uitgevoerd via in situ QXAS gekoppeld aan modulatie-excitatiespectroscopie (MES, figuur 3a), op basis van perturbatie van de gasvoeding. MCR-ALS bleek niet zo waardevol te zijn als bij het monster met een lager Sn-gehalte, omdat de snelheid waarmee de legering onder CO_2 verloren ging nu veel langzamer was voor het hogere Sn-gehalte. Wat Pt:In betreft, deze katalysator verloor de legeringsfase sneller dan Pt:Sn. Door MES-analyse van de Pt L_{III}-edge werd vastgesteld dat het In-gehalte aan het oppervlak van de Pt:In-nanodeeltjes (NP's) met de tijd toenam en In-rijk werd in vergelijking met de bulk, in tegenstelling tot Pt:Sn. In feite vond er een omkeerbaar proces plaats voor het Pt:In-monster, waarbij het monster oscilleerde tussen twee verschillende Pt-In-legeringsfasen. Er werd gekwantificeerd dat ongeveer 11 atomen per 100 actief deelnamen aan dit proces. Pt:Sn vertoonde in vergelijking een veel lagere gevoeligheid voor de opgelegde veranderingen, waarbij slechts 1 atoom op 100 reageerde.

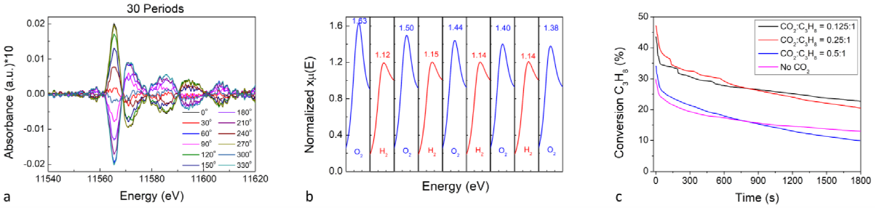

Figuur 3: a: *Gedemoduleerde spectra bestaande uit 24 spectra uitgemiddeld over 30 perioden voor de Pt:In-katalysator,* ***b:*** *gegevens voor Pt:Sn waarbij waarden in de grafieken de Pt L_{III}-rand piekhoogte weergeven die is bereikt aan het einde van een halve cyclus van 20 minuten in H_2 of O_2,* ***c:*** *C_3H_8-conversiegrafieken met verschillende voedingsverhoudingen voor CO_2-PDH over een Pt:Sn-katalysator.*

Aangezien de belangrijkste factor die de legeringsstabiliteit tijdens CO_2-PDH bepaalt, de verhouding tussen H_2 en CO_2 is, waarbij H_2 voortkomt uit de dehydrogenering van propaan, werd RWGS gekozen als modelreactie om de stabiliteit van de Pt-In- en Pt-Sn-legeringen te onderzoeken. Voor de in situ QXAS-metingen werden drie verschillende H_2:CO_2-

stroomsamenstellingen geselecteerd (1:1, 1:3 en 1:5). Toenemende CO_2 leidde tot een groter aantal oppervlakspecies die in reactie waren, waarbij de betrokkenheid ongeveer 12% was voor Pt:In. De kinetiek van verandering was langzamer voor Pt:Sn in vergelijking met Pt:In. Een ander kenmerk van de op Pt gebaseerde bimetaalkatalysatoren dat niet in detail is onderzocht, is de evolutie van de bimetaalkatalysatoren met progressieve H_2/O_2-redoxcycli (Figuur 3b). Dit is een cruciaal onderzoeksaspect, aangezien een typisch industrieel proces reactie-/regeneratiecycli omvat, waarbij de regeneratiecyclus inhoudt dat de gevormde cokes met O_2 wordt verwijderd, gevolgd door een regeneratiestap van de legering door reductie met H_2. In dit proefschrift is dit bestudeerd voor Pt:In en Pt:Sn via in situ QXAS. Voor Pt:In leidde het verhogen van het aantal redox-cycli tot sinteren van de NP's, terwijl het In-gehalte in de Pt-In-legering quasi constant bleef. Pt:Sn gedroeg zich daarentegen anders, in die zin dat het gehalte aan Sn in de Pt-Sn-legering toenam met de redoxcycli, terwijl de NP-grootte geen grote veranderingen vertoonde. Het volgen van de verandering van de In K-staprand tijdens al deze in situ-experimenten bracht een verlies van In aan het licht en de totale In hoeveelheid die tijdens deze experimenten verloren ging, werd gekwantificeerd op 24%. Deze verliezen traden alleen op onder reductieve atmosfeer en bij temperaturen boven 780 K. Dit gedrag van In is een mogelijke reden voor het gemak waarmee de Pt:In NP's sinteren, heel wat vlotter dan Pt:Sn. Dergelijke verliezen werden niet gedetecteerd aan de Sn K-edge.

Omdat dergelijke gedetailleerde inzichten beschikbaar waren voor de Pt:In- en Pt:Sn-katalysatoren, werden beide vervolgens gebruikt voor testen in PDH en CO_2-PDH, samen met een monometallische Pt-katalysator. Een derde katalysator, Pt:Ga (atoomverhouding = 1:1,2, Pt = 3 gew.%), werd ook in deze tests opgenomen, aangezien deze laatste ook een mogelijke kandidaat voor PDH bleek te zijn op basis van literatuuronderzoek, en bovendien heeft het een ander CO_2-oxidatie-/reductiepotentieel in vergelijking met In en Sn. Al deze katalysatoren werden gedragen op $MgAl_2O_4$ (107 m^2/g). Het potentieel voor oxidatie door CO_2 volgt als rangorde Ga > In > Sn, en in het verlengde hiervan is de prestatie voor CO_2-PDH geordend als: Pt:Sn > Pt:In > Pt:Ga > Pt. Om elke twijfel over de inherente activiteitsverschillen tussen de katalysatoren weg te nemen, werden ze getest op PDH met H_2 als bijvoeding. Alle drie de katalysatoren (Pt:Ga, Pt:In en Pt:Sn) vertoonden vergelijkbare propaanconversies in PDH.

Het veranderen van de gasverhouding van CO_2:C_3H_8 van 0 naar 0,125 verbeterde de activiteit sterk door combinatie van RWGS en omgekeerde Boudouard-reacties (Figuur 3c). Nog hogere verhoudingen leidden tot een lagere C_3H_8-conversie voor alle katalysatoren. In Pt:Ga en Pt:In was dit verlies het gevolg van segregatie van de legeringen veroorzaakt door CO_2, terwijl het voor Pt:Sn voortkwam uit een lagere beschikbaarheid van adsorptieplaatsen. Het toepassen van een aantal H_2/O_2-redoxcycli als voorbehandeling leidde tot een lagere activiteit in CO_2-PDH door een toename van het promotorgehalte in de Pt-M-legering voor Pt:Ga en Pt:Sn. Voor Pt:In leidden redoxcycli tot sinteren van de katalysator, zoals werd gevonden door middel van XAS-karakterisering, en dit leidde tot een daling van de activiteit. Voor de RWGS-reactie v werden voor alle katalysatoren evenwichtsconversies bereikt. Kwantificering van de totale hoeveelheid koolstof gevormd op niet-gepromoveerd en gepromoveerd Pt voor CO_2-PDH leverde volgende rangorde op: Pt > Pt:Ga > Pt:In > Pt:Sn, d.w.z. het omgekeerde van de prestatie.

Tenslotte werd het effect onderzocht van het aanbrengen van een alumina (Al_2O_3) coating door atomaire laagafzetting (ALD), met een dikte van ongeveer ~1 nm, op twee Pt:Ga-katalysatoren (Pt:Ga/$MgAl_2O_4$ & Pt/MgGaAlO) voor PDH. Het Pt:Ga/$MgAl_2O_4$ is een monster dat is bereid door beginnende natte impregnatie van zowel Pt als Ga op een spinel-achtige drager $MgAl_2O_4$. Pt/MgGaAlO daarentegen heeft een drager van het hydrotalciet-type met ingebouwd Ga, waarop Pt is geïmpregneerd. De 2 monsters zullen naar verwachting verschillen in de manier waarop legeringsvorming tussen Pt en Ga plaatsvindt. Voor het met Ga geïncorporeerde monster moet het Ga vanuit de drager worden geleverd om de Pt-Ga-legering te vormen (Figuur 4), terwijl voor het monster met geïmpregneerd Pt en Ga legeringsvorming op het oppervlak moet plaatsvinden via mobiele Pt en Ga nanodeeltjes.

Om het effect van het aanbrengen van een dergelijke coating op de stabiliteit van de katalysator te begrijpen, werd een gecombineerd SAXS-XAS experiment uitgevoerd. Met deze technieken is vastgesteld dat de coating de mobiliteit van metaal nanodeeltjes (NP's) aan het oppervlak beperkt, waardoor sinteren van de katalysator wordt voorkomen. Voor de Pt:Ga/$MgAl_2O_4$-katalysator belemmerde de aanwezigheid van de coating echter ook de legeringsvorming tussen Pt en Ga. Dit was evenwel niet het geval voor de Pt/MgGaAlO-katalysator, omdat het Ga nu vanuit de drager wordt aangeleverd (Figuur 4). De bevindingen van SAXS en XAS werden ook weerspiegeld in de PDH-activiteitstesten.

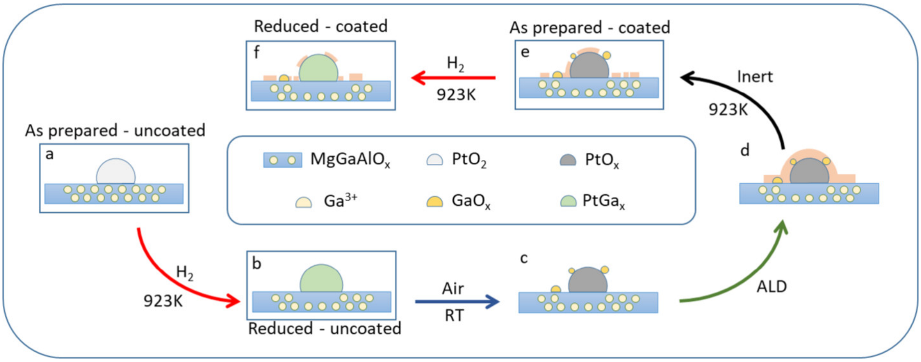

Figuur 4: *Schema voor de gecoate en niet-gecoate (1 nm) Ga-geïncorporeerde monsters.* ***a:*** *als bereide staat voor niet-gecoat monster.* ***b:*** *gereduceerde toestand voor niet-gecoat monster. Voor dit monster neemt al het Pt deel aan de vorming van legering.* ***c:*** *gedeeltelijke oxidatie van Pt en Ga bij blootstelling aan de atmosfeer, wat leidt tot segregatie van legering.* ***d:*** *coating met aluminiumoxide door ALD leidend tot gecoate toestand.* ***e:*** *als bereide toestand voor de gecoate katalysator na inerte calcinering.* ***f:*** *gereduceerde toestand voor gecoat monster. Opmerking: de fractie van Ga in de Pt-Ga$_x$-legering wordt niet beïnvloed. Al het Ga dat verloren gaat bij gedeeltelijke oxidatie of vanwege belemmering van de mobiliteit door de coating op het oppervlak, wordt teruggewonnen via de drager.*

De gecoate $10Al_2O_3$/Pt:Ga/$MgAl_2O_4$ presteerde slechter dan zijn niet-gecoate tegenhanger vanwege de beperkte legeringsvorming in aanwezigheid van de coating. De gecoate en niet-gecoate Pt/MgGaAlO-katalysatoren werden getest in PDH na 1, 5 en 10 H_2/O_2-redoxcycli om het effect van de coating op activiteit en stabiliteit te zien. De coating bleek de totale hoeveelheid koolstof die tijdens PDH werd gevormd te verminderen en de snelheid van deactivering voor het gecoate monster bleek langzamer dan voor de niet-gecoate tegenhanger. Verder werd een directe correlatie tussen toenemende laagdikte en een verminderde activiteit voor PDH bevestigd. Voor vergelijkbare propaanconversies leidde een toenemende laagdikte echter tot een lagere koolstofvorming. Tenslotte werden de gecoate en niet-gecoate Pt/MgGaAlO-monsters onderworpen aan in totaal 40 redoxcycli en vervolgens onderzocht met scanning transmissie-elektronenmicroscopie (STEM DF). Door middel van deeltjesgrootteverdelingen van STEM-beelden werd vastgesteld dat de coating de mate van sintering van het monster verminderde. Grotere coatingdikte vertoonde een directe correlatie met een lagere graad van sintering van de metaal nanodeeltjes aan het oppervlak.

Op basis van dit onderzoekswerk ligt de belangrijkste uitdaging voor Pt-gebaseerde bimetaalkatalysatoren in het vermogen om een constant promotorgehalte in de Pt-M-legering te behouden gedurende de hele levensduur van de katalysator. De veranderingen in het promotorgehalte in de legering die optreden tijdens de regeneratiestappen beïnvloeden de prestaties voor CO_2-PDH en PDH. Een manier om dit te omzeilen zou zijn om fase-zuivere nanolegeringen te bereiden, door b.v. colloïdale synthese en daaropvolgende depositie op een drager zoals $MgAl_2O_4$. Dit kan worden gevolgd door het aanbrengen van een coating zoals aluminiumoxide via ALD om de nanodeeltjes te stabiliseren en veranderingen in de samenstelling van de legering tijdens de regeneratiestappen van de katalysator te voorkomen. Een andere mogelijkheid zou kunnen zijn om de katalysator te bereiden door middel van conventionele impregnatietechnieken op een $MgAl_2O_4$-drager en de katalysator te onderwerpen aan 3 tot 5 H_2/O_2-redoxcycli, gevolgd door een coatingtoepassing om verdere grote veranderingen in de samenstelling van de legering te voorkomen. In het geval van een drager van het hydrotalciet-type ligt de uitdaging in de keuze van de belading van de promotor die in de drager moet worden opgenomen. Als de belading te hoog is, dan zal met verhoogde H_2/O_2-redoxcycli het promotorgehalte in de legering continu toenemen, zelfs in aanwezigheid van een coating, omdat de promotor wordt aangeleverd vanuit de drager. Een ander aspect dat zou kunnen worden onderzocht, is het gedrag van een Pt:Sn-katalysator die is gecoat voor CO_2-PDH. Aangezien de coating helpt om koolstofvorming te onderdrukken, kan dit leiden tot een langere levensduur van de activiteit voor een dergelijke gecoate Pt:Sn-katalysator in CO_2-PDH.

Chapter 1

Introduction

1.1 Background

Propylene is one of the most important compounds in industry. With an annual production of about 140 million tonnes (2022 projected), it is the second most important olefin. Ethylene, with a production of 205 million tonnes (2022 projected), comes in first place. A majority of the propylene produced is consumed in the production of polypropylene (Figure 1.1) through the polymerization process. Polypropylene is the most widely used thermoplastic polymer and a key material for plastic parts applied in several industries, including packaging, electronics and electrical, automotive, textile, living hinges and more. Other derivatives of propylene find application in various branches, including Cosmetics and Personal Care, Food & Beverage, Pharmaceuticals, Building & Construction, Automotive and others (textile, paper and pulp, electronics, consumer goods, chemicals). Therefore, the major end-use industries are Automotive, Packaging, Construction and Textiles. Hence, growth in these sectors will augment the demand for propylene.[1]

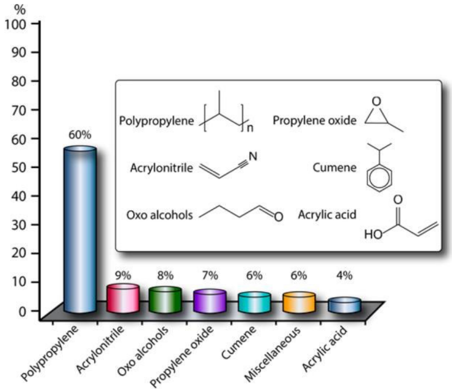

Figure 1.1: *Main propylene derivates in industry.*[2]

Asia-Pacific at present dominates the market for propylene globally and the current projections indicate further growth in demands due to booms in the automobile, construction, packaging and textile sectors in the region. A way to show this is to compare the global average consumption of plastics per capita (HDPE, LLDPE, LDPE, PP, etc), which is 28 kg/annum (Table 1.1), while for a developing nation like India, it currently lies at ~11 kg/annum. The actual number for a developed nation such as the USA is 109 kg/capita. If the population numbers are taken into account, then it is quite apparent that the propylene demand is bound to rise in Asia-Pacific.

Table 1.4: *Per capita plastic consumption per year in kg and the respective plastic waste generation per annum.*[3–5]

Nation	Per capita consumption (kg)	Plastic waste generation per annum (mil tons)
USA	109	37.83
Europe	65	40.12
China	38	5.98
Brazil	32	11.8
Global average	28	-
India	11	4.49

*Data from 2019

It is commonly stated that there is a “Propylene gap” which has to be filled.[6,7] As of today (December 2021), there is a real possibility to produce an excess of propylene, compared to the demands, but the production is actually lower than the demands (Figure 1.2). In 2012, it was expected that this gap between propylene production and demand would continue to grow until 2020.[6] Yet, in 2019, it was foreseen that this trend would persist.[8] In 2015, it was estimated that the supply was already 14 % below the demand.[7] This phenomenon can be ascribed to two evolutions. First, the rate at which new steam crackers or FCC units are being built, is outgrown by the rate at which the propylene demand increases.[9] Secondly, propylene is only a by-product of the latter two processes.[9,10] This is a problem especially with steam cracking as the product yield is heavily dependent on feedstock and operating conditions.[6] In recent years, this feedstock has shifted mainly from naphtha towards ethane, driven by the increasing availability and decreasing prices of ethane from shale gas.[10,11] This is particularly the case for the Middle East and North America,[9] but other markets could be influenced as well due to decreasing transportation costs of ethane.[10] Steam cracking with lighter feedstocks, especially ethane, results in lower propylene yields compared to naphtha.[6] Consequentially, the propylene production via steam cracking has fallen in recent years.[7,9,11]

The “propylene gap” can be filled by on-purpose propylene production technologies, such as propane dehydrogenation (PDH, eq. 1.1), methanol to olefins (MTO) and methanol to propylene (MTP). As of today, PDH is the primary process for on-purpose propylene production and it is expected to maintain that position.

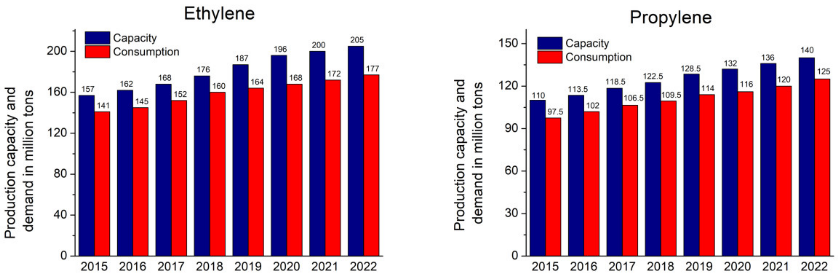

Figure 1.2: *Ethylene and propylene demand and production capacity worldwide from 2015 to 2022.*[12,13]

1.2 Propane Dehydrogenation (PDH)

1.2.1 Non-oxidative PDH

In PDH, propane is catalytically converted to propylene (eq. 1.1). The reaction is endothermic and equilibrium limited as the number of moles of gases increases. As per Le Chatelier's principle, this equilibrium can be shifted towards the products by reducing the partial pressure of propane and increasing the reaction temperature. Therefore, PDH is typically conducted at temperatures of about 823-873 K and leads to a propane conversion of ~50% at 1 bar (Figure 1.3a). The partial pressure is reduced by the addition of steam as a diluent (industrial processes), so as to shift the equilibrium towards the products.[14] The presence of steam however, leads to a much higher energy demand, but on the other hand it helps to control the carbon formation on the catalyst.

$$C_3H_{8\,(g)} \leftrightharpoons C_3H_{6\,(g)} + H_{2\,(g)} \qquad \Delta H_{298} = +124.3\ \mathrm{kJ/mol} \quad (1.1)$$

$$C_3H_{6\,(g)} \leftrightharpoons C_3H_{4\,(g)} + H_{2\,(g)} \qquad \Delta H_{298} = +164.9\ \mathrm{kJ/mol} \quad (1.2)$$

$$C_3H_{8\,(g)} \leftrightharpoons 3C_{(s)} + 4H_{2(g)} \qquad \Delta H_{298} = +104.6\ \mathrm{kJ/mol} \quad (1.3)$$

Further dehydrogenation of the formed propylene is also a possibility (eq. 1.2), which would thereby reduce the selectivity towards propylene. Deep dehydrogenation (eq. 1.3) entails the conversion of propane to coke and hydrogen. All these processes are endothermic and the deep dehydrogenation products are the main precursors to coke formation (e.g. CCH_3 and CH) on the catalyst, which then assists towards its deactivation through blockage of active sites.[15–17] The implication from this is that a catalyst has to be selected, which has the potential to interact with propane strongly enough to dehydrogenate it, but at the same time interact weakly with the formed propylene. Typically, a Pt-based catalyst is employed for this process, which has tendency to interact more strongly with propylene than with propane.[17] Co-feeding of hydrogen with propane can assist to partially overcome this problem. Hydrogen coverage of the catalytic surface leads to a lower coverage with deeply dehydrogenated products, weakens the interaction between propylene and the catalyst surface, and increases the energy barrier for further dehydrogenation of olefins.[18]

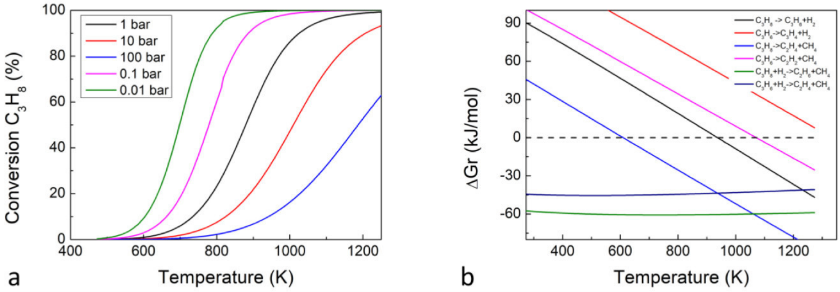

Figure 1.3: a: *Equilibrium conversion of C_3H_8 at varying temperatures and pressures for non-oxidative PDH.* ***b:*** *Gibbs free energy of reaction at 1 bar. Data obtained from pure component analysis in Aspen Plus v11. Results in accordance with* [19].

Side reactions: A multitude of side reactions can occur parallel to the dehydrogenation reaction, such as hydrogenolysis, cracking and isomerization. These are the result of thermal and catalytic processes. The reason for the side reactions is due to the higher reactivity of the olefins compared to the paraffins from the presence of the pi electrons. All of these reactions require catalytic sites of a specific nature.[15]

Hydrogenolysis consists of C-C bond scission followed by the addition of hydrogen to the fragments (eq. 1.7, 1.8). This typically takes place on the low coordinated sites of Pt. Cracking on the other hand can occur through both thermal and catalytic processes (eq. 1.5, 1.6). At the operating conditions for PDH, thermal cracking has no noteworthy occurrence when compared to the catalytic counterpart, which is facilitated by large Pt ensembles. Catalytic cracking requires a carbocation intermediate, which would require both Bronsted and Lewis acid sites. Isomerization typically has a relatively low change of standard reaction enthalpies, since only a change in structure takes place. This is illustrated in eq. 1.4 for the isomerization between propyne and propadiene. Isomerization reactions are often facilitated over larger Pt ensembles and occur via species located on either Bronsted acid sites or sites active for PDH.[15,20]

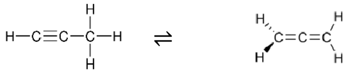

ΔH_{298} = +3.8 kJ/mol (1.4)

$C_3H_{8\,(g)} \leftrightharpoons C_2H_{4(g)} + CH_{4(g)}$ ΔH_{298} = +82.6 kJ/mol (1.5)

$C_3H_{6\,(g)} \leftrightharpoons C_2H_{2(g)} + CH_{4(g)}$ ΔH_{298} = +132.1 kJ/mol (1.6)

$C_3H_8 + H_2 \leftrightharpoons C_2H_6 + CH_4$ ΔH_{298} = -53.9 kJ/mol (1.7)

$C_3H_6 + H_2 \leftrightharpoons C_2H_4 + CH_4$ ΔH_{298} = -42.1 kJ/mol (1.8)

Compromises: The dehydrogenation reaction occurs through C-H bond cleavage, while a majority of the side reactions proceed through C-C bond cleavage.[15] High temperature operation promotes the C-H bond cleavage and thereby an equilibrium propane conversion. However, the undesired C-C bond cleavages are promoted through kinetics and thermodynamics at these conditions. This is illustrated through the Gibbs free energy of reaction vs. temperature plots (Figure 1.3b). With increasing temperature, both dehydrogenation reactions and side reactions shift towards thermodynamically more spontaneous behaviour. It follows that a compromise between selectivity and conversion should be made when specifying a reaction temperature. Additionally, the catalyst design is also subject to compromise at first sight. Acidic sites favour the adsorption of both the necessary propane and hydrogen, but also facilitate side reactions.

Catalyst deactivation: Deactivation of the employed catalyst with time-on-stream (TOS) usually occurs through carbon formation, leading to blocking of active sites, and sintering due to high temperature operation. For this reason, a regeneration cycle is generally employed, which consists of first exposing the catalyst to oxygen to burn off the coke deposits through combustion, followed by a hydrogen treatment to regenerate the reduced state, i.e. the active phase for dehydrogenation.

The precursors of coke-forming processes result from deep dehydrogenation and side reactions, which in turn require specific sites. These coke precursors then polymerize into graphene-like structures.[15,18] Catalyst deactivation that can be ascribed to coke formation has been observed for Pt-, V-, and Cr-based catalysts.[21] In a literature review article, Sattler et al.[15] report that coke formation is generally facilitated by acid sites on the catalyst surface, as well as by certain site geometries. The exact coke forming mechanisms can differ per catalyst type. For Pt-based catalysts specifically, the geometries that contribute to coke formation are larger Pt ensembles and undercoordinated sites (i.e. steps, edges, etc).[22,23] Vu et al.[24] showed through the use of XRD, XPS and TPO that pre-graphite-like carbon is the main component of coke on a Pt-Sn/Al_2O_3 catalyst. Redekop et al.[25] reported that coke on a Pt/Mg(Al)O_x catalyst is composed of graphene sheets. It was also determined that the graphene sheets formed on small NPs (1.5-2 nm) would continuously shift onto the support, while larger particles (5-10 nm) form encapsulating graphitic layers. Wang et al.[26] identified three types of coke to form for a Pt:Sn catalyst: pre-graphite, aromatics, and aliphatics. The aliphatics, aromatics and pre-graphite accounted for 69.0 wt%, 4.4 wt% and 26.6 wt%, respectively.

Sintering, on the other hand, is an irreversible process compared to coke formation. It will lead to a reduction in active sites availability. Sintering has been observed for Pt-based catalysts and to a lesser extent Cr-based catalysts. V-based catalysts are more resistant to sintering.[21] Generally, sintering is facilitated if the interaction between the active metal and the support is weak, or if the operating temperature is above the Hüttig and/or Tamman temperature. At the Hüttig temperature ($\sim 0.3 \cdot T_{melt}$), sintering of atoms at a particle's surface starts to occur because the temperature becomes sufficiently high to allow diffusion of atoms into the lattice. At the Tamman temperature ($\sim 0.5 \cdot T_{melt}$), also bulk atoms gain sufficient mobility to take part in the sintering process.[27] Sintering is also caused during the regeneration step for Pt-based catalysts. Regeneration involves the treatment of the catalyst in a high temperature oxidative atmosphere, which results in sintering of the Pt particles mainly through the Ostwald ripening mechanism and subsequently irreversible catalyst deactivation. The Tamman temperature for Pt is 1023 K.[28–30]

1.2.2 Oxidative dehydrogenation of propane (ODP) & CO_2-assisted PDH (CO_2-PDH)

The issues associated with PDH that have been discussed so far were the deactivation through carbon formation due to cracking and side reactions, and sintering of the catalyst. Thermodynamics is also an aspect that can be an issue as PDH is equilibrium limited. A means to overcome this would be to employ oxidative dehydrogenation of propane with O_2, N_2O, SO_2 or CO_2.[2,31–34] The idea is to consume the formed product H_2 with the inlet oxidant in order to shift the equilibrium towards the products. An added benefit lies in the fact that this oxidant can also consume the formed carbon and in turn suppress total carbon formation. The use of N_2O and SO_2 is not recommended from a safety point of view and hence most literature is focussed on O_2 and CO_2.[31,33]

The advantage of using oxygen to perform oxidative dehydrogenation of propane (ODP) is that it allows to avoid equilibrium limitations even at lower temperatures than PDH, as it is an exothermic process (eq. 1.9).[32] The drawback is that it makes heat control essential and can lead to accelerated sintering of the catalyst through temperature increases. Another drawback is the possibility of deep oxidation of propane and propylene to CO_x, which inevitably leads to loss of selectivity and yield of propylene.[32,35]

$$C_3H_{8\,(g)} + 0.5O_2 \leftrightharpoons C_3H_{6\,(g)} + H_2O_{(g)} \qquad \Delta H_{298} = -117.6 \text{ kJ/mol} \quad (1.9)$$

The alternative can be to use a mild oxidant such as CO_2, which would help negate the problem with deep oxidation. CO_2 has a low cost, high availability and as a greenhouse gas its active utilization is recommended.[31,36] CO_2 can help to increase the conversion of propane by consumption of produced H_2 through the reverse water gas shift reaction (RWGS), (eq. 1.10), thereby shifting the dehydrogenation reaction towards product formation. Prior studies have shown that the RWGS reaction accelerates the formation of propylene and promotes its desorption from the catalyst surface.[37,38] As additional advantage, CO_2 can react with surface carbon by means of the reverse Boudouard reaction (eq. 1.11) to mitigate carbon formation. Oxidative dehydrogenation of propane by CO_2 (CO_2-PDH) (eq. 1.12) and propane dry reforming (DRP, eq. 1.13) are two possible pathways by which CO_2 and propane can react. The difference between CO_2-PDH and ODP is that in contrast to the latter, CO_2-PDH is an endothermic process (ΔH_{298} = +164 kJ/mol), allowing more control over temperature.

$CO_{2\,(g)} + H_{2\,(g)} \leftrightharpoons CO_{(g)} + H_2O_{(g)}$ $\Delta H_{298} = +41$ kJ/mol (1.10)

$C + CO_2 \leftrightharpoons 2CO$ $\Delta H_{298} = +172$ kJ/mol (1.11)

$CO_2 + C_3H_8 \leftrightharpoons C_3H_6 + CO + H_2O$ $\Delta H_{298} = +164$ kJ/mol (1.12)

$3CO_2 + C_3H_8 \leftrightharpoons 6CO + 4H_2$ $\Delta H_{298} = +620$ kJ/mol (1.13)

Typically, the ratio of CO_2:C_3H_8 in the feed used is more than 1 as this is thermodynamically favourable as shown by the calculations of Michorczyk et al.[39,40] and Bawah et al.[41] It was established that a ratio of 5 was ideal for better performance in terms of selectivity and conversion (Figure 1.4c). This is due to the interplay between propylene formation, hydrogen formation and consumption and CO formation. Besides temperature, the obtained syngas composition is influenced by the CO_2 partial pressure. Increasing CO_2 partial pressure leads to an increased CO:H_2 molar ratio.

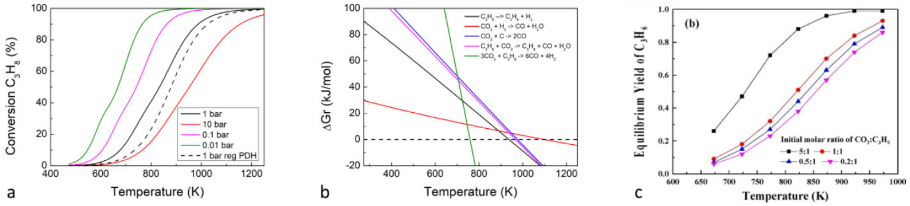

Figure 1.4: ***a:*** *Equilibrium conversion of C_3H_8 during CO_2-PDH at varying temperatures and pressures at an inlet ratio of CO_2:C_3H_8 = 1:1. The dashed line represents the equilibrium conversion for non-oxidative PDH, shown as a reference.* ***b:*** *Gibbs free energy of reaction at 1 bar.* ***c:*** *equilibrium yield of propylene at varying temperatures and ratios of CO_2:C_3H_8.*[33,40]

The effect of temperature is reflected in the change in the Gibbs free energy of reaction at 1 bar (Figure 1.4a). The change in Gibbs free energy of both the non-oxidative PDH and the CO_2-PDH reaction becomes negative at elevated temperatures. However, also DRP becomes highly spontaneous with increasing temperature, affirming the fact that this reaction occurs simultaneously with dehydrogenation, and is therefore a competing reaction.[42,43] When Figure 1.3b and Figure 1.4b are compared, it can be concluded that side reactions such as cracking and hydrogenolysis also remain possible at typical operating conditions for CO_2-PDH. However, the reactions with positive impact, i.e. RWGS and reverse Boudouard also become more favourable at elevated temperatures, mitigating the negative impacts of side reactions.[43]

Again, a temperature compromise has to be sought for CO_2-PDH, as is the case for non-oxidative PDH. Moreover, adsorption of CO_2 requires basic sites, whereas adsorption of propane and side reactions require acidic sites.[31] Catalyst design should thus also consider these (different, parallel) requirements.

1.3 Catalyst Selection

Catalyst selection comprises the selection of support, choice of active metal and choice of promoter for the active metal. As these are important aspects, they should be given some consideration. Two broad categories are discussed.

1.3.1 Support selection

As mentioned in section 1.2.2, CO_2-PDH requires the presence of 2 types of sites for the reaction to take place effectively, basic sites for CO_2 and acidic sites for propane and hydrogen. The other aspect is the surface area of the employed support. Higher surface area will lead to better dispersion of the active phase, and hence to high surface to volume ratio.

An analysis of the support effect for PDH has been performed by Zhang et al.[44] They tested ZSM-5, γ-Al_2O_3, mesoporous alumina and SBA-15 and concluded that the selected support is the main factor to determine the porous character and the acidic properties of the corresponding catalyst. ZSM-5 contains strong acid sites and hence induces more cracking reactions, while the porous character of γ-Al_2O_3 leads to more coke accumulation. SBA-15 induces agglomeration of metallic particles and easy reduction of the promoter Sn in that work, which ends up being disadvantageous. Their conclusion was that mesoporous alumina was the best, based on their requirements. More recently, the hydrotalicite type MgAlO support, with/without incorporated promoter, and a $MgAl_2O_4$ spinel type support have attracted interest and have been investigated in detail for PDH and other reactions. $MgAl_2O_4$ has been reported to exert strong stabilization of small metal NPs, hence demonstrating enhanced catalytic activity and durability in harsh conditions such as methane reforming.[45,46]

Hydrotalcites (HTLs) belong to the class of layered double hydroxides. Divalent M^{2+} anions (e.g. Mg^{2+}) that are octahedrally coordinated with OH- anions form brucite-like sheet structures. When trivalent M^{3+} anions (e.g. Al^{3+}) replace part of the M^{2+} anions, the brucite-like sheets gain a net positive charge. Interaction with anions to compensate this charge leads to the formation of a stacked structure of brucite-type sheets, alternated with anion interlayers. Upon heating, this structure collapses and yields mixed metal oxides.[47] Two steps can be observed during this structure change: a dehydration up to 473 K, and a collapse of the lamellar structure between 573 and 673 K. During the dehydration, Al^{3+} cations can migrate into the interlayer in which they become tetrahedrally coordinated instead of octahedrally. During the collapse, the lamellar structure is transformed into a 3-D network. Consequentially, the mobility of the Al^{3+} cations is decreased. Since surface Al^{3+} cations are responsible for maintaining Pt dispersion, notably stable catalysts can be obtained. Moreover, high porosities can be achieved, which can additionally contribute to the metal dispersion. Moreover, it has been reported that HTLs can supply promotor elements, incorporated into the support, e.g. Mg(In)(Al)O, Mg(Ga)(Al)O, towards the surface.[16,48–50]

The spinel $MgAl_2O_4$ on the other hand is less basic than MgO, but yields strong metal support interactions and highly dispersed and stable Pt catalysts. Especially $MgAl_2O_4$(111) facets are suited to stabilize Pt. It is reported that the relatively high Al:Mg ratio can play a role.[51] The high mechanical strength also makes it a support suitable for PDH reactions.[15]

1.3.2 Active component selection

Catalyst selection for dehydrogenation depends on the paraffin length as is depicted in Table 1.2.

Table 1.5: *Performance of dehydrogenation catalysts*

Active Component of Catalyst	**Dehydrogenation of Light Paraffin**	**Dehydrogenation of Paraffins C_{10}-C_{14}**	**Dehydrogenation of Ethyl Benzene to Styrene**
Pt/Sn	Excellent	Excellent	Poor
Cr oxides	Excellent	Moderate	Good
Fe oxides	Absent/poor	Not available	Excellent
Ga system	Excellent	Not available	Excellent

The major catalytic systems that have been reported in scientific and patent literature for dehydrogenation activity are: 1. Group VIII metals (mainly platinum with tin) supported on alumina and with promoters, 2. Chromium oxides on alumina with promoters, 3. Iron oxides supported with promoters and 4. Gallium included in a zeolite structure or as a supported oxide.

The Pt-Sn and Cr catalysts are typically used for industrial PDH in the 4 most common commercial processes. The entire list of commercial processes is displayed in Table 1.3. As can be observed, a majority of them employs a Pt-Sn catalyst.

CrO_x-based catalysts are applied in the commercialized Catofin and FBD-4 processes. The reaction of alkane molecules occurs at the Cr-O sites. For a fresh chromium catalyst, there are a number of chromium ions with varying valence states, Cr^{6+}, Cr^{5+}, Cr^{3+}, Cr^{2+}, that play differing roles in the PDH process.[52,53] Sattler and coworkers found reduction of Cr^{6+} to Cr^{3+} occurs initially during the dehydrogenation reaction, and Cr^{3+} is considered to be the active site.[54] The main causes for deactivation for a Cr catalyst are carbon formation and chromium aggregation. CrO_x/Al_2O_3 is the catalyst used industrially, and there are reports that the ionic radii of Cr^{3+} and Al^{3+} are very similar, allowing for diffusion of Cr^{3+} into the Al_2O_3 lattice, leading to the formation of the spinel phase and subsequent loss of activity.[55,56] CrO_x also collapses and aggregates during the regeneration process.[57]

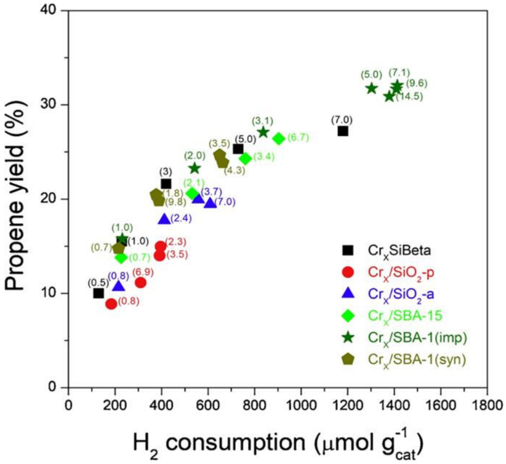

Figure 1.5: *Variation of propylene yield with hydrogen consumption for CrO_x based catalysts in CO_2-PDH. Values in brackets indicate total Cr content.*[58]

Cr catalysts for CO_2-PDH require dispersion at lower oxidation states (Cr^{3+}/Cr^{2+}) as these determine the yields of C_3H_6 attained. The structural evolution depends strongly on the textural properties of the support for Cr.[33] Figure 1.5 shows the correlation of C_3H_6 yield with the number of available redox sites, which emphasizes the important role of redox Cr species.[58] There are two types of redox cycles that have been proposed (Figure 1.6), which are

$Cr^{6+} \leftrightarrow Cr^{3+}/Cr^{2+}$ and $Cr^{3+} \leftrightarrow Cr^{2+}$. The former is proposed on MCM-41, TUD-1[59] and Al_2O_3 supported catalysts,[60–62] while the latter is known for Ni-promoted[63] and unpromoted CrO_x/SiO_2.[64]

In short, CrO_x catalysts have high reactivity and selectivity but low stability, with about 1 mol g_{Cr}^{-1} h^{-1} at a deactivation rate of 0.5 h^{-1}, as well as high toxicity. Therefore, low toxicity and stable alternative catalysts are increasingly desired.[57]

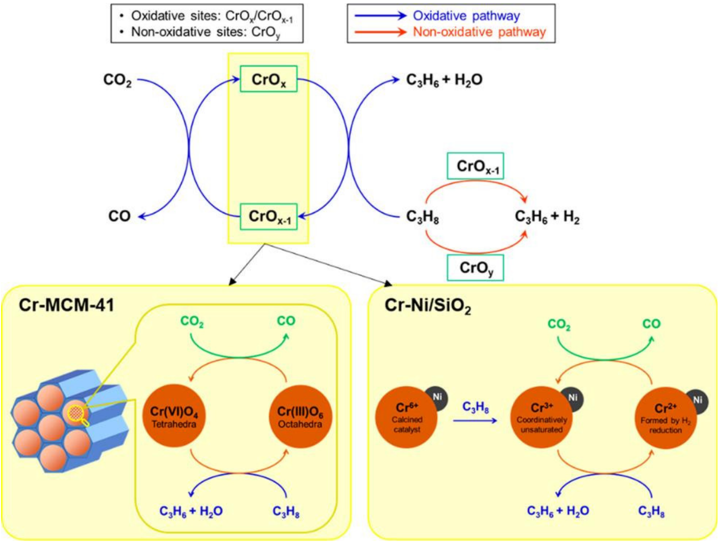

Figure 1.6: *Proposed redox and non-redox pathways on supported Cr-catalysts with their relation with Cr-active sites in CO_2-PDH.*[60,61,63,65,66]

A scan of the literature for CO_2-PDH reveals that the catalysts investigated are overwhelmingly metal oxides such as CrO_x,[60,67–71] VO_x,[72–76] MoO_x,[77,78] GaO_x,[74,79–85] and InO_x.[35,86,87] No literature is available for Pt-based catalysts for CO_2-PDH. When taking into account that most commercialized processes use Pt-based catalysts for PDH, it would make sense to investigate these as well for CO_2-PDH, since if there is actually a benefit of using this catalyst by the thermodynamic shift through RWGS, or by the reverse Boudouard reaction, then it would, in theory, not require major overhauls to existing plants to implement a change in the feed. There is the added aspect that Pt-based catalysts perform better than the oxide-based catalysts as the yields are obtained at lower space-times. An estimation of the average specific activity of Pt-based catalysts compared to CrO_x and GaO_x-based catalysts shows that Pt has a turnover frequency which is 4 orders of magnitude higher ($3*10^{-1}$ s^{-1} vs. $8*10^{-5}$ s^{-1}).[15]

Aside from this, the deactivation rate of Pt-based dehydrogenation catalysts is lower compared to metal oxide dehydrogenation catalysts (Figure 1.7).

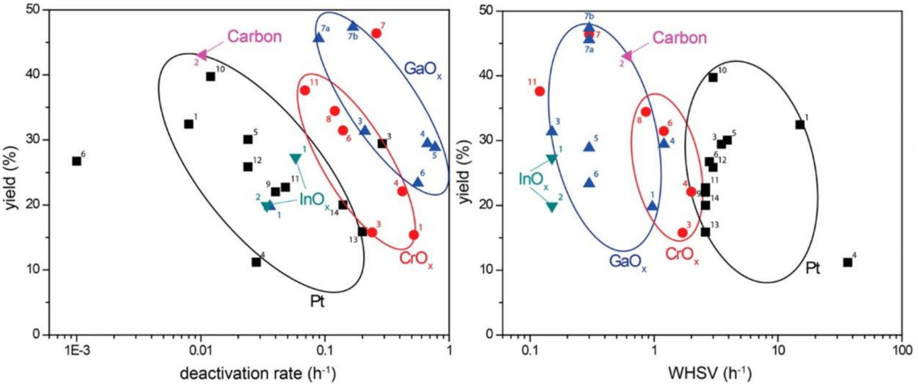

Figure 1.7: *Propylene yield of different types of catalysts during non-oxidative propane dehydrogenation for deactivation rate (left) and space velocity (right).*[15]

An example of an industrial process is the STAR process, which comprises of 1 or 2 stages, reforming plus an optional oxy-dehydrogenation reactor, using Pt-Sn impregnated on a zinc or magnesium aluminate support. In the first reformer reactor, the hydrocarbon is fed along with steam at a molar ratio between 3.5 and 4.2 with respect to propane.[88] The steam takes care of carbon removal, while adding heat capacity to the process. In the oxy-dehydrogenation reactor, oxygen is typically fed at molar ratios ranging from 0.08 to 0.16 so that it may react with the product hydrogen to form H_2O, in order to shift the equilibrium towards propylene. As such, CO_2-assised PDH could combine the effects of H_2O and O_2 from the STAR process in one: carbon control and equilibrium shift.

The selection made so far is a Pt-based catalyst supported on a $MgAl_2O_4$ spinel or MgAlO hydrotalcite type support for PDH and CO_2-PDH. Pt is used with a variety of promoters in literature of which the most prominent are Sn, In and Ga. All three promoters have been reported to show good activity towards PDH, mitigate sintering and to suppress carbon formation. The way this is achieved is through alloying with Pt, which influences both the geometric and electronic properties of the active metal. For CO_2-PDH, the interaction between CO_2 and the promoter should however also be taken into account.

Table 1.6: *Existing propane and butane dehydrogenation technologies, ordered by industrial maturity.*[89,90]

Technology and Licensor	**CATOFIN**	**Oleflex UOP**	**STAR**	**FBD**	**PDH**	**FLOTU**	**FCDh™**	**SABIC**	**K-PRO™ (KBR)**
License Holder	CB&I ABB Lummus	UOP LCC (Honeywell)	Krupp-Uhde	Yarsintez-Snamprogetti	Linde-BASF-Statoil (Sintef)	Tsinghua	Dow	SABIC	Kellogg Brown and Root LLC
Reactor	Adiabatic fixed bed	Adiabatic moving bed	Adiabatic	Fluidized bed	Isothermal fixed bed	Bimodal Fluidized bed	Fluidized bed	Fluidized bed	Fluidized bed
Operation	Cyclic	Continuous	Cyclic	Continuous	Cyclic	Continuous	Continuous	Continuous	Continuous
Catalyst	CrO_x/Al_2O_3	Pt-Sn/Al_2O_3 + alkali	Pt-Sn/Zn-Al_2O_3/Ca-Al_2O_3	CrO_x/Al_2O_3 + alkali	Pt/MgAlO; Pt-Sn/ZrO_2	Pt-Sn/SAPO-34	Pt-Ga-K/Si-Al_2O_3	Pt-Sn/K/SAPO-34	-
Heat management	Pre-heaters, regeneration	Interstage heating, regenerated catalyst	Furnace and ODH*	Regenerated catalyst	Furnace	Regenerated secondary catalyst	-	Integrated FBR with internal regenerator	-
T (K)	838-923 K	823-893 K	DH: 823-863 K ODH*: ~873 K	808-863 K	~863 K	843 - 883 K	~873 K	833 - 873 K	~873 K
P (bar)	0.3-0.5	2-3	5-6	0.5-1.5	~1	0.5-1.5	~1	0.1-6	1.5
Cycle time	15-30 min	-	7 h	-	9 h	-	-	15-30 min	-
WHSV/h^{-1}	<1	4-13	0.5-10	-	-	-	-	-	-
Dilution gas	none	Cyclic H_2	Steam	none	none	-	N_2	-	-
Development stage	Commercial	Commercial	Commercial	Commercial	Pilot plant	Pilot plant	Retrofitting planned	-	-

*ODH is oxidative dehydrogenation in the presence of oxygen.

Geometrically, the structure sensitivity of the side reactions and the structure insensitivity of the PDH reaction are exploited through the addition of the promoter. Also coke precursors adsorb on larger Pt ensembles. The addition of a promoter leads to the formation of smaller ensembles through “dilution” of the Pt. This in turn assists towards the migration of the coke precursors to the support, which thereby helps to maintain the activity of the Pt sites. Moreover, hydrogenolysis side reactions often require low-coordinated Pt sites. It is believed that the promoter selectively covers these sites. Another geometric effect is that sintering of Pt is prevented because the promoter partially covers Pt clusters.[15]

Electronically, alloying influences the electron density of Pt, which affects the adsorption of the hydrocarbons. Due to this, there is now a higher electron density in the 5d band of Pt,[16,91,92] which causes an increase in the energy barrier for the dissociative adsorption of propane. This change in electron density also leads to weaker adsorption of propylene on the Pt surface and suppresses the formation of propylidyne, an important precursor of coke. Ideally, the degree of Pt promotion should be controlled to find an optimal balance between an increase in propylene selectivity and a decrease of propane conversion.

All three catalysts Pt:Sn, Pt:In and Pt:Ga have been characterized independently and studied with some level of detail, particularly the Pt:Sn system, to determine their compositions and state when performing the PDH reaction. Aspects investigated for the Pt:Sn system in the past are:

1. Effect of H_2/O_2 redox cycles on the composition of the Pt-Sn alloy (increases the Sn content),[93]

2. Effect of Sn/Pt ratio and reduction temperature on alloy composition (higher T –> more Sn in Pt-Sn alloy, higher Sn loadings–> more Sn in Pt-Sn alloy),[94]

3. DFT studies on most stable structure expected (the surface forms a Pt_3Sn state, which is thermodynamically most favourable, while the core remains in a more Sn-rich state).[95]

4. Celik and co-workers used DFT to construct alloy models by replacing the surface Pt atoms with Sn atoms, indicating that the PT-Sn alloy has a face centered cubic (fcc) structure. They reported that CH_3C, which is a coke precursor, is formed at the three-fold sites if Pt(111). For PtSn(111) surface, no three-fold sites exist and therefore CH_3C is unstable, leading to

suppression of coke formation. They also predicted that a similar effect of alloy formation can be expected with post-transition metals such as Ga, In.[96,97]

5. Use of a support such as γ-Al_2O_3 or Mg(Al)O leads to the stabilization of Pt nanoparticles,[98,99] even without the addition of Sn.[22,100] However, Sn plays a crucially important role in the re-dispersion of the Pt particles through redox treatments (H_2/O_2) that are employed during catalyst regeneration. Weckhuysen and co-workers observed that atomically dispersed Sn on γ-Al_2O_3 plays a role in nucleation sites that assist in Pt re-dispersion.[93,100]

6. XAS studies have shown that the addition of promoters such as Sn, Ga, or In leads to the shift in the Pt L_{III}-edge white line (WL) position to higher energies.[101–104] This shift of edge energy, which represents the transition energy of electrons from $2p_{3/2}$ orbital to the vacant 5d orbital, is attributed to an increase in the energy level of the vacant 5d orbital. Deng et al.[105] investigated the electronic state of Pt by calculating the d-band vacancy based on the WL intensity in Pt L_{III}-edge X-ray absorption near edge structure (XANES). It was concluded that the particle size affects the WL intensity and therefore similar NP sizes should be used for comparative studies.[106,107]

Passos et al.[108] studied the Pt:In catalyst for cyclohexane dehydrogenation and methylcyclopentane hydrogenolysis, from which it was determined that the presence of In leads to a decrease in hydrogenolysis selectivity and an increase in selectivity for dehydrogenation and aromatization products. It was also concluded that In dilutes Pt more homogenously than Sn and is therefore, more ideal as promoter. Similar conclusions were reached by others.[109,110] Pt:In was then used for PDH by Sun et al.,[16] who concluded that In helped to improve the selectivity towards propylene, reduce coke deposits and the In/Pt ratio had a strong effect in ethane dehydrogenation (EDH) and PDH. Wegener et al.[91] looked into the structures formed between Pt and In for EDH and concluded that during the process of alloy formation, an In-rich alloy forms on the surface ($PtIn_2$), while an In poor alloy remains in the core (Pt_3In). In that same work it was mentioned that some In loss occurred. Filez et al.[111,112] studied this system further to determine the kinetics of changes during H_2/O_2 redox cycles. Tolek et al.[113] studied this catalyst for PDH and compared the effect of preparation method on activity. They found that an In-modified MgAlO support (hydrotalcite type) performed best due to better metal-support interaction, leading to better Pt-In alloy formation, which in turn led to weaker binding of propylene.

Pt:Ga hasn't been studied as extensively as the Pt:Sn or Pt:In systems for light alkane dehydrogenation, but the conclusions as to the behaviour of such a bimetallic system are similar to those for Pt:In and Pt:Sn. They are that it assists towards mitigating carbon formation and re-dispersion, while being beneficial to use towards PDH.[47–49,103,114,115]

1.3.3 Other potential improvements

There is a potential to improve the catalyst even further through the application of a coating. The coating can stabilize the nanoparticles (NPs) against sintering. The application of such a coating has so far been utilized for monometallic Pt catalysts with an alumina coating, and the findings from that research were that the coating indeed suppressed sintering of the catalyst and at the same time increased the selectivity towards the desired product propylene.[116] It was speculated that this improvement in selectivity was a result of the coating selectively binding to the undercoordinated sites of the NPs, thereby leaving the more selective terrace sites available for dehydrogenation.

Coating has been applied successfully for other reactions such as SiO_2 coated Au/TiO_2 catalysts for CO oxidation,[117] alumina coated Pd catalysts for hydrogenation of 1,3 butadiene,[118] Atomic Layer Deposition (ALD)-based Al_2O_3 coated Pd-based catalysts for oxidative dehydrogenation of ethane,[119] MgO coated Ni catalysts for reforming of methane,[120] and others.[121,122] The results hold promise and indicate it is an option that can equally be investigated for PDH. So far however, this coating procedure has only been applied to monometallic catalyst systems and not yet for a bimetallic catalyst.

The application of such a coating can be performed by Atomic Layer Deposition (ALD), which is a powerful tool for the modification of solid surfaces.[123] ALD utilizes sequential self-saturating reactions between gaseous molecules and a solid surface to grow thin films in a layer by layer fashion.[123] An ALD process typically consists of alternating two different precursor pulses A and B, in a cyclic fashion which allows to deposit material with atomic layer precision in a conformal way.

1.4 Thesis scope and objectives

So far, it has been detailed that there are a number of issues associated with PDH, for which there are potential solutions such as addition of a promoter, use of a specific support, introduction of a co-feed and application of a coating. Although a lot of research on bimetallic Pt catalysts has been performed, a systematic analysis through advanced characterization techniques, detailing the differences between the promoters and their subsequent effect on activity towards PDH and CO_2-PDH, is not present in literature.

In short, the following bullet points are the factors that play a role in the PDH reaction:

- Promoter element (Sn, In, Ga)
- Amount of promoter element (phase of alloy?)
- Co-feed effect on activity (CO_2, H_2)
- Ratio of co-feed with propane
- Effect of CO_2 on the bimetallic alloy (oxidation?)
- Nanoparticle size effects
- Support effect (surface area, promoter incorporated support Mg(Ga)AlO)
- Effect of application of redox cycles on the catalyst (H_2/O_2 or H_2/CO_2) (to mimic regeneration steps used in industry)
- Effect of applying a coating to a bimetallic catalyst (reduced sintering?)

The objective of the present research is to investigate all of these factors and to arrive at a conclusion regarding the potential of applying CO_2 as a co-feed with propane for a Pt-based bimetallic catalyst. To this end, the use of advanced characterization techniques such as in situ QXAS and SAXS is employed extensively in order to gain a foothold of the behaviour of the bimetallic alloy under different gas atmospheres.

1.5 Outline

This thesis is a compilation of published journal articles and manuscripts intended to be submitted in the near future. There is a short introduction at the beginning of each chapter relevant to the work. In total, this thesis contains 7 chapters: this introduction, a materials and methods chapter, 4 result chapters and a chapter with general conclusions on the research.

Chapter 2 contains the synthesis protocols followed towards the preparation of Pt:M/$MgAl_2O_4$

and Pt/MgGaAlO catalysts, followed by a general overview of ALD, for the application of a coating. As part of the methods, a general overview of XAS, SAXS and CO-DRIFTS is presented, followed by the general protocol employed towards activity testing of the catalysts.

Chapter 3 consists of detailed QXAS characterization and activity results for the Pt:Sn/$MgAl_2O_4$ (3 wt% Pt) catalysts towards CO_2-PDH. Two Pt:Sn catalysts were tested, the difference being the surface area of the $MgAl_2O_4$ support (125 vs. 5 m^2/g), which led to differences in the deposited NP size. The samples were characterized with in situ QXAS to see the effect of CO_2 on the integrity of the Pt-Sn alloy, followed by activity tests for PDH and CO_2-PDH. A big data technique, Multivariate Curve Resolution with Alternating Least Squares (MCR-ALS) with Principal Component Analysis (PCA), was employed on the collected QXAS data, measured during a flow perturbance between H_2 and CO_2, of 1 min each, to see the changes occurring to the alloy. Following this extensive characterization and activity test protocol, a reaction network is proposed.

Chapter 4 contains a comprehensive in situ QXAS characterization analysis, coupled with Modulation Excitation Spectroscopy (MES), of Pt:In and Pt:Sn catalysts and the benefits/drawbacks of each. Both catalysts are supported on $MgAl_2O_4$ with a surface area of ~115 m^2/g. The difference between the Pt:Sn catalyst analysed in this chapter with the one from Chapter 3, is the content of Sn, which is much higher in this study (3 wt% vs. 0.35 wt%). The in situ experiments varied from H_2-TPR to CO_2-TPO, H_2/O_2 redox and RWGS. For the MES analysis, a flow perturbation of 1 min each between different ratios of $H_2:CO_2$ (2:1 to 2:3), was applied to both Pt:Sn and Pt:In catalysts and evaluated for the NP surface engagement. The redox cycle experiments led to an understanding on the change in promoter content with increasing number of cycles.

Chapter 5 contains the activity test results for Pt:Ga, Pt:In and Pt:Sn catalysts for PDH and CO_2-PDH, and evaluates the benefits/drawbacks of each promoter element towards the reactions. The catalysts were tested for changing ratios of $CO_2:C_3H_8$ and for different H_2/O_2 redox cycles and the effect on activity. Redox cycles serve to mimic the reaction/regeneration cycles that are typically employed for industrial catalysts, and this experiment is applied in both PDH and CO_2-PDH. The chapter also contains a CO-DRIFTS analysis for all 3 catalysts after differing redox cycles. The Pt:In and Pt:Sn catalysts are the same as in Chapter 4, while Pt:Ga is additional in this part.

Chapter 6 explores the potential benefits/drawbacks of applying an alumina (Al_2O_3) coating through ALD to two Pt:Ga catalysts (Pt:Ga/$MgAl_2O_4$ and Pt/Mg(Ga)AlO). A combination of small-angle X-ray scattering (SAXS) and X-ray absorption spectroscopy (XAS) was employed on the samples to gain insight into the effect of this coating on catalyst stability. They were then tested for PDH to corroborate the SAXS/XAS findings.

Chapter 7 summarizes the findings from this research work contained throughout the different chapters. Some future research suggestions are then provided.

1.6 References

1. Propylene Market Analysis : Plant Capacity , Production , Operating Efficiency , Technology , Process, Demand & Supply , End Use , Distribution Channel , Regional Demand , 2015-2030. *CHEMANALYST* (2021). Available at: https://www.chemanalyst.com/industry-report/propylene-market-633. (Accessed: 10th November 2021)

2. Carrero, C. A., Schloegl, R., Wachs, I. E. & Schomaecker, R. Critical Literature Review of the Kinetics for the Oxidative Dehydrogenation of Propane over Well-Defined Supported Vanadium Oxide Catalysts. *ACS Catal.* **4**, 3357–3380 (2014).

3. Ritchie, H. & Roser, M. Plastic pollution. *Our World in Data* (2018). Available at: https://ourworldindata.org/plastic-pollution.

4. R., J. J. *et al.* Plastic waste inputs from land into the ocean. *Science (80-.).* **347**, 768–771 (2015).

5. Bhutra, S. As India stares at single-use plastic ban, country's per capita consumption far behind world average. *CNBC* (2019). Available at: https://www.cnbctv18.com/economy/petrol-gets-cheaper-by-rs-607-per-litre-in-delhi-rs-587-in-mumbai-11344652.htm.

6. Akah, A. & Al-Ghrami, M. Maximizing propylene production via FCC technology. *Appl. Petrochemical Res.* **5**, 377–392 (2015).

7. Plotkin, J. S. The Propylene Gap: How Can It Be Filled? ACS News Industrial Chemistry & Engineering. (2015).

8. Marsh, M. & Wery, J. On-purpose propylene production. *Digital Refining* 10–12 (2019). Available at: https://www.digitalrefining.com/article/1002264/on-purpose-propylene-production.

9. Ding, J. & Hua, W. Game Changers of the C3 Value Chain: Gas, Coal, and Biotechnologies. *Chem. Eng. Technol.* **36**, 83–90 (2013).

10. Amghizar, I., Vandewalle, L. A., Van Geem, K. M. & Marin, G. B. New Trends in Olefin Production. *Engineering* **3**, 171–178 (2017).

11. Bruijnincx, P. C. A. & Weckhuysen, B. M. Shale Gas Revolution: An Opportunity for the Production of Biobased Chemicals? *Angew. Chemie Int. Ed.* **52**, 11980–11987 (2013).

12. Global ethylene demand and capacity 2015-2022. *Bloomberg; Krungsri Research; Statista estimates* (2022). Available at: https://www.statista.com/statistics/1246694/ethylene-demand-capacity-forecast-worldwide/. (Accessed: 10th November 2021)

13. Global propylene demand and capacity 2015-2022. *Bloomberg; Krungsri Research; Statista estimates* (2022). Available at: https://www.statista.com/statistics/1246689/propylene-demand-capacity-forecast-worldwide/. (Accessed: 10th November 2021)

14. Khare, G. P. & Porter, R. A. Platinum and Tin-Containing catalyst and use thereof in alkane dehydrogenation. (1994).

15. Sattler, J. J. H. B., Ruiz-Martinez, J., Santillan-Jimenez, E. & Weckhuysen, B. M. Catalytic Dehydrogenation of Light Alkanes on Metals and Metal Oxides. *Chem. Rev.* **114**, 10613–10653 (2014).

16. Sun, P., Siddiqi, G., Vining, W. C., Chi, M. & Bell, A. T. Novel Pt/Mg(In)(Al)O catalysts for ethane and propane dehydrogenation. *J. Catal.* **282**, 165–174 (2011).

17. Bhasin, M. M., McCain, J. H., Vora, B. V, Imai, T. & Pujadó, P. R. Dehydrogenation and oxydehydrogenation of paraffins to olefins. *Appl. Catal. A Gen.* **221**, 397–419 (2001).

18. Saerens, S. *et al.* The Positive Role of Hydrogen on the Dehydrogenation of Propane on Pt(111). *ACS Catal.* **7**, 7495–7508 (2017).

19. Du, X. *et al.* Catalytic dehydrogenation of propane by carbon dioxide: a medium-temperature thermochemical process for carbon dioxide utilisation. *Faraday Discuss.* **183**, 161–176 (2015).

20. Hackler, R. A. *et al.* Isomerization and Selective Hydrogenation of Propyne: Screening of Metal–Organic Frameworks Modified by Atomic Layer Deposition. *J. Am. Chem. Soc.* **142**, 20380–20389 (2020).

21. Sokolov, S., Stoyanova, M., Rodemerck, U., Linke, D. & Kondratenko, E. V. Comparative study of propane dehydrogenation over V-, Cr-, and Pt-based catalysts: Time on-stream behavior and origins of deactivation. *J. Catal.* **293**, 67–75 (2012).

22. Wu, J., Peng, Z. & Bell, A. T. Effects of composition and metal particle size on ethane dehydrogenation over PtxSn100−x/Mg(Al)O (70⩽x⩽100). *J. Catal.* **311**, 161–168 (2014).

23. Peng, Z. *et al.* High-resolution in situ and ex situ TEM studies on graphene formation and growth on Pt nanoparticles. *J. Catal.* **286**, 22–29 (2012).

24. Vu, B. K. *et al.* Location and structure of coke generated over Pt–Sn/Al2O3 in propane

dehydrogenation. *J. Ind. Eng. Chem.* **17**, 71–76 (2011).

25. Redekop, E. A. *et al.* Early stages in the formation and burning of graphene on a Pt/Mg(Al)Ox dehydrogenation catalyst: A temperature- and time-resolved study. *J. Catal.* **344**, 482–495 (2016).

26. Wang, H.-Z. *et al.* Coke Formation on Pt–Sn/Al2O3 Catalyst for Propane Dehydrogenation. *Ind. Eng. Chem. Res.* **57**, 8647–8654 (2018).

27. Dai, Y., Lu, P., Cao, Z., Campbell, C. T. & Xia, Y. The physical chemistry and materials science behind sinter-resistant catalysts. *Chem. Soc. Rev.* **47**, 4314–4331 (2018).

28. Im, J. & Choi, M. Physicochemical Stabilization of Pt against Sintering for a Dehydrogenation Catalyst with High Activity, Selectivity, and Durability. *ACS Catal.* **6**, 2819–2826 (2016).

29. Zhu, J. *et al.* Size-Dependent Reaction Mechanism and Kinetics for Propane Dehydrogenation over Pt Catalysts. *ACS Catal.* **5**, 6310–6319 (2015).

30. Wang, L., Wang, L., Meng, X. & Xiao, F.-S. New Strategies for the Preparation of Sinter-Resistant Metal-Nanoparticle-Based Catalysts. *Adv. Mater.* **31**, 1901905 (2019).

31. Ansari, M. B. & Eon-Park, S. Environmental Science MINIREVIEW. *Energy Environ. Sci.* **5**, 9419–9437 (2012).

32. Thirumala, Y. R. P. & Hari, B. B. Oxidative dehydrogenation of ethane to ethylene on Cr2O3/Al2O3– ZrO2 catalysts : the influence of oxidizing agent on ethylene selectivity. *Appled Petrochemical Res.* **4**, 247–252 (2014).

33. Atanga, M. A., Rezaei, F., Jawad, A., Fitch, M. & Rownaghi, A. A. Applied Catalysis B : Environmental Oxidative dehydrogenation of propane to propylene with carbon dioxide. *Appl. Catal. B Environ.* **220**, 429–445 (2018).

34. Badstube, T., Papp, H., Dziembaj, R. & Kustrowski, P. Screening of catalysts in the oxidative dehydrogenation of ethylbenzene with carbon dioxide. *Appl. Catal. A Gen.* **204**, 153–165 (2000).

35. Chen, M. *et al.* Applied Catalysis A : General Study in support effect of In2O3 / MO x (M = Al , Si , Zr) catalysts for dehydrogenation of propane in the presence of CO 2. *"Applied Catal. A, Gen.* **407**, 20–28 (2011).

36. Pakhare, D. & Spivey, J. Chem Soc Rev noble metal catalysts. *Chem. Soc. Rev.* **43**, 7813–7837 (2014).

37. Shen, Z. *et al.* Applied Catalysis A : General Dehydrogenation of ethane to ethylene over a highly efficient Ga2O3 / HZSM-5 catalyst in the presence of CO2. *Appl. Catal. A Gen.* **356**, 148–153 (2009).

38. Krylov, O. V, Mamedov, A. K. & Mirzabekova, S. R. The regularities in the interaction of alkanes with CO2 on oxide catalysts. *Catal. Today* **24**, 371–375 (1995).

39. Michorczyk, P. & Ogonowski, J. Dehydrogenation of propane to propene over gallium

oxide in the presence of CO2. *Appl. Catal. A Gen.* **251**, 425–433 (2003).

40. Michorczyk, P., Ze, K., Niekurzak, R. & Ogonowski, J. Dehydrogenation of propane with CO2 – a new green process for prope- ne and synthesis gas production. **14**, 77–82 (2012).

41. Bawah, A.-R., Lucky, R. A. & Hossain, M. M. Oxidative dehydrogenation of propane with CO2 - A green process for propylene and hydrogen (syngas). *Int. J. Hydrogen Energy* **46**, 3401–3413 (2021).

42. Gomez, E. *et al.* Combining CO2 reduction with propane oxidative dehydrogenation over bimetallic catalysts. *Nat. Commun.* **9**, 1–6 (2018).

43. Gomez, E., Yan, B., Kattel, S. & Chen, J. G. Carbon dioxide reduction in tandem with light-alkane dehydrogenation. *Nat. Rev. Chem.* **3**, 638–649 (2019).

44. Zhang, Y. *et al.* Comparative study of bimetallic Pt-Sn catalysts supported on different supports for propane dehydrogenation. *J. Mol. Catal. A Chem.* **381**, 138–147 (2014).

45. Tuo, Y. *et al.* Partial positively charged Pt in Pt/MgAl2O4 for enhanced dehydrogenation activity. *Appl. Catal. B Environ.* **288**, 119996 (2021).

46. Wang, H. *et al.* Hierarchical Fe-modified MgAl2O4 as a Ni-catalyst support for methane dry reforming. *Catal. Sci. Technol.* **10**, 6987–7001 (2020).

47. Filez, M. *et al.* Unravelling the formation of Pt-Ga alloyed nanoparticles on calcined Ga-modified hydrotalcites by in situ XAS. *Chem. Mater.* **26**, 5936–5949 (2014).

48. Siddiqi, G., Sun, P., Galvita, V. & Bell, A. T. Catalyst performance of novel Pt/Mg(Ga)(Al)O catalysts for alkane dehydrogenation. *J. Catal.* **274**, 200–206 (2010).

49. Sun, P., Siddiqi, G., Chi, M. & Bell, A. T. Synthesis and characterization of a new catalyst Pt/Mg(Ga)(Al)O for alkane dehydrogenation. *J. Catal.* **274**, 192–199 (2010).

50. Galvita, V., Siddiqi, G., Sun, P. & Bell, A. T. Ethane dehydrogenation on Pt/Mg(Al)O and PtSn/Mg(Al)O catalysts. *J. Catal.* **271**, 209–219 (2010).

51. Shan, Y.-L., Wang, T., Sui, Z.-J., Zhu, Y.-A. & Zhou, X.-G. Hierarchical MgAl2O4 supported Pt-Sn as a highly thermostable catalyst for propane dehydrogenation. *Catal. Commun.* **84**, 85–88 (2016).

52. Fridman, V. Z., Xing, R. & Severance, M. Investigating the CrOx/Al2O3 dehydrogenation catalyst model: I. identification and stability evaluation of the Cr species on the fresh and equilibrated catalysts. *Appl. Catal. A Gen.* **523**, 39–53 (2016).

53. Fridman, V. Z. & Xing, R. Investigating the CrOx/Al2O3 dehydrogenation catalyst model: II. Relative activity of the chromium species on the catalyst surface. *Appl. Catal. A Gen.* **530**, 154–165 (2017).

54. Sattler, J. J. H. B., Mens, A. M. & Weckhuysen, B. M. Real-Time Quantitative Operando Raman Spectroscopy of a CrOx/Al2O3 Propane Dehydrogenation Catalyst in a Pilot-Scale Reactor. *ChemCatChem* **6**, 3139–3145 (2014).

55. Sattler, J. J. H. B. *et al.* Operando UV-Vis spectroscopy of a catalytic solid in a pilot-scale reactor: deactivation of a CrOx/Al2O3 propane dehydrogenation catalyst. *Chem. Commun.* **49**, 1518–1520 (2013).

56. Conley, M. P., Delley, M. F., Núñez-Zarur, F., Comas-Vives, A. & Copéret, C. Heterolytic Activation of C–H Bonds on CrIII–O Surface Sites Is a Key Step in Catalytic Polymerization of Ethylene and Dehydrogenation of Propane. *Inorg. Chem.* **54**, 5065–5078 (2015).

57. Chen, S. *et al.* Propane dehydrogenation: catalyst development, new chemistry, and emerging technologies. *Chem. Soc. Rev.* **50**, 3315–3354 (2021).

58. Michorczyk, P. *et al.* Effect of dealumination on the catalytic performance of Cr-containing Beta zeolite in carbon dioxide assisted propane dehydrogenation. *J. CO2 Util.* **36**, 54–63 (2020).

59. Burri, A., Hasib, M. A., Mo, Y.-H., Reddy, B. M. & Park, S.-E. An Efficient Cr-TUD-1 Catalyst for Oxidative Dehydrogenation of Propane to Propylene with CO2 as Soft Oxidant. *Catal. Letters* **148**, 576–585 (2018).

60. Takehira, K. *et al.* Behavior of active sites on Cr-MCM-41 catalysts during the dehydrogenation of propane with CO2. *J. Catal.* **224**, 404–416 (2004).

61. Takehira, K. *et al.* CO2 Dehydrogenation of Propane over Cr-MCM-41 Catalyst. in *Carbon Dioxide Utilization for Global Sustainability* (eds. Park, S.-E., Chang, J.-S. & Lee, K.-W. B. T.-S. in S. S. and C.) **153**, 323–328 (Elsevier, 2004).

62. Shishido, T., Shimamura, K., Teramura, K. & Tanaka, T. Role of CO2 in dehydrogenation of propane over Cr-based catalysts. *Catal. Today* **185**, 151–156 (2012).

63. Yun, D. *et al.* Promotional Effect of Ni on a CrOx Catalyst Supported on Silica in the Oxidative Dehydrogenation of Propane with CO2. *ChemCatChem* **4**, 1952–1959 (2012).

64. Michorczyk, P. & Ogonowski, J. Role of CO2 in dehydrogenation of propane over CrOX/SiO2 catalyst with low Cr content. *React. Kinet. Catal. Lett.* **92**, 61–68 (2007).

65. Jiang, X. *et al.* Oxidative Dehydrogenation of Propane to Propylene with Soft Oxidants via Heterogeneous Catalysis. *ACS Catal.* **11**, 2182–2234 (2021).

66. Michorczyk, P., Pietrzyk, P. & Ogonowski, J. Preparation and characterization of SBA-1–supported chromium oxide catalysts for CO2 assisted dehydrogenation of propane. *Microporous Mesoporous Mater.* **161**, 56–66 (2012).

67. Cavani, F., Ballarini, N. & Cericola, A. Oxidative dehydrogenation of ethane and propane : How far from commercial implementation ? **127**, 113–131 (2007).

68. Wang, H.-M., Chen, Y., Yan, X., Lang, W.-Z. & Guo, Y.-J. Cr doped mesoporous silica spheres for propane dehydrogenation in the presence of CO2: Effect of Cr adding time in sol-gel process. *Microporous Mesoporous Mater.* **284**, 69–77 (2019).

69. Agafonov, Y. A., Gaidai, N. A. & Lapidus, A. L. Influence of the preparation conditions for catalysts CrOx/SiO2 on their efficiency in propane dehydrogenation in the presence CO2. *Russ. Chem. Bull.* **63**, 381–388 (2014).

70. Michorczyk, P., Ogonowski, J. & Zeńczak, K. Activity of chromium oxide deposited on different silica supports in the dehydrogenation of propane with CO2 – A comparative study. *J. Mol. Catal. A Chem.* **349**, 1–12 (2011).

71. Wu, R. *et al.* Hydrothermally prepared Cr2O3–ZrO2 as a novel efficient catalyst for dehydrogenation of propane with CO2. *Catal. Commun.* **39**, 20–23 (2013).

72. Sugiyama, S., Osaka, T., Hirata, Y. & Sotowa, K. Enhancement of the activity for oxidative dehydrogenation of propane on calcium hydroxyapatite substituted with vanadate. *Appl. Catal. A Gen.* **312**, 52–58 (2006).

73. Balogun, M. L., Adamu, S., Ba-Shammakh, M. S. & Hossain, M. M. Promotional effects of CO2 on the oxidative dehydrogenation of propane over mesoporous VOX/γAl2O3 catalysts. *J. Ind. Eng. Chem.* **96**, 82–97 (2021).

74. Farsad, A., Lawson, S., Rezaei, F. & Rownaghi, A. A. Oxidative dehydrogenation of propane over 3D printed mixed metal oxides/H-ZSM-5 monolithic catalysts using CO2 as an oxidant. *Catal. Today* **374**, 173–184 (2021).

75. Liu, Y. *et al.* Oxidative Dehydrogenation of Propane to Propene over Barium Promoted Ni-Mo-O Catalyst. *React. Kinet. Catal. Lett.* **73**, 199–208 (2001).

76. Chen, K., Bell, A. T. & Iglesia, E. The Relationship between the Electronic and Redox Properties of Dispersed Metal Oxides and Their Turnover Rates in Oxidative Dehydrogenation Reactions. *J. Catal.* **209**, 35–42 (2002).

77. Balogun, M. L., Adamu, S., Bakare, I. A., Ba-Shammakh, M. S. & Hossain, M. M. CO2 Assisted Oxidative Dehydrogenation of Propane to Propylene over Fluidizable MoO3/La2O3-γAl2O3 Catalysts. *J. CO2 Util.* **42**, 101329 (2020).

78. Bakhtyari, A., Zafarnak, S., Taghvaei, H., Rahimpour, M. R. & Iulianelli, A. Simultaneous production of ethylene and hydrogen through carbon-dioxide-assisted conversion of ethane over cobalt-molybdenum catalysts. *J. CO2 Util.* **47**, 101499 (2021).

79. Zheng, B., Hua, W., Yue, Y. & Gao, Z. Dehydrogenation of propane to propene over different polymorphs of gallium oxide. *J. Catal.* **232**, 143–151 (2005).

80. Zhang, L. *et al.* Facile synthesis of SiO2 supported GaN as an active catalyst for CO2 enhanced dehydrogenation of propane. *J. CO2 Util.* **38**, 306–313 (2020).

81. Nakagawa, K. *et al.* Role of Carbon Dioxide in the Dehydrogenation of Ethane over Gallium-Loaded Catalysts. *J. Catal.* **203**, 87–93 (2001).

82. Chen, M. *et al.* Dehydrogenation of propane over spinel-type gallia–alumina solid solution catalysts. *J. Catal.* **256**, 293–300 (2008).

83. Cheng, Y. *et al.* Ga2O3/HSSZ-13 for dehydrogenation of ethane: Effect of pore geometry of support. *Catal. Commun.* **71**, 42–45 (2015).

84. Michorczyk, P., Kuśtrowski, P., Kolak, A. & Zimowska, M. Ordered mesoporous Ga2O3 and Ga2O3–Al2O3 prepared by nanocasting as effective catalysts for propane dehydrogenation in the presence of CO2. *Catal. Commun.* **35**, 95–100 (2013).

85. Sattler, J. J. H. B. *et al.* Platinum-Promoted Ga/Al2O3 as Highly Active, Selective, and Stable Catalyst for the Dehydrogenation of Propane. *Angew. Chemie Int. Ed.* **53**, 9251–9256 (2014).

86. Chen, M. *et al.* Dehydrogenation of propane over In2O3–Al2O3 mixed oxide in the presence of carbon dioxide. *J. Catal.* **272**, 101–108 (2010).

87. Chen, M. *et al.* Study in support effect of In2O3/MOx (M=Al, Si, Zr) catalysts for dehydrogenation of propane in the presence of CO2. *Appl. Catal. A Gen.* **407**, 20–28 (2011).

88. Beccari, M. & Romano, U. *Encyclopaedia of Hydrocarbons: Refining and petrochemicals, Volume 2*. *Refining and Petrochemicals* **II**, (2006).

89. Nawaz, Z. Light alkane dehydrogenation to light olefin technologies: a comprehensive review. *Rev. Chem. Eng.* **31**, 413–436 (2015).

90. Degnan, T. Fluidized bed propane dehydrogenation technologies challenge established fixed and moving bed processes. *Focus Catal.* **2019**, 1–2 (2019).

91. Wegener, E. C. *et al.* Structure and reactivity of Pt–In intermetallic alloy nanoparticles: Highly selective catalysts for ethane dehydrogenation. *Catal. Today* **299**, 146–153 (2018).

92. Anres, P., Gaune-Escard, M., Hayer, E. & Bros, J. P. The Pt⍰In system: Enthalpies of formation of liquid and solid alloys. *J. Alloys Compd.* **221**, 143–152 (1995).

93. Iglesias-juez, A. *et al.* A combined in situ time-resolved UV – Vis , Raman and high-energy resolution X-ray absorption spectroscopy study on the deactivation behavior of Pt and Pt A Sn propane dehydrogenation catalysts under industrial reaction conditions. *J. Catal.* **276**, 268–279 (2010).

94. Deng, L., Miura, H., Shishido, T. & Hosokawa, S. Dehydrogenation of Propane over Silica-Supported Platinum – Tin Catalysts Prepared by Direct Reduction : Effects of Tin / Platinum Ratio and Reduction Temperature. **0012**, 2680–2691 (2014).

95. Wang, J. *et al.* On the Role of Sn Segregation of Pt-Sn Catalysts for Propane Dehydrogenation. *ACS Catal.* **11**, 4401–4410 (2021).

96. Hook, A. & Celik, F. E. Predicting Selectivity for Ethane Dehydrogenation and Coke Formation Pathways over Model Pt–M Surface Alloys with ab Initio and Scaling Methods. *J. Phys. Chem. C* **121**, 17882–17892 (2017).

97. Hook, A., Massa, J. D. & Celik, F. E. Effect of Tin Coverage on Selectivity for Ethane Dehydrogenation over Platinum–Tin Alloys. *J. Phys. Chem. C* **120**, 27307–27318 (2016).

98. Hun, K. J. *et al.* Coordinatively Unsaturated Al3+ Centers as Binding Sites for Active Catalyst Phases of Platinum on γ-Al2O3. *Science (80-.).* **325**, 1670–1673 (2009).

99. Shi, L. *et al.* Al2O3 Nanosheets Rich in Pentacoordinate Al3+ Ions Stabilize Pt-Sn Clusters for Propane Dehydrogenation. *Angew. Chemie Int. Ed.* **54**, 13994–13998 (2015).

100. Pham, H. N., Sattler, J. J. H. B., Weckhuysen, B. M. & Datye, A. K. Role of Sn in the Regeneration of Pt/γ-Al2O3 Light Alkane Dehydrogenation Catalysts. *ACS Catal.* **6**, 2257–2264 (2016).

101. Xin, H., Schweitzer, N., Nikolla, E. & Linic, S. Communications: Developing relationships between the local chemical reactivity of alloy catalysts and physical characteristics of constituent metal elements. *J. Chem. Phys.* **132**, 111101 (2010).

102. Uemura, Y. *et al.* In situ time-resolved XAFS study on the structural transformation and phase separation of Pt3Sn and PtSn alloy nanoparticles on carbon in the oxidation process. *Phys. Chem. Chem. Phys.* **13**, 15833–15844 (2011).

103. Searles, K. *et al.* Highly Productive Propane Dehydrogenation Catalyst Using Silica-Supported Ga–Pt Nanoparticles Generated from Single-Sites. *J. Am. Chem. Soc.* **140**, 11674–11679 (2018).

104. Saito, H. & Sekine, Y. Catalytic conversion of ethane to valuable products through non-oxidative dehydrogenation and dehydroaromatization. *RSC Adv.* **10**, 21427–21453 (2020).

105. Deng, L. *et al.* Elucidating strong metal-support interactions in Pt–Sn/SiO2 catalyst and its consequences for dehydrogenation of lower alkanes. *J. Catal.* **365**, 277–291 (2018).

106. Bazin, D., Sayers, D., Rehr, J. J. & Mottet, C. Numerical Simulation of the Platinum LIII Edge White Line Relative to Nanometer Scale Clusters. *J. Phys. Chem. B* **101**, 5332–5336 (1997).

107. Tew, M. W., Miller, J. T. & van Bokhoven, J. A. Particle Size Effect of Hydride Formation and Surface Hydrogen Adsorption of Nanosized Palladium Catalysts: L3 Edge vs K Edge X-ray Absorption Spectroscopy. *J. Phys. Chem. C* **113**, 15140–15147 (2009).

108. Passos, F. B., Aranda, D. A. G. & Schmal, M. Characterization and Catalytic Activity of Bimetallic Pt-In/Al2O3 and Pt-Sn/Al2O3Catalysts. *J. Catal.* **178**, 478–488 (1998).

109. Meriaudeau, P. *et al.* Studies on PtxIny Bimetallics in NaY: I. Preparation and Characterization. *J. Catal.* **152**, 313–321 (1995).

110. Mériaudeau, P., Thangaraj, A., Dutel, J. F., Gelin, P. & Naccache, C. Studies on PtxInyBimetallics in NaY: II. Further Characterization Results and Catalytic Properties. *J. Catal.* **163**, 338–345 (1996).

111. Filez, M., Redekop, E. A., Poelman, H., Galvita, V. V & Marin, G. B. Advanced Elemental Characterization during Pt–In Catalyst Formation by Wavelet Transformed X-ray Absorption Spectroscopy. *Anal. Chem.* **87**, 3520–3526 (2015).

112. Filez, M. *et al.* Kinetics of Lifetime Changes in Bimetallic Nanocatalysts Revealed by Quick X-ray Absorption Spectroscopy. 12430–12434 (2018). doi:10.1002/anie.201806447

113. Tolek, W., Suriye, K., Praserthdam, P. & Panpranot, J. Effect of preparation method on the Pt-In modified Mg(Al)O catalysts over dehydrogenation of propane. *Catal. Today*

358, 100–108 (2020).

114. Redekop, E. A. *et al.* Delivering a Modifying Element to Metal Nanoparticles via Support: Pt–Ga Alloying during the Reduction of Pt/Mg(Al,Ga)Ox Catalysts and Its Effects on Propane Dehydrogenation. *ACS Catal.* **4**, 1812–1824 (2014).

115. Filez, M. *et al.* The role of hydrogen during Pt–Ga nanocatalyst formation. *Phys. Chem. Chem. Phys.* **18**, 3234–3243 (2016).

116. Lu, Z. *et al.* Atomic Layer Deposition Overcoating Improves Catalyst Selectivity and Longevity in Propane Dehydrogenation. *ACS Catal.* **10**, 13957–13967 (2020).

117. Ma, Z., Brown, S., Howe, J. Y., Overbury, S. H. & Dai, S. Surface Modification of Au/TiO2 Catalysts by SiO2 via Atomic Layer Deposition. *J. Phys. Chem. C* **112**, 9448–9457 (2008).

118. Yi, H. *et al.* Precisely Controlled Porous Alumina Overcoating on Pd Catalyst by Atomic Layer Deposition: Enhanced Selectivity and Durability in Hydrogenation of 1,3-Butadiene. *ACS Catal.* **5**, 2735–2739 (2015).

119. Lu, J. *et al.* Coking- and Sintering-Resistant Palladium Catalysts Achieved Through Atomic Layer Deposition. *Science (80-.).* **335**, 1205 LP – 1208 (2012).

120. Jeong, M.-G. *et al.* High-performing and durable MgO/Ni catalysts via atomic layer deposition for CO2 reforming of methane (CRM). *Appl. Catal. A Gen.* **515**, 45–50 (2016).

121. Pham, H. N. *et al.* Carbon Overcoating of Supported Metal Catalysts for Improved Hydrothermal Stability. *ACS Catal.* **5**, 4546–4555 (2015).

122. Hong, J. *et al.* Plasma Catalytic Synthesis of Ammonia Using Functionalized-Carbon Coatings in an Atmospheric-Pressure Non-equilibrium Discharge. *Plasma Chem. Plasma Process.* (2016). doi:10.1007/s11090-016-9711-8

123. Detavernier, C., Dendooven, J., Pulinthanathu Sree, S., Ludwig, K. F. & Martens, J. A. Tailoring nanoporous materials by atomic layer deposition. *Chem. Soc. Rev.* **40**, 5242–5253 (2011).

Chapter 2

Experimental methods

In this thesis, a wide variety of catalyst synthesis, characterization and testing procedures has been employed. This chapter details: 1. The means by which the catalysts were synthesised, 2. The characterization techniques employed and a brief overview of them. A more detailed account of X-ray absorption spectroscopy (XAS) and Small angle X-ray scattering (SAXS) is provided (theory and analysis), as they constitute a major component of the research. 3. Finally, all the activity tests are detailed as this pertains to data acquisition and analysis.

2.1 Synthesis of Heterogeneous Catalysts

2.1.1 Support Preparation

The support $MgAl_2O_4$ (spinel) was prepared by co-precipitation from an aqueous solution of $Mg(NO_3)_2.6H_2O$ (99%, Sigma-Aldrich) and $Al(NO_3)_3.9H_2O$ (98.5%, Sigma-Aldrich) (molar ratio Mg/Al = 1/2). NH_4OH (ACS reagent, 28.0-30% NH_3 basis) was used as the precipitating agent in order to maintain a pH of 10 at 333 K.[1] The precipitate was then dried at 393 K for 12 h and calcined in air at different temperatures, depending on the targeted surface area. The higher the temperature, the lower the surface area and vice-versa. The actual temperature values can be found in the respective results chapters.

Ga incorporated Mg(Ga)AlO hydrotalcite (HTL) material with 1 wt% Ga was prepared according to the procedure described in the work by Sun et al.[2], by co-precipitation from an aqueous solution of Mg (Sigma-Aldrich, 98-102), Al (Sigma-Aldrich, 98.5) and Ga (Sigma-Aldrich, 99.99%) nitrates, mixed with a 1.1 mol/L NaOH (Sigma-Aldrich, >98%) solution. The latter was then aged for 24 h at room temperature, subsequent to which it was dried at 393 K overnight in air and calcined in air at 973 K (2 K/min heating rate) for 10 h to obtain the final support.

2.1.2 Catalyst Preparation

Incipient wetness (co)-impregnation was the method of preparation employed for the respective catalysts. The targeted loading of Pt was 3 wt% throughout this thesis, while that of the promoter varied. The precursors used were: 1. Pt - $H_2PtCl_6.xH_2O$ (>99.9%, Sigma-Aldrich), 2. Sn - $SnCl_2$ (>99.9%, Sigma Aldrich), 3. Ga - $Ga(NO_3)_3.xH_2O$ (Sigma-Aldrich, 99.99%), 4. In - $In(NO_3)_3 \cdot xH_2O$ (Sigma-Aldrich, 99.99%).

The catalysts prepared are listed in Table 2.1.

2.1.3 Alumina Coating Procedure

Part of the two samples Pt:Ga/$MgAl_2O_4$ and Pt/Mg(Ga)AlO (number 8 and 10 in Table 2.1), was coated with a layer of alumina by means of Atomic Layer Deposition (ALD) in a high vacuum pump type ALD system. The precursor for this application was Tri Methyl Aluminum (TMA) with water as reactant and each with exposure times of 30 s. The deposition temperature was 423 K, while the pressure was 5 10^{-3} mbar. The thickness of the coating depends on the number of cycles of TMA/H_2O pulses that are applied on the sample. Previous work[3,4] has shown that 10 cycles of pulses corresponds to about ~1 nm of coating thickness. In order to avoid hindrance of alloy formation by the coating, e.g. by physically separating the individual Pt and Ga particles, the two samples were first reduced under a H_2-atmosphere in order to form a Pt-Ga alloy beforehand. These samples were then taken from the reduction setup to the ALD setup in order to apply the alumina coating. During this transfer the sample was exposed to atmosphere at room temperature, which could lead to partial oxidation of the sample. The samples were then coated with 10 cycles of ALD coating, hence a layer thickness of ~1 nm, and will henceforth be represented as $10Al_2O_3$/Pt:Ga/$MgAl_2O_4$ and $10Al_2O_3$/Pt/MgGaAlO in this work. Once the coating was applied, the samples were annealed under inert atmosphere (Ar) for 1.5 h at 923 K to induce cracks in the overlayer and assure accessibility to the active sites. This brings the coated catalysts in their as prepared state. The entire scheme of catalyst preparation is shown in Figure 2.1. A monometallic Pt/$MgAl_2O_4$ sample with a 1 nm coating was prepared along with the Pt:Ga samples (prepared for activity tests). In addition, two samples were prepared with 40 cycles of coating (~4 nm thickness: $40Al_2O_3$/Pt:Ga/$MgAl_2O_4$ & $40Al_2O_3$/Pt/MgGaAlO), which were mainly utilized for activity tests (PDH).

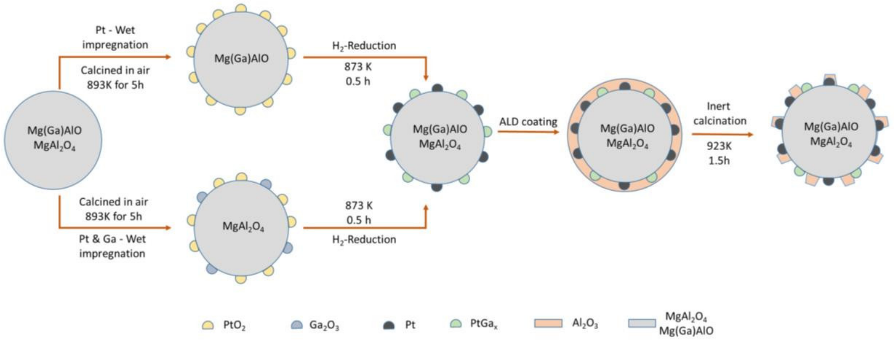

Figure 2.1: *Schematic of preparation of as prepared coated catalysts*

Table 2.1: *Overview of synthesized catalysts*

Sr No	Support	Catalyst	Loadings	label
1.	$MgAl_2O_4$ (HSA)	Pt	3 wt% Pt	Pt/HSA
2.	$MgAl_2O_4$ (LSA)	Pt	3 wt% Pt	Pt/LSA
3.	$MgAl_2O_4$ (HSA)	Pt:Sn	3 wt% Pt 0.4wt% Sn	Pt:Sn/HSA
4.	$MgAl_2O_4$ (HSA)	Pt:Sn	3 wt% Pt 3 wt% Sn	Pt:Sn
5.	$MgAl_2O_4$ (LSA)	Pt:Sn	3 wt% Pt 0.4 wt% Sn	Pt:Sn/LSA
6.	$MgAl_2O_4$ (HSA)	Pt:In	3 wt% Pt 3 wt% In	Pt:In
7.	$MgAl_2O_4$ (HSA)	Pt:In	3 wt% Pt 6 wt% In	Pt:In6
8.	$MgAl_2O_4$ (HSA)	Pt:Ga	3 wt% Pt 0.3 wt% Ga	Pt:Ga/$MgAl_2O_4$
9.	$MgAl_2O_4$ (HSA)	Pt:Ga	3 wt% Pt 1 wt% Ga	Pt:Ga
10.	Mg(Ga)AlO_x	Pt:Ga	3 wt% Pt 1 wt% Ga	Pt/MgGaAlO
11.	$MgAl_2O_4$	Al_2O_3/Pt:Ga	1 nm (10 cycles) and 4nm (40 cycles coating on catalyst number 8	10Al_2O_3/Pt:Ga/$MgAl_2O_4$ 40Al_2O_3/Pt:Ga/$MgAl_2O_4$
12	Mg(Ga)AlO_x	Al_2O_3/Pt:Ga	1 nm (10 cycles) and 4nm (40 cycles coating on catalyst number 10	10Al_2O_3/Pt:Ga/MgGaAlO 40Al_2O_3/Pt:Ga/MgGaAlO
13.	$MgAl_2O_4$ (HSA)	Al_2O_3/Pt	1 nm (10 cycles) coating on catalyst number 1	10Al_2O_3/Pt/$MgAl_2O_4$

2.2 Catalyst Characterization Methods

2.2.1 Surface Area and Porosity

The surface area and porosity of the materials are measured by N_2 adsorption-desorption at 77 K using a 5 point BET method (Micromeritics Tristar-II). The Brunauer-Emmett-Teller (BET) specific surface area (5 p/p_0 points), Barrett-Joyner-Halenda (BJH) average pore volume and average pore size (15 p/p_0 points), as well as the Harkins and Jura pore size distribution (ca. 40 pore width points) are determined. The samples were first degassed at 413 K for 2 h to remove any volatile adsorbates from the surface. The sample holders were then placed in the Micromeritics setup where they get suspended in liquid nitrogen, such that the target temperature of 77 K is reached.

This method assumes the catalyst can be modelled as a collection of parallel cylindrical pores. The Kelvin equation for capillary condensation is used, assuming a hemispherical liquid-vapour meniscus and a well-defined surface tension. The BJH theory uses a reference isotherm to account for thinning of the adsorbed layer; the Kelvin equation is only applied to the ‘core’ fluid.[5] For the complete pore diameter distribution, a Harkins and Jura adsorption model for slit pores was assumed. For a more detailed description of the Harkins and Jura model, the reader is referred to chapter 7 of Powder Surface Area and Porosity of S. Lowell and J.E. Shields.[5]

2.2.2 Elemental Analysis

Inductively coupled plasma optical emission spectroscopy (ICP-OES, iCAP 7400 instrument from Thermo Scientific) was employed to determine the bulk compositions of the catalysts. Mineralization of the samples was achieved by peroxide fusion.

2.2.3 Electron Microscopy

Scanning Electron Microscopy with Energy Dispersive X-ray **(SEM-EDX)** was performed on the support to obtain an estimate of the amounts of Mg and Al. A SEM JEOL JSM 5400 equipped with an INCA x-act extension (Oxford instruments) for Energy Dispersive X-ray (EDX) measurements was used for this purpose.

Dark field scanning transmission electron microscopy **(STEM DF)** was used to collect images, from which a particle size distribution/average particle size could be obtained. EDX was used for the local chemical analysis and mapping. The samples were deposited onto a lacey carbon film on a copper grid support. A JEOL JEM-2200FS, Cs corrected microscope at 200 kV, equipped with a Schottky-type field-emission gun (FEG) and EDX JEOL JED-2300D, was used for the measurements.

2.2.4 CO-DRIFTS

CO-DRIFTS (Tensor 27, Bruker, with MCT detector) experiments were performed to confirm formation of the alloys of Pt-Ga, Pt-In & Pt-Sn and to track the evolution of the alloy with increasing number of H_2/O_2 redox cycles. Each of the Pt:Ga/$MgAl_2O_4$, Pt:In/$MgAl_2O_4$ and Pt:Sn/$MgAl_2O_4$ catalysts were first subjected to multiple redox cycles (1, 5 and 10) at 873 K. The samples were then collected and mixed with KBr (inert material for infrared measurements) in a material/KBr ratio of 1/20 in order to assure a good signal to noise ratio. This diluted sample was then transferred to the in situ DRIFTS cell, mounted in a Selector™ accessory and evacuated. The redox cycles were not performed in the DRIFTS cell due to temperature limitations of the cell.

In the DRIFTS cell, a hydrogen gas flow (20% H_2/Ar) was passed over the sample, while increasing the temperature to 723 K (temperature limit of the setup). That temperature was held for 30 min to regain/reform the Pt-M alloy that might have segregated during exposure to atmosphere at RT during the mixing process with KBr. Cool down under 20% H_2/Ar to 313 K was subsequently ensued. At 313 K, the gas flow was switched to He and a background spectrum collected. Once this measurement was performed, the gas flow was switched to 1% CO/He for a period of 1 h. A set of 100 scans were collected following the CO exposure and the data averaged to get a good quality spectrum. All measurements were performed in absorbance mode between 400 cm^{-1} to 4000 cm^{-1} with a resolution of 2 cm^{-1}. Data analysis was performed with the OPUS 7.2 software (Bruker).

2.2.5 H_2-TPR and H_2-Pulse Chemisorption

H_2-TPR and H_2-pulse chemisorption (Micromeritics Autochem II) were performed to determine the general reduction profile and the % dispersion of the samples. Prior to the measurements, about 0.1 g of the dry sample was subjected to a pre-treatment step under 10% O_2/He at 873 K for 1 h, to remove any surface bound gases/impurities. Following this, the sample was cooled down to room temperature (RT) and the gas flow was switched to 60

Nml/min of 5% H_2/Ar for H_2-TPR. Once the flow was stable, a ramp rate of 10 K/min was employed to arrive at a target temperature of 873 K, which was held there for 30 min to ensure complete reduction. During this process, data acquisition was taking place by means of an inbuilt thermal conductivity detector (TCD), which was calibrated for 5% H_2/Ar. Once this 30 min hold time finished, the gas flow was switched to Ar at 873 K and a cooling process to 313 K was started. As soon as that temperature was reached and stable, H_2-pulse chemisorption was conducted and the volume of chemisorbed H_2 was determined based on the loop volume used, which was 0.17484 cm^3/g. This value was then used to determine the number of active sites and the % dispersion.

2.3 X-Ray Absorption Spectroscopy (XAS)

Since the discovery by Wilhelm Conrad Rontgen in 1895, x-rays have become an indispensable tool for studying the structure of matter. In the coming sections, the phenomenon of X-ray Absorption Spectroscopy (XAS) is explained and XAS data analysis is described.

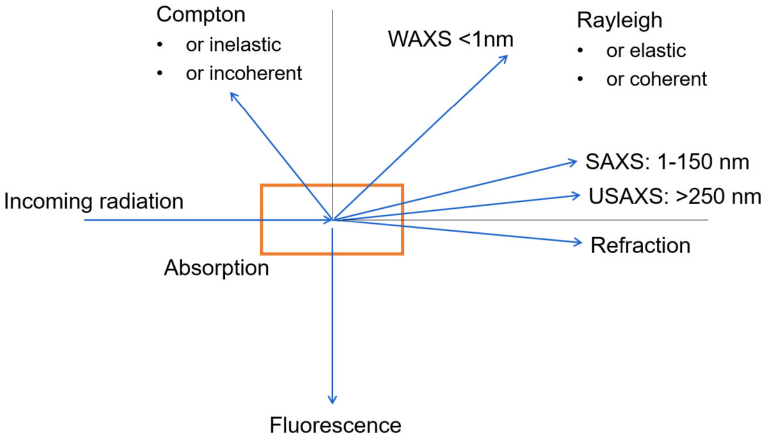

Figure 2.2: *Schematic of x-ray interaction with matter*

2.3.1 X-ray Interaction with Matter

X-rays interact with matter in two different ways (Figure 2.2 & 2.5).[6] First, x-rays can be absorbed by atomic electrons which are subsequently expelled from their core level to unoccupied electron states above the Fermi level. The unoccupied states can either be valence orbitals (bound-bound transition) or the continuum (bound-unbound transition). If the core electron is excited to the continuum, the excess photon energy is transferred to the so-called photoelectron as kinetic energy. The second type of interaction is x-ray scattering, in which the original direction of the incident x-rays is altered upon collision with matter. This scattering process can occur with (Compton scattering) or without energy loss (Rayleigh scattering).

2.3.2 Synchrotron basics

A synchrotron is a design of a cyclical particle accelerator, in which a beam of charged particles passes repeatedly through a magnetic field to deviate them from a linear trajectory. This field adjusts to maintain control over the path of the beam as it moves around the circular ring. The principle was developed by Vladimir Veksler in 1944, with the first electron synchrotron built in 1945 and the first proton synchrotron built in 1952.

The synchrotron can be thought of as an improvement of the cyclotron, that was designed in the 1930s. In cyclotrons, a beam of charged particles moves through a constant magnetic field that guides the beam on a spiral path, and then passes through a constant electromagnetic field that provides an increase in energy on each pass through the field. This bump in kinetic energy means the beam moves through a slightly wider circle on the pass through the magnetic field, getting another bump, and so on until it reaches the desired energy levels.

What makes the synchrotron an improved version of the cyclotron is that instead of using constant fields, the synchrotron applies a field that changes in time. As the beam gains energy, the field adjusts accordingly to hold the beam in the center of the tube that contains the beam. This allows for greater degrees of control over the beam and the device can be built to provide more increases in energy throughout a cycle.

One specific type of synchrotron design is called a storage ring, which is conceived for the sole purpose of maintaining a constant energy level in a beam. Many-body accelerators use the main accelerator structure to speed up the beam to the desired energy level, then transfer it into the storage ring to be maintained until it can collide with another beam moving in the opposite direction. This effectively doubles the energy of the collision without having to build two full accelerators to get two different beams up to full energy level. This is the case for synchrotrons such as CERN. In synchrotrons, where measurements like XAS, XPS, etc are the sole purpose (generation of x-rays), the particle beam is “accelerated” through bending magnets or insertion devices (undulators). Therefore, synchrotrons are a derivative of many body accelerators (Figure 2.3).

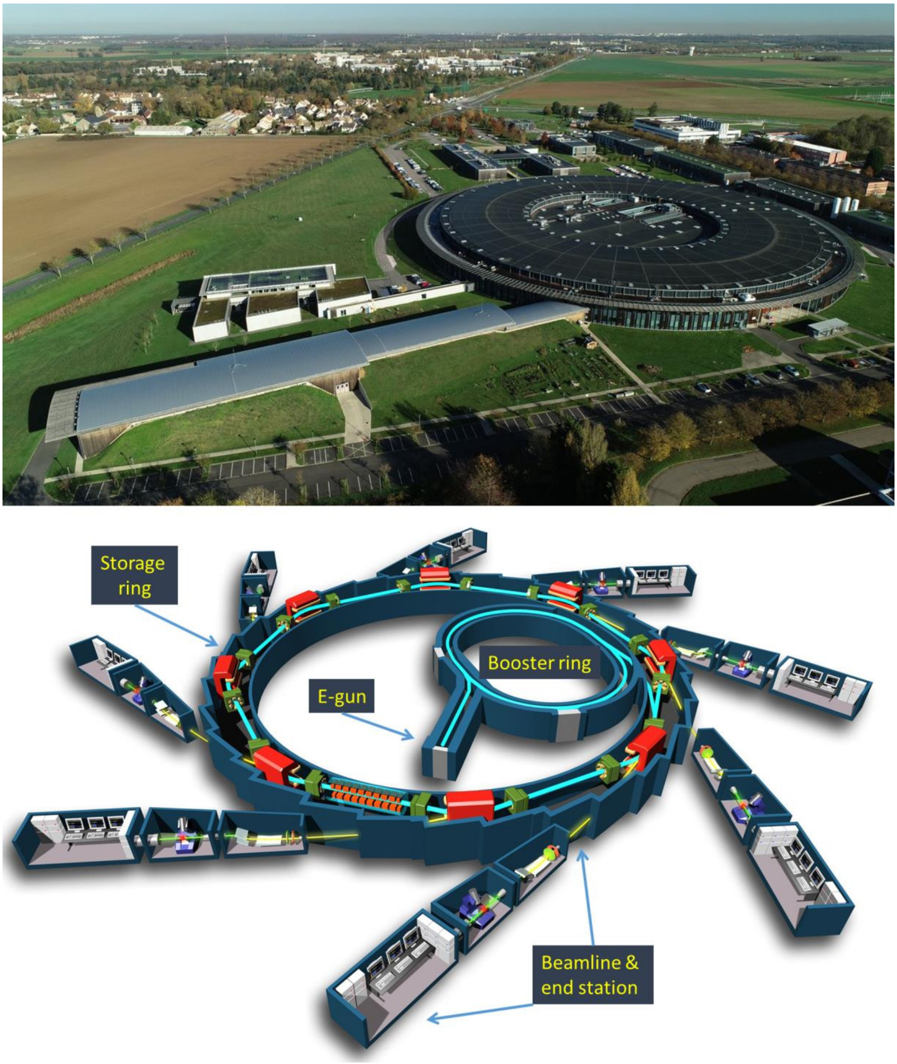

Figure 2.3: *Top image shows the sky view of the SOLEIL synchrotron situated at Saint-Aubin, France. The image below that is a schematic diagram of synchrotron SOLEIL. The synchrotron emits "synchrotron radiation", especially x-rays; these are sent into the various beamlines (the straight lines branching out of the synchrotron). Each beamline contains scientific instruments, experiments etc. and receives an intense beam of radiation.*[7]

This beam is then employed for x-ray based measurements in beamlines, i.e. the location where x-ray measurements take place. They are typically placed tangentially to the storage ring as shown in Figure 2.3.

2.3.3 Introduction to XAS

Figure 2.4 shows that the probability of x-ray absorption in the x-ray regime is orders of magnitude higher than Rayleigh and Compton scattering, implying that x-ray absorption is the dominant process for Pt atoms.[8] In comparison to the smooth scattering cross-sections, the x-ray absorption cross section shows multiple discontinuities. These sudden jumps are termed 'edges' and originate from x-ray absorption by electrons at different core electron levels. At (above) the edge energy, the x-ray energy equals (exceeds) the energy difference between the initial and final electron states. When the x-ray energy is below the edge energy, no x-ray absorption and photoelectric excitation can occur. The gradual increasing of the x-ray energy from below to above the edge energy results in the observed sharply rising edge features.

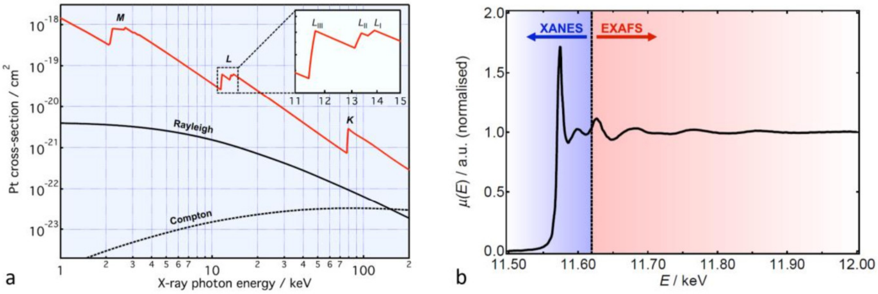

Figure 2.4: a: *Platinum x-ray absorption (red) and scattering (black) cross sections as a function of photon energy. The inset of a shows the Pt* L_I*,* L_{II} *and* L_{III}*-edges which are located around 12 KeV.* ***b:*** *Pt* L_{III}*-edge showing the XANES and EXAFS regions.*[8]

These described edges form the basis for x-ray absorption spectroscopy (XAS).[9,10] A XAS spectrum is usually recorded by scanning over energies (E) from below to above the edge energy (E_0). The x-ray absorption coefficient displays modulations which are superimposed on a non-oscillatory background. The background can be thought of as the absorption signal of an isolated atom, which does not have neighbours in the near environment, and therefore is named 'atomic background'.[9,10] In the event of neighbouring atom presence, modulations are possible through scattering of the excited photoelectron by these surrounding atoms and subsequent signal interference. These modulations contain detailed information on the atomic structure as well as the electronic properties of the materials.[9,11]

Hence, XAS refers to the details of how x-rays are absorbed by an atom at energies near and above the core-level binding energies of that atom. XAS spectra are sensitive to the coordination chemistry, formal oxidation state, distances and the coordination number and species of the atoms immediately surrounding the selected element. XAS can be used in a variety of systems and bulk physical environment.

As it is an atomic probe there are certain constraints on the samples to be studied. XAS can be employed for essentially every element in existence as all of them contain core level electrons. The advantage of using XAS is that there is no requirement of crystallinity of the sample, which makes it one of the few select techniques that is available to probe non-crystalline and highly disordered materials.

XAS measurements are quite straightforward, as long as there is availability of intense and tuneable x-rays. This is usually only possible at synchrotrons and therefore the history of development of XAS closely parallels that of synchrotron radiation. Nowadays, there are possibilities of very fast measurements of in situ chemical processes with high spatial resolution and at extreme conditions of temperature and pressure.

Although these measurements are relatively simple, the complete understanding and mastering of data treatment and analysis is challenging. Fortunately, an accurate and precise understanding of XAS spectra has become more routine over the years due to the availability of numerous theoretical an analytical tools.

XAS can be divided into 2 regimes as shown in Figure 2.4, namely: x-ray absorption near edge spectroscopy (XANES, $E - E_0 < 50$ eV), and extended x-ray absorption fine structure spectroscopy (EXAFS, $E - E_0 > 50$ eV). Through XANES, the oxidation state and coordination chemistry of the absorbing atom are established, while through EXAFS it is possible to determine the coordination numbers, distances and (nature of) neighbours to the absorbing atom.[12,13] The latter is achieved by fitting of the modulations that arise through scattering of the excited photoelectrons from neighbouring atoms as mentioned earlier.

2.3.4 XAS Measurements and Data Reduction

X-rays are light with energies ranging from ~ 500 eV to 500 keV. In this energy range, light is absorbed by all matter through the photoelectric effect. In this process, an x-ray photon is absorbed by an electron in a tightly bound quantum core level (such as the 1s or 2p level) of an atom (Figure 2.5).

The degree of x-ray absorption by matter can be quantified by the linear absorption coefficient μ according to Lambert Beer's law (eq. 2.1):

$$I_t = I_0 e^{-\mu x} \qquad (2.1)$$

where I_0 is the incoming x-ray intensity on a sample, x is the sample thickness and I_t is the intensity transmitted through the sample.

Through rearranging and application of natural logarithms on both sides, the expression for the linear absorption coefficient for transmission experiments is found (eq. 2.2):

$$\mu = \frac{\ln\left(\frac{I_0}{I_t}\right)}{x} \qquad (2.2)$$

The absorption coefficient, commonly represented as the total absorption μx is thus proportional to $\ln(I_0/I_t)$.

It is generally preferred to measure XAS in transmission as then an optimal S/N ratio can be attained. This is usually the case when μx = 2.5[8] above the edge and/or the edge step $\Delta\mu(E)x = 1$.[14] These criteria can be fulfilled by varying the sample thickness or through dilution with an inert material, while keeping the thickness constant. Care has to be taken to ensure uniformity of the sample bed with absence of any pinholes, as this can be detrimental to the signal quality. The grain size of the catalyst required is typically quite small (~50 µm) and achieved by crushing and sieving.

There are additional means, other than photoelectric absorption, by which the measurement of the x-ray absorption can be attained, albeit indirectly (Figure 2.5). These are x-ray emission and auger decay which are both de-excitation processes. After the loss of the core electron through excitation by the x-rays, a core hole is present. The atom is then considered to be in an excited state and relaxation occurs through filling of the core holes with electrons of higher levels. This transition from a higher to lower energy level leads to energy release in the form of fluorescent x-rays or by auger electron emission.[6,8,9] The former is dominant in the hard x-ray regimes (> 2keV) while the latter prevails at lower energies (< 2keV). These alternatives are valuable in instances where transmission measurements may not be feasible. Therefore, the XAS spectra are then recorded as the fluorescence (I_f) and electron yields (I_e), respectively. The detector is then typically placed at right angle to the incoming beam for fluorescence measurements to minimize the detection of scattering peaks. Auger measurements have to be performed in vacuum and are therefore not compatible with in situ XAS measurements.

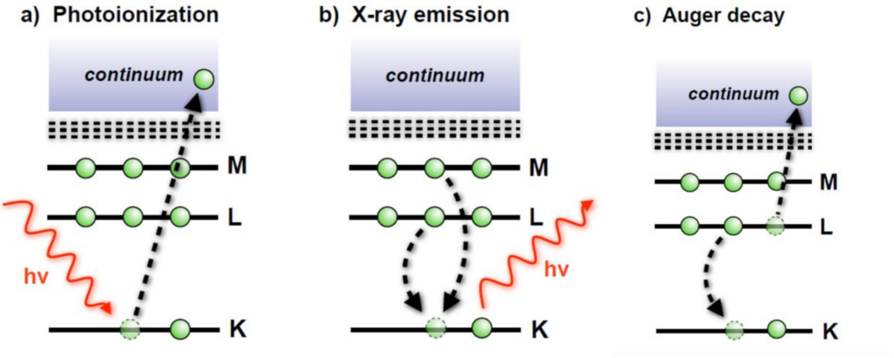

Figure 2.5: *Schematic energy level diagrams of atomic excitation and relaxation processes.* ***a:*** *X-ray absorption through photo-ionization,* ***b:*** *X-ray emission yielding fluorscent x-rays and* ***c:*** *Auger decay leading to auger electrons.*[8]

Regardless of how the absorption spectrum is measured, transmission or fluorescence, the data reduction and analysis remains the same. First, the raw data are reduced to yield XANES and EXAFS signals. According to Koningsberger et al., this should be done in five consecutive steps (Figure 2.6):[9,11]

1. *Pre-edge background subtraction:* a Victoreen ($V(E) = C_0 + C_1/E + C_2/E^2$) is fitted through the pre-edge region, extrapolated and subtracted from the absorption spectrum μ(E).
2. *Edge energy E_0 determination: it is defined as* the first maximum of the first derivative of the absorption spectrum.
3. *Fitting the atomic background μ_0:* a cubic spline function is fitted to the absorption signal in the range above the edge energy E_0. By means of a smoothing factor, the background is optimized and is chosen not to remove any oscillations of the data signal.

4. *Normalization of the edge step:* the total absorption signal $\mu(E)$ is divided by the value of $\mu_0(E_0 + 50)$, namely the atomic background around 50 eV above the edge energy E_0. This generates the normalized absorption spectrum.
5. *Isolation of the EXAFS signal $\chi(k)$:* the atomic background μ_0 is subtracted from the normalized absorption spectrum and subsequently the resulting $(\mu - \mu_0)$ is divided by the same atomic background, yielding $(\mu - \mu_0)/\mu_0 = \chi(E)$. Finally, the E-space EXAFS signal is transformed to k-space ($k = \sqrt{2m(E - E_0)/\hbar^2}$), eventually resulting in the k-space EXAFS signal $\chi(k)$. This can then be Fourier transformed into the R-space, to be used for EXAFS analysis.

The most confusing and error prone step in XAS data reduction is the determination and removal of the post-edge background spline function that approximates the single-atom absorption. The main aspect to be taken care of in this step is to only remove the low frequency components of $\mu(E)$.

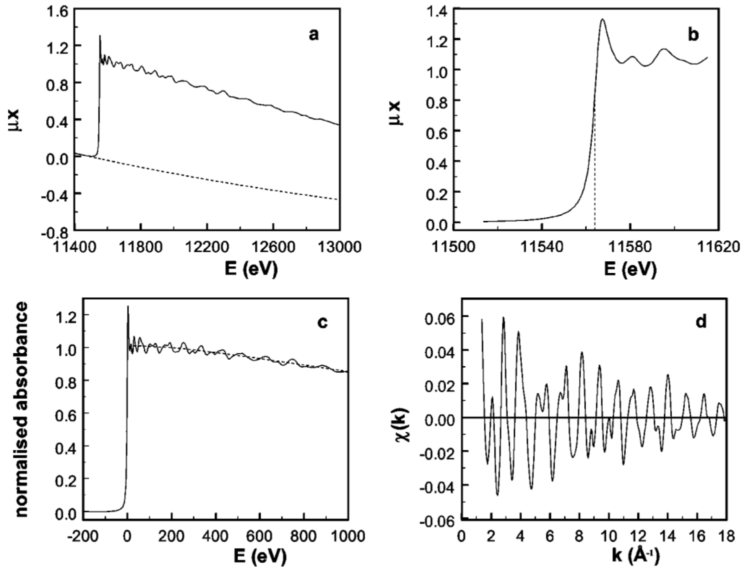

Figure 2.6: *Various steps of XAS data processing,* ***a:*** *pre-edge background removal,* ***b:*** *determination of edge energy position E_0,* ***c:*** *post-edge background removal and normalization and* ***d:*** *isolation of the XAS signal and transformation into k-space.*[9]

2.3.5 XANES

XANES measurements are performed typically within 30 eV of the main absorption edge. In this work, extensive XANES analysis of Pt-based samples is presented and the terms that will be regularly mentioned are the white line (WL) intensity and position. White line intensity is the intensity of the rising edge feature and this is proportional to the number of transitions taking place. WL position is the energy value of the WL maximum of the normalized XAS spectrum.

The rising edge of the absorption spectrum originates from the bound-bound transitions of the core electron level to electron orbitals above the Fermi level. The number of transitions is proportional to the density of unoccupied final electron states (Pauli's principle).[15] Based on this principle, two electrons cannot be in the same quantum state and therefore, the excitation of a core electron to a filled orbital is forbidden, which decreases the probability of such a transition. If the final orbital state is empty (high density of unoccupied states), core electron transitions can occur, which gives rise to a strong white line intensity through the higher number of x-ray absorption events. If the final state is the valence band, the XANES white line is a sensitive tool for probing the density of unoccupied states and therefore the atom's oxidation state.[10,16] For the Pt L_{III} edge, the XANES white line intensity monitors $2p_{3/2} \rightarrow 5d_{5/2}$ transitions and is known to exhibit linear proportionality with the Pt oxidation state.[11]

In general for the L-edges, only dipolar transitions are possible i.e., 2s → p, 2p → s or d, while for K-edges both dipole and quadrupole transitions are possible: 1s → p, s → d, p → f. Typically the s → d transitions are forbidden according to the dipole selection rule, but p-d hybridization of the x-ray absorber's orbitals through binding with other atoms can make s → d transitions partially allowed.[10,16] This and other types of hybridization give rise to pre-edge peaks, which yield information on the local geometry around the x-ray absorber. These pre-edge peaks are very sensitive to changes in that local environment, as perturbed atomic configurations can change the hybridization and therefore inhibit partially allowed transitions.[11,17] However, in this work In and Sn K-edges are measured. For both the In and Sn K-edges, the transitions that occur are 1s → 5p (as the 4d orbitals are completely filled $4d^{10}$), which are dipolar transitions and therefore no pre-edge features are expected/observed.

The white line position can serve as a tool for compound identification. This position changes based on electron donation/acceptance and can indicate aspects such as alloy formation/segregation or oxidation. Finally, the oscillations shortly above the edge are caused by multiple scattering (MSc) of the photoelectron by the absorber's neighbours.[17]

2.3.6 EXAFS

In this section, information will be provided on the steps employed for fitting of the EXAFS data. To get more theoretical information on the concepts of EXAFS, the reader is directed to the works of D.C. Koningsberger and S. Calvin.[9,13]

The main objective of an EXAFS analysis is to obtain quantitative structural information of the local environment of an absorbing atom. The general EXAFS equation is (eq. 2.3):

$$\chi(k) = \sum_{j=1}^{path} \frac{S_0^2 . N_j F_j^{eff}(k) . e^{-2k^2\sigma_j^2} e^{\frac{-2R_j}{\lambda(k)}}}{kR_j^2} sin[2kR_j + \delta_j(k)] \qquad (2.3)$$

where:

1. k is the photoelectron wave number as described earlier, calculated by $k = \sqrt{2m(E - E_0)/\hbar^2}$.
2. S_0^2 is the amplitude reduction factor, which accounts for the energy loss of the photoelectron caused by many-body effects.
3. N_j is the number of equivalent scattering paths j and represents the coordination number for SS (single scattering) paths.
4. R_j represents the photoelectron half path lengths of path j and equals to the average interatomic distance between the scatterer and the x-ray absorber for SS paths.
5. $F_j^{eff}(k)$ is the effective photoelectron backscattering amplitude function of the scatterers in path j.
6. $\delta_j(k)$ is the phase factor, which accounts for the effect of the absorber and scatterer atomic potentials.
7. σ_j^2 is the squared Debye-Waller (DW) bond length disorder factor, which corresponds to the average squared deviation in interatomic absorber-scatterer bond length relative to the average interatomic distance R_j, i.e. $\langle(r_j - R_j)^2\rangle$, for SS paths.

8. $\lambda(k)$ is the energy-dependent mean free path distance of the photoelectron and accounts for the finite lifetime of the excited state.

The parameters of the experimental EXAFS signal that are fit/modelled through this EXAFS equation are the coordination numbers N_j, interatomic distances R_j, and the Debye-Waller factors σ_j. The E_0, R_j, N_j, σ_j, and S_0 are estimated through the minimization of the objective function during EXAFS modelling. The three k-dependent parameters ($F_j^{eff}(k)$, $\delta_j(k)$, $\lambda(k)$) are obtained independently prior to modelling either by experimental extraction from reference materials, or by theoretical ab initio computation. Over the past years, the ab initio FEFF code (from $F_j^{eff}(k)$ ~ Feff) has made major steps forward and now allows to exclude the need for experimentally obtained k-dependent parameters.[11,18,19]

EXAFS modelling can be performed in both k-space and R-space. Modelling in k-space is only advised when the full R range is selected for modelling. It is also possible to model in the inverse Fourier transformed or Fourier filtered q-space. This however suffers from truncation effects and overlapping shells in R-space.

Prior to R-space EXAFS modelling, the k-space signal is prepared to yield the highest possible signal quality in R-space. First, the original k-space signal is multiplied by a rectangular windowing function to select the data which are kept for further analysis. The low k-region (k < 3 Å^{-1}) is eliminated since it contains XANES contributions. In addition, the windowing function cuts the noisy high k-region signal portion of the k-space EXAFS signal. Truncation by a purely rectangular shaped windowing function will yield truncation ripples in the R-space signal. For this reason, smoothly edged windowing functions are used to prevent such truncation ripples. In addition to signal windowing, an optimal k-weight for the k-space EXAFS signal should be selected such that the signal amplitude is concentrated in the middle of the windowing function and is dampened at the window edges.

The k-dependent parameters can be calculated from first principles by using the FEFF code, incorporated as part of the Artemis software, or through the JFEFF software, which is included in the IFEFFIT package.[18,19] In the FEFF routine, all possible photoelectron backscattering paths are calculated based on an input structure, supplied as a list of (x,y,z)-coordinates around the x-ray absorber. Subsequently, the most intense paths are selected for inclusion in the EXAFS model based on their overall amplitude contribution to the EXAFS signal.[19] For each selected photoelectron backscattering path, the backscattering amplitude function, phase shift and photoelectron mean-free path are then calculated.[20]

During R-space EXAFS modelling, the IFEFFIT program fits the structural model to the experimental EXAFS signal by minimizing the so-called chi-squared objective function (eq. 2.4):[18]

$$\chi^2 = \frac{N_{idp}}{N_{pts}\epsilon^2}\sum_{i=1}^{N_{pts}}[Re\big(\chi_e(R_i) - \chi_t(R_i)\big)^2 + Im\big(\chi_e(R_i) - \chi_t(R_i)\big)^2] \qquad (2.4)$$

where N_{pts} is the number of data points used for data fitting, ϵ is the measurement uncertainty and $\chi_e(R_i)$ and $\chi_t(R_i)$ are the complex Fourier transforms of the experimental and theoretical $\chi(k)$ signals, respectively. This χ^2 should not be confused with the EXAFS fine structure $\chi(E)$, $\chi(k)$ or $\chi(R)$. ϵ is calculated based on the average Fourier transformed EXAFS signal between R = 15-25 Å. At these radial distances, no significant signal is expected above noise level. For this reason, ϵ is used as quantification of the measurement uncertainty. N_{idp} represents the number of independent points and is a measure for the information content of the data. This number can be calculated based on the principles of information theory (eq. 2.5):[21]

$$N_{idp} = \frac{2\Delta k\Delta R}{\pi} + 1 \qquad (2.5)$$

where Δk and ΔR are the ranges for fitting employed in k- and R-space. The true content of an EXAFS signal is about 2/3 N_{idp} or less, which is shown through Bayesian methods.[22] The number of fitting parameters therefore should remain within this limit. In practice, N_{idp} amounts to ~ 8 – 10, implying that the number of photoelectron scattering paths should remain low, as each path can potentially require 4 or more fitting parameters (E_0, R_j, N_j, σ_j, S_0). Therefore the total number of parameters used during EXAFS modelling should be reduced and this can be achieved through correlating different parameters in a physically acceptable way.

Besides the χ^2 function, IFEFFIT also provides an additional related statistical parameter, being reduced chi-square χ_v^2 = $\chi^2/\, v$, where $v = \ N_{idp} - N_{par}$, and N_{par} is the number of parameters employed for the fit.[23] This reduced chi-square is better suited for model discrimination within the same dataset as it includes the number of parameters of the EXAFS model. A good fit should yield χ_v^2 values of around 1 if ϵ is a random fluctuation. In practice, these values are much higher (from 10 to 100's).[17] The reason for this is due to the poor theoretical description of the experimental EXAFS signal by the FEFF code, as well as the nature of ϵ, which is a poor estimate for measurement uncertainty.

χ^2 and χ_v^2 chi-squared values are only suited for comparison between different fits. Taking into account their absolute value, it is challenging to distinguish between truly bad fits, large theoretical errors or noisy data. Due to this, a more absolute measure for the goodness of a fit is provided by the R-factor (eq. 2.6).[23]

$$R - Factor = \frac{\sum_{i=1}^{N_{pts}}\left[Re\left(\chi_e(R_i) - \chi_t(R_i)\right)^2 + Im\left(\chi_e(R_i) - \chi_t(R_i)\right)^2\right]}{\sum_{i=1}^{N_{pts}}\left[Re\left(\chi_e(R_i)\right)^2 + Im\left(\chi_e(R_i)\right)^2\right]} \qquad (2.6)$$

Representing the fractional sum of squared residual misfits. Good fits typically have R-factors below 0.02 and χ_v^2 above 10.[23] If the R-factor is above 0.1, then the fit is not good, while within 0.05 it is okay.

Subsequent to modelling the Fourier transformed EXAFS signal, the structural parameters R_j, N_j, σ_j are obtained. Based on the near-neighbour coordination numbers N_j, calculations can be performed to obtain the shape and size of nanoparticles.[24,25] The first 2 coordination numbers N_1 and N_2 are good probes to determine the cluster size and are independent of cluster shape.

2.3.7 Actual XAS data measurements

In this thesis, numerous XAS datasets are presented. These XAS measurements were conducted at 2 synchrotrons located in France, namely: European Synchrotron Radiation Facility (ESRF, 6 GeV), located in Grenoble, and synchrotron SOLEIL (2.75 GeV), situated in Saint-Aubin.

The ROCK beamline was used at the SOLEIL synchrotron, which possesses the capability for QXAS measurements. The edges measured were the Pt L_{III}-edge (11564 eV), Sn K-edge (29200 eV) and In K-edges (27940 eV). Measurement was performed in transmission in most cases. In chapter 3, the measurement at the Sn K-edge was performed in fluorescence. The Pt L_{III}-edge and the In/Sn K-edges were measured in parallel using a Si(111) and Si(220) oscillating monochromator, by means of a macro for fast edge switching.[26,27] Further details of measurements can be found in chapters 3 & 4. It is possible to measure in the energy range of 4-40 keV while the critical energy is 8.65 keV. For this reason, the data that would be obtained at Sn and In K-edges would be more noisy than those obtained at the Pt L_{III}-edge, and therefore the noise would not be plainly due to the loadings of the samples. One of the main advantages of the ROCK beamline is the possibility for the measurement of two different edges during the same experiment (Pt L_{III}-edge with Sn K-edge or In K-edge) through its edge jumping feature. The disadvantage of this edge jumping feature is that, it takes about 30s to change between the two monochromators, during which time some valuable data may be lost. However, the advantage of measuring two edges outweighs the disadvantage.

The DUBBLE beamline at the ESRF was used for XAS measurements.[28] SAXS was also measured in parallel at this beamline, the results of which are presented in chapter 6. This was a regular XAS measurement, not QXAS, and it was performed at the Pt L_{III}-edge. At the DUBBLE beamline (BM26A) it was possible to measure in the energy range of 5-30 keV with a critical energy at 9.689 keV. The beamline however ceased to exist as of December 2018 and a new beamline: BM 14, will be its replacement once commissioned.

For all measurements, the samples were loaded into a quartz capillary reactor fixed with quartz wool plugs. This reactor was then mounted in a frame and connected to gas feed lines through Swagelock fittings.

2.3.8 QXAS vs. XAS experimental setups

XAS measurements are usually measured at beamlines due to the requirement of a continuous source of radiation and tuneable x-ray energies for measurement at different edges. Typical XAS setups employed at synchrotron beamlines are as represented in Figure 2.7. X-rays pass through a monochromator in order to select a specific energy for the beamline. In the case of standard XAS, this monochromator consists of two single crystal Si lattices that select an energy through Bragg's law for constructive interference on a crystal lattice. The crystal lattices are chosen depending on the energy range in which the measurements are to be performed.

At beamlines, focussing mirrors (not shown in Figure 2.7) allows for collimating (focussing) of the beam (x-rays), after which part of the beam is "cut-off" to the required beam size by passing through a slit. This beam is then typically sent through an ionisation chamber and subsequently onto the sample. These ionisation chambers[14] allow for the measurement of beam intensity before (I_0) and after (I_t) coming into contact with the sample. For the latter type of intensity, a choice must be made between measurement in transmission (I_t) or in fluorescence (I_f).

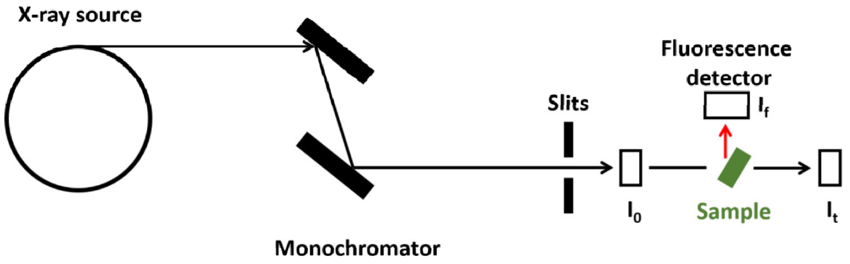

Figure 2.7: *Schmatic representation of an experimental setup used for XAS measurements.*

In this work, quick XAS (QXAS) is employed for the data presented in chapters 3 and 4. In order to perform QXAS it is necessary to quickly change the Bragg angle between the monochromator crystal between two values corresponding to the extremes of the desired absorption spectrum and repeat this movement over and over. QXAS differs from standard XAS in that it allows for fast, time-resolved measurements. The latter is based on a dedicated adaptation of the setup, namely the use of an oscillating monochromator. An example is presented in Figure 2.8 & 2.9.[29,30]

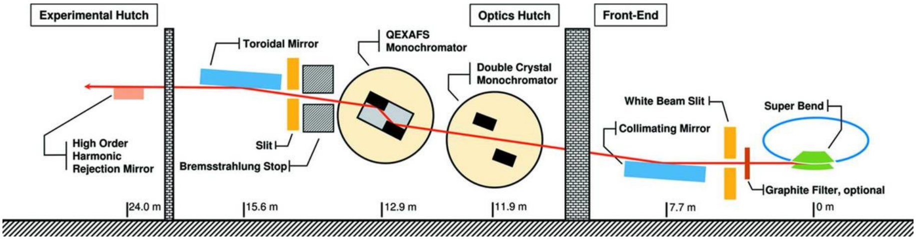

Figure 2.8: *Schematic view of the QXAS setup used at the SuperXAS beamline of the Swiss Light Source.*[29]

The case presented in Figure 2.8 consists of two Si single crystals mounted on a stage which is rotated by a torque motor to change the Bragg angle.[29] A similar setup is at the ROCK beamline.[30] The oscillating behaviour of this monochromator, along with specialized sensors and data acquisition techniques, allow for rapid and repetitive energy scans. As a result, the time resolution is improved to the order of ~s or even ~ms, compared to the order of minutes for a ‘standard’ XAS measurement.[29–31] At the ROCK beamline, it is possible to record spectra with an oscillating frequency up to 20 Hz, i.e. 25 ms per spectrum.[26,30] In conjunction with in situ measurements, this permits the detection of fast chemical reactions and short-lived intermediates.[29–32]

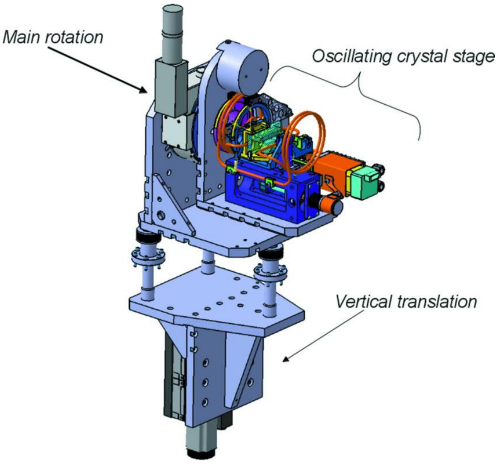

Figure 2.9: *View of the monochromator main components: a vertical motorized stage holds the main rotation; this is necessary to align the oscillating crystal stage to an average Bragg angle. The oscillating stage produces the fast oscillation and controls its amplitude.*[30]

The disadvantage of QXAS is the sheer amount of data obtained. Typical data volumes are in the order of TB, but can be reduced to GB through averaging of the spectra. For this reason, big data methods are required.

2.3.9 Analysis methods for QXAS data

There are a few methods by which such large datasets can be handled. A common approach employed to extract the different components from a series of spectra is a combination of principal component analysis (PCA) with least squares fitting of a linear combination of spectra of reference species to approximate the samples composition at a given time instant.[33–35] This method shall henceforth be referred to as PCA-LCF and its entire procedure is presented in Figure 2.10a. A disadvantage of this method is that such references – if available – may not be representative of the species in the sample. In some cases, such as for alloys, these spectra are not available. Furthermore, the candidate spectra are mostly obtained from bulk species, which can deviate from spectra of surface species both in energy shifts and amplitude.[36] As a result, the compositional evolution found through LCF may not be an accurate representation of the changes occurring in the sample. To overcome this problem, recent studies have shown a keen interest in blind source separation methods such as multivariate curve resolution with alternating least squares (MCR-ALS).[34,36–40] The biggest hurdle with this method is the non-unicity of the solution as well as the need for high-quality data, i.e. low noise. For more details on the mathematical background of these methods, the reader is referred to relevant literature on the topic.[13,31,33,34,41,42]

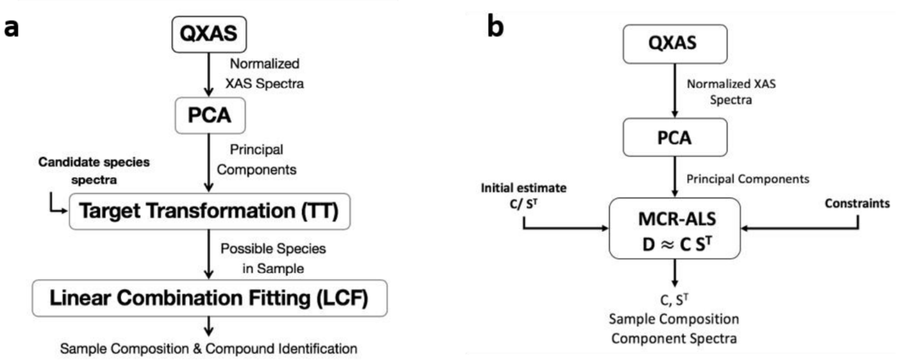

Figure 2.10: a: *PCA-LCF procedure and* ***b:*** *MCR-ALS procedure.*[42]

In brief, MCR-ALS is by definition a 'soft modelling method that focusses on describing the evolution of experimental multicomponent measurements through their pure component contributions'.[38] As the name implies, the method consists of 2 steps: MCR, in which the data matrix is approached by a bilinear relation, and ALS, in which an iterative least squares procedure is applied to find the optimal solutions.[34,41] The procedure for MCR-ALS is presented in Figure 2.10b.

2.3.10 Modulation Excitation Spectroscopy (MES)

EXAFS, in principle, is able to provide element specific local electronic/structural information directly. However, it is limited in certain ways as it averages over all the atoms of the element under the x-ray beam and does not (generally) permit discrimination between bulk and surface states. This is highly contrasting to the surface functional details that are yielded through e.g. vibrational spectroscopic techniques. Only a few spectroscopic techniques, of which infrared has been one for a considerable amount of time, are able to assess the local metal structure at work during the adsorption of a chemical species. This requires a high spatial and temporal resolution in general.[43–46] Though conventional approaches to EXAFS data collection do not permit an intrinsically high time resolution to be attained, a number of variants, based on diverse ideas and technical developments, have arisen that permit this x-ray based spectroscopy to be applied in a highly time-resolved fashion.[47,48]

These are categorized in terms of their capacity to address the behaviour under easily reversible/repeatable processes. Step scan[48] and the more recent "gating"[49] approaches to the induction of time resolution in scanning EXAFS experiments are limited to the study of highly reversible and/or rapidly repeatable systems and experiments. Quick-XAS (QXAS) does not have this limitation and offers the possibility of high spectral rates, which is essential for studying processes that may be fast, but may not present the above mentioned characteristics.

The QXAS approach does come with intrinsic caveats, checks and balances that have to be applied when using it to study working catalysts. However, they have been refined and applied successfully to the in situ study of working catalysts and a range of problems in chemistry, materials science and physics.[47,50,51]

It is established that the application of small perturbations to a chemical system and observing the changes of the system as a response, can provide insight into the kinetics and mechanistic aspects that is above and beyond what is achievable through steady-state experiments. This gives rise to the field of relaxation methods[52,53] for the study of kinetic events using, for example, step changes in one system parameter (T or P for instance).

Progression to the use of continuous fast transients leads to relaxation experiments such as, steady-state isotopic transient kinetic analysis (SSITKA),[54–56] where the catalyst environment is suddenly perturbed by the introduction of an isotope. This is typically employed in combination with DRIFTS to discriminate catalytically relevant species from the spectator species.

A further dimension is added beyond this single perturbation, through the notion of "modulation".[57] Periodic changes of the feed to a catalyst are intrinsic to, for instance, the operation of a three way catalyst (TWC),[58] and NO_x storage reduction (NSR) catalysts for the abatement of exhaust gases of vehicles.[59] Therefore, this method of operation is not only attractive to assess the presence of intermediate and active species, but even more so because it is applied in real world situations, under which catalysts of the sort being studied here actually operate.

In situ characterization with periodic change of an external parameter (concentration, temperature, pressure, etc.), termed as modulation excitation spectroscopy (MES),[32,57,60–62] is therefore another analytical tool, which may allow to tackle the problem of active components and sites. In a concentration modulation experiment, the concentration of the feed to the sample in the reactor is periodically changed between two values. This means that the reaction is turned on and off through periodic admission of one of the two reactants, or a periodic variation of one of the reactants, while keeping the other constant. This should entail a periodic change of the catalytic species involved, i.e. responding to the perturbation, which would be reversible with time. A typical example would be to cycle between reducing and oxidising conditions at a fixed temperature.[61] This continuous perturbation of the steady-state conditions can be coupled to a demodulation function (eq. 2.7):[57]

$$\mu(E,\Delta\varphi) = \frac{2}{T}\int_0^T \mu\,(E,t) Sin\left(\frac{360^o}{T}t + \Delta\varphi\right) dt \qquad (2.7)$$

This function transforms (demodulates) the time-resolved spectra $\mu(E,t)$ into phase-resolved spectra $\mu(E,\Delta\varphi)$ using phase-sensitive detection (PhSD).[57,63,64] This is performed in this work, by means of a sine function with a period of 120 s and a phase shift of $\Delta\varphi$, $0^o \leq \Delta\varphi < 360^o$. Following the modulation experiment, data are treated according to equation 2.7, yielding demodulated spectra, which are subsequently compared with so-called difference spectra. A difference spectrum is typically generated from low temperature XAS measurements of standard references, which are subtracted from each other. Notwithstanding the in situ, often high temperature character of such modulation experiments, the demodulated spectra typically provide better quality than the difference spectra. A schematic representation is shown in Figure 2.11.

The demodulated spectra contain information only of the signals that are affected by the modulation and the delay with which they respond to the external stimulus. Based on the phase lags ($\Delta\varphi$) between the stimulus and the response of certain signals in one experiment, species with varying kinetics and thereby their reactivity can be segregated. For these reasons, the demodulation technique is promising to distinguish between the active and spectator species in a catalytic experiment. Finally, the demodulated spectra can be compared with the difference spectra to get quantitative estimation of species engagement.

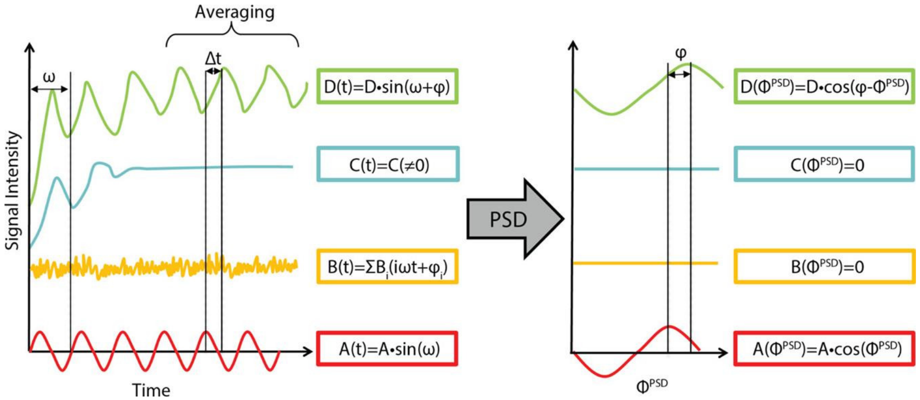

Figure 2.11: *Schematic representation of the working principle of PhSD (named PSD in the figure). A(t) is the stimulation function, B(t) is noise, C(t) is a response of a spectator species, and D(t) is the response of an active species. In the current scenario, the stimulation function is a sine wave with frequency ω. Demodulation using PhSD transforms time-domain spectra to the phase domain. The spectra are now a function of the phase angle ΦPhSD. Instead of appearing at a certain time delay Δt, in the phase domain, the absolute phase delay φ contains information about the dynamics and kinetics of the studied system.*[65]

2.4 Small Angle X-ray Scattering (SAXS)

In the last two decades, small angle x-ray scattering (SAXS) has become an established technique for structural characterization at the nanoscale of catalyst particles supported on high surface area materials. Through SAXS, information can be attained about the catalyst particle size (in the range of 1-50 nm), particle shape and distribution. The advantage of using this technique over others like TEM is that the scattered signal contains information averaged over millions of catalyst particles, whereas in TEM the analysis is very limited in space and also time-consuming as in many instances it is mainly done manually. A synchrotron x-ray beam diameter of the order of 100 µm probes about 100 million catalyst nanoparticles within an acquisition time of seconds to minutes.[66] Using TEM, a minimum of around 200 catalyst nanoparticles must be examined to attain representative statistics. The other advantage of SAXS is that this technique can be implemented in situ, which allows one to test the catalysts during reaction or under similar conditions. Finally, for supported materials containing high-Z elements, the support phase itself can give high contrast, rendering the supported nanoparticles close to invisible. In such case, SAXS can provide a means to extract experimental structural data on the catalyst particles at the nanoscale. Small particles in an x-ray beam will also scatter x-rays due to discontinuities in the electron density between the particles and the surrounding medium. This implies that the particles need not be crystalline. Further advantages are that SAXS is a non-destructive technique, it can be performed on conductive samples and requires limited sample preparation.

The difficulty for lab-based SAXS measurements lies in the fact that porous supports themselves obscure the scattering by the metal particles. This makes it very challenging to perform measurements at lab-scale. There are a few means by which this can be tackled. One way would be to apply high pressure on the catalyst samples, compressing it in order to make the pores collapse.[67] Another possibility would be to employ pore maskants with an electron density similar to the support, such as CH_2I_2, that can eliminate support interference.[68]

As alternative option, one can make use of synchrotron sources for x-ray energy. This would then make it feasible to use anomalous small-angle x-ray scattering (ASAXS), which exploits the fact that the scattering factor of e.g. a metal atom varies close to its absorption edges, whereas the scattering factor of the support remains constant. Hence, by taking the difference of two SAXS measurements close to an absorption edge of the metal of interest, one obtains the small-angle scattering curve of the metal particles without the support contribution.[69,70] For more details on the mathematical background of SAXS data processing, the reader is referred to relevant literature on the topic.[66]

2.4.1 SAXS Measurements

ASAXS measurements in this thesis are conducted on Pt:Ga catalysts at the DUBBLE beamline[28] of the ESRF synchrotron (6 GeV, current 160-200 mA, Grenoble, France). Measurements were performed in transmission mode at Pt L_{III}-edge and the data were collected by means of a Pilatus detector. The Q-range for analysis can be determined based on the sample-to-detector distance employed (Figure 2.12), which in this case was 2.180 m. Based on this distance, the Q-range for analysis ranges from 1.8 to 4.1 nm^{-1}.

When the sample-to-detector distance is much lower, the scattering angle increases, which in turn makes it into a wide angle x-ray scattering (WAXS). X-ray diffraction in essence is a type of WAXS, where the scattering arises from crystals and produces Bragg peaks (diffraction peaks) as a function of the scattering angle (or spots/rings in 2D patterns). The difference between WAXS and SAXS is the length scale they correspond to: WAXS detects ordering of individual atoms, while SAXS probes larger structures, based on electron density differences. When using transmission geometry and a 2D detector, switching between SAXS and WAXS can easily be done by moving the detector closer to the sample.

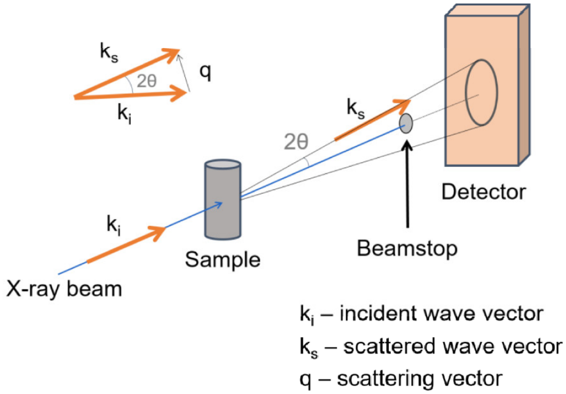

Figure 2.12: *Schematic representation of SAXS measurement.*

2.4.2 SAXS Data Reduction

The ASAXS measurements were performed in parallel to XAS measurements for bimetallic Pt:Ga catalysts. A photodiode was used as detector for collection of the XAS data and at the same time served as beam stop for the SAXS detector. There are multiple steps to undertake in order to extract data, as the measured scattering profiles contain information of the support along with the metal nanoparticles.

The steps followed for experiments and data treatment for a Pt:Ga/$MgAl_2O_4$ catalyst are (Figure 2.13):

1. During in situ measurements, the same experiments employed for Pt:Ga/$MgAl_2O_4$ have to be repeated for the bare support $MgAl_2O_4$, to provide a background basis for ASAXS.
2. ASAXS measurements for the empty capillary and a standard silver behenate (as distance calibration) have to be performed.

3. The energies used for ASAXS for this specific sample have to be just before and beyond the Pt L_{III}-edge, which is at 11400 eV and 11560 eV.
4. Azimuthal integration of the collected images. Application of this routine leads to the conversion of each of these images into a scattering profile $i_{scat}(q)$, whereby the intensity (measured in counts) is reported as a module of the scattering vector (eq. 2.8):

$$q = \frac{4\pi}{\lambda} sin(\theta) \tag{2.8}$$

5. Use the generated 1D profile for the standard silver behenate sample (empty capillary subtracted) to determine the exact sample-to-detector distance and integration parameters (X and Y pixel coordinates of direct beam, tilt rotation, and angle of tilt).
6. Carry out integration of all experimental data once the values are set.
7. Subtract empty capillary contribution from all integrated profiles in the region of interest (ROI: 1.8-4.1 nm^{-1}).
8. Subtract the support ($MgAl_2O_4$) contribution from the respective experiments to obtain the contribution of the nanoparticles.
9. Normalize all the datasets for visualization in order to qualitatively assess the changes that occurred to the sample.
10. Fit all the data (model) to obtain the nanoparticle size distribution.

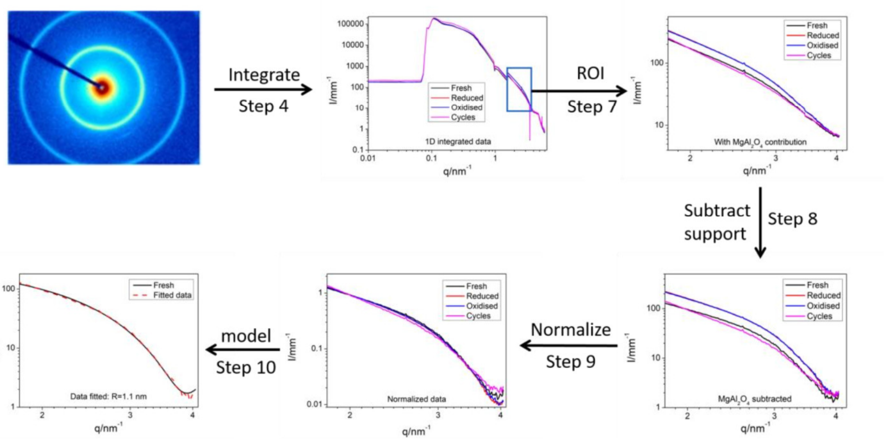

Figure 2.13: *Data treatment procedure for SAXS. The steps indicated in the picture are the data treatment steps described in § 2.4.2.*

2.5 Activity Tests

Activity tests were carried out in a fixed bed plug flow reactor (inner diameter (i.d.) of 7.5 mm) placed in an electric furnace. Quartz reactors were used for the experiments at atmospheric pressure. Typically, about 0.1 g of the catalyst was homogeneously diluted with α-Al_2O_3 and placed onto a quartz wool plug. The catalyst bed temperature was measured by K-type thermocouples touching the inside and outside of the reactor at the height of the catalyst bed.

The setup used is a step response instrument, which can be broadly divided into three sections, namely the feed, reactor and analysis sections (Figure 2.14). A detailed flow diagram along with a list of symbols can be found in Appendix A. The advantage of the setup is that there is an ability to choose between various types of feed gases or liquids (which will be vaporized) and an inert flow through the reactor. It therefore provides flexibility to perform reactions under different feed specifications without changing the reactor conditions of temperature and pressure. An additional advantage of this setup is the fast switching between different feed streams through a fast four way valve, enabling the users to simulate a "step response" or an "alternate pulse" experiment in the desired feed conditions.

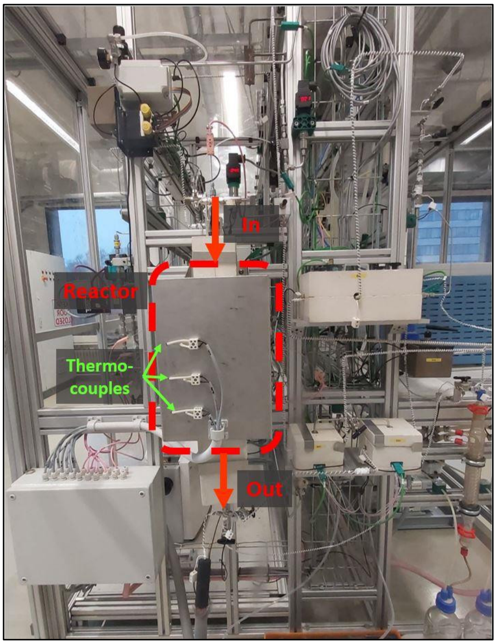

a

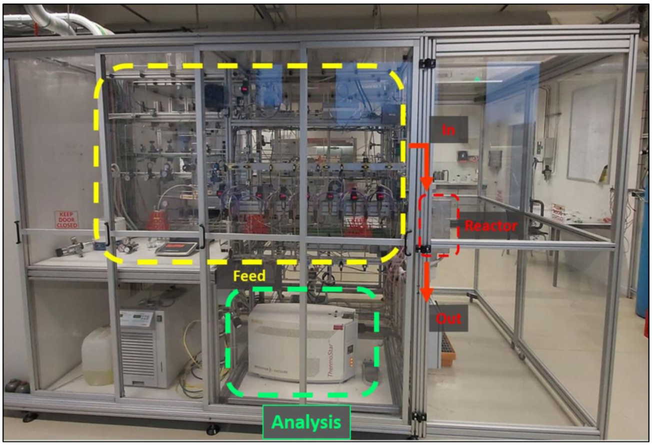

b

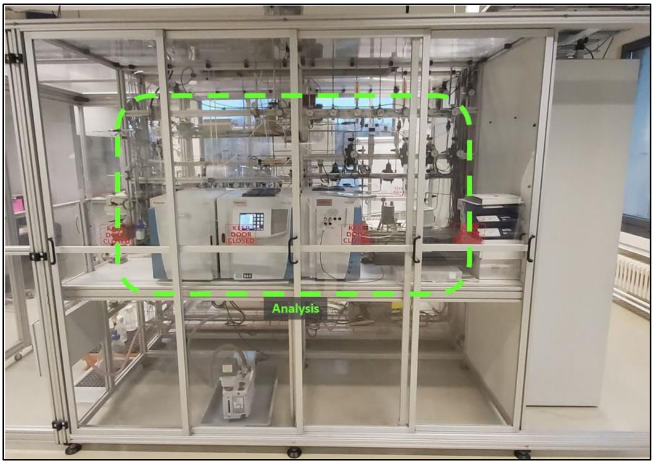

c

Figure 2.14: *Overview of the step-response setup showing the* ***a:*** *reactor,* ***b:*** *feed and* ***c:*** *analysis sections. The image b also has an analysis section with the MS situated below the feed MFC's.*

The incoming gas flows are controlled via calibrated Bronckhorst mass flow controllers (MFC). Calibration curves and conversion factors for the MFC's were used to convert the MFC set-point to the actual volumetric flow. For complete details on the activity measurements performed (gas flows, pre-treatment, etc.), the reader is directed to the respective results chapters.

The reactor outlet is connected with an Omnistar Pfeiffer mass spectrometer (MS) and a Gas Chromatograph (GC: Trace 1300, Thermo Scientific equipped with two thermal conductivity detectors (TCDs) and one Flame ionisation detector (FID)). The amu signals of C_3H_8 at 29 amu, CO_2 at 44 amu, CO at 28 amu, CH_4 at 16 amu, C_3H_6 at 41 amu, C_2 at 27 and 28 amu, H_2O at 18 amu and Ar at 40 amu were tracked. As a result of the amu selection being followed, there are a number of overlapping signals, which were separated by sending gas mixtures of C_3H_8, CH_4, O_2, CO_2, and H_2 at 3 different partial pressures with respect to the makeup Ar at room temperature (RT). These are used to create calibration curves for the MS and then applied to separate each individual gas contribution from each amu. In many instances, both the GC and the MS were employed, which resulted in accurate mass balance closures (< 5% deviation).

The following expressions are used to determine the activity of the different catalysts. The conversion (X_{C3H8}) of propane was calculated as shown in eq. 2.9:

$$X_{C3H8} = \frac{F^0_{C3H8} - F_{C3H8}}{F^0_{C3H8}} * 100\% \qquad (2.9)$$

where $F_{C3H8}{}^0$ and F_{C3H8} are the inlet and outlet flow of propane (C_3H_8) (mol s^{-1}). The selectivity (S_{C3H6}) towards propylene (C_3H_6) was calculated based on eq. 2.10:

$$S_{C3H6} = \frac{F_{C3H6}}{F^0_{C3H8} - F_{C3H8}} * 100\% \qquad (2.10)$$

where F_{C3H6} is the outlet flow rate of C_3H_6 (mol s^{-1}).

The space time yield (STY) of C_3H_8 (mol_{C3H8} s^{-1} kg_{Pt}^{-1}, eq. 2.11), was calculated based on the outlet molar flow rates, as measured relative to the internal standard, which in this case was Ar. The space time yield of propylene (STY, mol_{C3H6} s^{-1} kg_{Pt}^{-1}) was calculated as per eq. 2.12:

$$STY_{C3H8} = \frac{F_{C3H8}}{m_{Pt}} \qquad (2.11)$$

$$STY_{C3H6} = \frac{F_{C3H6}}{m_{Pt}} \qquad (2.12)$$

with m_{Pt} (kg) the mass of Pt loaded into the catalyst bed.

The C_3H_8 consumption rate (mol s^{-1} kg_{Pt}^{-1}, eq. 2.13), was calculated based on the difference between the inlet and outlet molar flow rates, as measured relative to the internal standard Ar.

$$C_3H_8\ consumption\ rate = \frac{F^0_{C3H8} - F_{C3H8}}{m_{Pt}} \qquad (2.13)$$

All reactions were performed in the kinetic regime.

2.6 References

1. Longo, A. *et al.* What Makes Fe-Modified MgAl2O4 an Active Catalyst Support? Insight from X-ray Raman Scattering. *ACS Catal.* **10**, 6613–6622 (2020).
2. Sun, P., Siddiqi, G., Chi, M. & Bell, A. T. Synthesis and characterization of a new catalyst Pt/Mg(Ga)(Al)O for alkane dehydrogenation. *J. Catal.* **274**, 192–199 (2010).
3. Solano, E. *et al.* In situ study of the thermal stability of supported Pt nanoparticles and their stabilization via atomic layer deposition overcoating. *Nanoscale* **12**, 11684–11693 (2020).
4. Solano, E. *et al.* Key role of surface oxidation and reduction processes in the coarsening of Pt nanoparticles †. *Nanoscale* (2017). doi:10.1039/c7nr04278g
5. Lowell, S. & Shields, J. E. *Powder surface area and porosity*. **2**, (Springer Science & Business Media, 1991).
6. Als-Nielsen, J. & McMorrow, D. *Elements of modern X-ray physics*. (John Wiley & Sons, 2011).
7. Ali, S. K. Synchrotron Radiation: Applications in Diagnosis and Treatment of Malignant Brain Tumors. in (ed. Das, U.) Ch. 18 (IntechOpen, 2011). doi:10.5772/21639
8. Van der Veen, R. M. *Ultrafast x-ray and optical spectroscopy of binuclear molecular complexes*. (EPFL, 2010).
9. Koningsberger, D. C., Mojet, B. L., van Dorssen, G. E. & Ramaker, D. E. XAFS spectroscopy; fundamental principles and data analysis. *Top. Catal.* **10**, 143–155 (2000).
10. Koningsberger, D. C. & Prins, R. X-ray absorption: principles, applications, techniques of EXAFS, SEXAFS and XANES. (1987).
11. Filez, M., Detavernier, C. promotor (viaf)313560819 & Marin, G. B. promotor (viaf)78456946. Alternative design of Pt-based catalysts : an X-ray spectroscopic view. (Gent : Universiteit Gent. Faculteit Ingenieurswetenschappen en Architectuur, 2015).
12. Newville, M. Fundamentals of XAFS. *Rev. Mineral. Geochemistry* **78**, 33–74 (2014).
13. Calvin, S. *XAFS for Everyone*. (CRC Press, 2013).

14. Bunker, G. *Introduction to XAFS: a practical guide to X-ray absorption fine structure spectroscopy*. (Cambridge University Press, 2010).

15. Basdevant, J.-L. & Rich, J. *Fundamentals in nuclear physics: From nuclear structure to cosmology*. (Springer Science & Business Media, 2005).

16. de Groot, F. M. F. AWARD PAPER: XANES spectra of transition metal compounds. in *Journal of Physics: Conference Series* **190**, 12004 (IOP Publishing, 2009).

17. Ankudinov, A. L., Ravel, B., Rehr, J. J. & Conradson, S. D. Real-space multiple-scattering calculation and interpretation of x-ray-absorption near-edge structure. *Phys. Rev. B* **58**, 7565 (1998).

18. Newville, M. IFEFFIT: interactive XAFS analysis and FEFF fitting. *J. Synchrotron Radiat.* **8**, 322–324 (2001).

19. Zabinsky, S. I., Rehr, J. J., Ankudinov, A., Albers, R. C. & Eller, M. J. Multiple-scattering calculations of X-ray-absorption spectra. *Phys. Rev. B* **52**, 2995 (1995).

20. Rehr, J. J. & Albers, R. C. Theoretical approaches to x-ray absorption fine structure. *Rev. Mod. Phys.* **72**, 621 (2000).

21. Brillouin, L. *Science and information theory*. (Courier Corporation, 2013).

22. Krappe, H. J. & Rossner, H. Error analysis of EXAFS measurements. *J. Synchrotron Radiat.* **6**, 302–303 (1999).

23. Newville, M. FEFFIT-Using FEFF to model XAFS data. *FEFFIT Progr. Doc.* (1998).

24. Frenkel, A. I., Hills, C. W. & Nuzzo, R. G. A View from the Inside: Complexity in the Atomic Scale Ordering of Supported Metal Nanoparticles. *J. Phys. Chem. B* **105**, 12689–12703 (2001).

25. Frenkel, A. I., Yevick, A., Cooper, C. & Vasic, R. Modeling the Structure and Composition of Nanoparticles by Extended X-Ray Absorption Fine-Structure Spectroscopy. *Annu. Rev. Anal. Chem.* **4**, 23–39 (2011).

26. La Fontaine, C., Belin, S., Barthe, L., Roudenko, O. & Briois, V. ROCK: A Beamline Tailored for Catalysis and Energy-Related Materials from ms Time Resolution to µm Spatial Resolution. *Synchrotron Radiat. News* **33**, 20–25 (2020).

27. La Fontaine, C., Barthe, L., Rochet, A. & Briois, V. X-ray absorption spectroscopy and heterogeneous catalysis: Performances at the SOLEIL's SAMBA beamline. *Catal. Today* **205**, 148–158 (2013).

28. Nikitenko, S. *et al.* Implementation of a combined SAXS/WAXS/QEXAFS set-up for time-resolved in situ experiments. *J. Synchrotron Radiat.* **15**, 632–640 (2008).

29. Muller, O., Nachtegaal, M., Just, J., Lutzenkirchen-Hecht, D. & Frahm, R. Quick-EXAFS setup at the SuperXAS beamline for in situ X-ray absorption spectroscopy with 10 ms time resolution. *J. Synchrotron Radiat.* **23**, 260–266 (2016).

30. Fonda, E. *et al.* The SAMBA quick-EXAFS monochromator: XAS with edge jumping. *J. Synchrotron Radiat.* **19**, 417–424 (2012).

31. Dent, A. J. Development of time-resolved XAFS instrumentation for quick EXAFS and energy-dispersive EXAFS measurements on catalyst systems. *Top. Catal.* **18**, 27–35 (2002).

32. Urakawa, A., Bürgi, T. & Baiker, A. Kinetic analysis using square-wave stimulation in modulation excitation spectroscopy: Mixing property of a flow-through PM-IRRAS cell. *Chem. Phys.* **324**, 653–658 (2006).

33. Manceau, A., Marcus, M. & Lenoir, T. Estimating the number of pure chemical components in a mixture by X-ray absorption spectroscopy. *J. Synchrotron Radiat.* **21**, 1140–1147 (2014).

34. Nayak, C., Bhattacharyya, D., Jha, S. N. & Sahoo, N. K. In Situ XAS Study on Growth of PVP-Stabilized Cu Nanoparticles. *ChemistrySelect* **3**, 7370–7377 (2018).

35. Jalilehvand, F. *et al.* Structural characterization of molybdenum (V) species in aqueous HCl solutions. *Inorg. Chem.* **46**, 4430–4445 (2007).

36. Cassinelli, W. H. *et al.* Multivariate curve resolution analysis applied to time-resolved synchrotron X-ray Absorption Spectroscopy monitoring of the activation of copper alumina catalyst. *Catal. Today* **229**, 114–122 (2014).

37. Fehse, M. *et al.* In-Depth Analysis of the Conversion Mechanism of TiSnSb vs Li by Operando Triple-Edge X-ray Absorption Spectroscopy: a Chemometric Approach. *Chem. Mater.* **29**, 10446–10454 (2017).

38. de Juan, A. & Tauler, R. Multivariate Curve Resolution (MCR) from 2000: Progress in Concepts and Applications. *Crit. Rev. Anal. Chem.* **36**, 163–176 (2006).

39. Voronov, A. *et al.* Multivariate curve resolution applied to in situ X-ray absorption spectroscopy data: An efficient tool for data processing and analysis. *Anal. Chim. Acta* **840**, 20–27 (2014).

40. Rochet, A., Ribeiro Passos, A., Legens, C. & Briois, V. Sulphidation study of a dried Ni/Al2O3 catalyst by time-resolved XAS-MS combined with in situ Raman spectroscopy and multivariate Quick-XAS data analysis. *Catal. Struct. React.* **3**, 33–42 (2017).

41. Jaumot, J., de Juan, A. & Tauler, R. MCR-ALS GUI 2.0: New features and applications. *Chemom. Intell. Lab. Syst.* **140**, 1–12 (2015).

42. De Coster, V., Poelman, H. promotor & Sabbe, M. copromotor. Analysing Big Data: QXAS on Ni-Fe catalysts. (2019).

43. Ferri, D. *et al.* First steps in combining modulation excitation spectroscopy with synchronous dispersive EXAFS/DRIFTS/mass spectrometry for in situ time resolved study of heterogeneous catalysts. *Phys. Chem. Chem. Phys.* **12**, 5634–5646 (2010).

44. Ferri, D., Newton, M. A. & Nachtegaal, M. Modulation Excitation X-Ray Absorption Spectroscopy to Probe Surface Species on Heterogeneous Catalysts. *Top. Catal.* **54**,

1070 (2011).

45. Weckhuysen, B. M. Chemical imaging of spatial heterogeneities in catalytic solids at different length and time scales. *Angew. Chemie Int. Ed.* **48**, 4910–4943 (2009).

46. Grunwaldt, J.-D. *et al.* Catalysts at work: From integral to spatially resolved X-ray absorption spectroscopy. *Catal. Today* **145**, 267–278 (2009).

47. Newton, M. A., Dent, A. J. & Evans, J. Bringing time resolution to EXAFS: recent developments and application to chemical systems. *Chem. Soc. Rev.* **31**, 83–95 (2002).

48. Bressler, C. & Chergui, M. Ultrafast X-ray absorption spectroscopy. *Chem. Rev.* **104**, 1781–1812 (2004).

49. Tada, M. *et al.* In situ time-resolved dynamic surface events on the Pt/C cathode in a fuel cell under operando conditions. *Angew. Chemie Int. Ed.* **46**, 4310–4315 (2007).

50. Newton, M. A. Dynamic adsorbate/reaction induced structural change of supported metal nanoparticles: heterogeneous catalysis and beyond. *Chem. Soc. Rev.* **37**, 2644–2657 (2008).

51. Pascarelli, S. & Mathon, O. Advances in high brilliance energy dispersive X-ray absorption spectroscopy. *Phys. Chem. Chem. Phys.* **12**, 5535–5546 (2010).

52. Strehlow, H. FUNDAMENTALS OF CHEMICAL RELAXATION. (1977).

53. Laidler, K. J. The development of the Arrhenius equation. *J. Chem. Educ.* **61**, 494 (1984).

54. Chuang, S. S. C., Brundage, M. A., Balakos, M. W. & Srinivas, G. Transient in situ infrared methods for investigation of adsorbates in catalysis. *Appl. Spectrosc.* **49**, 1151–1163 (1995).

55. Efstathiou, A. M. & Verykios, X. E. Transient methods in heterogeneous catalysis: Experimental features and application to study mechanistic aspects of the CH4/O2 (OCM), NH3/O2 and NO/He reactions. *Appl. Catal. A Gen.* **151**, 109–166 (1997).

56. Burch, R. The investigation of mechanisms in environmental catalysis using time-resolved methods. *Top. Catal.* **24**, 97–102 (2003).

57. Baurecht, D. & Fringeli, U. P. Quantitative modulated excitation Fourier transform infrared spectroscopy. *Rev. Sci. Instrum.* **72**, 3782–3792 (2001).

58. Heck, R. M. & Farrauto, R. J. Catalytic Air Pollution Control: Commercial. *Technol. Van Nostrand Reinhold, New York* (1995).

59. Roy, S. & Baiker, A. NO x storage− reduction catalysis: from mechanism and materials properties to storage− reduction performance. *Chem. Rev.* **109**, 4054–4091 (2009).

60. Bürgi, T. & Baiker, A. In situ infrared spectroscopy of catalytic solid− liquid interfaces using phase-sensitive detection: Enantioselective hydrogenation of a pyrone over Pd/TiO2. *J. Phys. Chem. B* **106**, 10649–10658 (2002).

61. Bürgi, T., Wirz, R. & Baiker, A. In situ attenuated total reflection infrared spectroscopy:

A sensitive tool for the investigation of reduction− oxidation processes on heterogeneous Pd metal catalysts. *J. Phys. Chem. B* **107**, 6774–6781 (2003).

62. Bürgi, T. & Baiker, A. Attenuated total reflection infrared spectroscopy of solid catalysts functioning in the presence of liquid-phase reactants. *Adv. Catal.* **50**, 227–283 (2006).

63. Serrer, M.-A. *et al.* Structural dynamics in Ni–Fe catalysts during CO2 methanation – role of iron oxide clusters. *Catal. Sci. Technol.* **10**, 7542–7554 (2020).

64. Gaur, A. *et al.* Probing the Active Sites of MoS2 Based Hydrotreating Catalysts Using Modulation Excitation Spectroscopy. *ACS Catal.* **9**, 2568–2579 (2019).

65. Müller, P. & Hermans, I. Applications of Modulation Excitation Spectroscopy in Heterogeneous Catalysis. *Ind. Eng. Chem. Res.* **56**, 1123–1136 (2017).

66. Binninger, T. *et al.* Particle-Support Interferences in Small-Angle X-Ray Scattering from Supported-Catalyst Materials. *Phys. Rev. Appl.* **3**, 24012 (2015).

67. Van Olphen, H. & Parrish, W. *X-ray and Electron Methods of Analysis*. **1**, (Plenum Press, 1968).

68. Renouprez, A., Hoang-Van, C. & Compagnon, P. A. Supported platinum catalysts—Small angle X-ray scattering and chemisorption. *J. Catal.* **34**, 411–422 (1974).

69. Rasmussen, F. B., Molenbroek, A. M., Clausen, B. S. & Feidenhans, R. Particle Size Distribution of an Ni/SiO2 Catalyst Determined by ASAXS. *J. Catal.* **190**, 205–208 (2000).

70. Chantler, C. T. Resonant Anomalous Scattering-Theory and Applications, edited by G. Materlik, CJ Sparks & K. Fischer. (1994).

Chapter 3

Behaviour of Platinum-Tin during CO_2-assisted propane dehydrogenation: Insights from quick X-ray absorption spectroscopy.

Abstract

CO_2-assisted propane dehydrogenation has been studied on Pt:Sn/$MgAl_2O_4$ catalysts with support surface area of ~127m^2/g or ~5m^2/g, 3wt% Pt and a Pt/Sn molar ratio of 3/1. In situ XAS was employed to track the dynamic changes occurring to the catalyst in presence of a reductive (H_2) or oxidative (CO_2) atmosphere. Reduction leads to the formation of a Pt-Sn alloy, the active compound for propane dehydrogenation. Oxidation by CO_2 led to the loss of the Pt-Sn alloy due to firstly oxidation of Sn to SnO and subsequent oxidation of SnO to SnO_2. The electronic and structural properties of the catalyst were determined by modelling of the EXAFS data. The Multivariate Curve Resolution-Alternating Least Squares (MCR-ALS) method was used in conjunction with the XAS data to determine the amount of Sn present in the Pt-Sn alloy phase and the phase of the alloy itself: after a single step reduction 42% of all Sn goes into the Pt_3Sn alloy, participating in the reaction, with the remainder being SnO_x. The percentage of Sn going into the Pt_3Sn alloy increased after 10 H_2/O_2 redox cycles to 72%. A combination of in situ XAS with CO_2-PDH activity data covering CO_2:C_3H_8 ratios from 0.25:1 to 1:1 allowed to show that CO_2 helps to improve conversion of propane by means of the reverse water gas shift reaction, wherein the product H_2 generated from PDH reacts with feed CO_2 to shift the equilibrium towards products. The reaction performed better at lower ratios of CO_2:C_3H_8. Increasing ratios of CO_2:C_3H_8 induced faster deactivation of the catalyst by the oxidation of Sn to SnO_x, leading to loss of Pt-Sn alloy. Suppression of carbon accumulation occurred by means of the reverse Boudouard reaction with the carbon formed during PDH. As possible reaction network for the entire CO_2-PDH reaction, a combination of Langmuir-Hinshelwood (L-H) and the Mars-van Krevelen mechanism (MvK) was proposed. The MvK steps were the oxidation of Sn to SnO by CO_2, which would then subsequently react with the H_2 and C generated from PDH that takes place on Pt sites by the L-H mechanism, to go back to the Pt_3Sn alloy.

The results of this chapter are published as:

N. V. Srinath, H. Poelman, L. Buelens, J. Dendooven, M.-F. Reyniers, G.B. Marin, V. V Galvita, Behaviour of Platinum-Tin during CO_2-assisted propane dehydrogenation: Insights from quick X-ray absorption spectroscopy, J. Catal. (2021). doi:https://doi.org/10.1016/j.jcat.2021.08.041.

3.1 Introduction

In chapter 1 it has been introduced that there is a potential benefit to adding CO_2 in the feed for PDH. CO_2 has a low cost, high availability and as a greenhouse gas its active utilization is highly recommended.[12] So far, the industrially used Pt:Sn catalyst has not been investigated for CO_2-PDH, as typically for this reaction the ratio of feed CO_2:C_3H_8 that is applied is larger than 1. The reason for this can be found in the thermodynamic calculations by Michorczyk et al.,[3] who investigated the effect of the ratio between CO_2 and C_3H_8. A CO_2:C_3H_8 ratio of 5 was ideal for better performance in terms of conversion and selectivity towards propylene. However, at such high ratio, Sn can get oxidised by CO_2 to SnO_2, leading to decomposition of the active Pt:Sn alloy phase,[4] required for the dehydrogenation reaction, and subsequent loss of activity. Thus, higher ratios of CO_2 to C_3H_8 will lead to lower Pt-Sn alloy stability.

If lower CO_2:C_3H_8 ratios were to be applied, e.g. CO_2:C_3H_8 = 1 or less, could the alloy and hence overall Pt:Sn catalyst stability be preserved? It would mean losing some of the benefits of a high molar ratio, like less carbon removal and less equilibrium shift, but might have advantages to compensate. Adding small amounts of CO_2 with respect to C_3H_8 is expected to help the process in a way similar to what oxygen does in the STAR process, through RWGS (eq 1.10) and the reverse Boudouard reaction (eq. 1.11). This would result in a lower rate of carbon formation on the catalyst surface, subsequently leading to long term stability and less frequent catalyst regeneration.

For CO_2-assisted PDH to become a valid alternative process, several factors need to be investigated as many open questions remain:

- What is the effect of the addition of CO_2 upon the catalyst structure?
- And how does this affect the reactivity?
- What is the stoichiometry of the Pt-Sn alloy during reaction?
- What is the stability of the Pt-Sn alloy under CO_2 and H_2 environment?
- Does CO_2 efficiently react with carbon on the catalyst surface?
- What is the role of SnO_x in reaction: carbon removal, PDH, RWGS?
- What is the mechanism by which CO_2 assists in the reaction?

This chapter focusses on answering the above questions by examining a Pt:Sn catalyst (3wt% Pt, Pt/Sn molar ratio of 3/1) for CO_2-assisted PDH. A magnesium aluminate spinel $MgAl_2O_4$ is used as support because of its proven stability, activity and lower rate of carbon formation with respect to other supports such as Al_2O_3, SiO_2, zeolites.[5–8] Propane and H_2 preferentially adsorb on acidic sites of the catalyst, while CO_2 prefers basic sites for adsorption. Therefore, $MgAl_2O_4$ makes an ideal support as it carries both these properties of MgO and Al_2O_3 (basic and acidic). To study the effect of particle size upon alloy formation, supports with 2 different surface areas are examined. The support surface area, high versus low, can be of importance as it determines how close the impregnated Pt and Sn are located with respect to each other, for a given loading. The latter can affect the ease of alloy formation, as well as the alloy nanoparticle (NP) size. In order to assess the effect of the support surface area, both a higher (HSA) and a lower surface area (LSA) $MgAl_2O_4$ support were used, whereby the HSA supported catalyst is expected to have a lower average NP size, while the LSA supported catalyst will have a larger average NP size. The support surface areas are controlled by varying the temperature at which the supports are calcined.

To access the local structure surrounding Pt and Sn in the nanoparticles, in situ QXAS is employed in order to examine the extent of reduction, the alloy phase formation and the oxidative state changes during exposure to H_2 and CO_2 during temperature programmed reactions. H_2/CO_2 isothermal redox experiments allow to determine which atmosphere has a more prominent effect on the catalyst. On the other hand, the reverse water gas shift (RWGS, eq. 1.10) is used as model reaction during in situ QXAS measurements, as it has both oxidizing (CO_2) and reductive (H_2) reactants, so that it mimics the CO_2-assisted PDH reaction. This will help to follow the stability of the Pt-Sn alloy under these atmospheres.

To link the structures obtained by QXAS for the Pt:Sn catalyst with its performance, activity tests are undertaken for PDH, alternate pulses of C_3H_8 with either CO_2 or O_2 and CO_2-PDH. The alternate pulse experiments are performed to determine if CO_2 reacts with the carbon on the catalyst surface. In order to assess the influence of CO_2 upon propane conversion and propylene yield, different ratios of CO_2:C_3H_8 are examined. Since CO_2 can potentially oxidise Sn to SnO_2, a possible reaction pathway is represented by eqs. 3.1 and 3.2, using both Pt and Sn sites, while regular propane dehydrogenation (eq. 1.1) would typically only take place on the Pt sites.

$$\text{Pt-Sn}_x + y\text{CO}_2 \rightarrow \text{Pt} + x\text{SnO/SnO}_2 + y\text{CO} \qquad (3.1)$$

$Pt + xSnO/SnO_2 + yH_2 \rightarrow Pt\text{-}Sn_x + yH_2O$ (3.2)

Through in situ QXAS, extensive catalyst characterization and a careful selection of experimental tests, this work brings new insight into the mechanism of the CO_2-assisted PDH, which will help in better catalyst selection. Particularly, it will facilitate the choice of an effective promoter to align with Pt and help to establish process conditions that can lead to higher efficiency.

3.2 Experimental section

3.2.1 Catalyst Preparation

3.2.1.1 Support preparation

Support $MgAl_2O_4$ was prepared by co-precipitation from an aqueous solution of $Mg(NO_3)_2.6H_2O$ (99%, Sigma-Aldrich) and $Al(NO_3)_3.9H_2O$ (98.5%, Sigma-Aldrich) (molar ratio Mg/Al = 1/2). NH_4OH (ACS reagent, 28.0-30% NH_3 basis) was used as precipitating agent in order to maintain a pH of 10 at 333 K. The precipitate was dried at 393 K for 12 h and calcined in air at 893 K for 6 h **(Higher surface area support – HSA)**. A different batch of $MgAl_2O_4$ support was prepared by calcination in air at 1373 K for 5 h subsequent to the drying step **(Lower surface area support – LSA)**. This method of preparation is similar to prior work from the lab.[8,9]

3.2.1.2 Catalyst Preparation

Pt:Sn catalysts with a Pt loading of 3 wt% (Pt/Sn molar ratio of 3/1) were prepared by incipient wetness impregnation on both supports ($MgAl_2O_4$, HSA and LSA) (label: Pt:Sn/HSA and Pt:Sn/LSA), using an aqueous solution of corresponding chlorides, $H_2PtCl_6.xH_2O$ (>99.9%, Sigma Aldrich) and $SnCl_2$ (>99.9%, Sigma Aldrich). Subsequently, the materials were dried at 393 K for 2 h and calcined in air (muffle oven) at 883 K for 5 h, yielding the 'as prepared' samples. In addition, monometallic $Pt/MgAl_2O_4$ (HSA) and $Pt/MgAl_2O_4$ (LSA) catalysts were prepared in order to serve as references.

3.2.2 Catalyst Characterization

The Brunauer-Emmett-Teller (BET) surface area was determined for all samples by N_2-adsorption at 77 K (five-point method, Tristar Micromeritics) after degassing the sample at 393 K for 2 h.

SEM-EDX was performed on all catalysts to obtain an estimate of their composition, using a SEM JEOL JSM 5400 equipped with an INCA x-act extension (Oxford instruments) for Energy Dispersive X-ray (EDX) measurements. The bulk compositions of the support and catalyst were determined by inductively coupled plasma atomic emission spectroscopy (ICP-OES, IRIS intrepid II XSP from Thermo Scientific). The samples were mineralized by peroxide fusion.

Dark field scanning transmission electron microscopy (STEM DF) was applied for structural analysis, while EDX was used for local chemical analysis. A JEOL JEM-2200FS, Cs-corrected microscope operated at 200kV, equipped with a Schottky-type field-emission gun (FEG) and EDX JEOL JED-2300D were used for the measurements. The samples were deposited onto a lacey carbon film on a copper grid support.

3.2.3 In situ quick XAS

Synchrotron-based *in situ* XAS experiments were conducted at the ROCK beamline of the 2.75 GeV SOLEIL light source (Saint-Aubin, France). QXAS measurements were performed in transmission at the Pt L_{III}-edge (11564 eV) and in fluorescence at the Sn K-edge (29200 eV). Both edges were measured in parallel using a Si(111) and Si(220) oscillating monochromator, by means of a macro for fast edge switching.[10,11] This allowed for quasi-simultaneous acquisition of spectra at both edges with a short delay (~60s) for the edge switch. The oscillating monochromator enables collection of multiple spectra in small time steps (~1 s, 2 Hz frequency). Upon extraction of all the raw XAS data using an interpolation grid, the XANES region of the data had measurement points every 0.25 eV at the Pt L_{III}-edge. At the Sn K-edge, the step used through the edge region was 1 eV.

Approximately 4 mg of as prepared material was loaded into a 1.5 mm quartz capillary reactor and kept in place by quartz wool plugs. The capillary reactor was mounted in a frame connected to gas feed lines through Swagelok fittings. An external heat gun was used in order to reach the temperature of 923 K, while the flows employed were maintained by means of calibrated Brooks mass flow controllers. The catalyst was subjected to several in situ treatments, indicated schematically in Figure 3.1. These included:

1. H_2-TPR (2 Nml/min H_2 & 5 Nml/min Ar, total flow = 7 Nml/min) up to 923 K to achieve alloy formation;

2. CO_2-TPO (2 Nml/min CO_2 and 5 Nml/min Ar, total flow = 7 Nml/min) to follow the effect of CO_2 on the alloy with temperature;

3. H_2-TPR to regenerate the Pt-Sn alloy prior to RWGS;

4. 10 Isothermal H_2/CO_2 redox cycles (mixture of 2 Nml/min H_2 with 5 Nml/min Ar alternated with mixture of 2 Nml/min CO_2 in 5 Nml/min Ar) to see the effect on the alloy and follow particle growth/sintering. In order to track the structural changes, a fast switching gas feed system was used for the redox cycles;

5. Reverse water gas shift reaction (RWGS) at 923 K (2 Nml/min H_2, 2 Nml/min CO_2 and 3 Nml/min Ar, total flow = 7 Nml/min)**.** RWGS was used as a model reaction for the in situ XAS measurements as the goal is to understand the stability of the Pt-Sn alloy in presence of both CO_2 and H_2 simultaneously, as would be the case during the CO_2-assisted PDH reaction. The H_2 would be generated by the dehydrogenation of propane, while the CO_2 would be in the feed.

In between treatments, the sample was cooled down in situ, in view of recording EXAFS at room temperature to limit temperature influence.

In addition to all the aforementioned experiments, measurements were performed at room temperature for the following reference samples: Pt-foil, Sn-foil, PtO_2, SnO_2 in view of fingerprint comparison and determining the amplitude reduction factor (S_0^2) values for subsequent use in fitting the experimental data. S_0^2 was determined (0.95) by fitting the first PtO_2 shell (Pt-O) with a standard Pt-O path of a PtO_2 crystal.

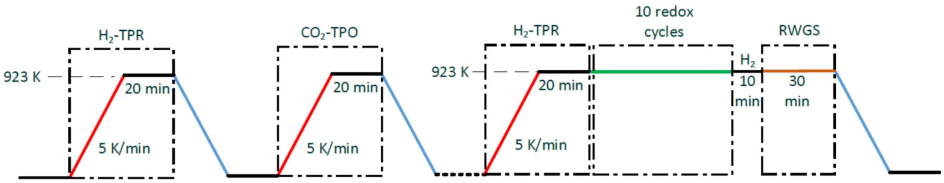

Figure 3.1: *Experimental scheme employed for in situ QXAS measurements.*

The EXAFS fitting results were obtained using the VIPER program,[12] and error bars were estimated with k^1/k^3 weighted fittings. The Fourier transformation of the data was performed with a Kaiser-Bessel window with a dk of 1.5. Once the value of S_0^2 was determined, it was fixed in the program to proceed with the fitting. The fitting at the Pt-edge was in general done in the R-range between 1.2 and 3.4 Å, while from 1.02 to 3.2 Å for the Sn-edge. Either 1 or 2 shells were used for fitting the data.

Sets of QXAS data were analyzed in a statistical manner by means of MCR-ALS (Multivariate Curve Resolution – Alternating Least Squares) to determine changes occurring to the alloy during the isothermal redox cycles. In view of this chemometric analysis, the QXAS data were normalized via the python normalization GUI developed by O. Roudenko.[11] A XAS_SVD toolbox,[13] with inbuilt PCA and associated tools,[14,15] was used for assessment of the number of principal components. MCR-ALS analysis was done in MATLAB with the toolbox developed by Tauler et al.[16] Number of components were determined from this PCA and the initial guesses for MCR-ALS were spectral type, obtained from the toolbox's inbuilt PURE initial estimation method.[16] For a more detailed review, the reader is directed to more specialized literature.[17,18]

3.2.4 Catalytic activity measurements

Activity and stability tests were performed at 873 K and 121.3 kPa in a quartz fixed reactor with an internal diameter of 7.5 mm housed inside an electric furnace. The activity of the blank reactor was measured under reaction conditions to affirm absence of any thermal and/or reactor effects on the measured activity. K-type thermocouples were used in order to measure the temperature of the catalyst bed and of the external reactor wall at the bed position. Calibrated Bronckhorst mass flow controllers were used in order to maintain the inlet gas flows. The catalyst sample with a particle size fraction of ~150 µm was diluted with α-Al_2O_3 for improved heat conductivity (ratio catalyst/inert = 1/5), placed in the reactor and kept in position by means of a quartz wool plug.

Prior to every experiment, the catalyst was reduced under a 100 Nml/min flow of 10% H_2/Ar at 873 K (heating rate of 10 K/min) for 30 min, after which the flow was switched to Ar. For CO_2-assisted PDH, a flow of CO_2:C_3H_8:Ar was fed with the total flow rate being fixed at 200

Nml/min. The ratio of CO_2:C_3H_8 was varied stepwise from 0.25:1 to 1:1, while keeping the flow of C_3H_8 fixed at 60 Nml/min.

A separate set of experiments, involving alternating feed flows of CO_2 and propane (both mixed with argon), was performed to determine the effect of CO_2 upon carbon on the surface of the catalyst and to establish if it is able to react with it, by means of the reverse Boudouard reaction, thereby (partially) regenerating the catalyst. For these experiments, 15 Nml/min flow of CO_2 and 40 Nml/min flow of C_3H_8 were alternated, while keeping the total flow at 200 Nml/min by using argon as diluent. The alternating flows were maintained for a period of 2 minutes each. Experiments were also performed with alternating flows of O_2 and propane, but in this case the flow of oxygen was kept at 10 Nml/min, while the diluent Ar was maintained at 190 Nml/min to keep a total flow of 200 Nml/min.

As a reference, a set of experiments of regular PDH was performed for all catalysts in order to determine their PDH activity. For the latter, a mixed flow of C_3H_8:H_2:Ar at a ratio of 1:1:3 was set with a total flow rate of 200 Nml/min.

The gases at the outlet of the reactor were analyzed using a calibrated OmniStar Pfeiffer mass spectrometer (MS) and a Trace 1300, Thermo Scientific equipped with two TCDs and 1 FID Gas Chromatograph (GC) in parallel. MS signals were recorded for all major fragments. For quantification of reactants and products, the MS was focussed to different amu signals. C_3H_8 was monitored at 29 amu, CO_2 at 44 amu, CO at 28 amu, CH_4 at 16 amu, C_3H_6 at 41 amu, C_2 at 27 and 28 amu and Ar at 40 amu. As there are several overlapping signals, the calibration of the MS was performed prior to the experiments by means of individual flows of each gas (at 3 different partial pressures) with argon at room temperature in order to generate a calibration curve. The calibration of propylene (C_3H_6) was done by means of data from the GC and applying it to the MS data, which then led to accurate mass balance closures (<5% error). For the GC calibration, Ar was used as internal standard, detected on the TCD channel. The CH_4 signals on the TCD were quantified using the Ar signal and subsequently this value for CH_4 was applied to the FID channel in order to quantify the signals for C_2, C_3H_8 and C_3H_6. To evaluate the significance of external and internal mass transfer limitations, the criteria of Carberry number[19] and Weisz-Prater[20] were applied, while for heat transport limitations the diagnostic criteria reported by Mears[21] were employed. These calculations allowed to perform all experiments without mass and heat transfer affecting the results (kinetic regime).

The conversion of propane, selectivity to propylene, propane consumption rate and STYs for propane and propylene has been calculated as per the equations described in chapter 2, § 2.5.

3.3 Results and discussion

3.3.1 Catalyst characterization

BET and porosity measurements were performed for all the as prepared supports and catalysts. The results are depicted in Table 3.1, together with SEM-EDX compositional results for the 2 supports and ICP values for the two Pt:Sn catalysts. The loadings of the supports are in accordance with expectation based on the synthesis. The surface areas of the HSA and LSA supports are very different, 126.7 vs. 5.4 m²/g respectively, as intended by use of a different calcination program in their preparation.

Table 3.1: *Chemical composition, BET and porosity results for all as prepared supports and catalysts, and mean particle size from STEM for reduced catalysts. Metal loading values for the Pt:Sn catalysts are derived from ICP measurements, while the values for the supports (HSA and LSA) follow from EDX measurements.*

Material label	**Metal Loading (wt%)**				**BET (m^2/g_{cat})**	**Pore volume (cm^3/g_{cat})**	**Mean particle size (nm)***
	Mg	Al	Pt	Sn			
$MgAl_2O_4$ (HSA)	14.5 ± 0.5	31.6 ± 1.1	-	-	126.7 ± 0.2	0.26 ± 0.02	
$MgAl_2O_4$ (LSA)	15.3 ± 0.4	32.3 ± 0.4	-	-	5.4 ± 0.1	0.026 ± 0.002	
Pt:Sn/HSA	13.8	32.4	2.24	0.34	98.1 ± 0.2	0.22 ± 0.02	1.5 ± 0.4
Pt:Sn/LSA	15.4	37.3	1.90	0.35	6.1 ± 0.1	0.020 ± 0.002	7.2 ± 1.8

* STEM particle size determined after H_2-TPR up to 923 K.

STEM DF images for the Pt:Sn/HSA and Pt:Sn/LSA, after 1 reduction step, are shown in Figure 3.2a and b along with the histogram (inset) for the particle size. The average particle size on the Pt:Sn/HSA sample (1.5 nm) is lower than that for the Pt:Sn/LSA (7.2 nm) sample, which is expected as the total wt% of Pt and Sn loaded is similar and the only difference is the available surface area of the support. At a first glance, it looks as if there are only 4 particles on the Pt:Sn/HSA sample (Figure 3.2a). However, a closer look shows that there are in fact a large number of smaller particles finely dispersed, reason for the low average size of particles obtained from the histogram. A second inset image in figure 3.2a with higher magnification emphasizes these smaller particles.

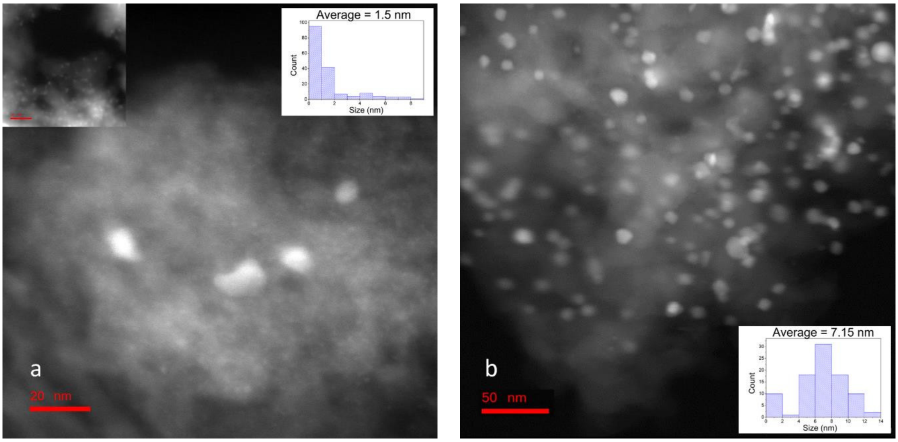

Figure 3.2: *STEM DF images of **a:** Pt:Sn/HSA (scale 20 nm) and **b:** Pt:Sn/LSA after one H_2-TPR step at 923 K (scale 50 nm). Insets: histograms of particle size image; extra inset in **a:** image at higher magnification to show the small Pt particles (scale 10 nm).*

3.3.2 XANES results during H_2-temperature programmed reduction (H_2-TPR), CO_2-temperature programmed oxidation (CO_2-TPO), isothermal H_2/CO_2 redox cycles and Reverse Water Gas Shift reaction (RWGS)

3.3.2.1 Pt-edge

The Pt XANES spectra acquired during different treatments, have all been normalized and then analysed based on the evolution of the white line (WL), comprising both the energy position of its maximum, as well as its intensity or height, both of which can be used to assess the state of the corresponding element. For high temperature measurements, temperature gives rise to thermal vibration of the atoms, increasing the noise level. As a result, the WL intensity of high-temperature XANES spectra is dampened and the amplitudes of post-edge peaks decrease with increasing temperature.[22] Wherever possible, WL intensities obtained at room temperature (RT) are mentioned. However, the high temperature XANES spectra from redox experiments such as H_2-TPR, CO_2-TPO will show WL intensity values that are lower than at RT, where the value was obtained after cool down in Ar. From experimental comparison, the WL intensities at RT are about 0.05 normalized absorption units higher than the values at 923 K. All values of WL intensities and positions subsequent to each experiment are listed in Table 3.2.

(i) H_2-TPR: The XANES evolution during TPR for the catalyst supported on HSA was markedly different from the catalyst on the LSA support (Figure 3.3). First, the white line intensity at the starting point of TPR is higher for the sample on HSA support when compared to the LSA supported sample, 2.4 vs. 1.5. Since this intensity is connected to the oxidation state of Pt, it indicates that Pt is initially in a more oxidised state on HSA than on the LSA support. This difference in the WL intensity and oxidation state can be ascribed to Pt having a larger average NP size on the LSA support, compared to the HSA, for the same wt% loading, see Table 3.1 and Figure 3.2.

Throughout the TPR, both white lines (WL) lose intensity as a result of the reduction process. For the HSA supported catalyst, the position of the white line maximum shifts from 11568.75 eV to 11567.5 eV (-1.25 eV shift), whereas for the LSA supported catalyst the WL first shifts from 11568 eV to 11566.75 eV (-1.25 eV shift) before returning to a higher energy position of 11567.5 eV (+ 0.75 eV shift).

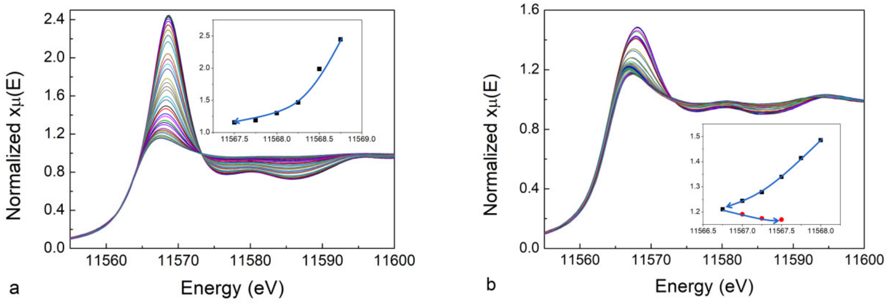

Figure 3.3: *XANES spectra at the Pt L_{III}-edge during H_2-TPR from room temperature (RT) to 923 K under a flow of 2 Nml/min H_2 mixed with 5 Nml/min Ar (total flow 7 Nml/min), for Pt:Sn samples supported on* ***a:*** *HSA and* ***b:*** *LSA. The insets for the two plots show the maximum values taken as average at each energy position. The arrows within the inset graphs provide a guide-to the-eye as to how the maxima positions shift with temperature and time.* ■, ●: *negative, positive position difference with respect to the previous data point.*

A similar measurement was performed for the monometallic Pt/LSA catalyst, where the WL maximum shifts from 11568.25 eV to 11566.5 eV (-1.75 eV). The final white line position of both Pt:Sn catalysts compared to the one for reference monometallic Pt/LSA catalyst (Appendix B-1, Figure B1) (11567.5 vs. 11566.5 eV) suggests that there is alloy formation between Pt and Sn, indicated by the shift in the white line position by +1 eV for the sample with Sn. For comparison, the WL position for the Pt foil was 11566.25 eV (Appendix B, Figure B2). The difference in the trend of the shifting WL between the Pt:Sn/HSA and the Pt:Sn/LSA samples indicates that alloy formation for the Pt:Sn/HSA sample is faster than for Pt:Sn/LSA owing to the smaller nanoparticles (NPs) on the former. The WL intensity for the Pt foil (1.24) and for monometallic Pt/LSA (1.25) after TPR, was higher than the one for the Pt:Sn/HSA (1.21) and Pt:Sn/LSA (1.19) samples. This is in accordance with other studies of Pt-based bimetallic alloys[23–28], where it was observed that alloy formation typically led to reduced WL intensities when compared to the monometallic counterpart, but it could also just be that the small particles for the Pt:Sn/HSA sample would lead to more metal-support interactions. A recent work by Yongxiao Tuo et al.[29], suggests that a strong interaction between Pt and $MgAl_2O_4$ occurs which would entail a partial positive charge which would then lead to this slight increase in white line intensity for Pt:Sn/HSA over Pt:Sn/LSA. There is an expectation of higher participation into alloy formation for the Pt:Sn/LSA, as the location of the Sn on the surface of the LSA sample should be close to the Pt particles due to its very low surface area as compared to the HSA sample.

(ii) CO_2-TPO: The H_2-TPR was followed in situ by a CO_2-TPO. For both LSA and HSA supported Pt:Sn samples, the CO_2-TPO step (RT to 923K) generates an increase in the WL intensity as well as a shift in its position, from 11567.5 eV to 11566.5 eV (-1 eV) for both samples (Figure 3.4). The latter indicates the loss of the Pt-Sn alloy, as the position moves back towards the one for monometallic Pt (Appendix B-1, Figure B1). At the same time, there is a partial increase in WL intensity. The CO_2-TPO was also performed for the monometallic Pt/LSA sample and here no changes to the WL intensity and position were observed with temperature (Appendix B-1, Figure B1b). The final WL intensities for the Pt:Sn/HSA and Pt:Sn/LSA were 1.42 and 1.30, respectively, while it was 1.25 for the monometallic Pt/LSA.

These results indicate the segregation of Pt from the Pt-Sn alloy during oxidation with CO_2 (metallic WL position). Since it is not possible to oxidise Pt with CO_2, see the unchanged Pt/LSA in Appendix B, Figure B1b, the only other option is that CO_2 oxidises Sn to SnO/SnO_2. The change in Pt-WL intensity could be due to Pt-O bonds in the Sn containing samples in contrast to the Pt-monometallic sample, leading to an increase in the d-orbital vacancies, which thereby entails an increase in WL intensity. However, the extent of WL intensity increase is different for the 2 samples: for the Pt:Sn/HSA sample it is larger (1.21 → 1.42) than for the Pt:Sn/LSA sample (1.19 → 1.30) and both end up higher than that for the monometallic Pt (1.25). The difference in the final WL intensities for Pt:Sn/HSA and Pt:Sn/LSA can be explained by the average Pt cluster size, which is smaller for the HSA sample compared to the LSA sample, cfr. the STEM results in § 3.3.1. The inference from this can be that once Sn is oxidised to SnO_2, the oxygen contribution from neighbouring SnO_2 to Pt is more significant when the Pt cluster size is small. This suggests that upon CO_2-TPO SnO_2 forms Sn-O-Pt bonds and when the Pt-cluster sizes are small the contribution of the oxygen neighbours of SnO_2 is significant enough to affect the WL intensity of the Pt-edge.

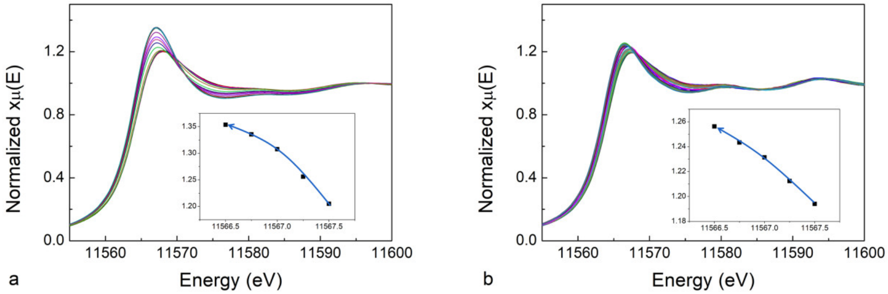

Figure 3.4: *XANES spectra at Pt L_{III}-edge during CO_2-TPO from RT to 923 K at a flow rate of 2 Nml/min of CO_2 mixed with 5 Nml/min of Ar (7 Nml/min total flow), for Pt:Sn samples supported on* ***a:*** *HSA and* ***b:*** *LSA. The inset for the two plots shows the maximum values taken as average at each energy position. The arrows within the inset graphs provide a guide-to the-eye as to how the maxima positions shift with temperature and time.*

(iii) Isothermal H_2/CO_2 redox cycles with MCR-ALS analysis: In order to mimic a series of reaction/regeneration cycles, 10 isothermal H_2/CO_2 redox cycles were performed at 923 K subsequent to a H_2-TPR reduction for the Pt:Sn/HSA sample, bearing the smallest particles. Each step of the redox cycle, i.e. the reduction step with H_2 and oxidation step with CO_2, took 1 min with a 1 min time gap between each step to facilitate the change of gas flows. Hence, one redox cycle took a total of 4 min.

Analysing the data through MCR-ALS showed that 2 components contribute to the Pt XANES spectra during redox cycling, alternating in weight (Figure 3.5a,b & Appendix B-6, Figure B8a, b). The WL positions of the MCR-ALS derived spectra are located at 11566.5 eV (component

1, present after each CO_2 step) and 11567.5 eV (component 2, present after each H_2 step), which point towards metallic and alloyed Pt, respectively. The respective WL intensities amount to 1.21 and 1.16, i.e. lower than the experimental values after CO_2-TPO (1.42) and H_2-TPR (1.21), which were however obtained at RT. Since the MCR-ALS procedure was applied to spectra recorded during isothermal redox cycles at 923 K, the WL intensity at 923 K is underestimated by about 0.05 normalised absorption units as indicated before. Hence, when this correction is applied, the WL position and intensity of component 2 obtained from MCR-ALS are very similar to those of Pt-Sn alloy (1.21). The corrected WL intensity of the CO_2-oxidised Pt component (component 1, 1.26 corrected intensity) is similar to the intensity of monometallic Pt, 1.25, and in the same position as that for the reduced monometallic Pt (11566.5eV).

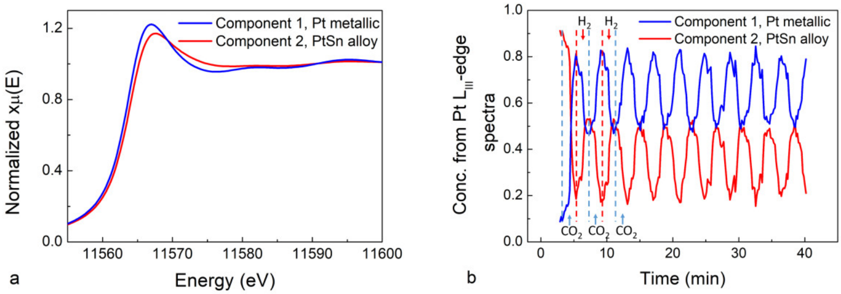

Figure 3.5: *MCR-ALS determination of* ***a:*** *XANES spectra at the Pt L_{III}-edge. It was found that 2 distinct components were present, which likely correspond to the Pt-Sn alloy and the monometallic Pt state* ***b:*** *Concentration profiles of the 2 components with time during H_2/Ar/CO_2 /Ar 1 min cycles. There were 10 H_2/CO_2 redox cycles that the catalyst sample was exposed to leading 10 oscillatory peaks.*

The graph of concentration profiles (Figure 3.5b) demonstrates that during the 4 min long isothermal redox cycles the Pt-Sn alloy state is not the major component of the sample present, except for short periods during the H_2 reduction steps. Even then, only ~50% of Pt reaches an alloyed state, while the rest remains more monometallic-like or partially oxidised by neighbouring SnO/SnO_2. There is, however, alloy present at all times in the sample during redox cycling under these conditions, with its concentration oscillating between ~20 % (at the end of the 1 min CO_2 exposure) and ~50% (end of 1 min H_2 exposure). During the H_2-reduction steps, extra Pt is taken up into the alloy again, amounting to about 50% of the Pt present.

Table 3.2: *Pt WL positions and intensities at RT for the different samples subsequent to each treatment. Intensity values obtained at high temperature (923 K) are corrected to a RT value (subtraction of 0.05 normalised absorption units, marked with *).*

WL position **WL height**	**Pt:Sn/HSA**	**Pt:Sn/LSA**	**Pt/LSA**	**Pt foil**
As prepared	11568.75 eV 2.4	11568 eV 1.5	11568.25 eV 1.62	11566.25 eV 1.24
Reduced	11567.5 eV 1.21	11567.5 eV 1.19	11566.5 eV 1.25	
CO_2 oxidised	11566.5 eV 1.42	11566.5 eV 1.30	11566.5 eV 1.25	
Redox H_2	11567.5 eV 1.21*			
Redox CO_2	11567 eV 1.26*			

There is another interesting aspect to account for from the graph of the concentration profiles (Figure 3.5b), where it can be seen that after the initial H_2-TPR reduction the concentration of the Pt-Sn alloy is close to ~90%, which then drops to ~20% once the sample is exposed to CO_2. This practically means that about 90% of the Pt present in the sample is initially in the alloy phase. The remaining Pt is likely not close enough to Sn on the HSA support, so that it does not get alloyed, only reduced, see the final spectrum of H_2-TPR.

(iv) RWGS: After redox cycling, which finished with a CO_2-oxidation step, Pt:Sn/HSA was exposed to H_2 for about 10 min at 923 K, before performing RWGS with a feed ratio of CO_2:H_2 = 1:1 at 923 K (B-5). A small change occurs to the sample during this reaction, with a slight increase in Pt L_{III} WL intensity (Figure B9a). Observation of each individual XANES spectrum with progressing time reveals that the sample reaches a "steady-state" within about 5 min of reaction and maintains that state for the remaining 25 min without undergoing any further changes. The position of the Pt WL remained the same throughout RWGS, implying presence of Pt-Sn alloy.

3.3.2.2 Sn-edge

Similar to the Pt-edge, the spectra at the Sn-edge are analysed for the same treatments (Figure 3.6). Since the measurements were run in parallel, the phenomena observed here can be correlated directly with the Pt-edge data. The Sn-edge spectra for the 2 as prepared samples

(Pt:Sn/HSA and Pt:Sn/LSA) are identical, showing Sn in a 4+ state for both catalysts, regardless of the support, with equal WL positions (29211 eV) and similar intensities (1.44 and 1.46).

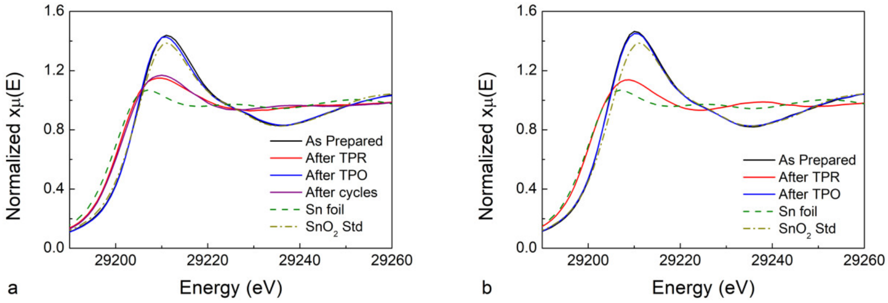

Figure 3.6: *All RT XANES spectra collected at the Sn K-edge subsequent to each treatment (H_2-TPR, CO_2-TPO, H_2/CO_2 redox cycles) for Pt:Sn supported on **a:** HSA and **b:** LSA. The plot also contains the Sn foil and SnO_2 XANES spectra.*

(i) H_2-TPR: Sn gets reduced in both HSA and LSA samples, as indicated by the change in WL position (B-2, Figure B3), shifting from 29211 eV to 29208 eV (-3 eV). Although the latter position is already closer to metallic Sn (WL for Sn foil at 29207 eV), the final WL intensity for the Pt:Sn/HSA sample after TPR is 1.14 and 1.13 for the Pt:Sn/LSA sample, while for the Sn foil it was only 1.07. This indicates that the Sn reduction is incomplete and/or an alloy has formed. The WL intensity of SnO and Pt-Sn alloys is similar based on theoretical XANES calculations, with a value of 1.16 for SnO, 1.04 for the Pt-Sn 1:1 alloy and 1.12 for the Pt-Sn 3:1 phase. The WL intensity at the end of TPR could hence point to SnO or a Pt:Sn 3:1 alloy in the samples. Based on the applied loadings and the observations at the Pt-edge, where close to full alloying was observed after reductive pre-treatment (Figure 3.5b), the presence of a Pt:Sn alloy phase with 3:1 stoichiometry is more likely.

(ii) CO_2-TPO: During the CO_2-TPO, Sn gets completely oxidised back to its initial Sn^{4+} state (B-2, Figure B4 & Figure 3.6). This can be observed by the WL position change from 29208 eV back to 29211 eV (+3 eV) and the concomitant increase in intensity to its original value (~1.44). Hence, CO_2 has the potential to drive Sn out of its alloyed state and fully oxidise Sn to SnO_2. The latter phenomenon also affects the Pt-edge indirectly: upon oxidation of Sn by CO_2, SnO_2 segregates from the Pt-Sn alloy phase, leaving Pt in a more metallic or even slightly oxidised state through contact with SnO_2.

(iii) Isothermal H_2/CO_2 redox cycles with MCR-ALS analysis: During isothermal redox cycling of the Pt:Sn/HSA sample, changes occur at the Sn-edge. Similar to Pt (Figure 3.5b), after the reducing pre-treatment the initial concentration of the alloyed or partially reduced SnO phase is over ~90%, leaving less than 10% of Sn in the sample fully oxidised. During cycling, also for Sn, 2 characteristic spectra were identified by MCR-ALS (Figure 3.7a). Component 1 is clearly SnO_2, while component 2 is similar to the Sn-edge spectrum obtained after H_2-TPR, so likely that of a Pt-Sn alloy or SnO or a combination of both. The WL positions of the 2 components were the same as those obtained for the experimental spectra for the "as prepared" and reduced state (after H_2-TPR), i.e. 29211 eV (component 1) and 29208 eV (component 2). The concentration profile for the 2 components (Figure 3.7b) reveals that only little extra Sn gets oxidised to SnO_2, yielding 15% of SnO_2 under CO_2 at 923 K.

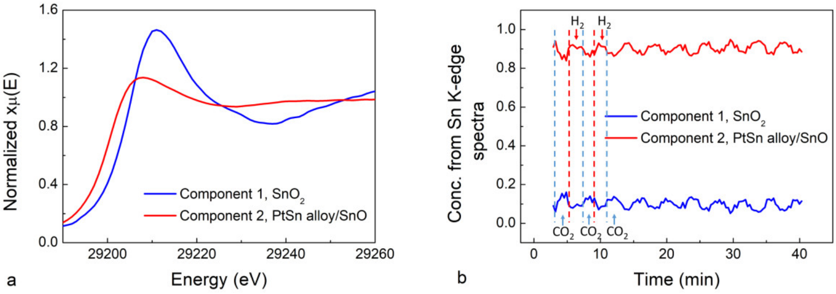

Figure 3.7: *MCR-ALS determination of* ***a:*** *XANES spectra at the Sn K-edge. It was found that 2 distinct components could be extracted, which likely correspond to the Pt-Sn alloy or SnO and the SnO_2 oxidised state;* ***b:*** *Concentration profiles of the 2 components with time during cycles of $H_2/Ar/CO_2/Ar$ for 1 min each. There were 10 H_2/CO_2 redox cycles at 923 K to which the catalyst sample was exposed leading to 10 oscillatory peaks.*

The major Sn component present in the sample throughout redox cycling is component 2 (>80%), which is the alloy/SnO state. Since the CO_2-TPO was capable of fully re-oxidising Sn to 4+ state, it is likely that the duration of CO_2 exposure in the redox cycles is too short to accomplish this. Instead, only a partial oxidation is realized, bringing only a small amount of Sn to SnO_2 state. However, the concentration profile at the Pt-edge (Figure 3.5b) shows a ~90% to ~20% decrease of the Pt-Sn alloy component upon the first 1 min exposure to CO_2, and from 50% to 20% in the next CO_2 half-cycles. This indicates that a major part of the originally alloyed Sn fraction does get oxidised by CO_2 and extracted from the alloy. Likely, this extracted Sn only gets oxidised to SnO rather than to SnO_2. Since the WL characteristics of SnO and Pt-Sn alloy are not readily distinguishable, the extracted and partially oxidised SnO fraction remains in component 2, leading to the observed Sn profile of Figure 3.7b.

(iv) RWGS: At the Sn edge small changes to the WL were observed during RWGS, which was performed after an intermediate H_2-reduction step subsequent to the isothermal redox cycles. The changes were similar to those occurring at the Pt-edge, where there was a slight increase in Pt L_{III} WL intensity during the first 5 min after which it reached a "steady state" (Figure B7 a&b). This would indicate that at the start of RWGS, Sn present in the alloy got partially oxidised by CO_2, the increase of WL intensity suggesting that it was to SnO (Sn^{2+}) and not to SnO_2 (Sn^{4+}), and segregated from the alloy, leading to the small WL increase for both edges. After this adjustment of the WL to the mixed RWGS feed, an equilibrium is reached between the CO_2 oxidation of Sn, and H_2 reduction of SnO, and at all times the Pt-Sn alloy does not get completely segregated as the position of the WL at the Pt L_{III} edge remained constant. Hence the mechanism by which the RWGS reaction proceeds would be as mentioned in eq. 3.1 & 3.2 (§ 3.1), occurring simultaneously.

3.3.3 EXAFS results subsequent to H_2-TPR, CO_2-TPO and RWGS

3.3.3.1 Pt-edge

Before and after each high temperature treatment, EXAFS spectra were recorded at room temperature. Fittings of the radial distributions were performed for 1 or 2 shells in the R-range of 1.4–3.2 Å. The crystal structures used for the fits were Pt crystal (Fm3m, cubic, Pt-Pt = 2.81 Å), Pt:Sn 3:1 crystal (Pm3m, cubic, Pt-Sn = 2.87 Å, Pt-Pt = 2.87 Å) and PtO_2 crystal (Pnnm, orthorhombic, Pt-O = 2.03 Å). Fits were also attempted with Pt:Sn 1:1 crystal ($P6_3/mmc$, hexagonal, Pt-Sn = 2.75 Å, Pt-Pt = 2.78 Å), which didn't yield results very different from those obtained with the Pt:Sn 3:1 crystal. All R-factors of fits were within 0.07.

(i) As Prepared sample: Fitting results are shown in Table 3.3 for the Pt:Sn/HSA sample, (Appendix B-3, Table B1 for Pt:Sn/LSA, Figure 3.8a and b for fitting figures, and Figure B5 for k-space). Based on the EXAFS signals and their fits, there are a few important takeaways. The difference in particle size between as prepared Pt:Sn on HSA and LSA support is visible in the EXAFS signal through the local Pt environment. Fitting for the freshly calcined sample on HSA support is possible with just a standard PtO_2 crystal structure (Pt-O = 2.03 Å), whereas for the sample supported on the LSA support, fitting requires both a Pt-O and a Pt-Pt shell. This is plausible based on the larger particle size of Pt on LSA support, see the STEM image in Figure 3.2, and the explanation in § 3.3.2.1.

(ii) After H_2-TPR: Fitting of the reduced state (after H_2-TPR) was performed with a Pt-Pt and a Pt-Sn shell. A fit was also performed with just a single Pt-Pt shell, but the R-factor improved significantly (0.13 to 0.03) upon introducing the Pt-Sn shell. The results of the fit for Pt:Sn/HSA indicate similar distances (2.72 Å and 2.65 Å) for the Pt-Pt and Pt-Sn shell. The total Pt coordination number (N) as $N_{Pt-Pt} + N_{Pt-Sn}$ amounts to 5.2 ± 0.7, which corresponds to a cluster size of ~0.7 nm[30,31], assuming a hemispherical nanoparticle shape. The fitting for Pt:Sn/LSA gave much higher coordination number values ($N_{Pt-Pt} = 8.18$ and $N_{Pt-Sn} = 2.45$), when compared to the Pt:Sn/HSA sample. The total Pt coordination number for the Pt:Sn/LSA sample now adds up to 10.6, which corresponds to ~6 nm clusters under the same assumption. The interatomic distances of the Pt-Pt and the Pt-Sn shell were also higher (2.77 Å and 2.74 Å) and thereby closer to the bulk values (Pt-Pt and Pt-Sn = 2.87 Å for the Pt:Sn 3:1 crystal). A smaller metallic bond distance together with a lower coordination number are commonly observed for small-sized particles of 1-5 nm[24], where lattice relaxation can lead to a 10% decrease in the metallic bond distances when compared to the bulk phase[32]. The particle size for Pt:Sn/HSA after H_2-TPR estimated from EXAFS is lower than for Pt:Sn/LSA (0.7 nm vs. 6 nm), thereby confirming the STEM result (Table 3.1, Figure 3.2). Moreover, the difference in size explains why alloying occurs faster for Pt:Sn/HSA. For an Au-Pt bimetallic system, Xiao et al.[33] showed that small nanoparticles have a negative heat of alloy formation, which means it favours the formation of nanoalloys, while with increasing nanoparticle size, the heat of formation increases. A similar effect can be expected for the current bimetallic Pt-Sn system, explaining the different trend of the XANES spectra observed during H_2-TPR for the 2 samples (Figure 3.3).

Based on the assumption that Sn is uniformly distributed throughout the alloy, the alloy composition can be estimated from eq. 3.3:[24]

$$\text{Fraction of Sn in alloy} = N_{Pt-Sn}/(N_{Pt-Sn}+N_{Pt-Pt}) \qquad (3.3)$$

However, N_{Pt-Pt} is an average of Pt in the alloy (90%) and of unalloyed Pt, likely pure metal after TPR, see the reduced state before redox cycling (Figure 3.5b). Hence, the N for alloyed

Pt only will reduce from 4.79 to 4.31 (for Pt:Sn/HSA), yielding an actual Sn fraction in the alloy of 9.3% in reduced state (after H_2-TPR).

While reduction from SnO to Sn is quite difficult, requiring high temperatures[34], the presence of Pt typically helps to reduce Sn at lower temperatures[35]. However, in the case of the Pt:Sn/HSA sample, the incipient wetness impregnation synthesis entails deposition of small particles spread over a large surface area (~125 m^2/g), so that the Pt location on the surface may not necessarily be close to the Sn. Therefore, not all SnO_2 gets reduced in a single H_2-TPR. For the Pt:Sn/LSA sample on the other hand, the composition of the alloy has ~23% of Sn after just one H_2-TPR. Here however, the probability of Pt being located close to the Sn is much higher as the support surface area is low (5 m^2/g).

(iii) After CO_2-TPO: Fitting of the oxidised Pt:Sn/HSA sample (after CO_2-TPO) is possible with a combination of both Pt-O and Pt-Pt shells. This contribution of oxygen is noticed at the Pt-edge due to the small size of the particles, which makes the fraction of Pt-O bonds sufficiently large compared to the Pt-Pt fraction to be detectable. The coordination number for these Pt-O bonds remains lower than for the Pt-Pt bonds, indicating that not the entire particle contains Pt-O bonds. As Pt cannot be oxidised by CO_2, this oxygen contribution comes from neighbouring Sn that was oxidised to SnO_2. Comparing the numbers for the O-shell fit for the fresh and CO_2-oxidised state reveals similar R values, while coordination is much lower with a higher value of the Debye-Waller factor after the CO_2-TPO. This means that Pt has less O-neighbours with more disorder in CO_2-oxidised Pt:Sn/HSA. In contrast, the Pt:Sn/LSA sample does not show the same Pt-O presence as the nanoparticle size is much larger and the contribution of oxygen from the segregated SnO/SnO_2 is too small to be seen at the Pt-edge (Figure 3.8a and b & B5). Therefore, using a Pt-Pt shell yields a good fit for Pt:Sn/LSA.

(iv) After RWGS: Finally, the Pt:Sn/HSA catalyst was exposed to 10 H_2/CO_2 redox cycles before performing a RWGS reaction, likely yielding again 90% of Pt in the alloy. After the reaction, fitting led to higher coordination number estimates ($N_{Pt\text{-}Pt} = 5.82$ and $N_{Pt\text{-}Sn} = 1.00$), compared to the state after one H_2-TPR. The increase in coordination to a total of 6.82 corresponds to clusters of ~1.5 nm, twice the original size of 0.7 nm. The latter follows from the fact that the catalyst was exposed repeatedly to environmental stress, by continuous alloy formation/segregation at a high temperature.

Table 3.3: *EXAFS fitting results at the Pt L_{III}-edge for Pt:Sn/HSA subsequent to each treatment. Bold values in brackets are Pt cluster sizes assuming hemispherical nanoparticle shape*[30]***.***

	Fresh	**Reduced**	**Oxidised**	**10 redox + RWGS**
N_{Pt-O}	5.0 ± 0.6		1.6 ± 0.3	
R_{Pt-O} (Å)	2.00 ± 0.01		2.00 ± 0.01	
σ^2_{Pt-O} (10^{-3} * Å^2)	3 ± 1		6 ± 2	
N_{Pt-Pt}		4.8 ± 0.5 **(~0.7 nm ± 0.1)**	5.5 ± 0.6	5.8 ± 0.4 **(~1.5 nm ± 0.2)**
R_{Pt-Pt} (Å)		2.72 ± 0.01	2.74 ± 0.007	2.75 ± 0.02
σ^2_{Pt-Pt} (10^{-3} * Å^2)		8 ± 1	8 ± 1	6 ± 1
N_{Pt-Sn}		0.5 ± 0.3		1.0 ± 0.5
R_{Pt-Sn} (Å)		2.65 ± 0.03		2.71 ± 0.02
σ^2_{Pt-Sn} (10^{-3} * Å^2)		6 ± 4		10 ± 3
ΔE_0 (eV)	5.8 ± 1.5	1.1 ± 1.4	3.8 ± 1.6	2.7 ± 0.7
R factor	0.04	0.03	0.03	0.02

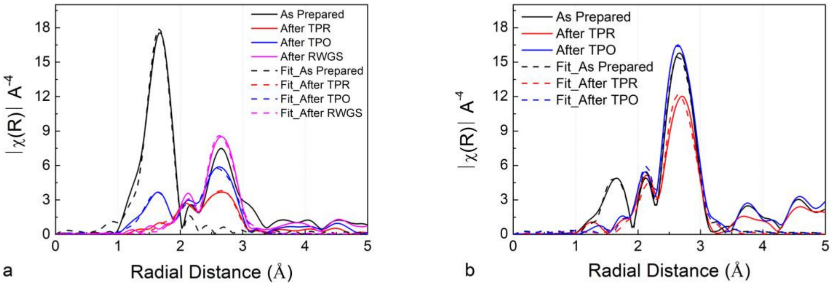

Figure 3.8: *Experimental k^3-weighted Fourier transformed EXAFS signals at RT at the Pt L_{III}-edge subsequent to each treatment (H_2-TPR, CO_2-TPO, H_2/CO_2 redox cycles) for Pt:Sn supported on **a:** HSA and **b:** LSA. The dashed lines depict the fits for each of the signals.*

Based on the overall N_{Pt-Pt} after RWGS, 5.82, the N for Pt-Pt only in the alloy reduces to 5.24, based on the average Pt in the Pt-Sn alloy, which together with $N_{Pt-Sn} = 1$ leads to ~16% of Sn in the alloy. These values indicate that, while after one H_2-TPR step, little of the Sn was yet participating in the Pt-Sn alloy formation, upon treatment with multiple redox cycles, more Sn got incorporated into the alloy.

3.3.3.2 Sn-edge

(i) As Prepared: Fitting results of the EXAFS data at the Sn-edge are depicted in Table 3.4 (Figure 3.9, Appendix B-4, Figure B6, and Table B2 for Pt:Sn/LSA). There are a few takeaways here as well. Firstly, fitting of the EXAFS spectra for the fresh (as prepared) samples is possible with a regular SnO_2 (Sn-O shell = 2.09 Å) crystal.

(ii) After H_2-TPR: Analysis of the reduced sample for the Pt:Sn/HSA was achieved with a Sn-O and a Sn-Pt shell. The latter yielded a fit with a relatively low coordination number of 3.56 and a relatively high error range for $N_{Sn\text{-}Pt}$. Following from the Pt-edge fit, Pt in the alloy has only ~9.3% of Sn neighbours, while based on the actual wt% of Pt and Sn present in the sample (Table 3.1, § 3.3.1), the maximal fraction of Sn possible in the Pt:Sn alloy would be 20%. This means that half of the Sn in Pt:Sn/HSA is not participating in alloy formation and is most probably present as SnO after reduction. However, the coordination number for the Sn-O shell is quite low for the reduced sample (0.89) when compared to the "as prepared" coordination number (5.10). Hence, it is very likely that there are Sn-Sn bonds present in the sample and the oxygen is located on the outer fringes of these clusters. An analysis was performed by Firet et al.[36] for a silver (Ag) system, where they modelled Ag-Ag clusters of different size to assess the effect on the Ag-O coordination number. It was found that even for small clusters of 3 and 4 Ag-Ag shells the Ag-O coordination dropped to values of 0.37 and 0.21, respectively. Based on this, it is plausible that small clusters of Sn-Sn with few Sn-O bonds are present, leading to low Sn-O coordination, especially in a reducing atmosphere of H_2 at these high temperatures (EXAFS measured at RT after cooling down from 923 K in H_2 atmosphere). The typical bond length for Sn-Sn is 2.35 Å, which falls within the fitting range. However, this path cannot be included for fitting in the specified region as the fit then covers 3 shells (Sn-O, Sn-Sn & Sn-Pt), and this would imply too many parameters and not enough independent points to perform a decent 3-shell fit. In addition, the signal to noise (S/N) ratio was not good enough to distinguish in complete detail the minor differences in the structure for such small nanoparticles (B-4, Figure B6). A fitting was attempted with just the Sn-O and Sn-Sn shells but did not yield a reasonable fit.

Fitting for the reduced state for Pt:Sn/LSA was more straightforward, yielding a N value of 7.6 for Sn-Pt and a very low coordination number for Sn-O of 0.42, which suggests that the majority of Sn present in the sample is participating in alloy formation. Based on the ICP composition of the sample (Table 3.1), the calculated maximum fraction of Sn possibly present in the Pt:Sn alloy would be ~23%. From the N values obtained in the Pt-edge fits, Sn constitutes ~24% of the alloy composition, hence it is likely that most of the Sn present in this LSA sample is indeed incorporated into the alloy. Clearly, the lower surface area of this support led to closer placement of Pt and Sn on the surface, so that Pt can facilitate SnO reduction.

(iii) After CO_2-TPO: Thirdly, complete oxidation of Sn to SnO_2 after the CO_2-TPO step takes place for both HSA and LSA supported samples, which confirms the observations made based on the XANES spectra. This leads to loss of the Pt:Sn alloy phase.

(iv) After RWGS: Finally, after 10 redox cycles, intermediate H_2 reduction and subsequent RWGS of Pt:Sn/HSA, there are observations similar to the ones at the Pt-edge. The coordination number of Sn-Pt increases from 3.56 after the single reduction step, to 7.69 after RWGS, indicating an increase in the nanoparticle size after the multiple redox cycles. A look into the k-space signals (Appendix B-4, B8 1b & 1d), shows a distinct difference between the "After-TPR" and "After-RWGS" signals, which wasn't really evident by mere inspection of the XANES signals.

Table 3.4: *EXAFS fitting results at the Sn K-edge for Pt:Sn/HSA subsequent to each treatment.*

	Fresh	**Reduced**	**Oxidised**	**10 redox + RWGS**
N_{Sn-O}	5.0 ± 0.9	0.9 ± 0.2	4.9 ± 0.9	0.6 ± 0.20
R_{Sn-O} (Å)	2.05 ± 0.01	2.07 ± 0.03	2.05 ± 0.01	2.08 ± 0.02
σ^2_{Sn-O} (10^{-3} * $Å^2$)	4 ± 0.9	2 ± 1	3 ± 1	3 ± 2
N_{Sn-Pt}		3.6 ± 1.7		7.7 ± 1.2
R_{Sn-Pt} (Å)		2.67 ± 0.01		2.75 ± 0.01
σ^2_{Sn-Pt} (10^{-3} * $Å^2$)		11 ± 3		15 ± 1.3
ΔE_0 (eV)	-1.3 ± 2.2	-4.6 ± 3.5	-2.1 ± 2.5	-1.1 ± 2.5
R factor	0.06	0.07	0.06	0.06

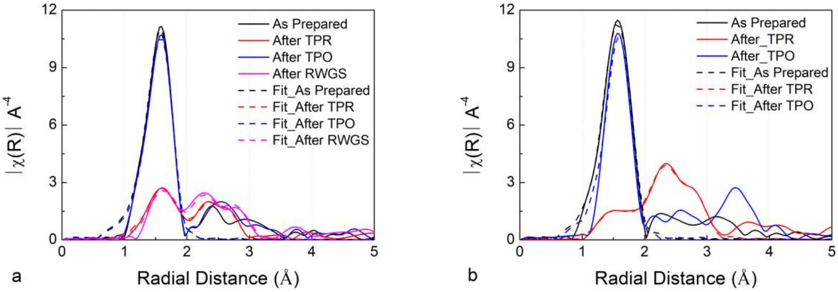

Figure 3.9: *Experimental k^3-weighted Fourier transformed EXAFS signals at RT at the Sn K-edge subsequent to each treatment (H_2-TPR, CO_2-TPO, H_2/CO_2 redox cycles) for Pt:Sn supported on **a:** HSA and **b:** LSA. The dashed lines depict the fits for each of the signals.*

3.3.4 Discussion based on XAS data

The above presented XANES and EXAFS data at both the Pt and Sn-edges can lead to an understanding of the nature and behaviour of the Pt:Sn alloy under different conditions. So far, the actual phase of the alloy in both samples has not been identified. Determining the phase would not be possible with only the EXAFS data, considering the Pt-Pt (2.78 Å) and Pt-Sn (2.75 – 2.87Å, depending on the alloy phase) distances are very similar. However, a combination of the EXAFS fits with the Pt:Sn phase diagram (Appendix B-7) and the MCR-ALS analysis for Pt:Sn/HSA from § 3.3.2.1 can lead to a general conclusion on the Pt:Sn alloy phase.

Information on the respective concentrations of the Pt:Sn alloy and monometallic Pt components obtained from MCR-ALS (Figure 3.5) show that around 90% of the Pt present in the sample participates in alloy formation (from the initial concentration in the concentration profile graph, Figure 3.5b), while about 90% of the Sn is present as an alloy or SnO. This is for the Pt:Sn/HSA as the MCR-ALS analysis was only performed for this sample. Now the coordination numbers for the reduced state of the sample were $N_{Pt\text{-}Pt} = 4.79$ and $N_{Pt\text{-}Sn} = 0.44$. The maximal Sn content possible in the alloy when all the Pt and Sn participate in alloy formation is 20%. But when only 90% Pt is participating in alloy formation, as is the case here, so the maximal Sn content can go up to 20/0.9 = 22.2%. Hence, for this sample only 9.3*100/22.2 = 41.8% of the Sn present in the sample is actually in the alloy phase (value 9.3% based on obtained coordination numbers, from § 3.3.2.1), meaning that 58.2% of the Sn is most likely present as SnO and SnO_2 after reduction.

Similarly, the Sn fraction in the alloy for the catalyst after RWGS would be 16%. This corresponds to 16*100/22.2 = 72% of the total Sn in the sample being present in the alloy state. This increase in amount of Sn being incorporated into the alloy state upon treatment with multiple redox cycles has been reported before and it increases with higher numbers of redox cycles[23,37]. A look into the phase diagram of Pt:Sn (B-7) shows that this percentage of Sn correlates to the 3:1 Pt:Sn alloy phase (Pt_3Sn). However, this phase diagram is applicable for bulk phases and should ideally be just used as a guide to arrive at an alloy phase. The Pt:Sn/HSA reduced state has a very low average particle size (~0.7nm), and therefore it is unlikely to have a well-mixed alloy state, but likely to have a configuration reported by A. Iglesias-Juez et al.[23] for low coordinated samples. There it is suggested the Sn atoms are located on the surface of the Pt nanoparticle entities. It was also suggested in the same work that there is a higher likelihood of having a well-mixed Pt-Sn alloy after multiple regeneration cycles. This would suggest a better mixed alloy state for the “after RWGS” state of the catalyst as this is also after the multiple H_2-CO_2 redox cycle treatments.

For the compositions being dealt with here, Pt:Sn can form majorly 2 alloy phases, Pt:Sn 1:1 and Pt:Sn 3:1. The Pt:Sn 1:1 crystal ($P6_3/mmc$, hexagonal) has a maximal possible Pt coordination for Sn as absorber of 6. However, the N values from the Sn-edge are higher than 6 for the RWGS state of Pt:Sn/HSA and the reduced state of Pt:Sn/LSA. It is lower than 6 for the reduced state of the Pt:Sn/HSA, and hence for that sample we cannot exclude the 1:1 phase. There is the added factor that the reduced state of the Pt:Sn/HSA catalyst has really low coordination numbers and hence the likelihood of a well-mixed phase is low. The Pt coordination for Sn in the Pt:Sn 3:1 crystal (Pm3m, cubic) on the other hand is 12. Therefore, in selected situations (Pt:Sn/LSA-reduced, Pt:Sn/HSA-After RWGS), determination of the average phase of the alloy can be done based just on the N values.

As no H_2/CO_2 redox cycles were performed for the Pt:Sn/LSA, the Sn composition in the alloy state cannot be determined. However, there is good reason to assume close to 100% of the Sn present in the sample is in the alloy phase after reduction of the sample. The reasoning for arriving at this judgement is that the $N_{Sn\text{-}Pt}$ is more than 6, pointing to the 3:1 Pt:Sn phase, which then means that the Sn can reach a maximal composition of 25% in the alloy state (B-7, Figure B10) beyond which the average phase will change. Fitting of the reduced data at the Sn-edge showed that the coordination number values of Sn-O were very low (0.42), which suggests that the majority of the Sn is reduced. As was determined in § 3.3.2.2, the actual composition of Sn is ~23%, which was matched by the value based on the N at the Pt-edge. This means that at least 23*100/25 = 92% of the Sn present in the sample is in the alloy state.

In a more recent work by Wang et.al.[38], the use of acid etching was employed to remove the surface Sn species, which led to a Pt-rich shell and during a subsequent reduction step, the Sn migrated to the surface to regain the Pt_3Sn alloy surface. They performed a number of DFT calculations and from it determined that the Pt_3Sn alloy surface is thermodynamically the most preferable structure. It is also suggested that the possibility to have a Sn-enriched surface alloy is unlikely through surface segregation of Sn. This would mean that when having lower amounts of Sn with respect to Pt, as is the case for Pt:Sn/HSA, there would be a higher probability of finding that Sn on the surface as a Pt_3Sn surface alloy. A similar result was also reported J. Llorca et al.[39].

The general schematic of what is occurring to the Pt:Sn/HSA catalyst during consecutive treatments is presented in Figure 3.10 based on the information obtained from XAS.

One of the important takeaways from the XAS data analysis is that not all the Pt and Sn participate in formation of the alloy when prepared on a higher surface area support, and it takes multiple redox cycles to force more of the Sn present in the sample to enter into the alloy phase. A possible way to circumvent this would be to prepare the sample by different methods such as colloidal synthesis [40,41], by incorporating the Sn into a hydrotalcite type support [42], or by means of a surface organometallic chemistry method to derive a surface enriched Pt-Sn nanoparticle [43].

Another possibility could be to use a different precursor which would allow for selective deposition of Sn onto the Pt so that the Pt can aid the reduction of SnO_2 [37].

However, if the sample is being prepared by wet impregnation, then it would be beneficial to subject the catalyst to multiple redox cycles (5-10 cycles), before proceeding to implement it for a reaction. Multiple redox cycles lead to an increase in the average cluster size, which is partially due to the incorporation of more Sn into the alloy, but also to the merging of smaller Pt particles under the thermal and environmental stress imposed on the catalyst.

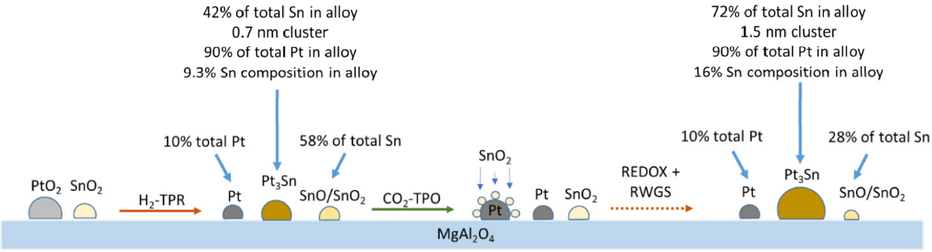

Figure 3.10: *Scheme depicting the evolution of the calcined Pt:Sn/HSA sample over different treatments based on the XAS data.*

The other important takeaway from the XAS analysis is that CO_2 does oxidise Sn to SnO and then subsequently to SnO_2, both isothermally and during the temperature programmed oxidation. It was found through the RWGS reaction data, that there is a steady-state equilibrium turnover between the Sn oxidation to SnO by CO_2, and SnO reduction to Sn by H_2. This is of course only applicable to Sn that was actually incorporated into the alloy. However, if the ratio of CO_2:H_2 would be increased, a slow oxidation of Sn can be expected, leading to gradual loss of the complete alloy. This Sn once oxidised would segregate from the alloy and likely move to the external surface of the Pt cluster, thereby forming a type of SnO_2 decoration around the Pt core as shown in the schematic of Figure 3.10.

3.3.5 Activity test results: Propane dehydrogenation (PDH), CO_2-assisted propane dehydrogenation (CO_2-PDH) and alternate pulses of CO_2:C_3H_8.

In order to link the results obtained from XAS to the catalysts' performance, a set of regular propane dehydrogenation experiments were performed.

3.3.5.1 Propane dehydrogenation (PDH)

Catalytic activity tests for PDH were performed for Pt/HSA, Pt/LSA, Pt:Sn/HSA and Pt:Sn/LSA after a H_2-reduction step. The results for these tests are shown in Figure B11 (B-8).

The general observation is that the addition of Sn improves the conversion and selectivity towards C_3H_6. In the case of the two catalysts (Pt and Pt:Sn) on LSA support, initial conversion for the monometallic catalyst was about 20%, while for the Pt:Sn/LSA it amounted to around 33%. The products formed during the reaction are CH_4, C_2H_4, C_2H_6, C_3H_6. The improvement in selectivity towards C_3H_6 is also very high, i.e. 66% selectivity towards C_3H_6 at 15% C_3H_8 conversion for the Pt catalyst vs. 99% selectivity at 28% C_3H_8 conversion for the Pt:Sn catalyst. This can be ascribed to the XAS observations for the Pt:Sn/LSA sample, indicating that most of the Pt and Sn are participating in alloy formation, enabling high selectivity and conversion. This conclusion is in line with the activity results presented by Haibo Zhu et al.[43] This also points towards lower carbon formation for an alloyed Pt:Sn catalyst than for a monometallic Pt catalyst, when compared at similar conversions, owing to the better selectivity in the case of the Pt:Sn.

For the Pt and Pt:Sn on HSA support, the improvement in C_3H_6 selectivity upon adding Sn is not as large as was observed for the LSA samples: 67% selectivity at 12.5% conversion for monometallic Pt/HSA vs. 77% selectivity at 12.5% conversion for Pt:Sn/HSA. The initial conversion of C_3H_8 for the Pt:Sn/HSA (15%) was slightly lower than that for the monometallic catalyst (16%). However, the yields of C_3H_6 were almost the same. When compared to the LSA support, the same Pt and Sn loading on HSA does not result in the same beneficial effect. This can be explained by the XAS observation that on the high surface area, not all the Pt and Sn are participating in alloy formation. However, the PDH reaction was performed after a single H_2-reduction step. When subjecting the catalyst to multiple redox cycles (5 cycles of H_2/CO_2) for activation, an improvement in propane conversion and selectivity towards propylene is observed. The selectivity towards propylene after the redox cycles reached 82.5% at 12.5 % conversion, i.e. an increase in selectivity with 5.5% when compared to the single reduction step. The overall consumption rate of C_3H_8 also increased 2-fold after redox cycling with a subsequent yield of C_3H_6 being about 2 times that of the single reduction step. The latter can be correlated to the results from XAS after RWGS, where after 10 redox cycles larger particles and more importantly larger Sn fractions in the alloy phase were found.

A final observation from these activity tests is that the samples supported on LSA generally performed better, i.e. the monometallic Pt/LSA did better than monometallic Pt/HSA, and Pt:Sn/LSA outperformed Pt:Sn/HSA. The latter implies that the nanoparticles on LSA (~5-7nm based on XAS-STEM) are more active than the ones on HSA (1.5 nm from XAS-STEM). However, this does not imply that the catalysts supported on LSA are better suited for long term application as they can sinter much more easily and lose activity after a few reaction/regeneration cycles. This was tested by subjecting the Pt:Sn/LSA to 10 redox cycles and the activity of the catalyst dropped from the original ~30% C_3H_8 conversion (Figure B11a) to values below 5%.

3.3.5.2 CO_2-assisted PDH

Adding CO_2 to the feed of propane might prove worthwhile during the dehydrogenation process as it can potentially react with H_2 formed by PDH through RWGS (eq. 1.10) and help to shift the equilibrium towards products. It can also potentially suppress carbon formation by means of the reverse Boudouard reaction (eq. 1.11). The Pt:Sn/HSA catalyst was used for CO_2-PDH activity tests, subsequent to treatment with 10 redox cycles in order to arrive at a stable alloy state.

The activity for the monometallic Pt/HSA catalyst is shown in supplementary B-9, Figure B14. The activity drops rapidly to zero in the absence of Sn, which means that the catalyst has deactivated completely. Sintering is not the reason as the activity was recovered when the catalyst was subjected to a O_2/H_2 redox cycle, so carbon is at the origin of deactivation for Pt/HSA. Indeed, the lower selectivity of the latter will lead to a higher rate of carbon formation than on Pt:Sn[23]. There is also the added aspect that CO, formed by RWGS at 873 K, poisons the Pt atoms as CO has an affinity to adsorb on Pt sites[44,45].

In CO_2-assisted PDH, addition of Sn as a promoter increases the activity drastically when compared to the monometallic Pt catalyst. The results for CO_2-assisted PDH for Pt:Sn/HSA are shown in Figure 3.11 and B-9, B13. A small amount of CO_2 in the feed increases the initial conversion when compared to the single propane feed (16% vs. 9% conversion). Three ratios of CO_2:C_3H_8 (0.25:1, 0.5:1 and 1:1) were tested for this reaction and it was observed that increasing CO_2 amounts negatively impacted the propane conversions. The formation of water was detected for all CO_2:C_3H_8 ratios, but in varying amounts, confirming that the RWGS reaction took place as is shown in Figure B13d. It is quite evident from the figure that an increased ratio of CO_2 in the feed, increased the amount of water formed.

A look into the activity graphs for the Pt:Sn catalyst indicates some interesting information. The initial rate at which the catalyst deactivates in the presence of CO_2 is slower than without CO_2 (Figure 3.11a). This gives an indication that the reverse Boudouard reaction is taking place, preventing carbon accumulation. The selectivity values are high (>95%), and this is interesting to note, as for this catalyst it has been observed in the previous § 3.3.4.1 that the selectivity values with extra H_2 added to the feed at similar conversions (around 15% propane conversion values) were about ~80%. This would mean at similar conversions the CO_2 helps to enhance the propylene yield.

However, over an extended period of time the activity of the reaction with CO_2 in the feed falls below that of the activity without CO_2. This is more pronounced when increasing amounts of CO_2 are added. The products formed are CH_4, C_2H_6, C_2H_4, C_3H_6, as well as CO and H_2O from RWGS taking place in parallel. This behaviour could indicate that alloy is lost, e.g. by slow oxidation of Sn to SnO and subsequently to SnO_2. With an increasing amount of CO_2 in the feed, this oxidation of Sn can proceed more quickly, leading to an accelerated loss of activity.

Subsequent to each of the reaction steps, the total carbon formed was evaluated. The carbon formed upon feeding CO_2:C_3H_8 = 0.5:1 vs. when not adding CO_2, is much lower (reduced by ~33%). These 2 specific activity plots were chosen as their conversions reached similar values so they allow for a good comparison for adding CO_2 vs. not adding CO_2 on carbon accumulation. The 0.25:1 ratio just had much higher activity and hence would accumulate more carbon over time and is therefore not used, but however, the values are presented in Figure B13e.

3.3.5.3 Alternate pulses of CO_2 and C_3H_8

A set of experiments with alternate flows of CO_2 and C_3H_8 of about 2 min each were performed on the Pt:Sn/HSA catalyst, to check whether CO_2 burns surface carbon by means of the reverse Boudouard reaction and thereby regenerates the catalyst (partially). Prior to performing these experiments, the catalyst was subjected to 5 redox cycles in order to increase the Sn fraction in the alloy. The results of these experiments are depicted in Figure 3.12. After every introduction of CO_2, the catalyst was partially regenerated, as the C_3H_8 conversion increased momentarily. Based on the XAS results, exposing the catalyst to CO_2 should be counterproductive as it destroys the alloy by oxidising Sn. Based on the MCR-ALS analysis (Figure 3.5b), a 1 min exposure to CO_2 leads to 70% loss of the alloy. This would mean that the conversion of propane should drastically drop after the first 2 min exposure to CO_2, but instead the activity slightly increased after exposure to CO_2 for a short period of time. A similar set of experiments involving alternate flows between C_3H_8 and Ar revealed no changes in the C_3H_8 conversion after Ar exposure (not shown). The observed regeneration proves that indeed CO_2 exposure helps to burn carbon and this carbon removal outweighs the alloy deterioration effect of CO_2. On the other hand, the H_2 formed from PDH can help to regenerate the alloy by reduction of the Sn that was oxidised during the CO_2 exposure.

The results observed confirm that the reverse Boudouard reaction is taking place. However, the absolute amount of carbon that was removed by CO_2 is very low and therefore difficult to quantify as it remains below the detection limits of the equipment. This would lead to the conclusion that CO_2 probably only removes the carbon present on the active sites, i.e. the Pt-Sn alloy, leading to a temporary increase in activity, which is lost rapidly as new carbon formation takes place during the subsequent PDH. Similar experiments were performed with alternating flows of C_3H_8/O_2 (Appendix B-9, Figure B12) in order to simulate a process as the one applied in industry, showing the same trend of partial catalyst regeneration. So, these results practically show that CO_2 can be used as a substitute to O_2 in the feed along with propane, as it does burn carbon.

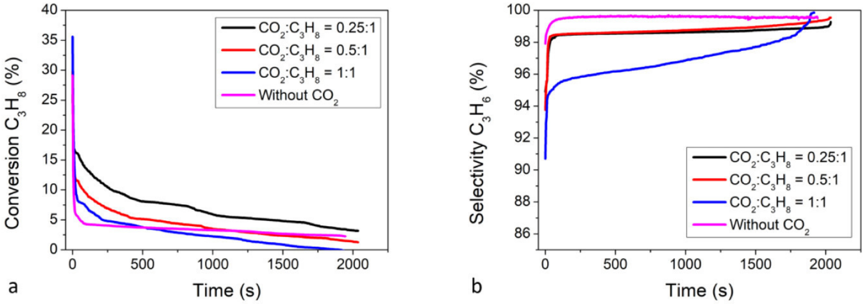

Figure 3.11: ***a:*** *Conversion and* ***b:*** *selectivity plots for CO_2-assisted PDH at different ratios of CO_2:C_3H_8 for the Pt:Sn/HSA catalyst (T=873 K and 1.2 bar, with flow of C_3H_8 being set at 60 Nml/min and a total flow set at 200 Nml/min). Plots for STY and C_3H_8 consumption rates are in Appendix B, Figure B13a, b, and c.*

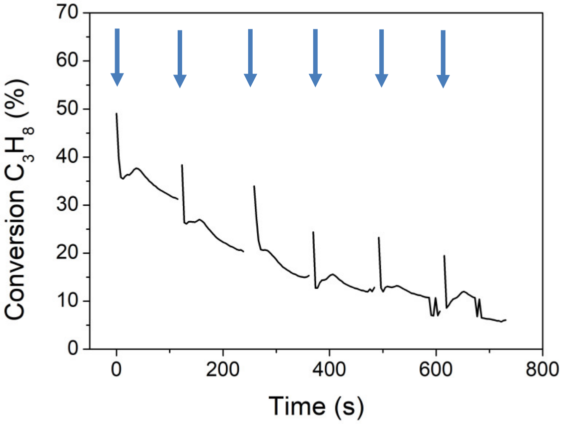

Figure 3.12: *C_3H_8/CO_2 cycles performed to determine the effect of CO_2 flow on the Pt:Sn/HSA catalyst after 5 redox cycles. The temporary increments in conversion follow upon exposure to a 15 Nml/min flow of CO_2 for 2 min (indicated by blue arrows). The time scale on the x-axis only shows the duration of sequential propane exposures. Temperature = 873 K, C_3H_8 flow = 40 Nml/min.*

Taking the oxidising effect of CO_2 into account, detrimental to the alloy, together with the aspect that RWGS is taking place, there is still potential to improve/maintain the C_3H_8 conversion by adding CO_2 provided that the ratio of CO_2 is fine-tuned based on total conversions obtained. From the observations made in the CO_2:C_3H_8 pulse experiments, it can be stated that the improvement in activity is majorly due to a thermodynamic shift in equilibrium to products by consumption of H_2 by CO_2 through RWGS as the amount of carbon burnt via the reverse Boudouard reaction is minimal. This would mean that it is very much possible to improve performance at even lower ratios of CO_2:C_3H_8.

3.4 Discussion

A combination of the information obtained from XAS and the CO_2-assisted PDH tests leads to multitude of factors to be considered in order to understand the reaction on the alloyed Pt:Sn catalyst.

During the isothermal redox (H_2/CO_2) cycles, alloy formation/segregation takes place during each individual gas feed. The results for the RWGS XAS measurements also revealed the same through equations3.1 and 3.2 in § 3.1. The XANES region for the RWGS gave insight that the alloy is in general retained, despite the continuous dynamic CO_2-oxidation and H_2-reduction that are taking place simultaneously. RWGS conversion at these conditions for this catalyst was found to be 45% (Appendix B-9, Figure B15). Now based on the information gained from all the studies, the mechanism through which the RWGS reaction takes place could very well be described by eqs. 3.1 and 3.2 (see § 3.1). This is pertinent as the RWGS occurred during the CO_2-assisted PDH reaction. A set of PDH experiments were performed on a 2% SnO_2/HSA catalyst and it showed no activity (0% C_3H_8 conversion). This leads to the understanding that the propane dehydrogenation occurs on the Pt sites and the H_2 formed from this dehydrogenation would help to reduce the catalyst back to the Pt_3Sn alloy.

There is also a possibility that the SnO/SnO_2 gets reduced by the carbon formed by the reaction (eq. 3.4 & 3.5). In order to confirm this, 2 qualitative experiments were performed where either a 10%SnO_2/HSA or 3:1 Pt:Sn/LSA (7 wt% Pt) sample were mechanically mixed with graphite and subsequently heated under inert (argon) to 873 K. Prior to mixing the Pt:Sn sample with graphite, the sample was first reduced under H_2 at 873 K and subsequently oxidised under CO_2, after which it was cooled down to room temperature (RT). This sample was then recovered and mixed with graphite. For each inert heating experiment, the outlet gas was tracked by means of a mass spectrometer (MS) at m/z signals of 28, 44, 40, 16 and 32. At around 853 K, peaks of CO_2 (m/z = 44) could be observed for the 10%SnO_2/HSA sample, while for the Pt:Sn/LSA sample stronger peaks of CO (m/z = 28) were observed. This confirms that it is plausible for carbon to reduce SnO_2 (~10%SnO_2/HSA) or SnO (~Pt:Sn/LSA) at the applied reaction temperatures. In order to disconsider any effects due to the graphite itself, 2 similar experiments were performed with a blank reactor and a reactor filled with only graphite, while tracking the same m/z signals through MS. There were no changes observed for these measurements at the m/z values of 28 and 44.

$SnO_2 + C \rightarrow Sn/SnO + CO_2$ (3.4)

$SnO + C \rightarrow Sn + CO$ (3.5)

The CO_2-assisted PDH reaction data (§ 3.3.4.2) showed that adding CO_2 to the feed improved conversion of propane, yield of propylene and decreased the total amount of carbon formed, when compared to not adding it to the feed. This indicates that CO_2 helps to decrease the initial amount of carbon formed by means of the reverse Boudouard reaction and by means of eq. 3.4 and 3.5. Increasing the ratio of CO_2 in the feed tends to decrease the activity. A closer inspection of the data indicates that the absolute C_3H_8 conversion values were close to ~10%. The flow rate of C_3H_8 was maintained at 60 Nml/min, while the flow of CO_2 for a ratio of 0.25:1 (CO_2:C_3H_8) was 15 Nml/min and 30 Nml/min at ratio of 0.5:1. The amount of H_2 formed at 10% conversion would be 60*0.10 = 6 Nml/min. The absolute amounts of unreacted CO_2 and H_2 would be respectively 12.3 Nml/min (for 0.25:1 ratio of feed) and 3.3 Nml/min. The unreacted amount of CO_2 in the case of a 2:1 feed ratio would be 27.3 Nml/min. These values are important as there would be a certain point when the ratio between CO_2:H_2 is reached where the oxidising capabilities of the CO_2 would supersede/override the reductive capabilities of H_2. This is a possible reason why a lower feed ratio of CO_2:C_3H_8 leads to better conversions and slower deactivation. Based on the aforementioned numbers, lower CO_2 flows of around 3 - 5 Nml/min (corresponding to a ratio of CO_2:C_3H_8 = ~1:12) could lead to better conversion of propane over an extended period of time as the amount of CO_2 would be enough to consume the small amount of H_2 generated by PDH through RWGS, while at the same time, not too much in excess to cause deactivation of the catalyst through oxidation of Sn. An even better way would be to try and create a dynamic system where the amount of CO_2 that is fed to the system is varied based on the propane conversion. As the conversion is dropping due to carbon formation so should the feed of CO_2 which would in turn mean lower

CO_2:C_3H_8 ratio with time. This would help create a system where the integrity of the Pt_3Sn alloy would be maintained at all times. A schematic representation of all possible reactions occurring is shown in Figure 3.13.

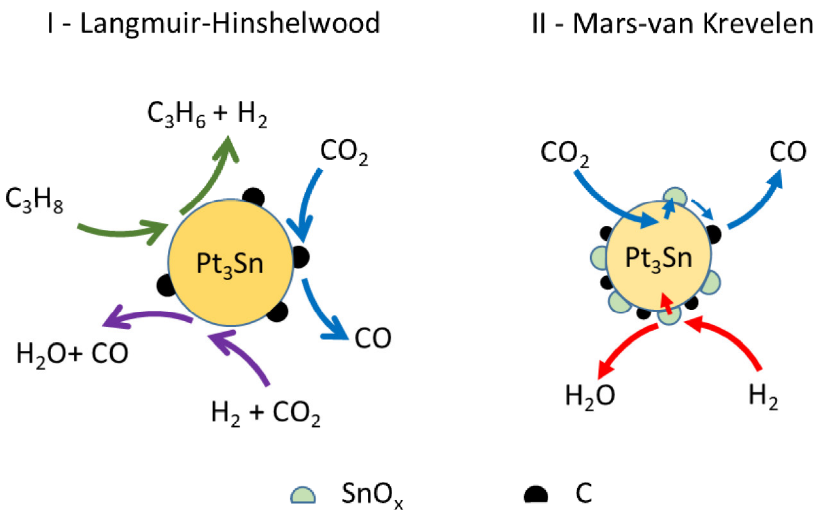

Figure 3.13: *Schematic representation of all reactions occurring on the catalyst during CO_2-assisted PDH. Part I of the scheme represents all the reactions taking place on the catalyst by the Langmuir-Hinshelwood mechanism, while part II represents the reactions occurring by Mars-van Krevelen mechanism. All reactions occur simultaneously. The catalyst goes from part I to part II in presence of CO_2, which would oxidise Sn to SnO, thereby segregating Sn from the Pt_3Sn alloy and then go back to part I through reduction by H_2 generated from PDH. (—) reduction, (—) oxidation, (—) PDH reaction, (—) RWGS reaction.*

Part of the reactions taking place in CO_2-assisted PDH occur via a Langmuir-Hinshelwood (L-H) mechanism, where the alloyed catalyst merely provides reactive sites. This is the case for PDH which is activated on Pt to form propylene and H_2, possibly leaving some C deposits. The CO_2 in the feed can remove these deposits via the reverse Boudouard reaction, while it can also interact with the H_2 formed from PDH by RWGS, both also according to a L-H mechanism. The presence of CO_2 in the feed however also leads to Mars-van Krevelen (MvK) type of reactions, as it causes partial segregation and re-oxidation of Sn from the alloy. The so formed SnO particles can again be reduced and alloyed by interaction with the PDH product H_2, or they can transfer O to nearby C deposits for their removal. All of these reactions occur simultaneously, with a delicate balance between oxidizing and reducing gases, as well as between active alloyed, oxidized and metallic sites.

3.5 Conclusions

A detailed analysis of a 3:1wt% Pt:Sn catalyst has been executed for the CO_2-assisted propane dehydrogenation reaction. The dynamic changes occurring to the catalyst in the presence of a reductive (H_2) and oxidative (CO_2) atmosphere were tracked by means of in situ XAS at both the Pt L_{III}-edge and Sn K-edge for Pt:Sn on $MgAl_2O_4$ support with high or low surface area (HSA or LSA). The data were then scrutinized in both the XANES and EXAFS regions, coupled with the use of MCR-ALS as big data technique in order to determine the real amounts of Pt and Sn participating in alloy formation, the ease of alloy formation based on nanoparticle size, the effect of CO_2 on the alloy, effect of redox cycles on the alloy integrity, and the average phase of the alloy. The conclusions from the XAS part of the study are summarized in the following 2 paragraphs.

The amount of Sn which gets incorporated into the Pt-Sn alloy increases with multiple H_2/CO_2 redox cycles, which also increase the nanoparticle size. For smaller nanoparticles, the Pt and Sn more readily form an alloy than for larger nanoparticles, and this was seen from XANES data of the H_2-TPR measurements for Pt:Sn/HSA & LSA. In the case of larger nanoparticles, PtO_2 first reduces into Pt before starting to form the alloy phase with Sn as observed from the WL positions. For smaller NPs, Pt immediately forms alloy with Sn, as soon as it is reduced from PtO_2.

The average phase of the alloy that is formed is Pt_3Sn, determined upon coupling the MCR-ALS results with the EXAFS fits and XANES analysis for the H_2-TPR spectra. This phase is also expected based on the loadings of the respective components. A major part of Sn present on the Pt:Sn/HSA catalyst is not alloyed after one H_2-reduction step (~58% of the Sn not in alloy), but upon multiple H_2/CO_2 redox cycles the amount of Sn incorporated into the alloy increases. For the Pt:Sn/LSA sample, 92% of the Sn present gets incorporated into the alloy after one H_2-reduction step. The lower surface area of the support led to closer placement of Pt and Sn on the surface leading to easier alloying and higher Sn compositions in alloy.

CO_2 is capable of oxidising Sn to SnO and subsequently to SnO_2. The oxidation to Sn^{2+} is much faster than oxidation to Sn^{4+}. This oxidation leads to loss of the alloy phase as SnO segregates.

The catalyst was subsequently tested for the PDH and CO_2-assisted PDH reaction at different ratios of CO_2:C_3H_8 to determine the CO_2 effects on activity, and in alternate cycle experiments between C_3H_8 and CO_2 to determine the capacity of CO_2 as a regenerative gas. The conclusions from the activity test results are summarized in the following paragraphs.

A ratio of CO_2:C_3H_8 of 0.25:1 gave better activity than ratios of 0.5:1 and 1:1. This suggests that lower ratios are favourable for the Pt:Sn catalyst, primarily due to the aspect that higher ratios of CO_2:C_3H_8 would lead to faster oxidation of Sn to SnO and SnO_2, subsequently leading to loss of the alloy phase and in turn a decrease in activity. This was determined from inspection of the selectivity plots. The presence of product H_2 helps to maintain the integrity of the alloy and therefore the amount of fed CO_2 along with propane needs to be match the conversions. Based on the experiments performed in this study, a ratio of CO_2:C_3H_8 equal to 1:12-15 in the feed would possibly lead to better yields. Ideally, the feed rate of CO_2 should be dynamically adjusted based on the conversion. When the catalyst is deactivating due to inevitable carbon formation from PDH, the absolute amounts of H_2 formed and entering the system also decrease, which thereby dynamically changes the CO_2:H_2 ratio for a constant CO_2 feed. This would lead to an increasing rate at which the Sn gets oxidised to SnO and subsequently SnO_2.

It is possible to reduce the SnO_2 with carbon. However, whether the reduction is to SnO or Sn could not be determined. CO_2 is able to react with the carbon by means of the reverse Boudouard reaction, but only for the carbon that is present on the active sites. The RWGS reaction takes place simultaneously to CO_2-PDH, thereby helping to improve activity by shifting equilibrium towards the products.

Appendix B : data

Pt L_{III}-XANES spectra, Sn K-XANES spectra, Pt L_{III}-EXAFS fits, Sn K-EXAFS fits, XANES during RWGS, MCR-ALS results, Pt:Sn phase diagram, PDH activity test results, CO_2-assisted PDH, C_3H_8/O_2 cycles, RWGS experiment.

3.6 References

1. Ansari, M. B. & Eon-Park, S. Environmental Science MINIREVIEW. *Energy Environ. Sci.* **5**, 9419–9437 (2012).
2. Pakhare, D. & Spivey, J. Chem Soc Rev noble metal catalysts. *Chem. Soc. Rev.* **43**, 7813–7837 (2014).

3. Michorczyk, P., Ze, K., Niekurzak, R. & Ogonowski, J. Dehydrogenation of propane with CO2 – a new green process for prope- ne and synthesis gas production. **14**, 77–82 (2012).

4. Srinath, N. V., Poelman, H., Dendooven, J., Marie-Francoise, R. & Galvita, V. V. REDOX evolution of Pt-Sn alloys studied by in situ XAS - Oral Presentation. *Eur. 2019 Conf.* (2019).

5. Shao, C.-T., Lang, W.-Z., Yan, X. & Guo, Y.-J. Catalytic performance of gallium oxide based-catalysts for the propane dehydrogenation reaction: effects of support and loading amount. *RSC Adv.* **7**, 4710–4723 (2017).

6. Zhang, Y. *et al.* Comparative study of bimetallic Pt-Sn catalysts supported on different supports for propane dehydrogenation. *J. Mol. Catal. A Chem.* **381**, 138–147 (2014).

7. Galvita, V., Siddiqi, G., Sun, P. & Bell, A. T. Ethane dehydrogenation on Pt/Mg(Al)O and PtSn/Mg(Al)O catalysts. *J. Catal.* **271**, 209–219 (2010).

8. Longo, A. *et al.* What Makes Fe-Modified MgAl2O4 an Active Catalyst Support? Insight from X-ray Raman Scattering. *ACS Catal.* **10**, 6613–6622 (2020).

9. Theofanidis, S. A., Galvita, V. V., Poelman, H. & Marin, G. B. Enhanced carbon-resistant dry reforming Fe-Ni catalyst: Role of Fe. *ACS Catal.* **5**, 3028–3039 (2015).

10. La Fontaine, C., Barthe, L., Rochet, A. & Briois, V. X-ray absorption spectroscopy and heterogeneous catalysis: Performances at the SOLEIL's SAMBA beamline. *Catal. Today* **205**, 148–158 (2013).

11. La Fontaine, C., Belin, S., Barthe, L., Roudenko, O. & Briois, V. ROCK: A Beamline Tailored for Catalysis and Energy-Related Materials from ms Time Resolution to µm Spatial Resolution. *Synchrotron Radiat. News* **33**, 20–25 (2020).

12. Klementev, K. V. Package "VIPER (visual processing in EXAFS researches) for windows". *Nucl. Instruments Methods Phys. Res. Sect. A Accel. Spectrometers, Detect. Assoc. Equip.* **448**, 299–301 (2000).

13. Rochet, A., Ribeiro Passos, A., Legens, C. & Briois, V. Sulphidation study of a dried Ni/Al2O3 catalyst by time-resolved XAS-MS combined with in situ Raman spectroscopy and multivariate Quick-XAS data analysis. *Catal. Struct. React.* **3**, 33–42 (2017).

14. Manceau, A., Marcus, M. & Lenoir, T. Estimating the number of pure chemical components in a mixture by X-ray absorption spectroscopy. *J. Synchrotron Radiat.* **21**, 1140–1147 (2014).

15. Nayak, C., Bhattacharyya, D., Jha, S. N. & Sahoo, N. K. In Situ XAS Study on Growth of PVP-Stabilized Cu Nanoparticles. *ChemistrySelect* **3**, 7370–7377 (2018).

16. Jaumot, J., de Juan, A. & Tauler, R. MCR-ALS GUI 2.0: New features and applications. *Chemom. Intell. Lab. Syst.* **140**, 1–12 (2015).

17. Cassinelli, W. H. *et al.* Multivariate curve resolution analysis applied to time-resolved synchrotron X-ray Absorption Spectroscopy monitoring of the activation of copper

alumina catalyst. *Catal. Today* **229**, 114–122 (2014).

18. Ruckebusch, C. & Blanchet, L. Multivariate curve resolution: a review of advanced and tailored applications and challenges. *Anal. Chim. Acta* **765**, 28–36 (2013).

19. Olsbye, U., Moen, O., Slagtern, Å. & Dahl, I. M. An investigation of the coking properties of fixed and fluid bed reactors during methane-to-synthesis gas reactions. *Appl. Catal. A Gen.* **228**, 289–303 (2002).

20. Froment, G. F. & Bischoff, K. B. *Chemical Reactor Analysis and Design*. (Wiley, 1990).

21. Mears, D. E. Diagnostic criteria for heat transport limitations in fixed bed reactors. *J. Catal.* **20**, 127–131 (1971).

22. Calvin, S. *XAFS for Everyone*. (CRC Press, 2013).

23. Iglesias-juez, A. *et al.* A combined in situ time-resolved UV – Vis , Raman and high-energy resolution X-ray absorption spectroscopy study on the deactivation behavior of Pt and Pt A Sn propane dehydrogenation catalysts under industrial reaction conditions. *J. Catal.* **276**, 268–279 (2010).

24. Sun, P., Siddiqi, G., Vining, W. C., Chi, M. & Bell, A. T. Novel Pt/Mg(In)(Al)O catalysts for ethane and propane dehydrogenation. *J. Catal.* **282**, 165–174 (2011).

25. Filez, M. *et al.* Kinetics of Lifetime Changes in Bimetallic Nanocatalysts Revealed by Quick X-ray Absorption Spectroscopy. 12430–12434 (2018). doi:10.1002/anie.201806447

26. Filez, M. *et al.* Unravelling the formation of Pt-Ga alloyed nanoparticles on calcined Ga-modified hydrotalcites by in situ XAS. *Chem. Mater.* **26**, 5936–5949 (2014).

27. Chen, X. *et al.* Electronic structure of nanoscale Cu/Pt alloys: A combined X-ray diffraction and X-ray absorption investigations. *Radiat. Phys. Chem.* **75**, 1622–1625 (2006).

28. Bus, E. & van Bokhoven, J. A. Electronic and Geometric Structures of Supported Platinum, Gold, and Platinum−Gold Catalysts. *J. Phys. Chem. C* **111**, 9761–9768 (2007).

29. Tuo, Y. *et al.* Partial positively charged Pt in Pt/MgAl2O4 for enhanced dehydrogenation activity. *Appl. Catal. B Environ.* **288**, 119996 (2021).

30. Frenkel, A. I., Hills, C. W. & Nuzzo, R. G. A View from the Inside: Complexity in the Atomic Scale Ordering of Supported Metal Nanoparticles. *J. Phys. Chem. B* **105**, 12689–12703 (2001).

31. Lei, Y., Jelic, J., Nitsche, L. C., Meyer, R. & Miller, J. Effect of Particle Size and Adsorbates on the L3, L2 and L1 X-ray Absorption Near Edge Structure of Supported Pt Nanoparticles. *Top. Catal.* **54**, 334–348 (2011).

32. Yevick, A. & Frenkel, A. I. Effects of surface disorder on EXAFS modeling of metallic clusters. *Phys. Rev. B* **81**, 115451 (2010).

33. Xiao, S. *et al.* Size effect on alloying ability and phase stability of immiscible bimetallic nanoparticles. *Eur. Phys. J. B - Condens. Matter Complex Syst.* **54**, 479–484 (2006).

34. Kim, B.-S., Lee, J., Yoon, H.-S. & Kim, S.-K. Reduction of SnO2 with Hydrogen. *Mater. Trans.* **52**, 1814–1817 (2011).

35. Śmiechowicz, I., Kocemba, I., Rogowski, J. & Czupryn, K. CO oxidation over Pt/SnO2 catalysts. *React. Kinet. Mech. Catal.* **124**, 633–649 (2018).

36. Firet, N. J. *et al.* Operando EXAFS study reveals presence of oxygen in oxide-derived silver catalysts for electrochemical CO2 reduction. *J. Mater. Chem. A* **7**, 2597–2607 (2019).

37. Bariås, O. A., Holmen, A. & Blekkan, E. A. Propane Dehydrogenation over Supported Pt and Pt–Sn Catalysts: Catalyst Preparation, Characterization, and Activity Measurements. *J. Catal.* **158**, 1–12 (1996).

38. Wang, J. *et al.* On the Role of Sn Segregation of Pt-Sn Catalysts for Propane Dehydrogenation. *ACS Catal.* **11**, 4401–4410 (2021).

39. Llorca, J., Homs, N., Fierro, J.-L. G., Sales, J. & Piscina, P. R. de la. Platinum–Tin Catalysts Supported on Silica Highly Selective forn-Hexane Dehydrogenation. *J. Catal.* **166**, 44–52 (1997).

40. Wang, X. *et al.* Colloidal Synthesis and Structural Control of PtSn Bimetallic Nanoparticles. *Langmuir* **27**, 11052–11061 (2011).

41. Wang, X. *et al.* Pt/Sn Intermetallic, Core/Shell and Alloy Nanoparticles: Colloidal Synthesis and Structural Control. *Chem. Mater.* **25**, 1400–1407 (2013).

42. Velu, S., Suzuki, K., Osaki, T., Ohashi, F. & Tomura, S. Synthesis of new Sn incorporated layered double hydroxides and their evolution to mixed oxides. *Mater. Res. Bull.* **34**, 1707–1717 (1999).

43. Zhu, H. *et al.* Sn surface-enriched Pt-Sn bimetallic nanoparticles as a selective and stable catalyst for propane dehydrogenation. *J. Catal.* **320**, 52–62 (2014).

44. Ahmad, R. & Singh, A. K. Simultaneous Site Adsorption Shift and Efficient CO Oxidation Induced by V and Co in Pt Catalyst. *J. Phys. Chem. C* **121**, 12807–12816 (2017).

45. Vandichel, M. & Grönbeck, H. Catalysis Science & Technology A dimer path for CO dissociation on PtSn †. *Catal. Sci. Technol.* **9**, 695–701 (2019).

Chapter 4

CO_2-assisted propane dehydrogenation over Pt: comparing promoters – Part 1 : detailed characterization by in situ QXAS with Modulation Excitation analysis

Abstract

The effect of changing the promoter element in a Pt-based catalyst was explored for regular and CO_2-assisted propane dehydrogenation (PDH, CO_2-PDH). Detailed characterization of Pt:In/$MgAl_2O_4$ (Pt:In) and Pt:Sn/$MgAl_2O_4$ (Pt:Sn) catalysts, with 3 wt% loading of Pt and 3 wt% of In or Sn, is performed through in situ Quick X-ray absorption spectroscopy (QXAS), coupled with Modulation Excitation spectroscopy (MES), based on flow perturbations. The catalysts were primarily studied for their behaviour in presence of CO_2, as this can play a role during CO_2-PDH. CO_2 is capable of oxidising both Sn and In to their respective oxides and this oxidation begins at low temperature (<500 K). RWGS was used as model reaction during the in situ QXAS measurements. During a CO_2-PDH experiment, the CO_2:H_2 ratio changes dynamically, which determines the stability of the Pt-M alloy. Increasing the ratio of CO_2:H_2 during reverse water gas shift (RWGS), did not lead to Pt-M alloy segregation, though the total extent of promoter oxidation increased slightly with increased CO_2:H_2 ratios, but the absolute amounts are still quite small. MES analysis of Pt L_{III}-XANES data for the Pt:In catalyst showed a shift in energy position to higher eV (0.6 eV shift), implying a surface more In-rich than the bulk. Moreover, a reversible process occurred between different alloy phases for Pt:In, with about 11 atoms out of 100 of the sample participating in this process. Pt:Sn showed much lower sensitivity to the changes imposed with only ~1 atom per 100 responding. However, an 8% change in white line (WL) intensity during RWGS implied that changes did occur to the Pt:Sn sample, albeit with slower kinetics than for Pt:In. H_2/O_2 redox cycles made Pt:In sinter, while keeping its alloy composition constant, identified as $Pt_{13}In_9$. In Pt:Sn, the H_2/O_2 redox cycles increased the Sn fraction around Pt. Moreover, with proceeding treatments the alloy phase changed from the initial Pt_3Sn to PtSn. Importantly, under reductive atmosphere at temperatures above 780 K, an In loss of 24% was tracked through monitoring of the edge jump values at the In K-edge, while no loss was noted for Sn in Pt:Sn.

The results of this chapter are submitted to J.Cat as:

N. V. Srinath, V. De Coster, H. Poelman, L. D'ooghe, J. Dendooven, M.-F. Reyniers, V. V Galvita, CO_2-assisted propane dehydrogenation over Pt: comparing promoters – Part 1 : detailed characterization by in situ QXAS with Modulation Excitation analysis

4.1 Introduction

From chapter 3,[1] it has been found that a Pt-based bimetallic catalyst can be beneficial for application in CO_2-assisted PDH (CO_2-PDH). A study on the effect of CO_2 upon the integrity of the Pt-Sn alloy was performed, indicating that CO_2 can oxidize and extract Sn from the alloy to SnO_2. In that study, the atomic ratio of deposited Sn relative to Pt was 1:3, which caused difficulties to come to alloy formation when the catalyst was prepared on a higher surface area support. From the activity test results, CO_2-PDH was suggested to proceed through a combination of both Langmuir-Hinshelwood (L-H) and Mars-van Krevelen mechanisms (MvK). It was also reasoned that an increased ratio of CO_2 with respect to H_2 could lead to alloy segregation through promoter oxidation. If that is the case, it would make sense to use another promoter such as In with Pt, and compare its behaviour in presence of CO_2 and H_2 with Sn. Compared to Sn, In has a different affinity for oxidation by CO_2 in that it is easier to oxidize. It has been reported that bulk In[2] cannot be oxidized by CO_2, but how about in the presence of Pt?

Therefore, a few pertinent questions would have to be answered:

- Can differing structures of the Pt-In and Pt-Sn alloy be confirmed through experiments?
- How do Pt:In and Pt:Sn behave in the presence of CO_2?
- Can In loss be quantified?
- Does the promoter affect the extent of sintering of the nanoparticles (NPs)?
- how does the alloy composition change with redox cycles?
- Is the alloy stable under different ratios of H_2:CO_2?

In the present study, higher atomic ratios between In and Sn with respect to Pt are chosen (~1.5:1). The purpose of using this ratio is because it is a ratio typically reported to be more active for PDH.[3,4] In essence, the answer to the first and second bullet point is already known for Pt:Sn from chapter 3,[1] where CO_2 is found to oxidize the promoter and segregate it from the Pt-Sn alloy, based on QXAS analysis. However, the amount of Sn in that work was low and the segregation from the alloy took place quite readily. It is plausible that if the Sn fraction is higher, then segregation would not occur as quickly. The support used is $MgAl_2O_4$ with a high surface area (~110 m^2/g), which is similar to the HSA support from chapter 3.[1] The latter was chosen so that the data from this work can be used in conjunction with the already obtained data,[1] in order to gain a holistic understanding of the Pt:Sn system (effect of particle size and promoter content).

In situ QXAS will be employed in this work to answer the questions listed. Measurements will be conducted at the Pt L_{III}-edge and the In/Sn K-edges during different experiments. QXAS will assess the local structure surrounding Pt and In/Sn and detect the changes occurring during RWGS with different ratios of H_2:CO_2 in order to assess alloy segregation. Experiments will also be run in conjunction to Modulation Excitation Spectroscopy (MES) with Phase Sensitive Detection (PhSD). Herein, the catalytic system is modulated by a periodic alternation between two externally applied conditions, which in this work will be the composition of the gas mixture.[5–9] Such experiment will help to determine the extent of participation of surface species in the H_2:CO_2 redox process. The latter is important because, at the moment, it is not understood how the CO_2-PDH reaction takes place over such a bimetallic catalyst system. Moreover, it can help to distinguish which is the major mechanism at play, L-H or MvK.

This is the first of a two-part study, which focusses on the detailed characterization of Pt:Sn and Pt:In catalysts, in order to gain a complete understanding of the structural behaviour under a redox environment (H_2:CO_2), and to determine the phases at play during the MES experiments. This information is crucial to understand the phenomena occurring during the activity tests, which will be detailed in part II. The latter part contains activity tests for Pt:In, Pt:Sn and a Pt:Ga catalysts for PDH, RWGS and CO_2-PDH, which are analysed accordingly to determine the benefits/drawbacks in the use of each promoter. Ga as a promoter was not analysed in this characterization part I, as a similar XAS analysis for a Pt:Ga catalyst with varying amounts of Ga has already been conducted (chapter 6),[10] and the understanding gained from that work can be extrapolated to part II of this work. The overall work brings insight into the phase changes during CO_2-PDH, their effects upon activity, selectivity and stability, and eventually the benefits/drawbacks of using a certain promoter in presence of CO_2.

4.2 Experimental Section

4.2.1 Catalyst Preparation

4.2.1.1 Support Preparation

$MgAl_2O_4$ support was synthesized by co-precipitation of $Mg(NO_3)_2.6H_2O$ and $Al(NO_3)_3.9H_2O$ with a molar ratio of Mg/Al equal to 1/2, using NH_4OH (ACS reagent, 28.0-30% NH_3 basis) as precipitation agent, while maintaining a pH of 10 at 333 K. The precipitate was filtered and dried at 393 K for 24h, following which it was calcined in air at 923 K for 5 h with a ramp rate of 2 K/min. This preparation method is similar to prior work.[1,10,11]

4.2.1.2 Catalyst Synthesis

Three catalysts: 1. Pt/$MgAl_2O_4$ (3wt%Pt), 2. Pt:In/$MgAl_2O_4$ (3wt% Pt, 3wt% In) and 3. Pt:Sn/$MgAl_2O_4$ (3wt% Pt, 3wt% Sn), were prepared by incipient wetness impregnation (co-impregnation). Precursors used were $H_2PtCl_6.xH_2O$ (>99.9%, Sigma-Aldrich), $In(NO_3)_3 \cdot xH_2O$ (Sigma-Aldrich, 99.99%) and $SnCl_2$ (>99.9%, Sigma Aldrich). Absolute ethanol was the solvent chosen for preparing the aqueous solution of the respective precursors for impregnation. All materials were subsequently dried at 393 K for 2h, followed by calcination in air at 903 K for 4.5h, yielding the "as prepared" samples. The Pt:In/$MgAl_2O_4$ and Pt:Sn/$MgAl_2O_4$ shall henceforth be labelled as Pt:In and Pt:Sn. The monometallic Pt/$MgAl_2O_4$ catalyst was prepared to serve as a reference.

A fourth catalyst Pt:In/$MgAl_2O_4$ (3wt% Pt, 6wt% In) with an increased In loading of 6% was prepared to serve as an extra sample for comparison purposes. The method of preparation was the same as that for Pt:In. This sample shall henceforth be referred to as Pt:In6.

4.2.2 Catalyst Characterization

Surface areas and pore volumes were determined for the samples subsequent to degassing at 413 K for 3 h, by means of N_2-sorption at 77 K (Micromeritics, Tristar), using a 5 point BET method (total surface area A_t).

SEM-EDX was performed on the support to obtain an estimate of the compositions of Mg and Al. A SEM JEOL JSM 5400 equipped with an INCA x-act extension (Oxford instruments) for Energy Dispersive X-ray (EDX) measurements was used for this purpose.

Inductively coupled plasma optical emission spectroscopy (**ICP OES**, IRIS intrepid II XSP from Thermo Scientific) was used to determine the bulk compositions of the catalysts and support. Mineralization was done by peroxide fusion for all samples.

Dark field scanning transmission electron microscopy **(STEM DF)** was used to collect images, from which a particle size distribution/average particle size could be obtained. EDX was used for the local chemical analysis and mapping. The samples were deposited onto a lacey carbon film on a copper grid support. A JEOL JEM-2200FS Cs corrected microscope, operated at 200 kV, equipped with a Schottky-type field-emission gun (FEG) and EDX JEOL JED-2300D, was used for the measurements.

4.2.3 In situ quick XAS

Synchrotron-based in situ XAS experiments were conducted at the ROCK beamline of the 2.75 GeV SOLEIL light source (Saint-Aubin, France). QXAS measurements were performed in transmission at the Pt L_{III}-edge (11564 eV), In K-edge (27940 eV) and Sn K-edge (29200 eV). Both edges (Pt and In/Sn) were measured in parallel using a Si(111) and Si(220) oscillating monochromator, by means of a macro for fast edge switching. This allowed for quasi-simultaneous acquisition of spectra at both edges with a short delay (~60s) for the edge switch. The oscillating monochromator enables collection of multiple spectra in small time steps (~1 s, 2 Hz frequency). Upon extraction of all the raw XAS data using an interpolation grid, the XANES region of the data had measurement points every 0.3 eV at the Pt L_{III}-edge. At the Sn K-edge, the step used through the edge region was 1 eV.

Approximately 5 mg of as prepared material was loaded into a 1.8 mm outer diameter (o.d.) quartz capillary reactor (wall thickness = 50 µm), and this bed was kept in place by means of quartz wool plugs. Mounting of the capillary reactor was done in a frame connected to gas feed lines through Swagelok fittings. An external heat gun was used in order to reach the desired temperature of 873 K, while the flows were maintained by means of calibrated mass flow controllers. The temperature for the capillary reactor was calibrated, through the use of a thermocouple placed in a capillary filled with inert material (support $MgAl_2O_4$), prior to the start of the sequence of experiments. The blower was placed under the capillary, and a temperature ramp was applied up to a blower set point temperature of 958 K. This set point of the blower led to a real process value of 873 K.

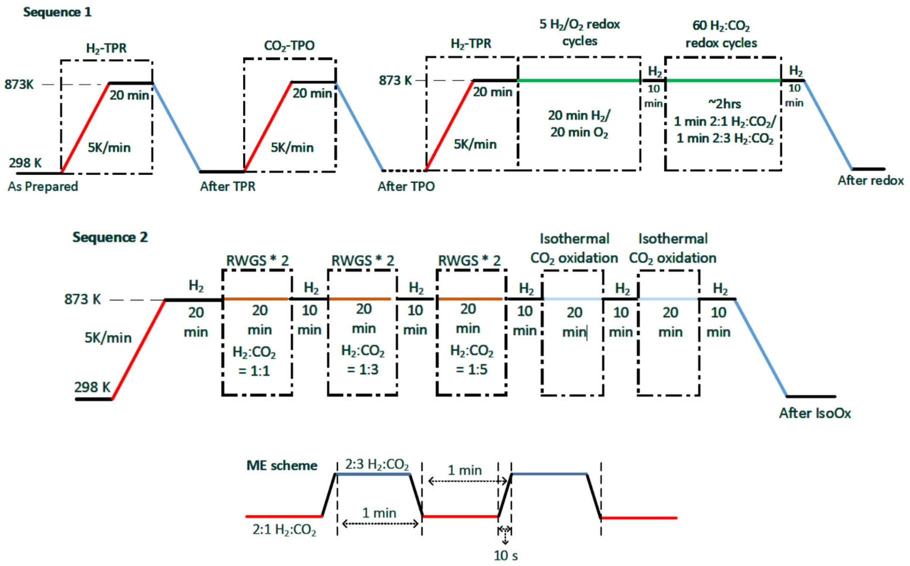

Figure 4.1: *Complete experimental scheme employed for in situ QXAS measurements. Sequence 2 started with an "As prepared" catalyst. ME scheme refers to the modulation excitation experiments. It is represented in sequence 1 as the 60 H_2:CO_2 redox cycles.*

The catalyst was subjected to several in situ treatments, indicated schematically in Figure 4.1 (sequence 1 with ME and sequence 2). Sequence 2 started with a fresh sample, hence not as continuation with the spent sample from sequence 1. The set of experiments performed included:

Sequence 1

1. H_2-Temperature Programmed Reduction (H_2-TPR) (1 Nml/min H_2 & 9 Nml/min He, total flow = 10 Nml/min) up to 873 K to obtain the alloy. Then cool down to room temperature (RT), to measure XAS for EXAFS modelling, as data will have better signal to noise (S/N) ratio at RT compared to 873 K. This state of the sample will be labelled as "After H_2-TPR";

2. CO_2-Temperature Programmed Oxidation (CO_2-TPO) (5 Nml/min CO_2 and 5 Nml/min He, total flow = 10 Nml/min) up to 873 K in order to observe the effect of CO_2 on the alloy with increasing temperature. Cool down to RT and measure EXAFS. This state of the sample will be labelled as "After CO_2-TPO";

3. H_2-TPR to regenerate the alloy prior to isothermal H_2/O_2 redox cycles;

4. Isothermal H_2 (1 Nml/min H_2 & 9 Nml/min He)/O_2 (1 Nml/min O_2 & 9 Nml/min He) redox cycles with a half-cycle lasting for 20 min each at 873 K. This is performed to increase the promoter content in the Pt-M alloy;

5. Isothermal H_2-reduction at 873 K for 10 min, prior to start of H_2:CO_2 redox cycles for Modulation-Excitation measurements (MES), to regain the alloy state;

6. Modulation Excitation Spectroscopy (MES) during QXAS experiments: 60 H_2:CO_2 cycles with 2 alternating ratios of H_2:CO_2 (2:1 and 2:3). Each ratio was held for 1 min, so 1 cycle constitutes 1 min of 2:1 and 1 min of 2:3 ratio of H_2:CO_2. The flows for each of the half-cycles were: 2 Nml/min H_2, 1 Nml/min CO_2 & 7 Nml/min He (total flow = 10 Nml/min) for the 2:1 H_2:CO_2 ratio, while for the 2:3 H_2:CO_2 ratio it was 2 Nml/min H_2, 3 Nml/min CO_2 & 5 Nml/min He (total flow = 10 Nml/min). This constitutes a concentration modulation experiment as there is a periodic variation of the flow of CO_2 with respect to H_2 and these concentrations are admitted to the capillary reactor for equal duration. In order to avoid pressure fluctuations during the gas flow adjustments, the switch was conducted over a 10s period through the use of a controller. Therefore, the flow rates would look something akin to the representation in Figure 4.1 as "ME scheme".

Throughout these repeated variations, time-resolved spectra were collected. A series of transient periods at the beginning of the experiments allow the system to reach an equilibrium state, followed by the actual data acquisition for the applied modulation.

All recorded spectra were energy-calibrated, averaged and normalized via the python normalization GUI developed by O. Roudenko.[12] Further analysis was performed by means of MATLAB scripts to handle the large datasets. Sets of 10 time-resolved spectra were averaged at a time, which corresponds to 5s of experimental time. This means that one period of 2 min is divided into 24 sections with a resolution of 5s and each section containing 10 spectra. Subsequently, to enhance the signal to noise ratio, averaging of the time-resolved spectra was undertaken over 30 periods (the last 30). Finally, phase-resolved spectra were obtained by correlations to periodic modulations using equation 4.1.[5,6,13]

$$\mu(E,\Delta\varphi) = \frac{2}{T}\int_0^T \mu(E,t)Sin\left(\frac{360^o}{T}t + \Delta\varphi\right)dt \qquad (4.1)$$

Demodulation of the time-resolved spectra μ(E,t) into phase-resolved spectra μ(E, $\Delta\varphi$) was performed by means of a sine function with a period of 120 s and a phase shift $\Delta\varphi$, $0^{o} \leq \Delta\varphi < 360^{o}$. The obtained phase-resolved spectra were analysed by comparison to reference spectra that were measured experimentally, which could be expected to form as intermediates during the modulations. Finally, the phase-resolved spectra were analysed qualitatively and quantitatively by comparing them to difference spectra of a few references (PtO_2, Pt/$MgAl_2O_4$) which are expected to appear in the two applied reaction conditions. This ME analysis method is similar to the work done by Gaur et al.[5]

This ME experiment is expected to move the promoter (In or Sn) in and out of the Pt-M alloy phase, with the amount of promoter participating in this process dependent on the gas mixture concentration admitted to the reactor. As such, this experiment can help to understand and identify the redox mechanism for these catalysts.

7. Cool down to RT to measure EXAFS. This state of the sample will be labelled as “After redox”.

<u>Sequence 2</u>

1. H_2-TPR (1 Nml/min H_2 & 9 Nml/min He, total flow = 10 Nml/min) up to 873 K to obtain the alloy;

2. Reverse water gas shift reaction (RWGS) at 873 K with ratios of H_2:CO_2 being 1:1, 1:3 and 1:5. The flow of H_2 was kept constant at 1 Nml/min, while the total flow of H_2 + CO_2 + He was fixed at 10 Nml/min. The measurement for each RWGS ratio was performed twice, as only 1 of the edges (Pt L_{III}- or In/Sn K-edges) was measured for each independent RWGS experiment. Subsequent to each RWGS experiment, an intermediate isothermal H_2-reduction was employed for 10 min to regain the alloy state, in the event that it might have been lost during RWGS;

3. Isothermal CO_2 oxidation at 873 K (“IsoOx”, 1 Nml/min CO_2 & 9 Nml/min He) to follow the alloy integrity at reaction temperature under CO_2. This was performed twice, the second time with a higher CO_2 flow rate (5 Nml/min, mixed in 5 Nml/min He). The two were performed to assess the effect of change of CO_2 partial pressure and to compare with the CO_2-TPO from sequence 1;

4. Isothermal H_2-reduction at 873 K for 10 min and cool down to RT for EXAFS. This state of the sample will be labelled as “After IsoOx”.

A set of reference samples was measured at RT in addition to the aforementioned experiments. These were: Pt-foil, Sn-foil, In-foil, PtO_2, SnO_2 and In_2O_3 in view of fingerprint comparison and to determine the amplitude reduction factor (S_0^2) values for fitting the experimental EXAFS data. S_0^2 was determined by fitting the first PtO_2 shell (Pt-O) with a standard Pt-O path of a PtO_2 crystal.

The VIPER program[14] was employed for fitting of the EXAFS data and the error bars were estimated with k^1/k^3 weighted fittings. The Fourier transformation of the data was performed with a Kaiser-Bessel window with a dk of 1.5. Once the value of S_0^2 was determined (0.95), it was fixed in the program to proceed with the fitting. The fitting at the Pt-edge was in general done in the range from 1.3-3.3 Å. Either 1 or 2 shells were used for fitting of the data.

4.3 Results and Discussion

4.3.1 Catalyst Characterization – ICP, EDX and BET

BET and porosity measurements for the support and the catalysts are depicted in Table 4.1, together with the SEM-EDX compositional result for the $MgAl_2O_4$ support and ICP values for the Pt:In and Pt:Sn catalysts. The catalysts have a slightly lower surface area and porosity than the bare support.

Table 4.1: *Chemical composition, BET and porosity results for the support and catalysts. Metal loading values for all the loaded catalysts is determined by ICP, while that of the support follows from EDX (in orange).*

Catalyst	**Metal Loading (wt%)**				**BET (m^2/g_{cat})**	**Pore volume (cm^3/g_{cat})**	**Average pore diameter (nm)**
	Mg	**Al**	**Pt**	**In or Sn**			
$MgAl_2O_4$	15.3	32.3			115.4	0.21	84.9
$Pt/MgAl_2O_4$	13.8	32.0	3.1		106.1	0.19	72.6
Pt:In	13.4	35.9	2.98	2.83 (In)	100.2	0.18	64.8
Pt:Sn	13.5	32.9	3.19	2.89 (Sn)	99.5	0.18	65.4
Pt:In6	13.4	32.8	2.89	5.74 (In)	-	-	-

4.3.2 XANES results during H_2-temperature programmed reduction (H_2-TPR), CO_2-temperature programmed oxidation (CO_2-TPO), Isothermal CO_2-oxidation (IsoOx), isothermal H_2/O_2 redox cycles and Reverse Water Gas Shift reaction (RWGS).

4.3.2.1 Pt-edge

The Pt XANES spectra have been analysed similarly to chapter 3,[1,10] i.e. normalized and examined based on the evolution of the white line (WL). Results for the Pt:In and Pt:Sn samples shall be discussed henceforth, while Pt:In6 and Pt/$MgAl_2O_4$ data are presented in the supporting information.

H_2-TPR: The XANES evolution at the Pt L_{III}-edge during the H_2-TPR for Pt:In and Pt:Sn is quite similar (Figure 4.2). Both samples have similar initial WL intensities, which indicates similar oxidation state of Pt and size of the nanoparticle (NP). The final WL position for both samples ends up at 11568.4 eV. A monometallic sample was measured during H_2-TPR previously, showing the WL position of the reduced monometallic Pt/$MgAl_2O_4$ catalyst to lie at 11566.5 eV[1]. To remain consistent with the samples tested for this work, a re-measurement of monometallic Pt/$MgAl_2O_4$ was performed. This guarantees that the normalization parameters are the same for all samples and the shifts observed remain relative to measurements made during this experimental campaign. The WL position of the maximum for the reduced Pt/$MgAl_2O_4$ was registered at 11567.2 eV (Appendix C, Figure C1). The WL maxima of the reduced samples of Pt:In and Pt:Sn are 1.2 eV above that of monometallic Pt, which confirms formation of a Pt-M alloy. Pt:Sn/HSA catalyst from chapter 3[1] showed the WL position for the reduced state of the bimetallic catalyst to be 1 eV above that of monometallic Pt, from which the alloy phase was determined to be Pt_3Sn. Given the current WL position at 1.2 eV above monometallic Pt, the alloy phase formed for Pt:Sn in the present scenario is probably very similar to that obtained previously. Similarly, a fingerprint comparison of the WL position and intensity of Pt:In with the work from Filez et al.[15] (Pt mono = 11567.8 eV vs. 11567.2 eV in this work, Pt_3In = 11568.8 eV vs. 11568.4 eV in this work, $Pt_{13}In_9$ = 11570 eV), indicates that the In content in the Pt:In alloy should be slightly more than that of the Pt_3In phase. The trend by which the spectra reach the final WL position of 11568.4 eV is similar to that observed for the smaller NPs from chapter 3,[1] implying that the size of the reduced NPs is likely in the range 0.7-1.2 nm.

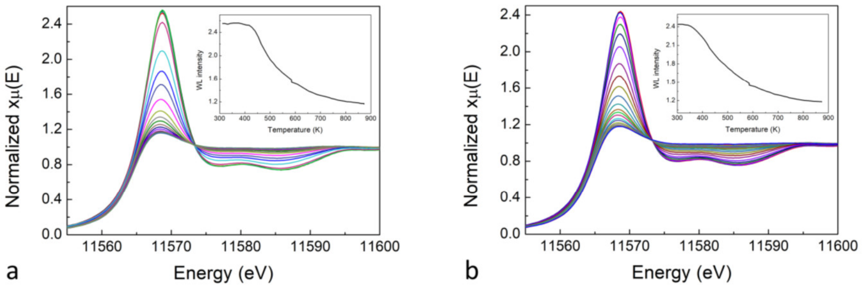

Figure 4.2: *XANES spectra at Pt L_{III} during H_2-TPR up to 873 K for* ***a:*** *Pt:In and* ***b:*** *Pt:Sn. Inset of graphs shows the WL intensity evolution with temperature. H_2 = 1 Nml/min, He=9 Nml/min (total flow = 10 Nml/min).*

CO_2-TPO: During this experiment (Appendix C, Figure C3), there is an increase in WL intensity and a position shift to lower energies (11567.2 eV), which indicates loss of the Pt-Sn and Pt-In alloys. At the end of CO_2-TPO, WL intensity values above those reached for monometallic Pt were noted (1.32 vs. 1.50 for Pt:In & 1.40 for Pt:Sn), pointing to partial oxidation of Pt. It was found that when Sn and Ga were oxidized by CO_2 to SnO_2 and Ga_2O_3, their oxygen contribution can be strong enough to influence the WL intensity of the Pt-edge for neighbouring Pt.[1,10] The latter can take place for the In-containing Pt:In sample as well. It was shown by Filez et al.[15] that indium, once separated from the Pt-In alloy upon oxidation (by O_2 in that work), tends to move out spinodally and ends up as an In_2O_3 crust surrounding a metallic Pt core. This means that for smaller nanoparticles there will be more In_2O_3 in contact with the core Pt because of higher NP surface availability, leading to higher probability of shared O between Pt and In_2O_3. The present evolution of the Pt WL under CO_2-TPO implies that In has undergone oxidation to In_2O_3 under the CO_2 atmosphere, which is however not typically expected for bulk In.[16]

Isothermal CO_2-oxidation at 873 K (IsoOx) (sequence 2): Both catalysts were exposed twice to a gas mixture of CO_2 and He at 873 K for 20 mins, with two different partial pressures of CO_2, to assess how this affects the alloy. Figure 4.3 shows the spectra for the 10% CO_2/He feed, while the 50% CO_2/He data are in Appendix C, Figure C4. The Pt:In sample comes close to the same state it had after the CO_2-TPO experiment (Figure C3), while Pt:Sn does not depict the same final state, as the WL intensity hardly changes. This indicates that the Pt-In alloy completely segregates in presence of CO_2 at 873 K, while Pt:Sn only shows a WL shift from 11568.4eV to 11567.8 eV (inset of Figure 4.3). Considering that the WL position is still higher than that of monometallic Pt (11567.2 eV), this shift does point to a reduced Sn content in the Pt-Sn alloy, changing its composition. Given more time, Sn might also completely segregate out of the alloy so that Pt:Sn reaches the state it had after the CO_2-TPO experiment with an apparently oxidized Pt state. The IsoOx experiment hence implies that In oxidizes more easily and quickly than Sn by CO_2. A higher partial pressure of CO_2 (Figure C4) in the feed showed no difference for Pt:In, while for Pt:Sn the WL was slightly higher.

After the IsoOx experiment, the sample was reduced for 10 min at 873 K before cooling down to RT to take the EXAFS spectra. The WL position for Pt:In and Pt:Sn returned at 11568.4 eV (same as "after TPR"), indicating the alloy phases were restored.

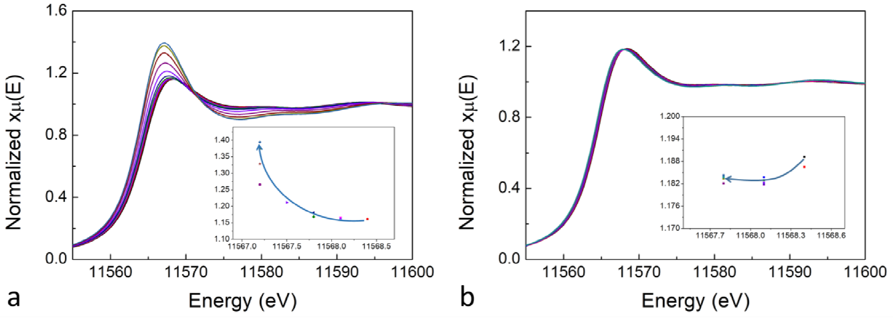

Figure 4.3: *XANES profiles at Pt L_{III} during isothermal CO_2-oxidation at 873 K for **a:** Pt:In and **b:** Pt:Sn. Insets show the evolution of the WL maxima during the oxidation. CO_2 = 1 Nml/min, He = 9 Nml/min (total flow = 10 Nml/min).*

Isothermal H_2/O_2 redox cycles (873 K): Figure 4.4 shows the spectra obtained at the end of each half-cycle of the H_2/O_2 redox experiment. The final WL intensity at the end of the H_2 half-cycles is quite consistent, while that for the O_2 half-cycles varies for the Pt:In and Pt:Sn samples, with an overall decreasing trend. Just like in the Pt:Ga system (chapter 6),[10] the variation of the WL intensity over the O_2 steps can have 2 major reasons: 1. Nanoparticle sintering and 2. Increase of promoter content in the Pt-M nanoalloy.

The WL evolution for Pt:Sn suggests an increase of the Sn content in the Pt-Sn alloy, due to the quite clear trend of decreasing WL intensity. Sintering is not considered a reason for this change, as the likelihood of NP sintering to this extent within a 2-3 redox cycles window is minimal. Pt:In on the other hand isn't readily changing in terms of WL intensity, implying a constant In-content, which however is at this stage speculative and would have to be confirmed through EXAFS fitting.

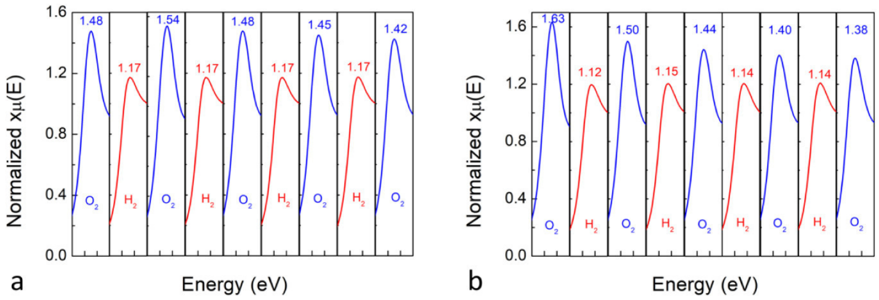

Figure 4.4: *white lines for Pt L_{III} during isothermal H_2/O_2 redox cycles at 873 K in* ***a:*** *Pt:In,* ***b:*** *Pt:Sn. Values within the graphs depict the WL height reached at the end of a 20 min half-cycle. Each half-cycle of (-) H_2 cycle for 20 min (1 Nml/min of H_2 + 9 Nml/min He) and (-) O_2 cycle for 20min (2 Nml/min 20% O_2/He + 8 Nml/min He). 5 total H_2/O_2 cycles were performed finishing with a H_2 half-cycle at the end (not all half-cycles shown).*

The final Pt L_{III} WL positions at the end of sequence 1 (Figure 4.1), i.e. after the H_2:O_2 redox + H_2:CO_2 redox for modulation excitation, were different for the 2 samples. Upon conclusion of the redox experiments, the samples were reduced at 873 K for 10 mins before cooling down to RT for EXAFS measurements. The WL position for Pt:In returned to 11568.4 eV, while for Pt:Sn it increased to 11569 eV. This change in WL position for Pt:Sn implies that the Sn content in the alloy increased during the redox steps.

Reverse Water Gas Shift reaction (RWGS): In chapter 3, RWGS with a feed ratio of 1:1 was performed over a Pt:Sn catalyst, keeping the Pt-Sn alloy intact.[1] In the present work, 3 ratios were tested (H_2:CO_2 = 1:1, 1:3 and 1:5) to see if the alloy segregates when exposed to more CO_2 in the feed. Even at the lowest 1:5 H_2:CO_2 ratio, the alloy does not segregate, but seems to remain quite stable (Appendix C, Figure C5). However, a closer inspection of the WL intensities reveals something interesting, namely that small changes do occur. For Pt:In, the increase in WL intensity is lowest for the 1:1 H_2:CO_2 ratio and in general goes up with decreasing ratio. For Pt:Sn, the final WL intensity was higher at lower ratios. These observations could be due to one of 2 reasons. First being that more of the In or Sn atoms are likely participating in a redox-type mechanism during RWGS when exposed to a higher ratio of CO_2:H_2. The actual percentage of In that gets oxidised is likely very small. The WL intensity increases initially and then remains stable throughout reaction, which shows that only a small amount of In is oxidized at the start of RWGS. Shortly hereafter, a reversible process sets in where the total In participation in this redox process is constant. The increase in WL intensity is more gradual for Sn when compared to In at the 1:1 ratio, evidencing the higher oxidation potential of In over Sn, hence the readiness of In surface atoms to oxidise. The second possibility could be something as simple as a small part of the In and Sn scavenge some CO_2 for their oxidation, after which a steady state is reached.

4.3.2.2 In/Sn-edge

Similar to the Pt L_{III}-edge, the spectra at the In- and Sn K-edges are analysed for most of the same experiments. The experiments not analysed at the In- and Sn-edges are: 1. RWGS: an error took place during data acquisition and 2. H_2:CO_2 redox cycles: data were too noisy to investigate through ME and PhSD. Figure 4.5 shows the RT XANES profiles at the In and Sn K-edges subsequent to every experimental treatment.

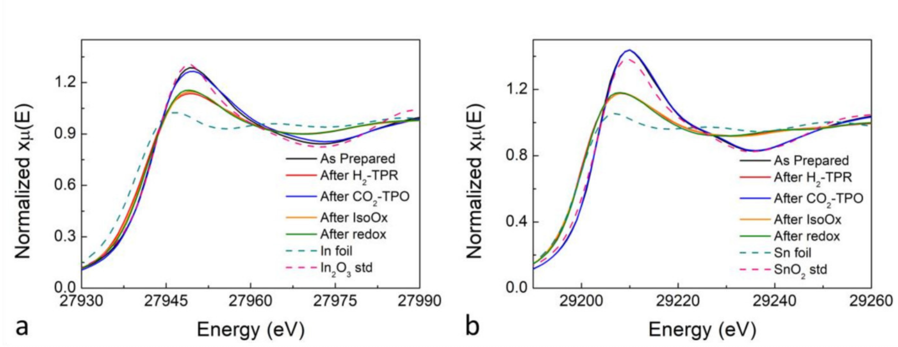

Figure 4.5: a: *Pt:In,* ***b:*** *Pt:Sn. All RT XANES spectra collected at the (a) In & (b) Sn K-edge subsequent to each treatment (H_2-TPR, CO_2-TPO, Isothermal CO_2-oxidation, H_2/O_2 & H_2:CO_2 redox cycles). The plots contain the reference spectra of In foil and In_2O_3 (in a), and Sn foil and SnO_2 (in b)*

H_2-TPR: The Sn WL maximum moved from 29210 eV (1.44 intensity) to 29208 eV (1.17 intensity), while for In it went from 27950 (1.26 intensity) to 27949.2 eV (1.14 intensity). Comparing the final position after H_2-TPR with the metal foil suggests that reduction is not complete for In and Sn (Figure 4.5), although both underwent reduction as detailed in Figure 4.6. At the Sn-edge, the final WL position and intensity (1.17) attained after reduction can match both SnO or Pt-Sn alloy (Appendix C, Figure C6). The H_2/O_2 redox cycle experiment data at the Pt-edge showed for Pt:Sn that the alloy content of Sn increased during subsequent redox cycles, therefore the final state of reduction at the Sn-edge should be that of a mix of SnO and Pt-Sn alloy, reflecting the incomplete SnO_2 reduction.

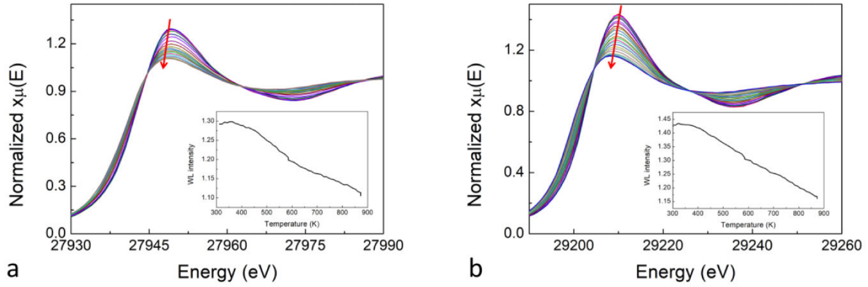

***Figure 4.6:** XANES profiles during H_2-TPR up to 873 K for **a:** Pt:In (In K-edge) and **b:** Pt:Sn (Sn K-edge). H_2 = 1 Nml/min, He = 9 Nml/min (total flow = 10 Nml/min), T_{max} = 873 K. Insets show the evolution of WL intensity with temperature.*

CO_2-TPO & Isothermal CO_2-oxidation: Both In and Sn underwent complete oxidation to the original state upon exposure to CO_2 in TPO (Appendix C, Figure C7). In moved back to 27950 eV with a concomitant increase in intensity to its original value of 1.25, while Sn returned to 29210 eV with an increase in WL intensity to 1.44.

During isothermal CO_2-oxidation (Appendix C, Figure C8 and C9), In oxidizes back to its initial state, while Sn seems to show minimal changes. For the latter, it must be kept in mind that the initial spectrum (after isothermal H_2-reduction) is in fact a mix of SnO and Pt-Sn alloy. The Pt-edge data already indicated that Sn did not segregate completely from the Pt-Sn alloy phase, while In did for Pt-In. The spectra taken at the In and Sn-edges during the same treatment align with those findings. However, during CO_2-TPO Sn did go back to the initial oxidized state, which suggests that it oxidizes more easily at lower temperatures? To understand this, a plot was made with the evolution of WL intensity versus temperature for Pt and In and Sn during CO_2-TPO (Figure 4.7). Both promoters were found to oxidize before Pt, as evidenced by their earlier rise in WL, and this at a relatively low temperature of <500 K. In more readily segregates from the alloy phase than Sn. In oxidizes at lower temperature as it directly changes to In_2O_3, while Sn turns into SnO first, before forming SnO_2. This transition is evidenced by the relatively constant WL intensity for Sn between 300-400 K, after which it begins to rise. Since SnO and Pt-Sn alloy have similar WL intensities and position (Appendix C, Figure C6), it can be assumed that at these low temperatures of 300-400 K, Sn is in fact oxidizing to SnO. While the Pt WL rises up directly for Pt:In, for Pt:Sn it goes through a dip initially. At the start of this dip, Sn shows an increase in WL intensity, indicating that oxidation and Sn loss from the alloy set in.

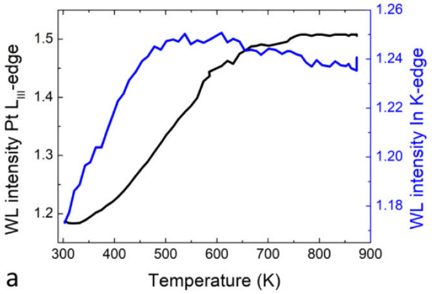

Figure 4.7: *WL intensity evolution for Pt L_{III}- (black), In K- or Sn K-edge (blue) during CO_2-TPO up to 873 K.* ***a:*** *Pt:In,* ***b:*** *Pt:Sn. graphs vs. temperature.*

Isothermal H_2/O_2 redox cycles (873 K): Isothermal H_2/O_2 redox cycles at the In and Sn-edges (Figure 4.8) revealed consistent profiles at the end of each of the individual half-cycles. This means that the state of In and Sn subsequent to each O_2 exposure is very similar to the original state.

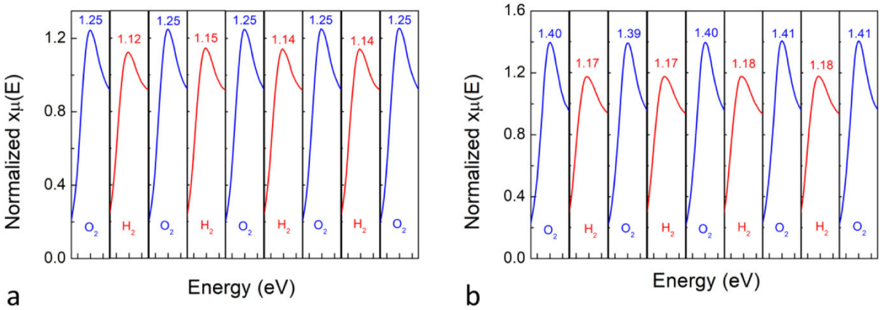

Figure 4.8: *white lines for In or Sn K-edge during isothermal H_2/O_2 redox cycles at 873 K in* ***a:*** *Pt:In,* ***b:*** *Pt:Sn. Values within the graphs depict the WL height reached at the end of a 20 min half-cycle. (-) H_2 half-cycle (1 Nml/min of H_2 + 9 Nml/min He) and (-) O_2 half-cycle (2 Nml/min 20% O_2/He + 8 Nml/min He). 5 H_2/O_2 cycles were performed in total, finishing with a H_2 half-cycle (not all half-cycles shown).*

4.3.3 EXAFS results of samples subsequent to H_2-TPR, CO_2-TPO, IsoOx & redox

4.3.3.1 Pt-edge

As explained in the experimental section, EXAFS spectra were recorded at RT before and after each high temperature treatment. Fittings were performed for 1 or 2 shells depending on the spectra in the R-range of 1.2-3.4 Å. The crystal structures used for the fits were: PtO_2 (Pnnm, orthorhombic, Pt-O = 2.03 Å & Pt-O = 3.14 Å), Pt (Fm3m, cubic, Pt-Pt = 2.81 Å), Pt:Sn 1:1 ($P6_3/mmc$, hexagonal, Pt-Sn = 2.75 Å, Pt-Pt =2.78 Å), Pt:In 3:7 (Im3m, cubic, Pt-In = 2.77 Å) and Pt:In 13:9 (C2/m, monoclinic, Pt-In = 2.74 Å, Pt-Pt = 2.78 Å). All R factors were within 0.05.

The fitting results for all the states of both Pt:In and Pt:Sn samples are presented in Table 4.2 and 4.3, while the R-space and k-space figures and fits are shown in Figure 4.9 & Appendix C, Figure C11. Fitting results for Pt:In6 are presented in Appendix C, Figure C12 and Table C1. An estimation of the fraction of In or Sn in the Pt-In/Sn alloy was made by means of equation 4.2, based on the assumption that the promoter is uniformly distributed throughout the alloy. The estimation of nanoparticle size is based on the work by Frenkel et al.[17], assuming a hemispherical cuboctahedron. The fractions and sizes are all shown in Tables 4.2 and 4.3.

Fraction of In or Sn in the alloy = $N_{Pt\text{-}In/Sn}/(N_{Pt\text{-}In/Sn} + N_{Pt\text{-}Pt})$ (4.2)

Pt:In showed no change in promoter content after longer experimental sequences, remaining more or less the same at around 40%. The N_{Tot} and bond distances of $R_{Pt\text{-}Pt}$ and $R_{Pt\text{-}In}$ did increase with experimental time, indicating an increase in NP size and therefore sintering occurred. The same however cannot be said for the Pt:Sn catalyst, which showed an increase in Sn content, while the total coordination number (CN, N_{Tot}) and the NP size remained quasi constant. This indicates no sintering took place for this sample during prolonged experiments, but rather the Sn content and therefore the average alloy phase present in the sample changed. This is consistent with the observations made from the XANES region, where the WL position was found to be different subsequent to different treatments for Pt:Sn, in contrast to Pt:In. So, throughout the sequence of experiments, the particles with In promotion grow in size, while for Pt:Sn, the promoter content keeps increasing.

Table 4.2: *EXAFS fitting results at the Pt L_{III}-edge, In fraction and NP size for the Pt:In catalyst subsequent to each experiment.*

	As Prepared	**After TPR**	**After TPO**	**After IsoOx**	**After redox**
N_{Pt-O}	6.2 ± 0.2		2.1 ± 0.4		`
R_{Pt-O} (Å)	2.00 ± 0.01		2.01 ± 0.01		
σ^2_{Pt-O} (10^{-3}*Å^2)	2.8 ± 0.2		5.2 ± 1.5		
N_{Pt-In}		2.2 ± 0.3		2.7 ± 0.5	3.5 ± 0.1
R_{Pt-In} (Å)		2.65 ± 0.01		2.68 ± 0.01	2.74 ± 0.01
σ^2_{Pt-In} (10^{-3}*Å^2)		8.6 ± 0.3		11 ± 0.2	11 ± 0.4
N_{Pt-Pt}		3.3 ± 0.7	6.2 ± 0.7	4.4 ± 0.7	5.4 ± 0.06
R_{Pt-Pt} (Å)		2.72 ± 0.01	2.75 ± 0.01	2.76 ± 0.01	2.83 ± 0.01
σ^2_{Pt-Pt} (10^{-3}*Å^2)		10 ± 1.6	7 ± 0.5	11 ± 1.3	13 ± 0.2
ΔE_0 (eV)	6.7 ± 0.4	-0.5 ± 0.4	7.5 ± 2.3	-1.4 ± 0.5	0.4 ± 0.2
R factor	0.02	0.04	0.03	0.04	0.03
In fraction (%)		**40.5**		**37.8**	**38.8**
N_{Tot}		5.5		7.1	8.9
NP size (nm)		**0.75 ± 0.13**		**1.4 ± 0.23**	**2.1 ± 0.03**

Table 4.3: *EXAFS fitting results at the Pt L_{III}-edge, Sn fraction and NP size for the Pt:Sn catalyst subsequent to each experiment.*

	As Prepared	**After TPR**	**After TPO**	**After IsoOx**	**After redox**
N_{Pt-O}	5.6 ± 0.4		1.9 ± 0.4		
R_{Pt-O} (Å)	2.00 ± 0.01		2.02 ± 0.01		
σ^2_{Pt-O} (10^{-3}*Å^2)	2.7 ± 0.5		7 ± 2		
N_{Pt-Sn}		2.7 ± 0.3		2.9 ± 0.3	4.0 ± 0.3
R_{Pt-Sn} (Å)		2.66 ± 0.01		2.66 ± 0.01	2.71 ± 0.01
σ^2_{Pt-Sn} (10^{-3}*Å^2)		9.6 ± 0.5		9.6 ± 0.6	6 ± 0.3
N_{Pt-Pt}		3.2 ± 0.6	6.3 ± 0.5	3.0 ± 0.6	2.1 ± 0.3
R_{Pt-Pt} (Å)		2.71 ± 0.01	2.74 ± 0.01	2.72 ± 0.01	2.71 ± 0.01
σ^2_{Pt-Pt} (10^{-3}*Å^2)		10 ± 1.5	7 ± 0.4	10 ± 1.5	4.9 ± 0.5
ΔE_0 (eV)	6.7 ± 1.0	1.4 ± 1.1	7.1 ± 2.7	1.1 ± 1.2	3.0 ± 0.7
R factor	0.04	0.03	0.04	0.03	0.01
Sn fraction (%)	-	**45.3**	**-**	**49.5**	**65.6**
N_{Tot}	-	5.9	-	5.9	6.1
NP size (nm)		**0.85 ± 0.13**		**0.85 ± 0.13**	**0.95 ± 0.08**

Some oxygen neighbours were observed at the Pt L_{III}-edge for the “After TPO” states, which is similar to the findings in prior work[1]. In brief, these O pertain to the CO_2-oxidized and segregated promoters, yet close enough to the small Pt NPs to provide some O neighbours with higher disorder. However, it is also possible that the presence of a promoter assists towards the partial oxidation of Pt, since this has been a recurring theme from prior works.[1,10] More specifically this oxidation of Pt likely occurs at the undercoordinated sites of the NP. This is stated based on a comparison of the extent of oxidation of Pt (CN of Pt-O obtained) for the various EXAFS fits from this work and the prior 2 works. The $N_{Pt\text{-}O}$ increases with decreasing NP size, and when the NP size decreases the number of sites with lower coordination increases.

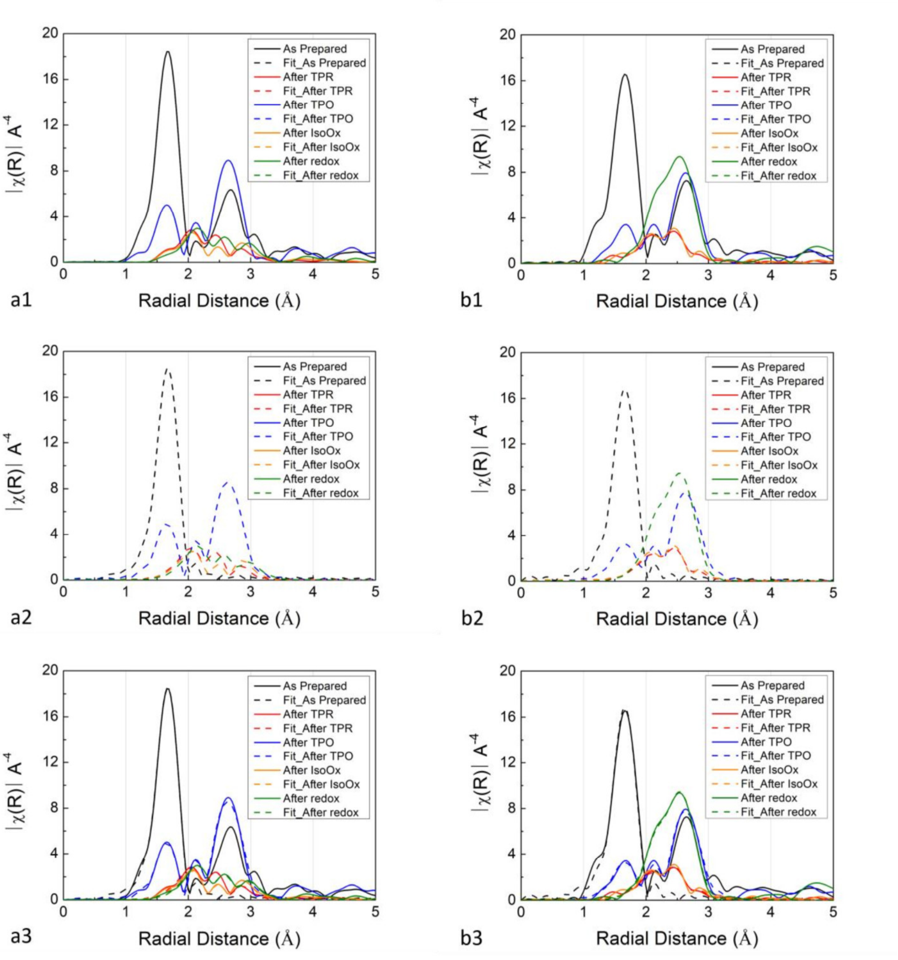

Figure 4.9: *Pt L_{III}-edge EXAFS spectra for **a:** Pt:In **b:** Pt:Sn. **1:** Fourier transformed R-space spectra subsequent to each treatment; **2:** Fit of R-space spectra; **3:** Merged graph including data and fit together.*

4.3.3.2 In/Sn-edge

Viewing the R-space spectra at the In-edge (Appendix C, Figure C13a) shows that there is minimal change in the state of In between the states “after TPR”, “After IsoOx” and “After redox”. This corroborates the EXAFS fitting at the Pt-edge, where it was determined that the content of In in the Pt-In alloy remained the same. Fitting of the In K-edge EXAFS was not performed for these three states as a large part of In_2O_3 did not reduce as evidenced by the R-space spectra (Appendix C, Figure C13a). Moreover, when viewed in k-space the data were quite noisy in the 6-8 $Å^{-1}$ region, where the Pt contributions are expected. Hence, only the first shells (In-O) of the states “As prepared” and “After TPO” were fit (Appendix C, Table C2). In underwent close to complete oxidation after CO_2-TPO, in line with the XANES results.

The Sn-edge R-space spectra corroborates the findings from the EXAFS fits at the Pt-edge (Appendix C, Figure C13b). Fitting was performed for the “As prepared”, “After TPO” and “After redox” states (Appendix C, Table C3). Sn underwent complete oxidation back to its original state after CO_2-TPO, in line with the XANES results. The data of “after TPR” and “After IsoOx” could not be fit because of the low signal to noise ratio, combined with the aspect that the Sn-Sn, Sn-O and Sn-Pt neighbours all show up in the same region between 2-3 Å. However, based on the EXAFS fitting at the Pt L_{III}-edge, the Sn content increases significantly for the state “After redox”, with a strong peak appearing at 2.5 Å (not phase-corrected), so that this peak of Sn-Pt could be fit.

4.3.4 Modulation Excitation XANES during H_2:CO_2 cycling

4.3.4.1 Pt:In

Phase-resolved spectra were obtained from the demodulated time-resolved XANES Pt L_{III} spectra by averaging 1, 5, 10, 15, 20 and 30 periods (Figure 4.10, 1 period of 120s = 24 spectra covering 5s, each of which are an average of 10 spectra, therefore a total of 240 spectra). This approach allows to eliminate static features and subsequently obtain a high S/N ratio. The actual gas flow measurements as detected through the mass spectrometer (MS) are represented in Appendix C, Figure C14.

During H_2:CO_2 cycling, a reversible process is taking place. Interestingly, the main peak shifts by 0.6 eV to higher energies over time when comparing period 1 to period 30, meaning that the surface acquires more In, i.e. forming an In-rich Pt-In alloy outer shell. This implies that two different alloy phases, with different In content, reside in the same NP at the same time. Wegener et al.[18] came to a similar conclusion from their work on a Pt-In alloy, where a $PtIn_2$ surface surrounding a core of Pt_3In was proposed.

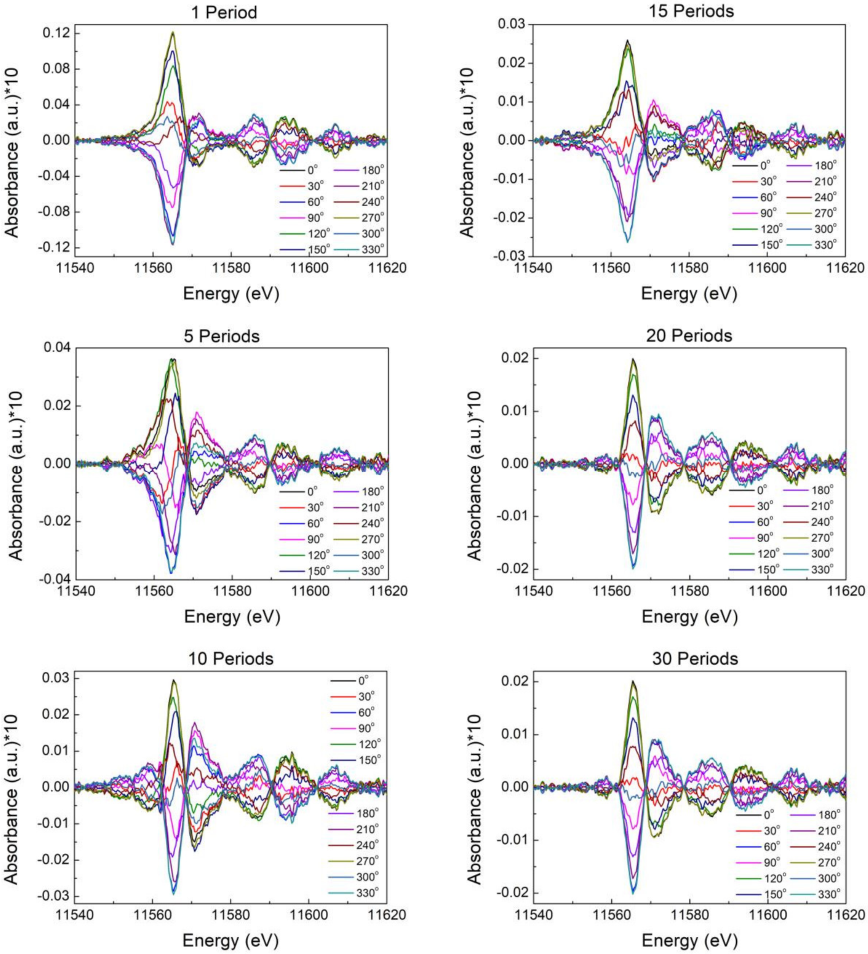

Figure 4.10: *Demodulated Pt L_{III} spectra for Pt:In consisting of 24 spectra each, averaged over 1, 5, 10, 15, 20 & 30 periods. ME spectra acquired at 873 K during H_2:CO_2 cycling.*

To gain an understanding of the redox process, it is imperative to compare the demodulated spectra with difference spectra (DS), based on the catalyst description obtained in the previous sections. A difference spectrum can e.g. be generated between PtO_2 and Pt, making use of the reference PtO_2 and the reduced state of the monometallic $Pt/MgAl_2O_4$ catalyst (termed DS_oxide in Figure 4.11-1). However, a fingerprint comparison of this PtO_2-Pt spectrum with the phase-resolved spectra shows no similarities except for the main peak (Figure 4.11-1). The latter is not unexpected as the Pt-In alloy remains stable throughout the RWGS experiments, regardless of the ratio between H_2:CO_2 (see § 4.3.2.1). A DS is typically generated based on the RT EXAFS measurements, which means that it is for the entire NP and not just for the surface which is probed during MES.

Since CO_2 can oxidize In, leading to alloy segregation of Pt:In, subtraction of Pt from Pt-In alloy could make a plausible DS. The latter was therefore generated from the state "After TPR" of the Pt:In catalyst and the reduced state of monometallic Pt/$MgAl_2O_4$ (called DS_mono) and used for comparison with the phase-resolved spectra (Figure 4.11-2).

Compared to DS_oxide, this DS_mono has an improved match with the averaged phase-resolved spectrum of period 1, but its first peak around 11566 eV is shifted by about 0.6 eV to higher energies. By comparing the maximal amplitude of DS_mono with the one for the phase-resolved spectrum, a quantification of the percentage of atoms participating in this change can be obtained. The amplitude of DS_mono being ~0.21, and for period 1 the maximum amplitude is ~0.012. Therefore for period 1, this amounts to about (0.012/0.21)*100 = 5.7% of all Pt species, not just surface Pt as this comparison is being made with a DS which accounts for bulk Pt. However, as mentioned before, surface atoms are being probed by MES. Given the size of the NPs (~1.5-2 nm), the surface to bulk ratio can be assumed to be about 50%, which would mean that 5.7/0.5 = 11.4% of the surface is participating in the reversible process. By the 30th period, this drops to ~1% of all surface atoms, i.e. 1 atom out of 100, which can be considered as measurement error. Therefore it can be concluded that the 2 DS created till now, are not adequate for comparison and some other phenomenon is occurring within the sample. For the Pt:Sn sample, isothermal oxidation in CO_2 made the phase of the Pt-Sn alloy change over time. This could be happening for the Pt:In sample as well, but how to create a DS without clear Pt-In alloy references? In the frame of the experiments conducted for this work, both Pt:In and Pt:In6 were measured (details of Pt:In6 in Appendix C, Figure C10). The position of the WL "after TPR" for Pt:In was 11568.4 eV, while for Pt:In6 it was 11569 eV. EXAFS fittings showed a clearly different In content in the alloy of both samples. Hence, it can be assumed that these pertain to two different Pt:In alloy phases, which, in absence of true alloy references, were used to generate a DS (named: DS_alloy, from the "After TPR" states of

Pt:In and Pt:In6 samples). Comparison of the latter with the phase-resolved spectrum (Figure 4.11-3) gives good agreement, apart from some minor differences in the range of 11560-11610 eV.

The +0.6 eV shift of the main peak in the demodulated phase-resolved spectra indicates an In enrichment at the surface. Considering the small size of the NPs, this must entail a change of composition in the core as well, as In is being lost to the surface. Hence, the sample undergoes a transition between two alloy states. However, not all the NPs present should necessarily have the same composition of Pt-In. Therefore, it can be possible that there is a percentage of NPs transitioning between e.g. Pt_3In and monometallic Pt, while others are transitioning between $Pt_{13}In_9$ and Pt_3In. and yet another part varies between monometallic and alloyed state. Based upon this model, an average DS can be created from "mono" and "alloy", with a multiplication factor applied to DS_mono as the phase-resolved spectrum matches better with DS_alloy. This DS (called DS_avg, Figure 4.11-4), matches almost perfectly with the phase-resolved spectrum for a multiplication factor applied to DS_mono of 0.3. The latter means that during H_2:CO_2 cycling about (0.3/(1+0.3)) * 100 = 23% of the sample is changing from Pt:In alloy to Pt mono, while the rest is oscillating between two Pt-In alloy states.

Period 1 quantifies to about 20% of the total Pt oscillating between states (0.012/0.06 = 20%, where 0.06 is the amplitude of the DS_avg). An assumption of ~50% surface species implies that 20/0.5 = 40% of the sample is oscillating between the alloy states. EXAFS determined that the average alloy has ~60% Pt on average, which means that the surface would have a 60:40 ratio between Pt:In. So the correction has to applied to the 40% which would lead to 40/1.2 = 33.3% of surface atoms.

By period 30, the percentage changes to 3.5% of total Pt, and applying the 50% assumption would mean a total of 7% Pt oscillating between the alloy states. However, now it must be kept in mind that by period 30, the surface is In enriched, which means that there is a lower amount of Pt available. If we assume the surface is $PtIn_2$ as was concluded by Wegener et al.,[18] then about 33% of the surface is Pt. From this, the corrected amount of Pt participation comes out to be 7/0.66 = 10.6% of Pt oscillating. So, about 11 atoms out of every 100 are oscillating between phases.

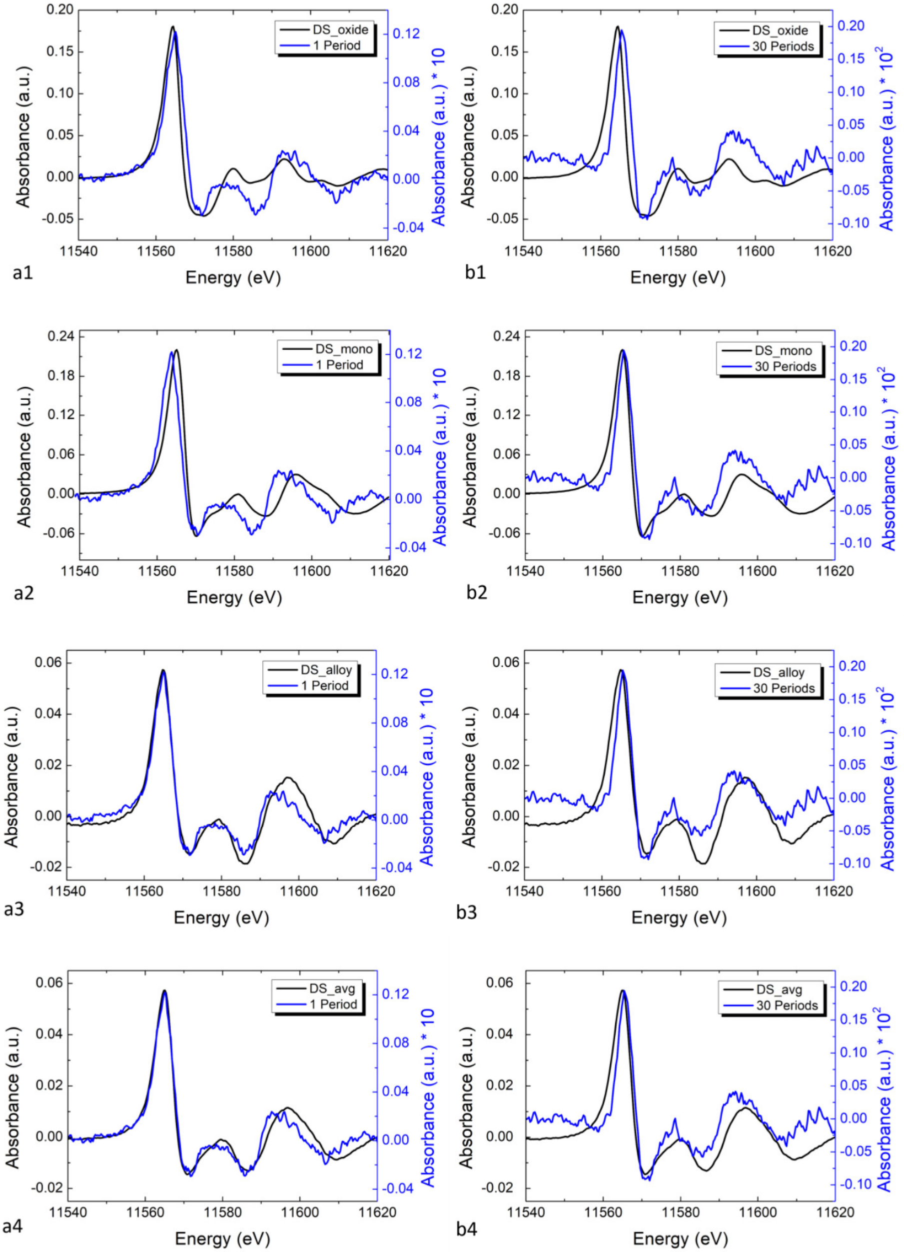

Figure 4.11: *Maximum amplitude demodulated Pt L_{III} spectra averaged over* ***a:*** *1 period,* ***b:*** *30 periods.* ***1:*** *Comparison with PtO_2-Pt difference spectrum (DS),* ***2:*** *Comparison with Pt-Pt:In (After TPR) DS,* ***3:*** *Comparison with Pt:In-Pt:In6 (After TPR states for both) DS and* ***4:*** *Comparison with average of Pt-PtIn and Pt:In-Pt:In6 DS.*

4.3.4.2 Pt:Sn

Similar to the Pt:In sample, an analysis was conducted with the Pt:Sn sample for the same experiment. Unlike what was observed for the Pt:In sample the phase-resolved spectra for Pt:Sn (Appendix C, Figure C15) show quite a low S/N ratio and minimal changes, including in the energy positions, implying that the alloy state remained consistent. The spectra seem to match closest with a DS created from the "After TPR" and "After redox" states (Figure C16). Quantification of the atoms participating in this change comes to about 1 per 100, which can be considered negligible.

At first sight, this result is at odds with previous work[1], where an MCR-ALS analysis determined that Sn goes in and out of the Pt:Sn alloy. However, careful analysis brings up a few reasons for this paradox. First, the amount of Sn in the Pt:Sn sample here is much higher than in that work (46% vs. 16%), which means only a small amount of Sn has to leave the sample through oxidation to see a difference in Pt state (from alloy to monometallic). Second, the gas flow used here oscillates between a 2:1 and a 2:3 H_2:CO_2 ratio, while previously pure H_2 and pure CO_2 were applied. Hence, in this work there is a constant H_2 presence that can help keep up the integrity of the alloy. Third, the Pt:Sn alloy in the present sample proves to be quite stable as even an isothermal CO_2 oxidation did not completely segregate Sn from the alloy through a 20 min exposure, while in the Pt:Sn sample with lower Sn content,[1] 70% of the Pt got segregated from the alloy in 1 min. Fourth, the RWGS experiments (Appendix C, Figure C5) showed that with the 1:1 H_2:CO_2 ratio the WL took a little while to stabilize, in contrast to the 1:3 and 1:5 ratios where it almost immediately reached its final WL intensity. The variation applied in the ME experiment, between 2:1 and 2:3 H_2:CO_2, is likely not strong enough to induce major changes to the alloy in the ME time frame. Larger variation of the H_2:CO_2 ratio would probably lead to larger changes observed through PhSD.

Therefore, it can be concluded that the Pt-Sn alloy in the present sample is stable during these ME experiments and that if employed during a CO_2-PDH experiment with similar flow conditions, Sn and Pt can be safely assumed to remain in alloyed state without segregation.

4.3.5 STEM Results

Subsequent to the XAS treatments, the samples were collected and examined with DF-STEM to see if the particle size distribution actually shows similar NP size as estimated from XAS.

The NP size for Pt:In amounts to 1.83 nm, while for Pt:Sn it is 1.56 nm (Appendix C, Figure C17). It is consistent with XAS in that the Pt:In NP are larger than Pt:Sn, but Pt:Sn is showing an average particle size that is higher than that estimated from XAS, while Pt:In has a lower one. This could arise from the aspect that both Sn and In are heavier elements than the support elements in $MgAl_2O_4$, which makes it impossible to distinguish Sn, SnO_2, In and In_2O_3, for example from Pt, Pt:In and Pt:Sn.

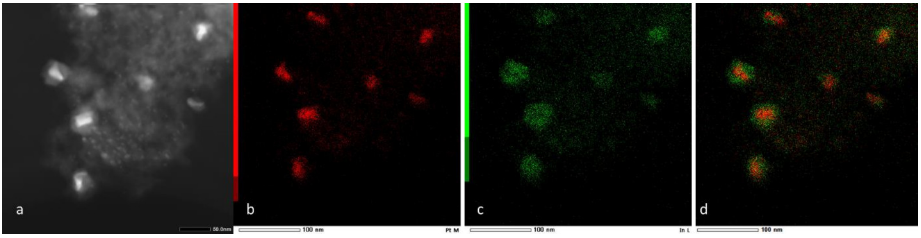

Figure 4.12: ***a:*** *STEM-DF image of PtIn6,* ***b:*** *Pt-EDX map,* ***c:*** *In EDX map,* ***d:*** *EDX Overlay with Pt and In.*

EDX mapping of the Pt:In sample with 6% In loading is presented in Figure 4.12. This sample was subjected to a high temperature H_2-reduction, followed by an oxidation step (under O_2 at 873 K). Once oxidised, the In separated from Pt and formed a kind of shell around it, thereby covering the undercoordinated Pt sites at the NP surface. This is as described in § 4.3.2.1. Remark that Figure 4.12a also shows In_2O_3 to be brighter than the background of the support.

4.4 Discussion

The difference in behaviour between In and Sn towards alloy formation with Pt can be explained based on the elemental compositions obtained from ICP (§ 4.3.1) and a knowledge of the alloy phases possible between Pt-In[18,19] and Pt-Sn[20] (Tables 4.4 and 4.5).

Based on the loadings from ICP, assuming pure alloy phase formation and all Pt and In taking part in the Pt:In alloy, the obvious alloy phase at 873 K would be Pt_2In_3. However, during the high temperature in situ XAS experiments, some In was lost from the catalyst (Appendix C, Figure C18). Hence, the alloy composition will rather match one with less In. An analysis of the amount of In lost and at which temperature it was lost, was performed based on the In-edge step. The latter correlates with the amount of In in the sample as seen by the x-ray beam. When In is lost e.g. by vaporization, the absorption by In decreases and the edge step will reduce concomitantly.

Table 4.4: *alloy phases possible at 873 K between Pt-In and their respective crystal details; Actual Pt = 38.26 at%, In = 61.73 at% (from ICP). In fraction of neighbours surrounding Pt based on equation 4.2.*

Alloy phase	**at% Pt**	**at% In**	**Bulk crystal CN**	**In fraction (%)**
Pt_3In_7	30	70	N_{Pt-Pt} = 0 N_{Pt-In} = 8	100
$PtIn_2$	33.3	66.7	N_{Pt-Pt} = 0 N_{Pt-In} = 8	100
Pt_2In_3	40	60	N_{Pt-Pt} = 3 @ 3.2 Å N_{Pt-In} = 8 @ 2.81 Å	72.7
$Pt_{13}In_9$	59.1	40.9	N_{Pt-Pt} = 6 N_{Pt-In} = 5	45.4
Pt_2In*	66.7	33.3	N_{Pt-Pt} = 7 N_{Pt-In} = 5	41.6
Pt_3In	75	25	N_{Pt-Pt} = 8 N_{Pt-In} = 4	33.3

**Pt_2In stable till 823 K*

The total loss of In based on the difference between the edge step from the "As prepared" and "After redox" state of the sample, was calculated to be ~24% of the total In present at the start (Figure 4.13). During CO_2-TPO, no In was lost, likely as it oxidized back to oxide before the temperature reached 500 K (Figure 4.7a). The losses in TPR begin to occur at around 780 K. The TPR profile for the In-edge (Figure 4.6a) shows that a major part of In in the sample is reduced by 700 K and therefore, In mainly gets lost in form of metal, not as oxide, and this from 780 K onwards. The vaporized In ends up getting deposited on the walls further down the reactor, where the temperature is lower. So ideally, In-based catalysts, where In is intended to be used in its reduced state, should be employed at temperatures below 780 K, regardless of whether it forms alloy with another metal.

Now, from the EXAFS analysis (Table 4.2) the In content remains constant around 40% throughout the entire experimental sequence, which means that the average alloy composition is stable. It can be speculated that the alloy phase present is $Pt_{13}In_9$, based on comparing the k-space spectra with the ones presented in the work of Filez et al.[15] However, the ratios of CNs for bulk crystals (Table 4.4) suggest that Pt_2In lies closer to the sample in this work. On the other hand, the Pt_2In phase is not very stable above 823 K,[19] while the sample in this work maintains its same composition, making the $Pt_{13}In_9$ or Pt_3In phase more likely. Based on the CNs and distances from the fits (Table 4.2), the $Pt_{13}In_9$ phase has a closer match than the Pt_3In phase, but a mix of these phases is equally possible.

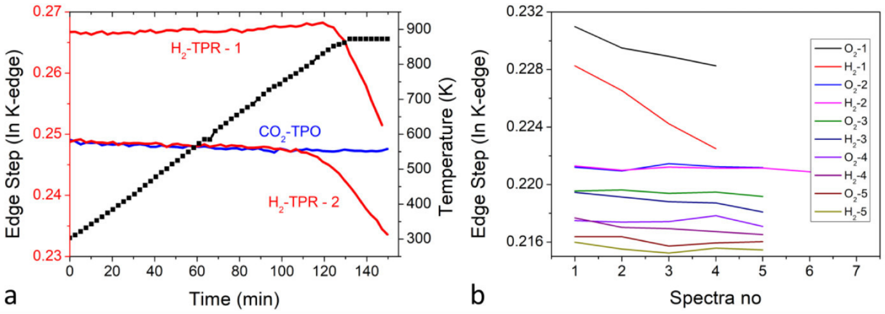

Figure 4.13: *In-edge step evolution with time and temperature during different treatments.* ***a:*** *During H_2-TPR, CO_2-TPO and a 2nd H_2-TPR,* ***b:*** *During H_2/O_2 redox cycles at 873 K.*

The ME experiments have shown that the surface alloy for Pt:In is In-rich, i.e. In migrates to the surface. A similar conclusion was arrived at by Wegener et al,[18] albeit for different experiments, where they determined that the surface alloy would be $PtIn_2$ for their system, while the bulk remained as Pt_3In. Hence, one can speculate that the alloy phase first formed during TPR is Pt_2In, which separates into $Pt_{13}In_9$ at the surface and a Pt_3In phase in the bulk at higher temperature (>823 K). Moreover, coupling the knowledge of an In-rich surface with the aspect of In loss and NP sintering (Table 4.2), it is very reasonable to assume that In actually assists the NP sintering by its high volatility.

Table 4.5: *alloy phases possible at 873 K between Pt-Sn and their respective crystal details; Actual Pt = 40.17 at%, Sn = 59.82 at% (from ICP). Sn fraction of neighbours surrounding Pt calculated from equation 4.2.*

Alloy phase	**at% Pt**	**at% Sn**	**Bulk crystal CN**	**Sn fraction (%)**
$PtSn_2$	33.3	66.67	$N_{Pt\text{-}Pt} = 0$ $N_{Pt\text{-}Sn} = 8$	100
Pt_2Sn_3	40	60	$N_{Pt\text{-}Pt} = 1$ $N_{Pt\text{-}Sn} = 7$	87.5
PtSn	50	50	$N_{Pt\text{-}Pt} = 2$ $N_{Pt\text{-}Sn} = 6$	75
Pt_3Sn	75	25	$N_{Pt\text{-}Pt} = 8$ $N_{Pt\text{-}Sn} = 4$	33.3

For Pt:Sn, assuming all Pt and Sn go into the alloy leads to Pt_2Sn_3 as possible alloy phase. However, the latter shows a very high theoretical Sn fraction surrounding Pt, namely 87.5%. Comparing the theoretical Sn fractions in Pt_3Sn, PtSn and Pt_2Sn_3 (Table 4.5) and the actual Snfractions surrounding Pt based on the fitted CN (Table 4.3) likely yields a more realistic view. The possible alloy for Pt:Sn at different stages of the experimental sequence now always lies between Pt_3Sn and Pt_1Sn_1, or comprises a mixture of these two, with shifting dominance towards Pt_1Sn_1 as experiments proceed. The average NP size is constant around 0.9 nm, which is approximately 30 atoms. Unlike In, no loss of Sn was detected based on the analysis of edge steps at the Sn-edge. Sintering of the Pt:Sn sample was also not observed, in line with results from chapter 3(for Pt:Sn/HSA),[1] where the temperature for the in situ experiments was higher (923 K vs. 873 K here).

Sn did not face the same issues as In and this aligns with the results from Wang et al,[21] who showed through DFT calculations that thermodynamically the most stable phase is Pt_3Sn and the possibility to have a Sn-enriched alloy is highly unlikely. This was also observed through the ME experiment where the Pt:Sn position did not change with respect to the original difference after reduction/alloy formation. All of the above make Sn a better choice as Pt promoter than In.

4.5 Conclusions

Numerous in situ XAS experiments were conducted for the Pt:In and Pt:Sn catalysts. The main aim was to find how these catalysts behave in a CO_2-atmosphere and in presence of both H_2 and CO_2 as in CO_2-assisted PDH.

XANES analysis clarified that a pure CO_2 atmosphere is capable of oxidizing both In and Sn. The In promoter oxidized more readily than Sn based on the isothermal CO_2-oxidation at 873 K. Analysis of the WL evolution during CO_2-TPO revealed that oxidation of In and Sn under a CO_2 atmosphere begins at low temperature <500 K and only after CO_2 starts to oxidize the In or Sn promoter, the WL of Pt begins to change, indicating a loss of the alloy.

When feeding H_2 and CO_2 together, an increase in the amount of CO_2 with respect to H_2 did not segregate the alloy. Only a slight increase in WL was noticed, indicating a larger number of surface species participating in the reaction. This was confirmed through the ME experiments, where a reversible process of alloying/de-alloying was observed. The actual fraction of Pt participating in this process was estimated to be about 11 atoms out of 100 for the Pt:In catalyst. Pt:Sn showed a much lower fraction in comparison. The latter was ascribed to the two feed compositions used for the ME experiment with insufficient difference to induce surface changes to the alloy. Employing more distinct conditions should lead to more total Pt engagement in the oscillation experiments.

EXAFS modelling of the data after distinct experiments revealed the Pt:In sample to have a constant In content in the Pt:In alloy, regardless of the treatments. One change that did occur to the Pt:In sample was the nanoparticle (NP) size, which sintered to form larger NP upon high temperature redox treatments. The latter can in part be enhanced by the high volatility of In, leading to 24% In loss over the sequence of experiments, and/or by the surface rearrangement of the Pt-In alloy during reaction at 873 K. The main alloy phase identified for Pt:In was $Pt_{13}In_9$, mostly present at the surface and as such the active phase, complemented with a Pt_3In phase in the bulk.

For the Pt:Sn sample, the Sn content in the Pt-Sn alloy increases with proceeding experiments. The average alloy phase was Pt_3Sn initially, which gradually shifted to Pt_1Sn_1 later on subsequent to further treatment. The average NP size was similar throughout all treatments, indicating no sintering took place, while also no loss of Sn was observed. All these factors combined suggest that Sn is a superior promoter for CO_2-assisted PDH when compared to In.

Appendix C : Data

XANES spectra for $Pt/MgAl_2O_4$. XANES profiles at Pt L_{III}-edge for Pt-In and Pt-Sn during CO_2-TPO, isothermal CO_2-oxidation 0.5 partial pressure of CO_2, RWGS experiments. XANES profiles at the In and Sn K-edges for Pt-In and Pt-Sn during CO_2-TPO and isothermal CO_2-oxidation. XANES and EXAFS analysis for PtIn6 with EXAFS fittings. EXAFS fitting graphs in R-space and k-space at the Pt L_{III}-edge for Pt-In and Pt-Sn. EXAFS fitting graphs in R-space, and results at In and Sn K-edges for Pt-In and Pt-Sn. Demodulated and difference spectra for Pt-Sn. DF-STEM with particle size distribution for Pt:In and Pt:Sn. Picture showing In loss.

4.6 References

1. Srinath, N. V. *et al.* Behaviour of Platinum-Tin during CO2-assisted propane dehydrogenation: Insights from quick X-ray absorption spectroscopy. *J. Catal.* (2021). doi:https://doi.org/10.1016/j.jcat.2021.08.041

2. Chen, M. *et al.* Applied Catalysis A : General Study in support effect of In2O3 / MO x (M = Al , Si , Zr) catalysts for dehydrogenation of propane in the presence of CO 2. *"Applied Catal. A, Gen.* **407**, 20–28 (2011).

3. Iglesias-juez, A. *et al.* A combined in situ time-resolved UV – Vis , Raman and high-energy resolution X-ray absorption spectroscopy study on the deactivation behavior of Pt and Pt A Sn propane dehydrogenation catalysts under industrial reaction conditions. *J. Catal.* **276**, 268–279 (2010).

4. Zhu, H. *et al.* Sn surface-enriched Pt-Sn bimetallic nanoparticles as a selective and stable catalyst for propane dehydrogenation. *J. Catal.* **320**, 52–62 (2014).

5. Gaur, A. *et al.* Probing the Active Sites of MoS2 Based Hydrotreating Catalysts Using Modulation Excitation Spectroscopy. *ACS Catal.* **9**, 2568–2579 (2019).

6. Serrer, M.-A. *et al.* Structural dynamics in Ni–Fe catalysts during CO2 methanation – role of iron oxide clusters. *Catal. Sci. Technol.* **10**, 7542–7554 (2020).

7. Ferri, D., Newton, M. A. & Nachtegaal, M. Modulation Excitation X-Ray Absorption Spectroscopy to Probe Surface Species on Heterogeneous Catalysts. *Top. Catal.* **54**, 1070 (2011).

8. König, C. F. J., Schildhauer, T. J. & Nachtegaal, M. Methane synthesis and sulfur removal over a Ru catalyst probed in situ with high sensitivity X-ray absorption spectroscopy. *J. Catal.* **305**, 92–100 (2013).

9. Müller, P. & Hermans, I. Applications of Modulation Excitation Spectroscopy in Heterogeneous Catalysis. *Ind. Eng. Chem. Res.* **56**, 1123–1136 (2017).

10. Srinath, N. V. *et al.* In Situ XAS/SAXS Study of Al2O3-Coated PtGa Catalysts for Propane Dehydrogenation. *ACS Catal.* 11320–11335 (2021). doi:10.1021/acscatal.1c03146

11. Longo, A. *et al.* What Makes Fe-Modified MgAl2O4 an Active Catalyst Support? Insight from X-ray Raman Scattering. *ACS Catal.* **10**, 6613–6622 (2020).

12. La Fontaine, C., Belin, S., Barthe, L., Roudenko, O. & Briois, V. ROCK: A Beamline Tailored for Catalysis and Energy-Related Materials from ms Time Resolution to µm Spatial Resolution. *Synchrotron Radiat. News* **33**, 20–25 (2020).

13. Ferri, D. *et al.* First steps in combining modulation excitation spectroscopy with synchronous dispersive EXAFS/DRIFTS/mass spectrometry for in situ time resolved study of heterogeneous catalysts. *Phys. Chem. Chem. Phys.* **12**, 5634–5646 (2010).

14. Klementev, K. V. Package "VIPER (visual processing in EXAFS researches) for windows". *Nucl. Instruments Methods Phys. Res. Sect. A Accel. Spectrometers, Detect. Assoc. Equip.* **448**, 299–301 (2000).

15. Filez, M. *et al.* Kinetics of Lifetime Changes in Bimetallic Nanocatalysts Revealed by Quick X-ray Absorption Spectroscopy. 12430–12434 (2018). doi:10.1002/anie.201806447

16. Chen, M. *et al.* Study in support effect of In2O3/MOx (M=Al, Si, Zr) catalysts for dehydrogenation of propane in the presence of CO2. *Appl. Catal. A Gen.* **407**, 20–28 (2011).

17. Frenkel, A. I., Hills, C. W. & Nuzzo, R. G. A View from the Inside: Complexity in the Atomic Scale Ordering of Supported Metal Nanoparticles. *J. Phys. Chem. B* **105**, 12689–12703 (2001).

18. Wegener, E. C. *et al.* Structure and reactivity of Pt–In intermetallic alloy nanoparticles: Highly selective catalysts for ethane dehydrogenation. *Catal. Today* **299**, 146–153

(2018).

19. Okamoto, H. In-Pt (Indium-Platinum). *J. Phase Equilibria Diffus.* **26**, 399 (2005).

20. Hu, J. *et al.* Optimization and Calculation of Pt-Sn Phase Diagram BT - Proceedings of the 2015 4th National Conference on Electrical, Electronics and Computer Engineering. in 623–629 (Atlantis Press, 2015). doi:https://doi.org/10.2991/nceece-15.2016.116

21. Wang, J. *et al.* On the Role of Sn Segregation of Pt-Sn Catalysts for Propane Dehydrogenation. *ACS Catal.* **11**, 4401–4410 (2021).

Chapter 5

CO_2-assisted propane dehydrogenation over Pt: comparing promoters - Part 2: Comprehensive performance evaluation.

Abstract

The effect of the promoter element in a Pt-based catalyst for CO_2-assisted propane dehydrogenation (CO_2-PDH) was explored. Ga, In and Sn were used to form Pt:Ga, Pt:In and Pt:Sn catalysts, supported on $MgAl_2O_4$. The potential for oxidation by CO_2 between the promoters is ordered as Ga > In > Sn and corollary to this the performance towards CO_2-PDH was Pt:Sn > Pt:In > Pt:Ga. These catalysts were tested for PDH as well, in order to rule out any inherent activity differences between the catalysts. All three catalysts (Pt:Ga, Pt:In and Pt:Sn) showed similar conversions of propane for PDH. Changing the feed ratio of CO_2:C_3H_8 from 0 to 0.125 strongly improved the activity through combination of RWGS and reverse Boudouard reactions. Higher ratios, however, led to lower C_3H_8 conversion for all catalysts. In Pt:Ga and Pt:In, this loss was due to alloy segregation induced by CO_2, while for Pt:Sn it arose from lower availability of adsorption sites. Applying a number of H_2/O_2 redox cycles as pre-treatment led to lower activity in CO_2-PDH due to an increase in promoter content in the Pt-M alloy for Pt:Ga and Pt:Sn. For Pt:In, redox cycles induced sintering of the catalyst, which led to a drop in activity with increasing redox cycles. Equilibrium conversions were achieved for all catalysts for the RWGS reaction. Quantification of the total amount of carbon formed on unpromoted and promoted Pt for CO_2-PDH yielded the order: Pt > Pt:Ga > Pt:In > Pt:Sn, in line with the performance.

The results of this chapter are submitted to J.Cat as:

N. V. Srinath, L. D’ooghe, H. Poelman, V. De Coster, J. Dendooven, M.-F. Reyniers, V. V Galvita, CO_2-assisted propane dehydrogenation over Pt: comparing promoters – Part 2 : Comprehensive performance evaluation.

5.1 Introduction

It is known from chapters 3 and 4 that CO_2 has the potential to oxidise both In and Sn to their respective oxides, and thereby segregate the Pt-M alloy. Therefore, use of elevated CO_2:C_3H_8 ratios is not be recommended. Similarly, a Pt:Ga catalyst under CO_2 atmosphere was also found to lose the alloy phase due to Ga oxidation.[1,2] Moreover, a higher CO_2:H_2 ratio also enables the dry reforming of C_3H_8 (eq 1.13, chapter 1).

Thermodynamic calculations for bulk components of Sn, In and Ga show that it is unlikely for them to get oxidised by CO_2. The Ellingham diagrams under O_2, CO_2 and H_2 atmospheres (Appendix D, Figure D1) show that the potential to be oxidised by CO_2 is ordered as Ga > In > Sn, while the potential to reduce under H_2 is of the order Sn > In > Ga. This implies that the potential for alloy segregation would be the lowest for Pt:Sn and highest for Pt:Ga, and once segregated it would be most difficult to for Pt:Ga to go back into alloy as it requires higher partial pressures of H_2 than those required for Pt:Sn. In is often chosen as promoter because its properties lie in between Sn and Ga. The results obtained through XAS analysis in part 1 (chapter 4), where it was shown that In oxidised and segregated from the Pt-M alloy more easily than Sn. These are consistent with the Ellingham diagrams (Appendix D, Figure D1) but however, these calculations pertain to bulk components, while nanoparticles (NPs) can behave differently as shown for other systems.[3,4] While the formation of these promoter oxides can lead to catalyst deactivation by loss of alloy and/or blockage of active sites, they can also take part in the CO_2-PDH reaction and help to remove carbon.

Due to the very different oxidation properties under CO_2, it is worthwhile to make a comparative study between the 3 promoters, to check their effectiveness in CO_2-assisted PDH in terms of overall activity and with respect to carbon formation. Another aspect to investigate is the influence of promoter content and how that affects activity. For this Pt-promoter study towards CO_2-asisted PDH, Ga, In and Sn are selected based on their proven efficacy for PDH,[1,5–10] while indium and gallium oxides as such have also shown to be viable catalysts for CO_2-PDH.[11–17]

Hence, catalysts Pt/$MgAl_2O_4$, Pt:In/$MgAl_2O_4$, Pt:Ga/$MgAl_2O_4$ and Pt:Sn/$MgAl_2O_4$ are tested in this work for CO_2-assisted PDH. The targeted Pt loadings during preparation are 3 wt%, while loadings of Ga, In and Sn were chosen such that the atomic ratios of M:Pt is ≈ 1.5 (excess of promoter vs. Pt). Detailed characterization through in situ XAS, BET, ICP and DF-STEM EDX is discussed in part 1 (chapter 4) for Pt:Sn and Pt:In. A similar catalyst with Pt and Ga has been characterized by XAS in previous work,[1] the results of which will be used to examine the activity results. In this second part of the work, further characterization through CO-DRIFTS, conventional H_2-TPR, H_2-pulse chemisorption and DF-STEM are provided.

Then, the performance of the catalysts is investigated in a multi-part study.

(i) First they are tested for PDH with a H_2 co-feed, following different levels of H_2/O_2 redox treatments (reduced, 5, 10 and 15 redox cycles). Hydrogen is fed along with propane in order to maintain catalyst stability during the reaction, and this reaction forms a background basis for the inherent activity of the three catalysts Pt:Ga, Pt:In and Pt:Sn.

(ii) They are then tested for CO_2-PDH to assess the effect of feed ratio of CO_2:C_3H_8 and of H_2/O_2 redox cycles on activity. Feeds with three different CO_2:C_3H_8 ratios, 8:1, 4:1 and 2:1, are applied, thereby varying the degree of promoter segregation, and the effect on overall performance is examined for each promoter. The catalysts are also tested for CO_2-PDH after 1, 3, 5, 7, 10, 15 and 20 redox cycles. From previous work,[1,8,10] such pre-treatment is known to increase the promoter content of the alloy, allowing to investigate how the changing composition of the Pt-M alloy affects its activity (for PDH and CO_2-PDH). Also, part 1 of this study indicates that application of redox cycles leads to increase in NP size for Pt:In but no changes occur to the composition of the Pt-In alloy; for Pt:Sn, the Sn content increases, while the NP size remains the same.

(iii) The catalysts are then used for RWGS experiments to determine if equilibrium conversions are reached. This allows to analyse whether a thermodynamic shift occurs during CO_2-PDH.

The combination of these experiments with the three promoter elements, complemented with the extensive XAS characterization of part 1, will allow for a comprehensive comparison of performance of Pt-based catalysts for CO_2-PDH.

5.2 Experimental Section

5.2.1 Catalyst preparation

A total of 4 catalysts (Pt/$MgAl_2O_4$, Pt:Ga/$MgAl_2O_4$, Pt:In/$MgAl_2O_4$ and Pt:Sn/$MgAl_2O_4$) are compared in this study. For details on the preparation of the support $MgAl_2O_4$, as well as Pt/$MgAl_2O_4$, Pt:In/$MgAl_2O_4$ and Pt:Sn/$MgAl_2O_4$, the reader is redirected to part 1 of this work.

The Pt:Ga/$MgAl_2O_4$ (3 wt% Pt, 1 wt% Ga) catalyst was prepared by incipient wetness impregnation, similar to the Pt:Sn and Pt:In catalysts, with $Ga(NO_3)_3.xH_2O$ (Sigma-Aldrich, 99.99%) as precursor for Ga, while $H_2PtCl_6.xH_2O$ (>99.9%, Sigma-Aldrich) was used for Pt. An aqueous solution containing the adequate amounts of precursor in absolute ethanol was prepared for impregnation. The sample was subsequently dried at 393 K for 2 h and calcined in air at 903 K for 4.5 h, yielding the “As prepared” sample. The catalysts shall henceforth be named as Pt, Pt:Ga, Pt:In and Pt:Sn.

5.2.2 Catalyst characterization

Pt, Pt:In and Pt:Sn catalysts have been characterized extensively in part 1 by BET, ICP, SEM EDX and XAS. BET and ICP for Pt:Ga are performed with the same setups and programs as presented in part 1 of this work and therefore the reader is redirected to part 1 for the setup details.

H_2-TPR and H_2-pulse chemisorption (Micromeritics Autochem II) were performed to determine the % dispersion and the reduction profile of the samples. Prior to the measurements, about 0.1 g of the dry sample was subjected to a pre-treatment step under 10% O_2/He at 873 K for 1 h, to remove any surface bound gases/impurities. Following this, the sample was cooled down to room temperature (RT), and the gas flow was switched to 60 Nml/min of 5% H_2/Ar for H_2-TPR. Once the flow was stable, a ramp rate of 10 K/min was employed to arrive at a target temperature of 873 K, which was kept for 30 min to ensure complete reduction. During this process, data acquisition was taking place by means of a thermal conductivity detector (TCD), calibrated for 5% H_2/Ar. After the 30 min dwell time, the gas flow was switched to Ar at 873 K and a cooling process to 313 K was started. As soon as that temperature was reached and stable, H_2-pulse chemisorption was started with a loop volume of 0.17484 cm^3/g. The latter was used to determine the volume of chemisorbed H_2 leading to the % dispersion.

Dark field scanning transmission electron microscopy **(STEM DF)** was applied before and after activity tests to collect images from which a particle size distribution (PSD)/average particle size could be obtained. The same setup was used as in part 1 (§ 4.2.2), for all samples in reduced and spent state.

CO-DRIFTS (Tensor 27, Bruker, with MCT detector) experiments were performed to confirm formation of alloys in Pt:Ga, Pt:In & Pt:Sn samples and to track the evolution of the alloy with increasing number of H_2/O_2 redox cycles. The redox cycles were not performed in the DRIFTS cell due to temperature limitations of the cell. Instead, each of the catalysts was first subjected to multiple redox cycles (1, 5 and 10) at 873 K in a fixed bed reactor. The samples were then collected and mixed with KBr (inert material for infrared measurements) in a material/KBr ratio of 1/20 in order to assure a good signal to noise ratio. This diluted sample was then transferred to the in situ DRIFTS cell, mounted in a Selector™ accessory, and evacuated.

In the DRIFTS cell, a hydrogen gas flow (20% H_2/Ar) was passed over the sample, while increasing the temperature to 723 K (temperature limit of the setup). That temperature was held for 30 min to regain/reform the Pt-M alloy, in case it might have segregated during exposure to atmosphere at RT during the mixing process with KBr. Cool down to 313 K was equally performed under 20% H_2/Ar. At 313 K, the gas flow was switched to He and a background spectrum measurement collected. Hereafter, the gas flow was switched to 1% CO/He for a period of 1 h. A set of 100 scans were collected following the CO exposure and the data averaged to get a good quality spectrum. All measurements were performed in absorbance mode between 400 cm^{-1} to 4000 cm^{-1} with a resolution of 2 cm^{-1}. Data analysis was performed with the OPUS 7.2 software (Bruker). These measurements are similar to prior work.[1]

5.2.3 Catalytic activity measurements:

All activity tests were performed at 873 K and 121.3 kPa in a quartz fixed bed reactor with an internal diameter of 7.5 mm housed inside an electric furnace. Prior to all activity measurements, the blank reactor was tested under reaction conditions to affirm the absence of any thermal and/or reactor/setup effects on the measured activity. The temperature of the catalyst bed and that of the external reactor wall at the bed position were measured with K-type thermocouples. Calibrated Bronckhorst mass flow controllers were used in order to maintain the inlet gas flows. A 100-200 µm sieved fraction range of the catalysts was diluted with α-Al_2O_3 for improved heat conductivity (ratio catalyst/inert = 1/5, 0.1 g catalyst), placed in the reactor and kept in position by means of a quartz wool plug.

The catalysts were heated under a 15 Nml/min H_2 and 90 Nml/min Ar gas mixture, at 10K/min to 873 K and held there for 30 min. After this step the gas flow is changed to 150 Nml/min Ar and held at 873 K for 1 h. This set of treatments was performed for all catalysts prior to the start of all the experiments.

Propane dehydrogenation (PDH): This reaction was performed at 873 K and 1.2 bars to check for intrinsic difference in activity between the 3 catalysts. A feed flow of C_3H_8:H_2:Ar = 4:4:7 was maintained with a total flow of 150 Nml/min (40 Nml/min C_3H_8 + 40 Nml/min H_2 + 70 Nml/min Ar = 150 Nml/min). The reaction was performed for 1.5 h after which the flow was switched to Ar. Subsequently the catalyst is exposed to a 100 Nml/min flow of 10% O_2/Ar for 10 mins to burn off all the carbon formed during the PDH reaction. This catalyst is then exposed to the H_2/Ar gas mix (15 Nml/min + 90 Nml/min) for 5 min to regenerate the alloy. The exposure to O_2 and H_2 gases constitutes 1 redox step (5 min O_2 + 5 min H_2). The final H_2/Ar step before performing the activity test for PDH is performed for 10 min while the O_2 step subsequent to a PDH reaction is for 10 min to confirm the burning off of all the carbon present in the sample, while the rest of the steps are 5 min each. The PDH was performed for the reduced sample, and subsequent to 5, 10 and 15 H_2/O_2 redox cycles.

CO_2-assisted PDH (CO_2-PDH): two different schemes of experiments were performed for all bimetallic catalysts which are designated as 'ratio' and 'redox' experiments. For the monometallic Pt catalyst, only the ratio experiments were performed.

Ratio experiments involved feeding the reactor a fixed total gas flow containing a mixture of CO_2, C_3H_8 and Ar of 150 Nml/min, with the flow of C_3H_8 fixed at 40 Nml/min. The CO_2 flow rate for these ratio experiments were 0, 5, 10 and 20 Nml/min (ratio CO_2:C_3H_8 = 0, 0.125:1, 0.25:1 and 0.5:1, respectively).

Redox experiments involved testing for CO_2-PDH over a period of 20 min, after subjecting the catalyst samples to 1, 3, 5, 7, 10, 15 and 20 (H_2/O_2) redox cycles. The inlet gas flows employed for CO_2-PDH were 40 Nml/min C_3H_8, 5 Nml/min CO_2 and 145 N/ml/min Ar (total flow rate = 150 Nml/min, ratio CO_2:C_3H_8= 0.125:1). 1 H_2/O_2 redox cycle involved exposing the sample first to a mixture of 15 Nml/min H_2 in 90 Nml/min Ar (H_2 step) for 5 min, followed by 100 Nml/min flow of 10% O_2/Ar (O_2 step of redox cycle). The final step is always the H_2-reduction step for 10 min, so that the active phase of the catalyst for reaction can be obtained. Subsequent to every CO_2-PDH activity step, including the ones for ratio studies, the O_2 step is employed for 10 min to burn off the carbon that has formed during the reaction.

RWGS experiments: RWGS was performed at three different ratios of H_2:CO_2 (1:1, 2:1 and 3:1). The flow rate of CO_2 was kept constant at 10 Nml/min, while the H_2 flow was varied from 10 Nml/min to 30 Nml/min. Ar was added in the feed to reach a total flow rate of 150 Nml/min.

Analysis of outlet gas flows from the reactor was undertaken through the combined use of a Gas Chromatograph (GC - Thermo Scientific equipped with two TCDs and one FID) and mass spectrometer (MS - Omnistar Pfeiffer). MS signals were recorded for all major fragments. For adequate quantification of reactants and products, the MS was focussed to different amu signals. 29 amu for C_3H_8, 41 amu for C_3H_6, 44 amu for CO_2, 28 amu for CO, 16 amu for CH_4, 18 amu for H_2O, 32 amu for O_2 and 40 amu for Ar. Measurement of these fractions entails a number of overlapping signals which need to be separated for the individual fractions by means of a calibration flow at RT. In view of this C_3H_8, CO_2, CH_4 and O_2 were flown in a mix with Ar at 3 different partial pressures to generate the required calibration curves. The calibration of propylene (C_3H_6) was done by means of data from the GC, by applying them to the MS data, which then led to accurate mass balance closures (<5% error).

Quantification of the GC chromatogram was done by means of Ar (detected by TCD), which was the internal standard for these experiments. The CH_4 signals on the TCD were quantified using the Ar signal and subsequently this value for CH_4 was applied to the FID channel in order to quantify the signals for C_2, C_3H_8 and C_3H_6. To ensure operation in the kinetic regime, the external mass transfer limitations were assessed using the criteria of Carberry[18] and Weisz-Prater,[19] while heat transport limitations were checked against the criteria of Mears.[20]

The conversion of propane, selectivity to propylene, propane consumption rate and STYs for propane and propylene has been calculated as per the equations described in chapter 2, § 2.5.

The Weight Hour Space Velocity (WHSV) employed for the experiments was 47.1 h^{-1}, which is much higher than the values typically used in PDH studies (eg: 4.7 h^{-1} by Ali et al.[21] and 0.64h^{-1} by Huan et al.[22]), as the objective of this work is to assess the deactivation profile for each promoter.

5.3 Results & Discussion

5.3.1 Catalyst Characterization – ICP, BET, H_2-TPR, H_2-Pulse Chemisorption and CO-DRIFTS.

5.3.1.1 ICP and BET

The values for the support $MgAl_2O_4$ and the catalysts Pt:In and Pt:Sn have been reported in § 4.3.1 of part 1 (chapter 4). The specific surface area, porosity and average pore diameter for Pt:Ga (Table 5.1) turn out lower than those obtained for the $MgAl_2O_4$ support.

Table 5.1: *Chemical composition, BET and porosity results for the Pt:Ga catalyst.*

Catalyst	Metal Loading (wt%)				BET (m^2/g_{cat})	Pore volume (cm^3/g_{cat})	Average pore diameter (nm)
	Mg	**Al**	**Pt**	**Ga**			
Pt:Ga	13.8	36.8	2.84	1.12	101.2	0.18	68.6

5.3.1.2 H_2-TPR and H_2-Pulse chemisorption

The H_2-TPR profiles showed one main peak for the monometallic sample and two major peaks for all three bimetallic samples, with a high temperature shoulder (Appendix D, Figure D2 a, b, c and d, Table D2).

Table 5.2: *Details for the H_2-TPR and H_2-pulse chemisorption. Plots of respective TCD signals in Appendix D, Figure D2 a, b, c & d.*

Sample	H_2-TPR			H_2-Pulse chemisorption		
	H_2-consumed (cm^3/g)	Theoretical consumption (cm^3/g)	Degree of reduction (%)	H_2-Volume consumed (cm^3/g)	dispersion (%)	Active particle diameter (nm)
Pt	5.11	6.9	74.0	0.92	57.6	1.9
Pt:Ga	6.57	11.9	55.1	0.55	34.0	3.3
Pt:In	11.0	20.4	53.7	0.45	26.3	3.6
Pt:Sn	9.02	18.2	49.5	0.21	11.5	8.2

The pulse chemisorption data are not consistent with the results obtained through XAS (part 1), in that the NP size obtained from pulse chemisorption is much higher (NP size from XAS = ~0.8-2 nm). This is due to the formation of Pt-M alloy, which reduces the amount of H_2 that can chemisorb when compared to monometallic Pt. As the promoters do not chemisorb H_2 as much as Pt, their incorporation into the Pt lattice makes them occupy sites, which would otherwise adsorb H_2. Still, the trend among the promoters is quite evident as it pertains to the amount of H_2 chemisorbed and it follows the order Ga > In > Sn.

5.3.1.3 STEM-DF

STEM images were collected for the 3 bimetallic samples after each different treatment step: 1. After reduction at 873 K (§ 5.3.1.2) and 2. After CO_2-PDH reaction for redox experiments (20 H_2/O_2 redox). This was performed in order to gauge how much the sample had sintered during the reaction process. The images are shown in Figure D3. The PSD reveals that no major changes in particle size occurred, but as explained in part 1, it is quite difficult to distinguish between the Sn, In, SnO_2, In_2O_3 and Ga from Pt, Pt:In and Pt:Sn. As a general conclusion, the extent of sintering isn't major, i.e. most NPs are smaller than 2 nm.

5.3.1.4 CO-DRIFTS

The obtained infrared absorption spectra (Figure 5.1) are interpreted based on literature on Pt/Al_2O_3,[23] Pt-Sn/Al_2O_3,[24] $Pt{:}In/Al_2O_3$,[25] and $Pt{:}Sn/MgAl_2O_4$,[26] catalysts. The $Pt/MgAl_2O_4$ spectrum shows similarities with the theoretical spectrum from literature: a small peak at 2117 cm^{-1}, a large peak at 2063 cm^{-1} with a shoulder at 2083 cm^{-1}, and a broad low peak around 1805 cm^{-1} are present. Based on the aforementioned literature, peak at 2117 cm^{-1} can be related to $Pt^{\delta+}$ or defect Pt sites. The latter possibility is more likely when complete reduction of Pt species is assumed. The peak at 2063 cm^{-1} can be assigned to linearly adsorbed CO onto Pt particles that do not possess extended crystal faces.[24] The shoulder at 2083 cm^{-1} relates to linearly adsorbed CO on well-defined crystal faces of Pt. The 1805 cm^{-1} peak can be assigned to CO adsorbed onto Pt in a bridged manner.

When comparing different numbers of redox cycles on the Pt:Ga, Pt:In and Pt:Sn samples (Figure 5.1), all in a reduced state, a shift in peak III is observed: from 2068 cm^{-1} (1 redox) to 2056 cm^{-1} (10 redox) for Pt:Ga, 2060 (1 redox) to 2062 cm^{-1} (5 redox), then to 2057 cm^{-1} for Pt:In, and 2062 (1 redox) to 2053 cm^{-1} (10 redox). This shift could be electronically or geometrically induced. An electronic effect is dependent on the CO surface coverage.[24] Since the samples were all exposed to CO for 1 hour, high CO surface coverages are assumed. Under these circumstances, a shift towards lower wavenumbers as observed could indicate an increased electron donation from Ga, In or Sn towards Pt. On the other hand, more redox cycles could induce larger particle sizes. An increase in particle size would lead to a shift in the opposite direction compared to the electronic effect at high CO coverage. From the particle size distributions derived from STEM images (Appendix D, Figure D3, a1 to c2), it can be concluded that the *average* metal particle size does not change substantially with increased redoxing, and that the *dominant* particle size also does not change. Hence, the shift pertains not to a geometric effect, but rather to electronic effects for Pt:Ga and Pt:Sn, which also confirms increased promoter content in the Pt-M alloy.

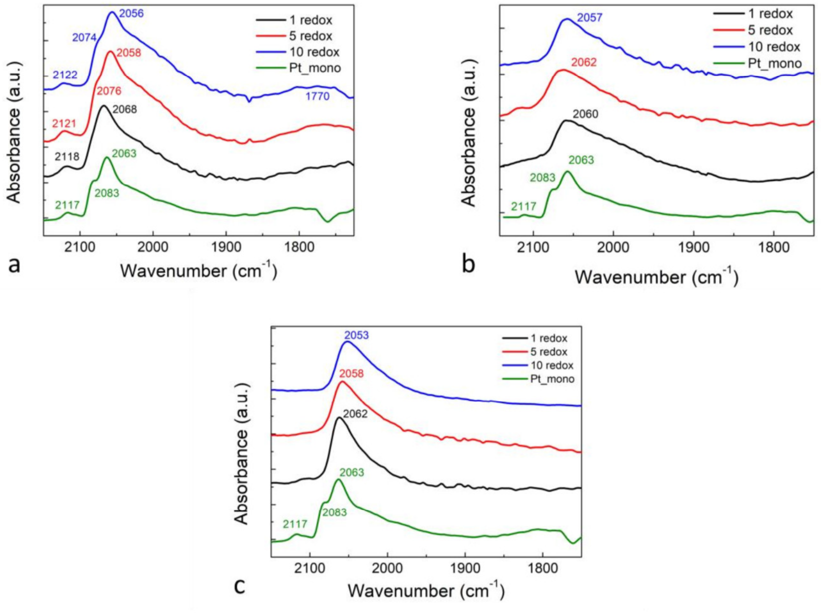

Figure 5.1 : *CO-DRIFTS on **a:** Pt:Ga **b:** Pt:In & **c:** Pt:Sn. CO-DRIFTS was measured subsequent to 1, 5, and 10 H_2/O_2 redox cycles, culminating with a reduction step.*

For Pt:In, there is initially a shift to higher wavenumbers when moving from 1 redox to 5 redox state, followed by a shift to lower wavenumbers when moving from 5 to 10 redox states. This result for Pt:In is consistent with the observations from XAS (part 1 - during the isothermal H_2/O_2 redox cycles). The initial shift to the left indicates an increase in the average nanoparticle (NP) size, while the later shift implies an increase of In the Pt-In alloy. However, it is known from XAS that the average In composition in the Pt-In alloy does not change drastically. This would imply that the observation when moving from 5 redox state to 10 redox state (shift to lower wavenumber), is probably due to an In rich surface as was found from XAS. Pt:Ga and Pt:Sn have these shifts to lower wavenumbers, primarily due to increase in composition of the promoter element throughout the alloy rather than just at the surface. These points are being mentioned here so that care is undertaken when interpreting CO-DRIFTS results in future research as the results can be misinterpreted.

5.3.2 Catalytic activity measurements

Since detailed characterization has been performed for the catalysts, activity tests for CO_2-PDH, with variable feed ratio and after multiple redox cycling can be investigated to come to a better understanding of the phenomena occurring. Comparison with a propane feed without CO_2 will aid in this perception.

5.3.2.1 Propane dehydrogenation reaction (PDH) Activity

PDH was performed for the Pt:Ga, Pt:In and Pt:Sn catalysts for the reduced, 5 redox, 10 redox and 15 redox states (details in § 5.2.3). All activity results for PDH are shown in Figure 5.2. This set of experiments is performed as a background basis for the activity of the 3 catalysts. It is quite clear that their overall performance ranks as Pt:Sn > Pt:Ga > Pt:In. Increasing H_2/O_2 redox cycles led to a rapid loss in activity for the Pt:In catalysts. This is explained through part 1 of this work, where it was determined that the Pt:In catalysts sinter with increasing redox cycles and this is the cause for the loss in activity.

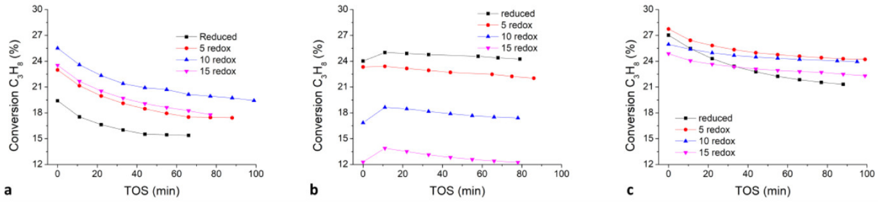

Figure 5.2: *Activity plots during PDH (conversion plots) for* ***a:*** *Pt:Ga,* ***b:*** *Pt:In and* ***c:*** *Pt:Sn. Flows for PDH: C_3H_8 = 40 Nml/min, H_2 = 40 Nml/min, Ar = 70 Nml/min. Total flow = 150 Nml/min. Catalyst amount = 0.1 g. T = 873 K. P = 1.2 bar. For selectivity and yield refer to Appendix D, Figure D4.*

Both Pt:Ga and Pt:Sn show relatively similar behaviour, i.e. an increase in activity with redox cycles and a subsequent loss in activity beyond a level of redox cycle treatments. This is occurs due to a change in the promoter composition in the Pt-M alloy as was shown for the Pt:Sn sample in part 1 and for a Pt:Ga system in[1]. All selectivities towards propylene are shown in

Appendix D, Figure D4, and they were all above 94%. But in general, it can be stated that the inherent activity difference between the 3 catalysts isn’t major.

5.3.2.2 Effect of CO_2 addition

For all catalysts, the CO_2:C_3H_8 ratio of 0.125:1 gives better activity than without CO_2 (Figure 5.3, Appendix D, Figure D5). Since the alloy is expected to remain stable in the absence of CO_2, it can be concluded that Pt:Sn (Figure 5.3d) is a better catalyst for PDH than Pt:Ga and Pt:In, as the latter two exhibit very low conversion of propane without any CO_2 flow. Even for the monometallic Pt catalyst (Figure 5.3a), the addition of CO_2 in small amounts (0.125:1) helps to increase the conversion from 2% to about 3.8%. This is probably due to CO_2 controlling the carbon formation on the Pt NP through the reverse Boudouard reaction. The same observation can be made for Pt:Ga where the conversion improved upon addition of a small amount of CO_2, in line with the findings from prior research.[10]

5.3.2.3 Effect of feed ratio (CO_2:C_3H_8)

Looking at the results for the feed ratio study (Figure 5.3 and Appendix D, Figure D5), the performance of Sn as a promoter for this reaction is obviously the best, followed by In and then Ga. Monometallic Pt catalyst gave the worst performance of all. The selectivity towards propylene obtained was >96% for all catalysts (Appendix D, Figure D6).

A low ratio of CO_2:C_3H_8 (0.125:1) gives high performance in terms of total conversion of propane and propylene yields for all catalysts (Appendix D, Figure D5 a-d1). It was shown in part 1 of this work that the Pt-Sn alloy is very stable in presence of both H_2 and CO_2, while the Pt-In alloy also did not segregate. However, the amount of NP surface atoms participating in the reaction was found to change with the CO_2:H_2 ratio that was employed and Pt:In was a much more dynamic system than Pt:Sn. With increasing feed ratio, the performance declines, especially for CO_2:C_3H_8 = 0.5:1. After 450 sec with the latter CO_2:C_3H_8 ratio, Pt:In and Pt:Ga show a similar overall conversion as the monometallic Pt catalyst. This indicates that both alloys most likely have segregated so that they are now showing activity as if they were monometallic Pt. Both In and Ga promoter elements have higher potential to get oxidised by CO_2 than Sn, based on thermodynamic calculations (Appendix D, Figure D1), the XAS results from part 1 and for Pt:Ga from literature.[1] Only Pt:Sn can withstand the higher CO_2 amount in the feed and keep up a significant propane conversion.

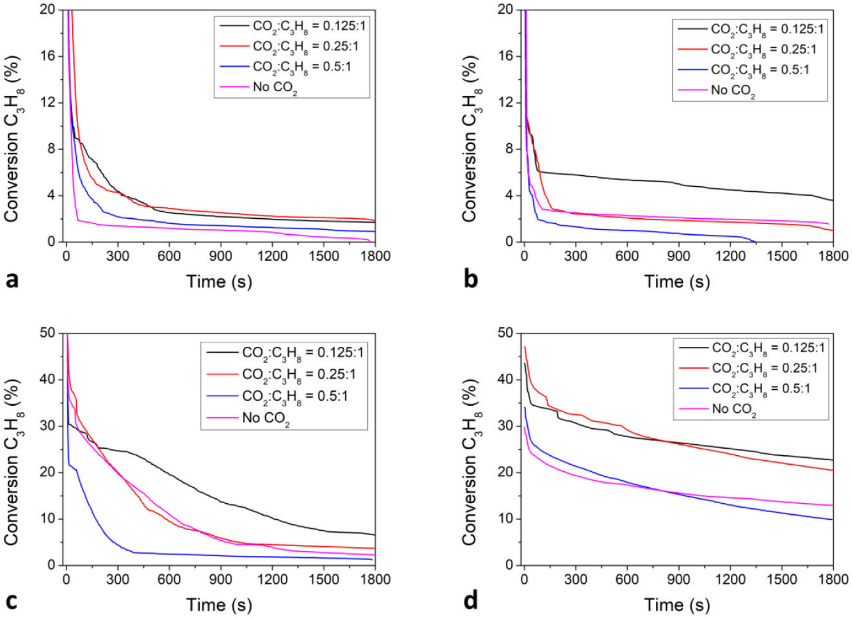

Figure 5.3: *C_3H_8 conversion plots with different feed ratios for* ***a:*** *Pt/$MgAl_2O_4$,* ***b:*** *Pt:Ga* ***c:*** *Pt:In and* ***d:*** *Pt:Sn. Flow rates: C_3H_8 = 40 Nml/min, CO_2 = 5, 10, 20 or 0 Nml/min depending on ratio, Ar = 105, 100, 90 or 110 Nml/min depending on ratio, Total flow = 150 Nml/min. Mass of catalyst = 0.1 g. For more detailed plots and space time yield plots, please refer to Appendix D, Figure D5.*

Deactivation occurs for all samples and all feed ratios, an abrupt initial decline followed by a more gradual decrease, but to a different degree. Compared to the bimetallic counterparts, Pt shows a much faster initial deactivation, regardless of the CO_2:C_3H_8 feed ratio employed, before stabilizing at very low conversion values of about 3%. In presence of CO_2, Pt will suffer from competition for adsorption sites between CO_2 and C_3H_8, decreasing its conversion, but also RWGS between CO_2 and H_2 will occur (Eq. 1.10), as well as carbon removal via equation 1.11, both favoring propane conversion. Nevertheless, carbon formation most definitely remains a major issue on monometallic Pt, as confirmed through quantification of the amount of carbon formed during the reaction (Figure 5.4).

On the bimetallic catalysts, after alloy formation, less Pt sites are available since part of the surface now consists of promoter element. The initially superior performance for Pt:In and Pt:Sn is due to the removal of product H_2 through RWGS, which leads to a shift in equilibrium towards products. Confirmation of RWGS taking place is obtained from monitoring the H_2O

(m/z = 18) and CO_2 (m/z = 44) signals (Appendix D, Figure D5 a-d 3 and 4). However, as deactivation takes place, the conversion of CO_2 will also change, based on the amount of H_2 in the system (Appendix D, Figure D5 a-d3). Therefore, with time the partial pressure of CO_2 with respect to H_2 will increase, which will subsequently lead to oxidation of the promoter and thereby loss of activity. So, CO_2 has an additional effect on the alloys, as it can oxidize and segregate the promoter from the alloy, giving even more rise to site blocking. Still, deactivation is less severe in all of the bimetallic catalysts than for Pt. Pt:Sn deactivates much slower when compared to Pt:Ga and Pt:In, indicating that this alloy is more stable under these experimental conditions. The MES experiments from part 1, showed that the Pt:Sn sample wasn't as susceptible to gas environment changes as the Pt:In sample, which leads to the conclusion that the Pt-Sn alloy remained stable during CO_2-PDH.

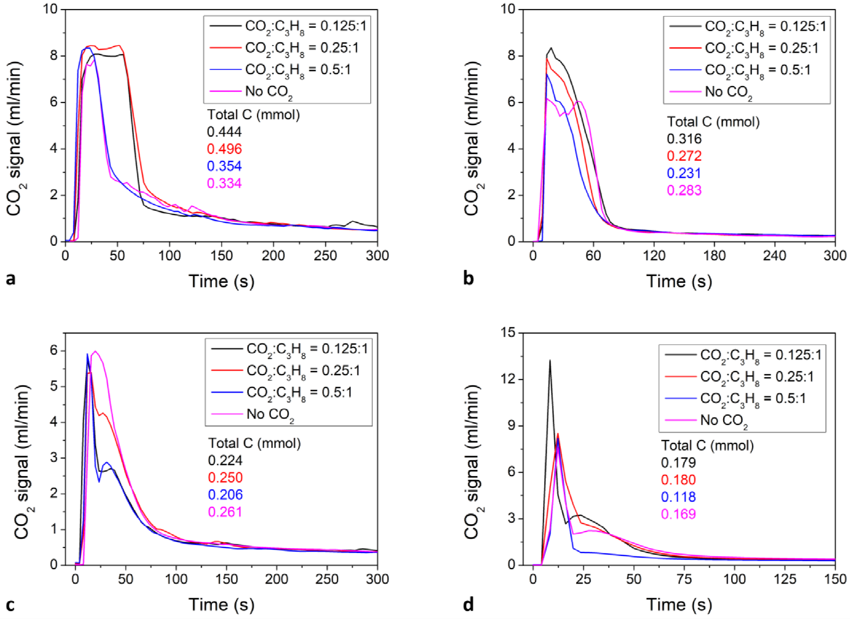

Figure 5.4: *m/z = 44 signal for the ratio studies of CO_2-PDH for* ***a:*** *Pt/$MgAl_2O_4$,* ***b:*** *Pt:Ga,* ***c:*** *Pt:In and* ***d:*** *Pt:Sn, during O_2 flow after each reaction step to quantify outlet CO_2 and thereby the carbon formed during reaction (integrated values show total CO_2 in mmol). For information on flow rates, please refer to experimental § 5.2.3.*

Despite its much higher activity, Pt:Sn has a lower amount of carbon formed when compared to Pt:In and Pt:Ga, leading to less deactivation (Figure 5.4). The extent of carbon formation orders as: Pt > Pt:Ga > Pt:In > Pt:Sn. Nevertheless, even for Pt:Sn deactivation proceeds faster when increasing CO_2 in the feed, especially for a CO_2:C_3H_8 feed ratio of 0.5:1 (Table 5.3). The difference between Pt:In and Pt:Ga, compared to Pt:Sn, can likely be attributed to loss of the alloy due to promoter oxidation by CO_2. This loss of alloy will lead to higher carbon formation, similar as for Pt.

Table 5.3: *Details of conversions at specific times for the ratio experiments over Pt:Sn.*

Ratio (CO_2:H_2)	Time 1 (s)	Conversion at time 1 – X1 (%)	Time 2 (s)	Conversion at Time 2 – X2 (%)
0.125:1	668	27.4	2094	21.7
0.25:1	690	27.9	1840	20.3
0.5:1	583	18.1	1730	10.2
0	690	16.8	1914	12.8

5.3.2.4 Effect of pre-treatment with H_2/O_2 redox cycles

In CO_2-assisted PDH, multiple redox cycles as activation pre-treatment mostly have a negative impact on initial activity for all bimetallic catalysts (Figure 5.5 and Appendix D, Figure D7). The only positive effect of redox cycling is seen for Pt:Sn, going from 1 to 3 redox cycles, but beyond this number, the initial activity goes down as well. Based on the XAS analysis for redox cycled catalysts, the changes induced by cycling, i.e. the higher promoter content in the Pt-M alloy for Pt:Ga and Pt:Sn, leads also for CO_2-PDH to differences in initial activity (Figures 5.5a and c). The activity increase for Pt:Sn from 1 to 3 redox cycles could then mean that the promoter content in the alloy after 1 redox cycle was not yet optimal for CO_2-assisted PDH and it improved after applying 2 more redox cycles.

The changing alloy composition with number of redox cycles has a twofold impact on the (initial) activity. First, a higher promoter content in the alloy entails that the alloy surface contains more promoter atoms next to Pt. Since Pt provides the sites for dehydrogenation, the activity will drop as the promoter content rises. The other reason, particularly for CO_2-assisted PDH, is that with more promoter in the sample, there is a higher risk of blocking the active Pt sites upon segregation of the promoter from the alloy by CO_2 oxidation. Specifically for Pt:Ga, this results in a severe drop in activity after only a short time on stream for all numbers of redox cycles, with little difference.

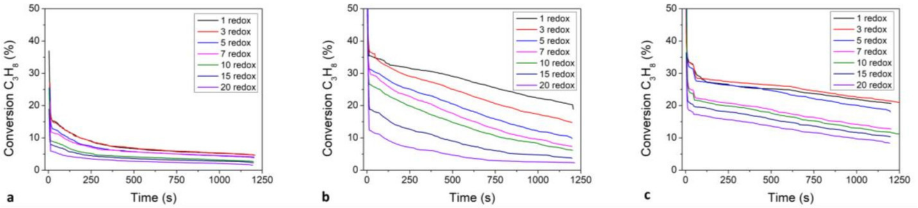

Figure 5.5: *C_3H_8 conversion plots after different number of redox cycling for **a:** Pt:Ga, **b:** Pt:In and **c:** Pt:Sn. Flow rates: C_3H_8 = 40 Nml/min, CO_2 = 5 Nml/min, Ar = 105 Nml/min, Total flow = 150 Nml/min. Mass of catalyst = 0.1 g. For more detailed plots and space time yield plots please refer to Appendix D, Figure D7.*

For Pt:In, increased redox cycling doesn't lead to an increase in promoter content in the alloy, but only to slight sintering of the catalyst. Nevertheless, multiple cycles of Pt:In lead to quite pronounced differences in initial activity with an obvious decline for higher numbers (Figure 5.5b).

With increasing time on stream, the general deactivation trends for these bimetallic samples are quite similar: a first steep fall, followed a more steady decline. Several elements play a role in this deactivation behaviour: some sintering, alloy segregation by CO_2, alloy formation by product H_2, carbon formation by C_3H_8 decomposition, H_2 removal by RWGS with CO_2, carbon removal by CO_2. The resulting deactivation will be a balance/trade-off between all of these. After the initial drop in activity, the deactivation profile for Pt:Sn follows a less steep trend compared to Pt:Ga and Pt:In. The carbon content of the spent samples follows a similar order to that obtained from the feed ratio study: Pt:Ga > Pt:In > Pt:Sn (Appendix D, Figure D7, a-c5). The low carbon amount on Pt:Sn, despite its much higher conversion, indirectly shows that Sn most likely doesn't segregate from Pt-Sn alloy. The alloy state on Pt:Sn forms less carbon, so that it maintains a better balance between all factors, ensuring higher activity.

5.3.2.5 RWGS

In order to assess the role of CO_2 in CO_2-PDH, as enabler of RWGS, a set of regular RWGS reactions was performed for the Pt:Ga, Pt:In and Pt:Sn catalysts (Appendix D, Figure D8). The experiments were run for 3 different ratios of H_2:CO_2 (3:1, 2:1 and 1:1) and compared with the equilibrium CO_2 conversions (59.8 %, 51.6 % and 37.8 % - Appendix D, Figure D9 a and b). All 3 catalysts readily reach equilibrium conversions for RWGS, which means that they most likely also reach equilibrium conversions during CO_2-PDH, as the flow of CO_2 during CO_2-PDH (5 Nml/min) is half of the value used for the RWGS experiments (10 Nml/min).

5.4 Discussion

To understand the process improvement in presence of CO_2, Figure 5.3, an analysis is made with the activity results for the better catalyst, i.e. Pt:Sn (Figure 5.3d). With the conditions employed here for CO_2-PDH, the equilibrium conversion of C_3H_8 is 64%, while the CO_2 conversion in RWGS likely reaches equilibrium values (Appendix D, Figure D9a, Figure D5 a-d3).

The inlet flow rate of C_3H_8 is 40 Nml/min and the conversion for the 0.125:1 CO_2:C_3H_8 ratio changed from 27.4 to 21.7 % from 660 s to 2000 s, while in absence of CO_2 it changed from 16.8% at 600 s to 12.8 % at 1900 s. As the selectivity towards C_3H_6 was > 98%, it can be safely assumed that H_2 is the only second product formed (via PDH reaction). This leads to a total amount of H_2 in the product stream of 10.96 Nml/min initially and 8.68 Nml/min finally. Similarly for the "no CO_2" experiment, it would be 6.72 Nml/min and 5.12 Nml/min, respectively (initial and final). The difference in H_2 flow rate with and without CO_2 for the initial state is then 10.96 – 6.72 = 4.24 Nml/min and 8.68 - 5.12 = 3.56 Nml/min for the final state.

The inlet CO_2 flow rate for 0.125:1 ratio was 5 Nml/min, therefore the initial and final H_2:CO_2 ratios would be 2.2:1 & 1.7:1, leading to respective equilibrium RWGS CO_2 conversions of 53% and 47% (Appendix D, Figure D9a). In practice, this amounts to a consumption of 2.65 and 2.35 Nml/min CO_2 and an equal amount of H_2, which determines the thermodynamic shift for PDH (2.65 and 2.35 Nml/min). The actual flow rate differences with and without CO_2 for the initial and final state, 4.24 Nml/min and 3.56 Nml/min, are however higher than those of CO_2 that can be consumed through RWGS, about ~10% higher than the RWGS equilibrium conversion, or ~0.5 Nml/min of CO_2 extra converted during the reaction. This proves that there is CO_2 consumption through a different process, most likely the reverse Boudouard reaction.

Carbon formation/accumulation is a known mechanism of deactivation in Pt-based PDH catalysts. The addition of CO_2 to the feed can alleviate this through the reverse Boudouard reaction. The occurrence of RWGS close to equilibrium conversion ensures that the partial pressure of CO_2 in the system remains lower than the one of H_2. This dominance of H_2 explains why the Pt-Sn alloy phase is retained.

Therefore the main components responsible for the improvement in activity during CO_2-PDH for the Pt:Sn catalyst, are the thermodynamic shift through RWGS and the reverse Boudouard reactions. If the Pt-Sn alloy had a lower composition of Sn, then the factor of alloy segregation would have to be considered as well, since only a small amount of Sn has to get oxidized to lose the alloy. Based on the change in white line (WL) intensity of the XANES spectra, part 1, changing ratios between H_2:CO_2 lead to a variation of NP engagement, which would cause the alloy to segregate in case of low Sn content. For Pt:Ga and Pt:In, it is safe to suggest that performing experiments close to equilibrium conversion at these conditions, would be the best strategy, as then the ratio between H_2:CO_2 would be higher and help to prevent deactivation by alloy segregation

H_2/O_2 redox cycle experiments before CO_2-PDH also affect the performance as they change the promoter content in the alloy. In Pt:Sn, a slight improvement occurs when pre-treating not once but 3 times with redox cycles, but higher cycle numbers lead to lower activity. The latter implies that for the Pt:Sn catalyst, 3 redox cycles yield the optimal composition of the alloy, giving balance on the one hand between alloy formation and segregation by H_2 and CO_2 respectfully, and on the other hand between carbon formation rom C_3H_8 and removal by CO_2. For Pt:Ga and Pt:In, the redox cycles before CO_2-PDH only have a negative effect on activity. This implies that the Ga and In do get oxidized and segregated from their respective alloy, leading to site coverage and concomitant activity decrease.

5.5 Conclusions

Pt, Pt:Ga, Pt:In and Pt:Sn catalysts were tested for CO_2-PDH and RWGS. All of them show improved performance upon addition of CO_2 to the feed. In general, the Pt:Sn catalyst performs much better than the Pt:In and Pt:Ga catalysts for CO_2-PDH and all bimetallic catalysts reached equilibrium conversion levels for RWGS.

A low ratio of CO_2:C_3H_8 (0.125:1) led to better propane conversion and performance for CO_2-PDH than higher ratios for all catalysts. The main reason for the improvement was the suppression of carbon formation through the reverse Boudouard reaction. Higher CO_2 ratios led to a negative effect on activity, which was most likely due to competitive adsorption of CO_2 and C_3H_8 and increased alloy segregation leading to blocking of active sites.

Increasing numbers of H_2/O_2 redox cycles led to higher promoter content in the alloy for Pt:Ga and Pt:Sn. Except for Pt:Sn going from 1 to 3 redox cycles, this increase mostly induced a drop in overall C_3H_8 conversion during CO_2-PDH. This was due to two reasons: 1. because the higher promoter content makes the alloy more prone to promoter extraction from the alloy by the presence of CO_2, leading to Pt site blocking and 2. The loss of number of available Pt sites on the surface of the NP with increased promoter content, which inherently leads to lower activity as the Pt sites are responsible for dehydrogenation. For Pt:In, redox cycling induces lower performance due to NP sintering and to loss of In from the alloy. For regular PDH, Pt:Sn and Pt:Ga maintained their activity with increased redox cycles while, Pt:In showed a drop in activity, which provides further confirmation that the Pt:In catalyst lost activity due to NP sintering, and not due to increased promoter content. The PDH activity data showed that the activity of the 3 catalysts were relatively similar and hence, the differences observed during CO_2-PDH has to be due to the presence of CO_2, and not due to inherent activity differences between the 3 catalysts.

Another positive effect of promoter addition were the lower amounts of overall carbon formation during CO_2-PDH, when compared to the monometallic Pt/$MgAl_2O_4$ catalyst. The total amount of carbon formed depended on the promoter used and ordered as Pt:Ga > Pt:In > Pt:Sn. Increased redox cycling was mostly beneficial for the amount of carbon formed, as were higher CO_2:C_3H_8 ratios.

Hence, the dehydrogenation of propane over Pt can benefit from promoter addition to the catalyst and CO_2 addition to the propane feed. The best promoter for Pt to employ in CO_2-PDH among the three promoters explored (Ga, In and Sn) is Sn, because the Pt:Sn alloy remains stable in the presence of CO_2. Moreover, the Pt:Sn sample forms less carbon than Pt:In and Pt:Ga. The main factors to control in order to actually gain process improvement with a CO_2 co-feed (CO_2-PDH), are the alloy composition, i.e. the promoter content, and the feed ratio CO_2:C_3H_8, which depends on the bimetallic catalyst being employed.

Appendix D : Data

Ellingham diagrams, H_2-TPR plots, DF STEM images, Activity test results for redox studies for PDH, ratio and redox studies for CO_2-PDH, example chromatogram from GC, RWGS experimental data, CO_2 and H_2 equilibrium conversion values during RWGS.

5.6 References

1. Srinath, N. V. *et al.* In Situ XAS/SAXS Study of Al2O3-Coated PtGa Catalysts for Propane Dehydrogenation. *ACS Catal.* 11320–11335 (2021). doi:10.1021/acscatal.1c03146

2. Srinath, N. V. *et al.* In situ XAS/SAXS study of Al2O3 coated PtGa/MgAl2O4 catalysts for alkane dehydrogenation. in *2019 AIChE Annual meeting (19-AIChE)* (American Institute of Chemical Engineers (AIChE), 2019).

3. Navrotsky, A., Mazeina, L. & Majzlan, J. Size-Driven Structural and Thermodynamic Complexity in Iron Oxides. *Science (80-.).* **319**, 1635 LP – 1638 (2008).

4. Navrotsky, A., Ma, C., Lilova, K. & Birkner, N. Nanophase Transition Metal Oxides Show Large Thermodynamically Driven Shifts in Oxidation-Reduction Equilibria. *Science (80-.).* **330**, 199 LP – 201 (2010).

5. Bariås, O. A., Holmen, A. & Blekkan, E. A. Propane Dehydrogenation over Supported Pt and Pt–Sn Catalysts: Catalyst Preparation, Characterization, and Activity Measurements. *J. Catal.* **158**, 1–12 (1996).

6. Iglesias-juez, A. *et al.* A combined in situ time-resolved UV – Vis , Raman and high-energy resolution X-ray absorption spectroscopy study on the deactivation behavior of Pt and Pt A Sn propane dehydrogenation catalysts under industrial reaction conditions. *J. Catal.* **276**, 268–279 (2010).

7. Redekop, E. A. *et al.* Delivering a Modifying Element to Metal Nanoparticles via Support: Pt–Ga Alloying during the Reduction of Pt/Mg(Al,Ga)Ox Catalysts and Its Effects on Propane Dehydrogenation. *ACS Catal.* **4**, 1812–1824 (2014).

8. Sun, P., Siddiqi, G., Vining, W. C., Chi, M. & Bell, A. T. Novel Pt/Mg(In)(Al)O catalysts for ethane and propane dehydrogenation. *J. Catal.* **282**, 165–174 (2011).

9. Sun, P., Siddiqi, G., Chi, M. & Bell, A. T. Synthesis and characterization of a new catalyst Pt/Mg(Ga)(Al)O for alkane dehydrogenation. *J. Catal.* **274**, 192–199 (2010).

10. Veeraraghavan Srinath, N. *et al.* Behaviour of Platinum-Tin during CO2-assisted propane dehydrogenation: Insights from quick X-ray absorption spectroscopy. *J. Catal.* (2021). doi:https://doi.org/10.1016/j.jcat.2021.08.041

11. Michorczyk, P. & Ogonowski, J. Dehydrogenation of propane to propene over gallium oxide in the presence of CO2. *Appl. Catal. A Gen.* **251**, 425–433 (2003).

12. Michorczyk, P., Kuśtrowski, P., Kolak, A. & Zimowska, M. Ordered mesoporous Ga2O3 and Ga2O3–Al2O3 prepared by nanocasting as effective catalysts for propane dehydrogenation in the presence of CO2. *Catal. Commun.* **35**, 95–100 (2013).

13. Zheng, B., Hua, W., Yue, Y. & Gao, Z. Dehydrogenation of propane to propene over different polymorphs of gallium oxide. *J. Catal.* **232**, 143–151 (2005).

14. Ren, Y., Wang, J., Hua, W., Yue, Y. & Gao, Z. Ga2O3/HZSM-48 for dehydrogenation of propane: Effect of acidity and pore geometry of support. *J. Ind. Eng. Chem.* **18**, 731–736 (2012).

15. Chen, M. *et al.* Applied Catalysis A : General Study in support effect of In2O3 / MO x (M = Al , Si , Zr) catalysts for dehydrogenation of propane in the presence of CO 2. *"Applied Catal. A, Gen.* **407**, 20–28 (2011).

16. Xu, B., Zheng, B., Hua, W., Yue, Y. & Gao, Z. Support effect in dehydrogenation of propane in the presence of CO2 over supported gallium oxide catalysts. *J. Catal.* **239**, 470–477 (2006).

17. Chen, M. *et al.* Dehydrogenation of propane over In2O3–Al2O3 mixed oxide in the presence of carbon dioxide. *J. Catal.* **272**, 101–108 (2010).

18. Olsbye, U., Moen, O., Slagtern, Å. & Dahl, I. M. An investigation of the coking properties of fixed and fluid bed reactors during methane-to-synthesis gas reactions. *Appl. Catal. A Gen.* **228**, 289–303 (2002).

19. Froment, G. F. & Bischoff, K. B. *Chemical Reactor Analysis and Design*. (Wiley, 1990).

20. Mears, D. E. Diagnostic criteria for heat transport limitations in fixed bed reactors. *J. Catal.* **20**, 127–131 (1971).

21. Motagamwala, A. H., Almallahi, R., Wortman, J., Igenegbai, V. O. & Linic, S. Stable and selective catalysts for propane dehydrogenation operating at thermodynamic limit. *Science (80-.).* **373**, 217 LP – 222 (2021).

22. Yan, H. *et al.* Tandem In2O3-Pt/Al2O3 catalyst for coupling of propane dehydrogenation to selective H2 combustion. *Science (80-.).* **371**, 1257 LP – 1260 (2021).

23. O'Brien, C. P., Jenness, G. R., Dong, H., Vlachos, D. G. & Lee, I. C. Deactivation of Pt/Al2O3 during propane oxidation at low temperatures: Kinetic regimes and platinum oxide formation. *J. Catal.* **337**, 122–132 (2016).

24. Balakrishnan, K. & Schwank, J. FTIR study of bimetallic Pt-Sn/Al2O3 catalysts. *J. Catal.* **138**, 491–499 (1992).

25. Marchesini, F. A., Gutierrez, L. B., Querini, C. A. & Miró, E. E. Pt,In and Pd,In catalysts for the hydrogenation of nitrates and nitrites in water. FTIR characterization and reaction studies. *Chem. Eng. J.* **159**, 203–211 (2010).

26. Zhu, H. *et al.* Sn surface-enriched Pt-Sn bimetallic nanoparticles as a selective and stable catalyst for propane dehydrogenation. *J. Catal.* **320**, 52–62 (2014).

Chapter 6

In situ XAS/SAXS study of Al_2O_3 coated Pt:Ga catalysts for propane dehydrogenation

Abstract

The effect of applying an alumina (Al_2O_3) coating by atomic layer deposition, with a thickness of about ~1 nm, on two Pt:Ga catalysts (Pt:Ga/$MgAl_2O_4$ & Pt/MgGaAlO) was explored for the propane dehydrogenation reaction (PDH). The combined application of Small Angle X-ray Scattering (SAXS) and X-ray Absorption Spectroscopy (XAS) was employed on the samples to gain insight into the effect of this coating on catalyst stability. The coating restricted the mobility of surface metal nanoparticles (NPs), thereby preventing sintering of the catalyst. On the Pt:Ga/$MgAl_2O_4$ catalyst, the presence of the coating hindered the alloy formation between Pt and Ga, while it did not negatively affect the formation of an alloy for the Pt/MgGaAlO catalyst as the Ga is delivered from the support. The SAXS and XAS findings were reflected in the PDH activity tests. The alumina coated Pt:Ga/$MgAl_2O_4$ performed worse than its uncoated counterpart due to the limited alloy formation in the presence of the coating. The coated and uncoated Pt/MgGaAlO catalysts were tested for PDH after 1, 5, and 10 H_2/O_2 redox cycles to see the effect of the coating on activity & stability. In general, the coating reduces the total amount of carbon formation, and the rate of deactivation for the coated sample is slower than for the uncoated counterpart. A higher thickness of coating led to reduced activity due to increased blockage of active sites but at the same time drastically reduced total carbon formation at similar conversions. The coated and uncoated Pt/MgGaAlO samples were then subjected to another 30 redox cycles (40 in total) and subsequently examined with STEM DF. Through particle size distribution of STEM images it is determined that the coating reduced the extent of sintering of the sample. The direct correlation between increased coating thickness and lower extent of sintering of the surface metal nanoparticles was confirmed.

The results of this chapter are published as:

N.V. Srinath, A. Longo, H. Poelman, R.K. Ramachandran, J.-Y. Feng, J. Dendooven, M.-F. Reyniers, V. V Galvita, In Situ XAS/SAXS Study of Al2O3-Coated PtGa Catalysts for Propane Dehydrogenation, ACS Catal. (2021) 11320–11335. doi:10.1021/acscatal.1c03146.

6.1 Introduction

In this chapter, two of the approaches mentioned in chapter 1 are combined for enhanced PDH performance: promoter addition and alumina coating. A Pt-based catalyst is used with a Ga promoter. Two types of supports are chosen: $MgAl_2O_4$ (spinel) and MgGaAlO (hydrotalcite type support). The difference in the investigated samples lies in the means by which the promoter Ga is delivered to Pt, and subsequently the extent of Pt-Ga alloy formation. Prior research showed numerous advantages of applying Ga as a promoter and provided a detailed analysis of the mechanism by which alloy formation takes place.[1,2] In addition, these catalysts are coated with alumina by means of a chemical vapour deposition technique, Atomic Layer Deposition (ALD), a powerful tool for controlled modification of solid surfaces.[3] Prior to the coating treatment, the catalysts are reduced under a H_2-atmosphere to form the Pt-Ga bimetallic alloy NPs. Subsequent to the coating, a thermal treatment step under Ar atmosphere is employed to crack the coating layer and make the catalyst (active sites) accessible to the gas feed. It has been demonstrated that such a thermal treatment can increase the overcoating layer porosity[4] by crack formation.[5,6] The porous and inert coating keeps the alloy NPs as small isolated units, while providing gas access through canals, thereby preventing surface nanoparticle sintering and loss of active sites from carbon blockage.[7,8]

Several questions need to be answered about the workability of such a coating for bimetallic NPs. First is to confirm whether the active sites remain accessible to the reactants. Second would be to determine if there are any interactions between the catalyst and the coating layer. A third aspect is if and how the activity towards propane dehydrogenation (PDH) is altered. Fourth is to see the effect of applying such a coating on the alloy formation, and finally to verify if this coating indeed prevents coke formation and sintering of the catalyst.

To examine the behaviour of coated versus uncoated Pt:Ga, a combined study of in situ Small Angle X-ray Scattering (SAXS) and X-ray Absorption Spectroscopy (XAS) was undertaken. XAS can yield detailed structural and electronic information of the local environment of both elements Pt and Ga under the alumina coating, even for nanosized particles (<2 nm). SAXS can track changes to the particle sizes during in situ treatments. However, when the nanoparticles are supported, SAXS can no longer monitor their variation in size as the support material itself will also scatter in the small angle region.[9] This hurdle can be circumvented by means of anomalous SAXS (ASAXS), making use of tuned X-ray energies.[10,11] The changes of the atomic form factors with energy around elemental absorption edges can be used to extract pure elemental scattering signals from SAXS curves, recorded at different x-ray energies on the same sample.[11] In situ experiments were performed during temperature programmed reduction and oxidation to assess the effect on alloy and coating, as well as during 5 H_2/O_2 redox cycles to mimic sintering.

Following extensive H_2/O_2 redox cycling, PDH experiments were performed, in order to follow the deactivation trends. In combination with the in situ SAXS/XAS and STEM detailed catalyst characterization, this work brings insight into the benefits/drawbacks of applying a coating on the surface of a supported bimetallic catalyst (Pt:Ga) for the propane dehydrogenation reaction. This will help to identify ideal process parameters, pertaining to the reaction and application of coating, to improve efficiency.

6.2 Experimental section

6.2.1 Catalyst Preparation

Two different supports are chosen: a $MgAl_2O_4$ spinel type support and a hydrotalcite-like support, where Ga is incorporated in view of pure alloy phase formation with Pt.[2,12] Pt is then wet-impregnated onto these supports, either alone on the hydrotalcite or co-impregnated with Ga on the spinel.

6.2.1.1 Support preparation

Support $MgAl_2O_4$ (spinel) was prepared by co-precipitation from an aqueous solution of $Mg(NO_3)_2.6H_2O$ (99%, Sigma-Aldrich) and $Al(NO_3)_3.9H_2O$ (98.5%, Sigma-Aldrich) (molar ratio Mg/Al = 1/2). NH_4OH (ACS reagent, 28.0-30% NH_3 basis) was used as the precipitating agent in order to maintain a pH of 10 at 333 K. The precipitate was then dried at 393 K for 12 h and calcined in air at 893 K for 6 h.[13]

Ga incorporated MgGaAlO hydrotalcite (HTL) material with 1 wt% Ga was prepared according to the procedure described in the work by Sun et al.[12], by co-precipitation from an aqueous solution of Mg (Sigma-Aldrich, 98-102), Al (Sigma-Aldrich, 98.5) and Ga (Sigma-Aldrich, 99.99%) nitrates mixed with a 1.1 mol/L NaOH (Sigma-Aldrich, >98%) solution. This solution was then aged for 24 h at room temperature subsequent to which it was dried at 393 K overnight in air and calcined in air at 973 K (2 K/min heating rate) for 10 h to obtain the final support.

6.2.1.2 Catalyst Preparation

3 wt% Pt was deposited onto both supports, $MgAl_2O_4$ and MgGaAlO, by incipient wetness impregnation. For the $MgAl_2O_4$ support, Ga was equally deposited by impregnation with a loading chosen such that the atomic ratio between Pt and Ga is 3:1. The latter ratio is required for Pt-based catalysts as the dehydrogenation typically takes place on the Pt sites, while the promoter helps the desorption of the propylene from the surface.[14–17] The samples were dried for 2 h at 393 K and calcined in air at 893 K for 5 h, yielding the as prepared, uncoated samples: Pt:Ga/$MgAl_2O_4$ (wet impregnated sample, WI) and Pt/MgGaAlO (incorporated sample, INC).

A Pt:Ga/$MgAl_2O_4$ catalyst with higher Ga loading was prepared to facilitate detection of the effect of multiple H_2/O_2 redox cycles on the alloy composition by means of Diffuse Reflectance Infrared Fourier Transform Spectroscopy with CO (CO-DRIFTS) experiments. This catalyst was prepared with a Pt loading of 2.2 wt% and 0.8 wt% of Ga, yielding an atomic ratio between Pt:Ga ~1:1. The preparation procedure of this catalyst is exactly the same as for the WI sample above.

In addition, a monometallic Pt/$MgAl_2O_4$ catalyst was prepared to serve as a reference.

6.2.1.3 Alumina coating procedure

The alumina coating procedure has been described in chapter 2, § 2.1.3. The reader is redirected to that section and Figure 2.1 for complete details.

6.2.2 Catalyst Characterization

N_2-adsorption at 77 K using a five point BET method (Tristar micromeritics) was performed after degassing the sample at 393 K for 3 h to determine the Brunauer-Emmett-Teller (BET) surface area of the as prepared samples. Dark field scanning transmission electron microscopy (STEM DF) was used to obtain images to perform a particle size distribution analysis. The samples were deposited onto a lacey carbon film on a copper grid support. The instrument used for these measurements was a JEOL JEM-2200FS, Cs-corrected microscope operated at 200 kV, which was equipped with a Schottky-type field-emission gun (FEG) and EDX JEOL JED-2300D. SEM-EDX measurements were obtained in a SEM JEOL JSM 5400 equipped with an

INCA x-act extension (Oxford instruments) to check the composition of the supports ($MgAl_2O_4$, MgGaAlO). Inductively coupled plasma optical emission spectroscopy (ICP-OES, iCAP 7400 instrument from Thermo Scientific) was employed to determine the bulk compositions of the catalysts. Mineralization of the samples was achieved by peroxide fusion.

CO-DRIFTS (Tensor 27, Bruker, with MCT detector) experiments were performed to determine the formation of a Pt-Ga alloy and the evolution of the alloy with increasing number of H_2/O_2 redox cycles. A Pt:Ga/$MgAl_2O_4$ catalyst was first subjected to multiple H_2/O_2 redox cycles (1, 5 and 10) at 873 K, subsequent to which the sample was collected and mixed with KBr (inert material for infrared measurements) in a material/KBr ratio of 1/20 in order to assure good signal to noise. This sample was then transferred to the in situ DRIFTS cell, which is mounted in a Selector™ accessory, and evacuated. The redox cycles were not performed in the DRIFTS cell due to temperature limitations of the cell. A flow of 20% H_2/He was then passed over the sample while increasing the temperature to 723 K, and held there for 30 mins in order to regain the alloy that may have decomposed from exposure to atmosphere during the process of mixing with KBr. This was followed by a cooldown to room temperature under 20% H_2/He, after which the gas flow was switched to He. A background spectrum measurement was taken after which 1% CO/He was sent onto the sample for 1 h. A set of 100 scans was recorded subsequent to the CO exposure and the data were averaged to get a good quality spectrum. All measurements were performed in absorbance mode between 400 cm^{-1} to 4000 cm^{-1} with a resolution of 2 cm^{-1}. Data analysis was performed with the OPUS 7.2 software (Bruker). A monometallic Pt/$MgAl_2O_4$ catalyst was also tested in order to see the difference from the bimetallic system.

Synchrotron-based in situ XAS and SAXS experiments were conducted at the DUBBLE beamline[18] of the ESRF synchrotron (6 GeV, current 160-200 mA, Grenoble, France). Measurements were performed in transmission at the Pt L_{III}-edge (11564 eV) and in parallel ASAXS measurements were collected by means of a Pilatus detector. The sample to detector distance was maintained at 2.180 meters to cover a desired Q-range from 1.8 to 4.1 nm^{-1}. Simultaneous collection of the XAS data was undertaken by means of a photodiode placed at the position of the SAXS detector beam stopper. The latter type of detector typically limits XAS acquisition to the XANES energy range, due to the low signal to noise ratio of diode detectors, with lower data quality at high energies (EXAFS region).[18,19]

A small amount of as prepared material (~4 mg), was inserted into a 1.5 mm quartz capillary reactor and fixed with quartz wool plugs. The capillary reactor was mounted in a frame connected to gas feed lines through Swagelok fittings. The DUBBLE gas rig system was employed to regulate gas flows through the capillary.[20] Optics alignment and energy referencing was performed using a Pt foil.

A set of in situ experiments were conducted on each catalyst, as represented in Figure 6.1. The experiments were performed as follows in the same sequence: **1.** H_2-TPR with 5% H_2/He (5 ml/min) at 10 K/min up to 923 K to reduce the catalyst and induce subsequent alloy formation, **2.** CO_2-TPO with flow rate of 2ml/min CO_2 diluted with 3 ml/min He, at 10 K/min up to 923 K, **3.** Following another H_2-TPR, isothermal O_2/H_2 redox cycles at 923 K with periodic switching of the gas between O_2 and H_2 ending with a H_2-reduction step, with each gas flow lasting 20 mins and a total of 5 cycles measured (300 min) to follow the effect on the alloy and to see particle growth/sintering. The gas flows used for the oxidation step were 2 ml/min of 20% O_2/He mixed with 3ml/min He, while for the reduction step it was 5 ml/min of 5% H_2/He. An external heat gun was employed to achieve the desired temperatures and the total flow was maintained at 5ml/min. XANES measurements were performed during all in situ measurements, while at room temperature, upon conclusion of each treatment, EXAFS measurements were collected.

To monitor the changes occurring to the Pt-Ga alloy under variable conditions i.e., during H_2-TPR (to form the Pt-Ga alloy), CO_2-TPO (to segregate the alloy), H_2/O_2 redox cycling (5 cycles to sinter the nanoparticles (NPs)), XAS is a necessity as the targeted PtGa particles are small (<2 nm). The reasoning behind using CO_2 as a gas for oxidation (CO_2-TPO) is that it will oxidise only the Ga present in the sample and not the Pt.[21,22]

In addition to the aforementioned experiments, XAS measurements were performed at room temperature for reference samples Pt foil and PtO_2, in order to obtain a standard measurement for fingerprint comparison of the data and for the determination of the amplitude reduction factor (S_0^2) for the EXAFS fitting. S_0^2 was determined by fitting the first PtO_2 shell (Pt-O) with a standard Pt-O path of a PtO_2 crystal.

The VIPER program[14] was employed for fitting of the EXAFS data and the error bars were estimated with k^1/k^3 weighted fittings. The Fourier transformation of the data was performed with a Kaiser-Bessel window with a dk of 1.5. Once the value of S_0^2 was determined (0.88), it was fixed in the program to proceed with the fitting. The fitting at the Pt-edge was in general done in the range from 1.2-3.4 Å. Either 1 or 2 shells were used for fitting of the data.

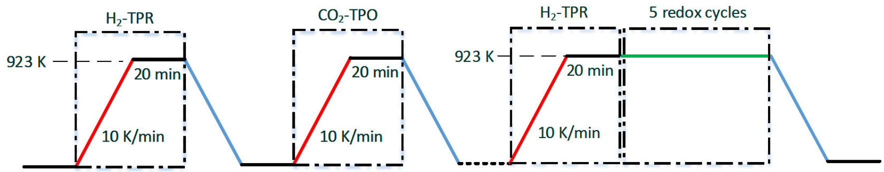

Figure 6.1: *Experimental scheme employed for in situ XAS/ASAXS measurements*

At room temperature, a 2D SAXS image was collected at 11400 and 11560 eV for 60 s to get good quality data. Then, by means of a trigger program, SAXS measurements (60 s) were taken throughout the temperature programmed experiments at 11400 eV at the start of each in situ XANES measurement to help track the changes occurring to the sample.

All in situ measurements were performed for the following samples: **1.** MgGaAlO, **2.** $MgAl_2O_4$, **3.** Pt/MgGaAlO, **4.** Pt/$MgAl_2O_4$, **5.** Pt:Ga/$MgAl_2O_4$, **6.** 10Al_2O_3/Pt/MgGaAlO, **7.** 10Al_2O_3/Pt:Ga/$MgAl_2O_4$. SAXS measurements were also taken for an empty capillary and a standard silver behenate sample for calibration of the patterns. The collected SAXS data were treated by performing an azimuthal integration of the images by means of the software fit2d. Application of this routine leads to conversion of each of these images into a scattering profile $i_{scat}(q)$, whereby the intensity (measured in counts) is reported as a module of the scattering vector.

$$q = \frac{4\pi}{\lambda}\sin(\theta)$$

The 1d profile of the silver behenate standard sample with known scattering pattern was processed in order to find the exact sample to detector distance and the integration parameters(X and Y pixel coordinate of direct beam, tilt rotation, angle of tilt). Once these were set, the azimuthal integration of all samples was carried forth.

As Pt:Ga forms only a small part of the sample in terms of the loadings (~3 wt%), most of the SAXS signal contribution is expected to come from the supports, $MgAl_2O_4$ and MgGaAlO. These signals hence form a background basis, which along with the empty cell contribution was subtracted from the patterns of the supported samples, to get the true 1D scattering profiles for Pt:Ga. In order to get average nanoparticle size values, the patterns were modelled with SASfit, under the fitting assumption of spherical particles and monodispersed sample. The complete details of the procedure employed for analysis are accessible in chapter 2, § 2.4.2.

6.2.3 Catalytic activity measurements

Catalytic activity and stability tests were performed at 873 K and 121.3 kPa in a quartz fixed reactor with an internal diameter of 7.5 mm that was housed inside an electric furnace. A blank reactor was also tested under reaction conditions so as to obtain the catalytic activity by subtraction of thermal and/or reactor effects that might take place. It was found however that there was no activity with a blank reactor. K-type thermocouples were used to measure the temperature of the catalyst bed and the temperature of the external wall of the reactor at the position of the catalyst bed. Gas flows were maintained by means of calibrated Bronckhorst mass flow controllers. The catalyst samples were sieved into size fractions with average size of ~150 µm. This was diluted with α-Al_2O_3 for improved heat conductivity (ratio catalyst/inert = 1/5), which was then placed in the reactor and held in position by means of a quartz wool plug.

Each coated catalyst tested was first heated under an inert atmosphere (Ar) up to 873 K, after which it was maintained under inert at that temperature for 1 h. Purpose of this treatment was to create cracks in the Al_2O_3 overlayer, so that the active sites are accessible for reaction. Subsequent to the inert treatment, all coated catalysts were reduced in situ under a 110ml/min flow of 10% H_2/Ar for 30 min, reoxidized for 10 min under a flow of 100 ml/min of 10% O_2/Ar and again reduced under a flow of 110 ml/min of 10% H_2/Ar for 20 min. This single redox sequence is conducted in situ prior to performance testing to ensure their proper initial state. Similarly, the uncoated samples were subjected to the same sequence of reduction, reoxidation and reduction.

Propane dehydrogenation reaction (PDH) was performed at 873 K and 1.2 bar pressure to check the activity. A feed flow of C_3H_8:H_2:Ar at a ratio of 1:1:3 was maintained with total flow rate at 200 ml/min. The reaction was performed for 2 h after which the flow was switched to Ar. This catalyst was then exposed for 10 min to a flow of 100 ml/min of 10% O_2/Ar, in order to burn off the carbon formed on the surface. Hereafter, a flow of 110 ml/min of 10% H_2/Ar was fed for 20 min to re-establish the reduced, active state. This cycle of exposure to oxidative and reductive atmospheres constitutes 1 redox cycle, simulating a regeneration step as is typically taking place in industrial processes. Each catalyst was exposed to multiple redox cycles as a means to hasten deactivation by sintering and to assess the effect of such cycles upon performance. PDH reaction for time steps of 1 h were performed after 1, 5, & 10 redox cycles to track the deactivation with number of redox steps. Subsequent to the PDH activity tests, the Ga-incorporated catalysts are then subjected to an extra 30 H_2/O_2 redox cycles at 923 K in order to cause sintering of the catalysts. These catalysts are then recovered for measurement by STEM-DF for a particle size distribution.

The gases at the outlet of the reactor were analyzed using a Trace 1300, Thermo Scientific equipped with two TCDs and 1 FID Gas Chromatograph (GC). Ar was used as the internal standard as it does not participate in the reaction. The detected CH_4 is quantified, which then forms the basis for quantification of the peaks of C_2, C_3H_8 and C_3H_6 recorded by the FID channel. A calibration gas mixture was used to determine the calibration factors for the different gases.

The carbon formed on the catalyst was also quantified to determine the amount deposited after a reaction step. Hereto, the outlet of the reactor was connected to a calibrated OmniStar Pfeiffer mass spectrometer (MS), in parallel to the GC. For PDH both analysis instruments were used, while for carbon quantification only the MS was employed. Amu signals of C_3H_8 at 29 amu, CO_2 at 44 amu, CO at 28 amu, CH_4 at 16 amu, C_3H_6 at 41 amu, C_2 at 27 and 28 amu and Ar at 40 amu were tracked. Overlapping signals in the MS were separated based on gas mixtures (C_3H_8, CO_2, O_2, H_2 and CH_4) with Ar, which were flown into the MS at 3 different partial pressures to create a calibration curve. With these and the GC data it was possible to attain <5% mass balance deviations upon analysis of the PDH reaction data. Carbon quantification was done based on the calibration curves of CO_2 and O_2.

All reactions were performed in the kinetic regime, i.e. negating any effects of mass and heat transfer limitations. This was done by evaluation of the criteria of Carberry number[24] and Weisz-Prater[25] for mass transfer (internal and external) limitations, and the criteria reported by Mears[26] for heat transfer limitations.

The conversion of propane, selectivity to propylene, and STYs for propane and propylene has been calculated as per the equations described in chapter 2, § 2.5.

6.3 Results and discussion

6.3.1 Catalyst characterization – BET, EDX and ICP

BET measurement results for the as prepared samples are depicted in Table 6.1, together with the EDX values. One observation is that the BET surface area and pore volume obtained for the coated samples are lower than those for the uncoated samples. This is expected as the layer is likely to block some pore openings during its application. Another noticeable aspect is that the average pore diameter is lower for the coated catalysts. This is explained by the work of J. Lu et al.[8] where they performed a similar alumina coating scheme for a Pd-based catalyst. New smaller pores are formed as a result of structural changes in the amorphous Al_2O_3 overlayer caused by dehydration,[27] the removal of carbon residues from the ALD process and dewetting of the Al_2O_3 overlayers at the surface of the Pt NPs.

Table 6.1: *BET results for the catalysts. Bulk compositions of the supports are derived from SEM-EDX, while for the uncoated catalysts, i.e. Pt/MgGaAlO and Pt:Ga/$MgAl_2O_4$, these follow from ICP-OES.*

Catalyst	**Metal Loading (wt%)**				**BET (m^2/g_{cat})**	**Pore volume (cm^3/g_{cat})**	**Average pore diameter (nm)**
	Mg	**Al**	**Pt**	**Ga**			
$MgAl_2O_4$	14.6±0.05	31.8±0.3			119.1	0.22	7.5
Pt:Ga/$MgAl_2O_4$	14.3	34.2	2.3	0.2	103.7	0.20	7.2
10Al_2O_3/Pt:Ga/$MgAl_2O_4$					96.4	0.15	6.1
40Al_2O_3/Pt:Ga/$MgAl_2O_4$					94.6	0.14	5.9
MgGaAlO	30.5±0.9	17.1±0.7		2.0±0.1	171.9	0.38	9.9
Pt/MgGaAlO	23.9	12.9	1.80	1.1	169.5	0.37	9.8
10Al_2O_3/Pt/MgGaAlO					138.4	0.33	9.5
40Al_2O_3/Pt/MgGaAlO					122.9	0.31	8.5

6.3.2 SAXS results

The normalized SAXS spectra for the doubly wet impregnated and the Ga-incorporated samples, both uncoated and coated, are shown in Figure 6.2 and Figure 6.3, respectively. The results presented here are based on ASAXS measurements at the Pt L_{III}-edge (11400 eV & 11560 eV), which means that the scattering profile is that of Pt NPs. By fitting the data with a model of monodisperse, spherical nanoparticles, the average Pt-related nanoparticle size on the surface of the support can be determined according to the procedure described in § 6.2.2.

Due to compromise undertaken for incorporating a parallel application of SAXS and XAS, it was not possible to explore a larger range of q values and therefore, monodisperse model was used for fitting the data. All fitted plots are shown in Appendix E (Figures E1 & E2).

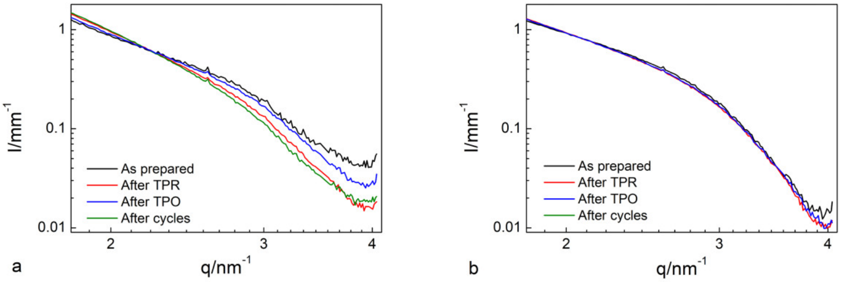

Figure 6.2: *Normalized SAXS data after each treatment for* ***a:*** *Pt:Ga/MgAl$_2$O$_4$ and* ***b:*** *10Al$_2$O$_3$/Pt:Ga/MgAl$_2$O$_4$. 5 redox cycles were applied for the "after cycles" profile. These SAXS measurements were collected at room temperature.*

Table 6.2: *Fitting results for Pt:Ga/MgAl$_2$O$_4$ and 10Al$_2$O$_3$/Pt:Ga/MgAl$_2$O$_4$, yielding the average particle* ***radius*** *with a 95% confidence interval.*

Treatment	Pt:Ga/MgAl$_2$O$_4$	10Al$_2$O$_3$/Pt:Ga/MgAl$_2$O$_4$
As Prepared	1.0 ± 0.1 nm	1.1 ± 0.1 nm
After TPR	1.3 ± 0.1 nm	1.2 ± 0.1 nm
After TPO	1.2 ± 0.1 nm	1.1 ± 0.1 nm
After 5 H$_2$/O$_2$ cycles	1.3 ± 0.1 nm	1.2 ± 0.1 nm

The change for the uncoated WI sample from as prepared to reduced state is from 2 to 2.6 nm (the values in the Tables 6.2 and 6.3 depict the **radius**). The SAXS analysis shows us that the Pt oxide is dispersed as 2 nm particles. Upon reduction, Ga enters into Pt to form the Pt-Ga alloy, along with Pt particles coming together, which can account for the increase in size to 2.6 nm. The coated sample has a larger initial size (2.2 nm) because there was a reduction prior to coating which could lead to some increase in the NP size. The increase to 2.4 nm after reduction is somewhat smaller than for the uncoated sample. After TPO, both uncoated and coated samples have slightly reduced in size (2.4 and 2.2 nm diameter). Assuming the NP is alloyed after the TPR step, the latter could point to Ga segregating from the Pt-Ga alloy during CO$_2$-TPO, which would indeed induce a slight reduction of the overall NP size of Pt upon the loss of Ga. The particle size slightly increases upon redox cycling.

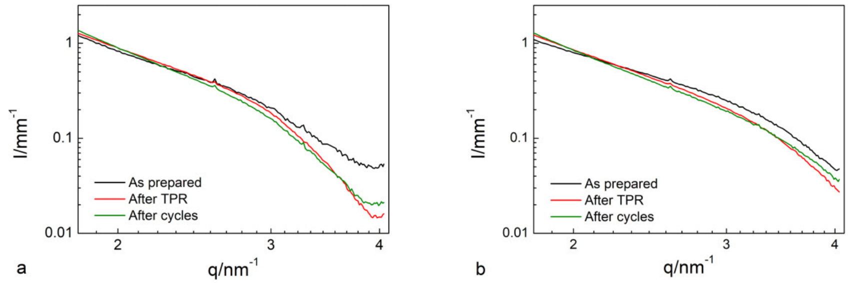

Figure 6.3: *Normalized SAXS data after each treatment for* ***a:*** *Pt/MgGaAlO and* ***b:*** *10Al_2O_3/Pt/MgGaAlO. 5 redox cycles were applied for the "after cycles" profile. These SAXS measurements were collected at room temperature.*

Table 6.3: *Fitting results for Pt/MgGaAlO and 10Al_2O_3/Pt/MgGaAlO, yielding the average particle* ***radius*** *with a 95% confidence interval.*

Treatment	Pt/MgGaAlO	10Al_2O_3/Pt/MgGaAlO
As Prepared	1.0 ± 0.1 nm	1.0 ± 0.1 nm
After TPR	1.2 ± 0.1 nm	1.1 ± 0.1 nm
After 5 H_2/O_2 cycles	1.2 ± 0.1 nm	1.1 ± 0.1 nm

The incorporated sample has small size particles in as prepared state, 2nm, corresponding to the wet-impregnated Pt oxide particles. Upon reduction, the alloy will form with Ga from within the support, leading to an increase in NP size to 2.4 nm for the uncoated, 2.2 nm for the coated sample. Redox cycling does not change these values.

A general observation from fitting of the SAXS data after cycling is that sintering of the samples did not take place. For the WI samples, the uncoated sample has a particle size varying between 2.0 nm to 2.6 nm (diameter), while for the coated it lies between 2.2 nm and 2.4 nm. For the Ga-incorporated samples, the uncoated sample has a particle size between 2.0 and 2.4 nm, while the coated sample varies between 2.0 and 2.2 nm. The range of variation for the coated samples is lower than for the uncoated, but as the values lie within the experimental error limits this cannot be used to state conclusively that the coating stabilizes the particle size.

6.3.3 CO-DRIFTS

A set of CO-DRIFTS experiments was performed on the Pt:Ga/$MgAl_2O_4$ catalyst with higher Ga loading to enhance possible changes in the composition of the Pt-Ga alloy with increasing redox cycles. The sample was calcined and reduced prior to the DRIFTS measurements, i.e. equivalent to 1 redox treatment. Figure 6.4 shows all the recorded spectra from CO-DRIFTS.

The peak position for the 1 redox state is located at 2068 cm^{-1}. Increasing redox cycles for the Pt:Ga sample lead to a shift in the position of the main peak to lower wavenumbers, which is an indicator of alloy formation between Pt and the promoter which in this case is Ga.[28–30] The shift increases with increasing number of redox cycles, which points to an increasing Ga content in the Pt-Ga alloy with more redox cycles which is ultimately the main takeaway from these experiments. This experiment also indicates that minimal sintering took place because, if there had been a significant change in the size of the nanoparticles, then the geometric effect would have come into play leading to the shift of the peak to higher wavenumbers.[28]

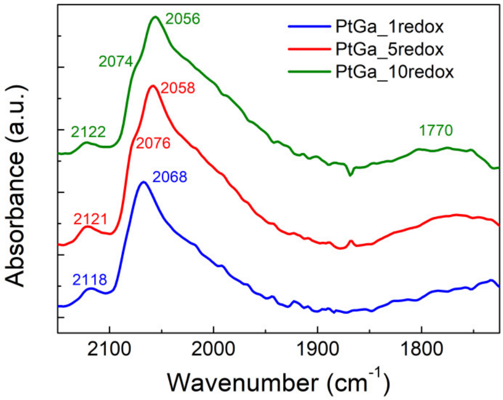

Figure 6.4: *FTIR spectra of CO adsorption on Pt:Ga/$MgAl_2O_4$. CO adsorption was measured subsequent to 1, 5, and 10 H_2/O_2 redox cycles, culminating with a reduction step.*

6.3.4 XANES Results

6.3.4.1 Pt:Ga/$MgAl_2O_4$ and $10Al_2O_3$/Pt:Ga/$MgAl_2O_4$

The XANES spectra of as prepared samples Pt:Ga/$MgAl_2O_4$ and $10Al_2O_3$/Pt:Ga/$MgAl_2O_4$ show a huge difference in white line intensity, see Figure 6.5. The starting WL intensity and position for the coated sample are both lower, indicating a less oxidised state for Pt.

During H_2-TPR, the catalysts underwent almost complete reduction (~ 97%) based on linear combination fitting (LCF) between the PtO_2 and Pt foil standards. At the end of the reduction, the white line (WL) position is at a higher eV energy (~1 eV higher, 11567.5 eV) than the Pt foil (11566.5 eV) for both samples, while the WL intensity remains slightly higher than for Pt foil, see Figure 6.5 and Figure E3 in Appendix E. This indicates that alloy formation is taking place between the Pt and Ga, for both samples.[31,32] Comparing the WL for the "as prepared" coated sample with the one after TPR, shows that despite the reduction before coating Pt was not alloyed at the start of the TPR, but rather in a partially oxidised state. Likely, the coating and/or annealing procedure oxidised the alloy and rearranged the oxides PtO_x and GaO_x on the support surface. So, applying a reduction treatment before the coating process appears to be at least partially ineffective and another reduction is required to form the alloy underneath the coating.

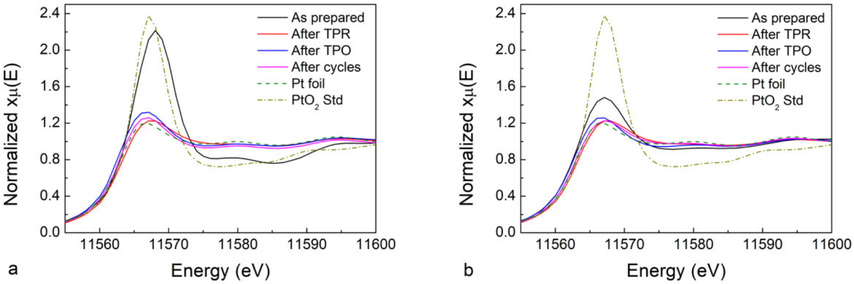

Figure 6.5: *RT XANES spectra before and subsequent to every treatment (H_2-TPR, CO_2-TPO, H_2/O_2 redox cycles finishing with a H_2-reduction step) for the Pt:Ga/$MgAl_2O_4$ samples (**a:** uncoated and **b:** coated)*

For both samples, the H_2-TPR was followed by cool down and a CO_2-TPO experiment from RT to 923 K. A partial increase in the WL intensity was observed as well as a shift in WL position (from 11567.5 eV to 11566.5 eV) towards the position for monometallic Pt after H_2-TPR (at 11566.5 eV), indicating loss of the Pt-Ga alloy. CO_2-TPO was also performed for the monometallic Pt/$MgAl_2O_4$ catalyst, where no changes in WL intensity (1.25 normalized absorption units) and position (11566.5 eV) were observed (Appendix E, Figure E3). Hence, CO_2 is not capable of oxidizing Pt directly and the WL increase for the two Pt:Ga catalysts has another cause. It should be noted that the absolute increase in WL intensity for the coated (1.22 to 1.25) and uncoated (1.22 to 1.32) samples is different (values from XAS at room temperature (RT)). Upon oxidation by CO_2, the WL of coated Pt:Ga reaches the same position and intensity as that of monometallic Pt, suggesting a mere return from alloyed to metallic state, due to segregation of Ga out of the alloy. For the uncoated sample, the WL rises higher than for Pt/$MgAl_2O_4$ (1.32 compared to 1.25), so it is plausible that not only Ga segregation occurs, but also a certain degree of oxidation. However, oxidation of Pt by CO_2 is not expected based on the response of monometallic Pt/$MgAl_2O_4$ to CO_2 (Appendix E, Figure E3). A similar observation was made in chapter 3 on Pt:Sn samples.[22,33] Therein, increases in WL intensity upon oxidation by CO_2 at the Pt L_{III}-edge for a bimetallic system involving Pt were strongly dependent on the nanoparticle size. In the current system however, SAXS data show that the difference in average nanoparticle size between coated and uncoated WI samples is minimal, hence size is not a cause for the difference in WL intensity after CO_2-TPO. Then, the partial oxidation of Pt must be related to the oxidation of Ga to Ga_2O_3 and these oxygen atoms are somehow shared with Pt. Since the WL increase for the coated sample is lower, this could mean that when the Ga segregates upon oxidation by CO_2 from the alloy, it cannot freely rearrange on the surface of Pt to share oxygen, as there is an alumina coating present blocking some sites.

Isothermal redox cycles with O_2/H_2 were performed at 923 K to mimic reaction/regeneration cycle steps. As expected, alternating alloy formation/segregation was taking place. The change of the WL intensity in each step of the redox cycling is shown in Appendix E, Figure E4, depicting the maxima reached at the end of each half-cycle. The extent of oxidation by O_2 for the uncoated sample decreases with increasing number of cycles, from 1.49 as WL intensity in the first O_2 half-cycle to 1.42, then 1.38 for the third half-cycle. This difference in extent of oxidation could be due to an increase in Ga composition in the sample with each cycle, as was indicated by the CO-DRIFTS experiments. The potential for Ga to oxidise is higher than for Pt, and therefore in the oxidation half-cycle Ga oxidises to Ga_2O_3 and gets extracted from the Pt-Ga alloy. There it could gradually cover the Pt sites and prevent its oxidation by O_2, leading to less regeneration of the Pt WL intensity with increasing redox cycles. A similar phenomenon is observed for the coated sample. The trend observed over the redox cycles could also be due to particle sintering, but as shown by SAXS, the nanoparticle size remains more or less similar, so this cause can be discarded.

6.3.4.2 Pt/MgGaAlO & 10Al_2O_3/Pt/MgGaAlO

In as prepared state, both incorporated samples have a Pt XANES spectrum that closely resembles that of their wet impregnated counterparts (Figure 6.6). Uncoated Pt/MgGaAlO contains highly oxidised Pt, while Pt appears more reduced in $10Al_2O_3$/Pt/MgGaAlO, but not alloyed.

H_2-TPR leads to a similar change as for the WI samples. However, the incorporated samples have lower final WL intensities than the WI samples, at about the same intensity as for the Pt foil (1.19), namely 1.18 (uncoated) and 1.19 (coated). The final position for these samples is at 11568 eV, 0.5 eV higher than for the WI samples. This indicates that there is deeper alloying and a larger fraction of Ga entering the Pt-Ga alloy compared to the WI counterparts, due to the promoter incorporation. During the reduction, Ga gets extracted from the support and migrates to the surface to form an alloy phase with the Pt nanoparticles.[2]

CO_2-TPO on the coated sample led to a WL intensity increase from 1.19 to 1.34, which indicates that the coating did not hinder the alloy segregation between Pt and Ga, giving rise to 'shared' oxidation of Pt for this sample. In fact, the WL intensity rises higher than for the coated WI sample (1.34 vs. 1.25 for the WI sample), pointing to a more oxidised state for Pt.

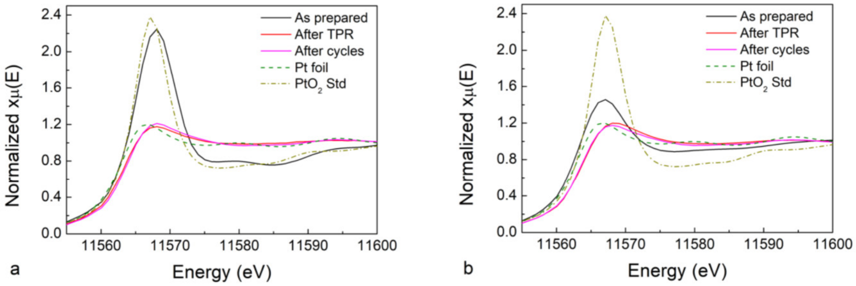

***Figure 6.6**: RT XANES spectra before and subsequent to every treatment (H_2-TPR, CO_2-TPO, H_2/O_2 redox cycles finishing with a H_2-reduction step) for the Pt/MgGaAlO samples (**a:** uncoated and **b:** coated)*

Similar to the wet impregnated samples, there is consistent alloy formation and segregation taking place during multiple O_2/H_2 redox cycles. The final state of Pt after 5 cycles lies close to the state after H_2-TPR for both samples (Appendix E, Figure E5). The incorporated samples show similar trends as the WI samples for consecutive redox cycles, i.e. a decreasing WL increase. Hence, the Ga fraction in the Pt-Ga alloy increases with the redox cycles, so that upon reoxidation larger Ga_2O_3 patches block more and more Pt sites.

6.3.5 EXAFS results

EXAFS fitting results for the Ga-incorporated samples are presented here in this work. The fitting of the data obtained for the WI samples was not straightforward as the S/N ratio was lower than for the incorporated samples (see Appendix E, Figure E7 for an example k-space signal).

EXAFS spectra were recorded before and after each high temperature treatment at room temperature. Fittings in general were performed for 1 or 2 shells depending on the spectra in the R-range of 1.2–3.4 Å. The crystal structures used for the fits were Pt-crystal (Fm3m, cubic, Pt-Pt = 2.81 Å), Pt:Ga 3:1 crystal (I4/mcm, tetragonal, Pt-Ga = 2.58 Å, Pt-Pt = 2.81 Å) and PtO_2 crystal (Pnnm, orthorhombic, Pt-O = 2.03 Å). All R-factors of the fits were within 0.06 and fitting results are shown in Table 6.4 and Figure 6.7.

Table 6.4: *EXAFS fitting results at the Pt L_{III}-edge for Pt/MgGaAlO and 10Al_2O_3/Pt/MgGaAlO catalysts for the as prepared and H_2/O_2 redox cycled (reduction as last) states.*

	Pt/MgGaAlO		**10Al_2O_3/Pt/MgGaAlO**	
	As Prepared	**After redox cycles**	**As Prepared**	**After redox cycles**
N_{Pt-O}	5.2 ± 1.1		2.1 ± 0.5	
R_{Pt-O}	2.01± 0.01		2.01 ± 0.01	
σ^2_{Pt-O} (10^{-3}*Å^2)	2.6± 0.1		2 ± 0.1	
N_{Pt-Ga}		1.6 ± 0.5		1.6 ± 0.5
R_{Pt-Ga}		2.62 ± 0.03		2.62 ± 0.02
σ^2_{Pt-Ga} (10^{-3}*Å^2)		6 ± 2		7 ± 2
N_{Pt-Pt}		7.4 ± 1.8	4.0 ± 0.6	7.3 ± 2.0
R_{Pt-Pt}		2.71± 0.02	2.70 ± 0.01	2.71 ± 0.02
σ^2_{Pt-Pt} (10^{-3}*Å^2)		12 ± 4	8 ± 1	14 ± 4
ΔE_0 (eV)	-4.6 ± 3.3	2.0 ± 4.8 eV	-4.9 ± 3.9	2.1± 3.5
R factor	0.06	0.04	0.06	0.04

The fitting of the “as prepared” uncoated sample was possible with a single Pt-O shell, while for the coated sample it was performed with both Pt-O and Pt-Pt shells. This is expected as the sample was reduced prior to coating with alumina, which is why there are Pt neighbours. The sample gets partially oxidised as has been mentioned before, due to which oxygen neighbours are observed.

Fitting results for “after H_2-TPR” state are not presented in this work as the data were not of sufficient quality for a reasonable fit (Appendix E, Figure E7). The fitting results for the state "after CO_2-TPO" is shown in Appendix E, Table E1 & Figure E8, for the coated incorporated sample. The coordination for the Pt-O shell is 2.03 with a distance of 1.91 Å. This distance is lower than what is typically expected for Pt-O (2.04 Å), which suggests that O is coming from the oxidised Ga. Since this O is shared, the bond distance is contracted due to the higher electronegativity of Pt over Ga.

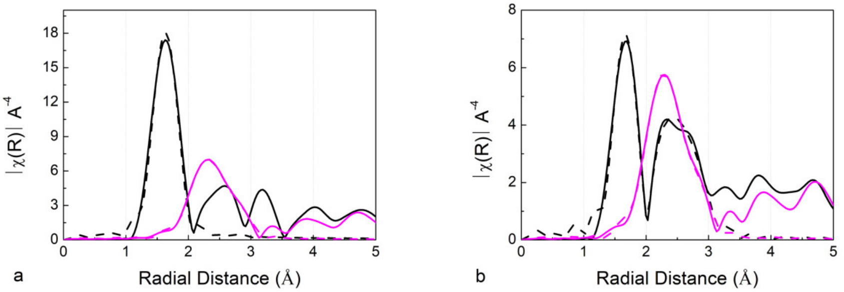

Figure 6.7: *Experimental k^3-weighted Fourier transformed EXAFS signals at RT at the Pt L_{III}-edge for* ***a:*** *Pt/MgGaAlO and* ***b:*** *$10Al_2O_3$/Pt/MgGaAlO. (—) As prepared and (—) after 5 O_2/H_2 redox cycles, with last H_2 exposure. The dashed lines depict the fits for each of the signals.*

After redox cycling, an alloy is formed between Pt and Ga as confirmed by the fitting results for the cycled state of the sample (Table 6.4). The similar values for the coordination numbers obtained for both the coated and uncoated samples, show that the alumina coating did not hinder the alloy formation between the Pt and Ga, which confirms the findings from the XANES results. The k-space signals (Appendix E, Figure E6) are very similar for both samples. The amount of Ga in the Pt-Ga alloy can be estimated by equation 6.1 based on the assumption that Ga is distributed uniformly throughout the alloy. The fraction of Ga in the alloy turns out to be 18% after redox cycles.

$$\text{Fraction of Ga in alloy} = N_{Pt\text{-}Ga}/(N_{Pt\text{-}Ga}+N_{Pt\text{-}Pt}) \qquad (6.1)$$

The nanoparticle size (after cycles) can be estimated from the sum of coordination numbers of Pt-Pt and Pt-Ga based on the assumption of a hemispherical nanoparticle shape.[34] The total N is $N_{Pt\text{-}Pt} + N_{Pt\text{-}Ga} = 1.60 + 7.30 = 8.90$, which leads to a cluster size of ~2.2 nm for both samples (coated and uncoated). This value matches the values obtained from SAXS (2.2 nm, Table 6.3), showing that combining XAS and SAXS leads to consistent results. Even with the use of a photodiode detector leading in some cases to lower S/N ratio (Appendix E, Figure E7), the XAS data are of sufficient quality to extract fitting values for the first and second shell of Pt neighbours for these states.

6.3.6 Activity tests – Propane Dehydrogenation (PDH)

Catalytic activity tests for PDH were performed for Pt/$MgAl_2O_4$, Pt:Ga/$MgAl_2O_4$, Al_2O_3/Pt:Ga/$MgAl_2O_4$, Pt/MgGaAlO and Al_2O_3/Pt/MgGaAlO. The results for these tests are shown in Figures 6.8 & 6.9 and Appendix E, Figures E9, E10 & E11.

Monometallic Pt activity (coated and uncoated): A set of PDH experiments were performed for the monometallic Pt/$MgAl_2O_4$ and 10Al_2O_3/Pt/$MgAl_2O_4$ catalysts for comparing the change in activity. Surprisingly, the coated catalyst performed better than the uncoated catalyst in terms of overall conversion (Appendix E, Figure E9). This was tested after 1 H_2-reduction step of 30 min at 873K and after 5 H_2/O_2 redox cycles with H_2-reduction as the last step. The redox cycles are performed as mentioned in § 6.2.3. However, the deactivation profiles are very similar for both catalysts, which suggests that there is probably less carbon formed on the coated sample than on the uncoated. Typically, undercoordinated sites are responsible for most carbon formation due to their inherent higher activity, but the presence of the alumina coating likely covers these sites.[35] This would lead to more active sites availability (prevention of blockage of sites by carbon) and therefore better overall conversions.

To see if this hypothesis is correct, the 2 catalysts were tested at the same conversion (~20%) for a TOS of 1.5 h, followed by burning off the carbon formed during PDH with O_2. The m/z signals at 44 and 32 were followed to quantify the amounts of carbon formed. For the coated sample the total amount of C was 0.617 mmol, while for the uncoated it was 0.763 mmol C. This is approximately a 20% reduction in the amount of carbon formed at the same conversion.

Pt:Ga WI samples (coated and uncoated): As expected, the addition of Ga as promoter to Pt in the WI catalyst (Figure 6.8) leads to an improvement in conversion[2] (pink to black squares). The addition of a coating over Pt:Ga brings down the activity (Figure 6.8, black to red and blue squares). The absolute conversions of propane for 40Al_2O_3/Pt:Ga/$MgAl_2O_4$ and the monometallic Pt/$MgAl_2O_4$ are very similar after 1 redox step. So, there is a marked difference between the coated and uncoated Pt:Ga catalysts after single redox activation, in that the uncoated samples showed much better performance in terms of activity and selectivity towards propylene. With increasing O_2/H_2 redox cycles, however, all the Pt:Ga catalysts show improvement in terms of activity (squares to circles). The latter can be ascribed to a higher amount of Ga in the Pt-Ga alloy, induced by the repeated alloying-segregating action of the redox cycles. The selectivity of uncoated Pt:Ga decreases upon subjugation to 5 redox cycles, just like for monometallic $Pt/MgAl_2O_4$. In contrast, the selectivity for the coated samples remains at similar levels after 1 and 5 redox cycles, despite an increase in propane conversion. Upon closer inspection of Figure 6.8b, it can be stated that with increasing TOS the selectivity of the ~4 nm coated sample becomes better than that of the ~1 nm coated sample. However, the total conversion of the ~1 nm coated sample is still higher and it provides higher yields of propylene. It can be speculated that the presence of the thicker coating just blocks more active sites for reaction, leading to lower activity, and the state of the Pt-Ga alloy in the $10Al_2O_3/Pt{:}Ga/MgAl_2O_4$ and $40Al_2O_3/Pt{:}Ga/MgAl_2O_4$ samples are quite similar after 5 redox cycles. The lower initial selectivity (compared to 1 nm coated sample) for the ~4 nm coated sample could have to do with the material properties of alumina itself, as it is slightly acidic, favouring more cracking reactions.

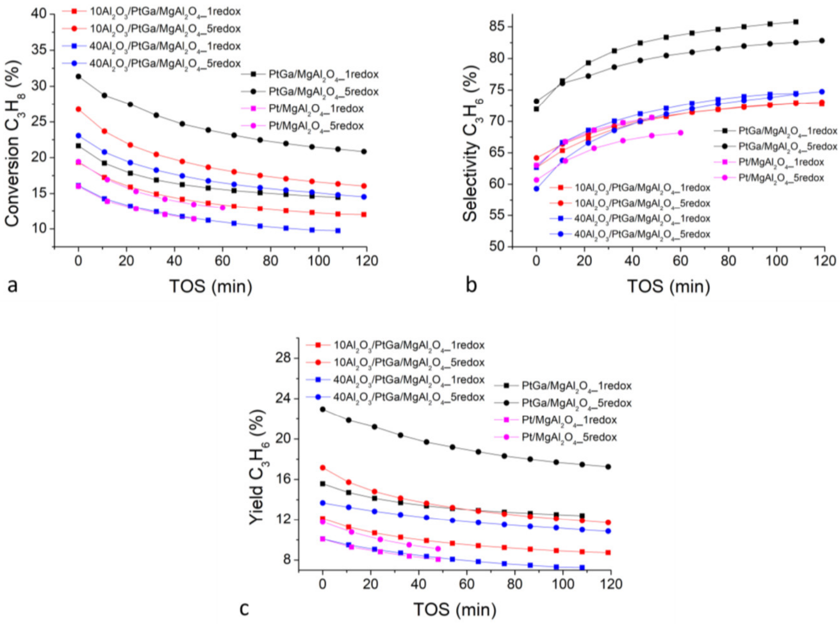

Figure 6.8: *Activity test results for PDH over the coated and uncoated Pt:Ga WI catalysts.* ***a:*** *Propane conversions for the different catalysts,* ***b:*** *Propylene selectivity* ***c:*** *propylene yields. Flows : C_3H_8 = 40 Nml/min, H_2 = 40 Nml/min Ar = 120 Nml/min. Ratio C_3H_8:H_2:Ar = 1:1:3. Total flow = 200 Nml/min. Catalyst amount = 0.1 g. T =873 K. P =1.2 bar. For STY refer to supporting information Figure E10.*

Incorporated samples: All the incorporated samples were tested for PDH after 1, 5 and 10 O_2/H_2 redox cycles. All detailed results are listed in Appendix E, Table E2 with plots in Figure E11 and Figure 6.9. Performance in terms of overall yield towards propylene of the Ga-incorporated samples was better when compared to the WI samples (after 1 and 5 redox cycles, Figure E12). The selectivity towards propylene was substantially higher for the Ga-incorporated samples (>95%, Figure 6.9) than for the WI samples (70-85 %, Figure 6.8). The findings from XAS provide an explanation, as after reduction and cycling the WL intensity in the XANES region was found lower for the incorporated samples than for the WI samples. The latter points to more Ga being present in the Pt-Ga alloy, accounting for the better performance. The superior performance of the incorporated samples over the WI samples is in line with literature.[2,12]

The 1nm alumina coated incorporated sample at first glance does not show a big difference in terms of performance towards PDH when compared to the uncoated sample (after 5 redox and 10 redox). However, the uncoated catalyst loses more activity for the same duration of reaction. The loss in performance for the uncoated sample with 1 redox cycle (25% to 16% over 2 h) is much higher than for the coated sample ($10Al_2O_3$/Pt/MgGaAlO: 31.7 to 25.9% over 2 h). This difference could be due to the preparation of the 2 catalysts: the coated sample has essentially undergone several extra steps before and after coating (pre-reduction, air exposure, inert annealing, which is reflected in the activity. Most likely, the uncoated catalyst after one redox treatment will not have the same Ga promotion as the coated sample. This is confirmed from Figure E5 where the first O_2 half cycle led to a WL maximum of 1.45 for the uncoated sample, while it was 1.41 for the coated sample. The total amount of carbon formed cannot be compared as the conversions are completely different.

Performance after 5 redox cycles for the uncoated and $10Al_2O_3$/Pt/MgGaAlO samples can be compared due to their similar initial activities (Figure 6.9). The coated sample loses less activity (loss of 2.3% propane conversion) over a longer duration of reaction (2 h) than the uncoated sample (2.76% in 1 h). The total amount of carbon formed during the reaction is also very similar (1.05 mmol vs. 1 mmol C), even though the coated sample was tested for PDH for 2 h against 1 h for the uncoated sample after 5 redox cycles (details Appendix E, Table E2). The result is the same after 10 redox cycles as well, where the coated sample still performs better than the uncoated sample.

A sample with a coating thickness of ~4 nm is also tested ($40Al_2O_3$/Pt/MgGaAlO) and performs worse than the uncoated and 1 nm coated samples, which is in line with what was observed for the WI samples. The thicker the coating, the more loss of active sites for reaction.

The activity for the $10Al_2O_3$/Pt/MgGaAlO sample was not affected by the coating as much as the $40Al_2O_3$/Pt/MgGaAlO sample. The reason for this could be found in the SAXS result. According to SAXS, the average PtGa nanoparticle sizes are about 2-2.4 nm, while the thickness of coating for the $10Al_2O_3$/Pt/MgGaAlO sample is ~1 nm. As the latter is smaller than the NP itself, redox cycling could move the coating off the top surface of the NP towards the sides, thereby blocking some undercoordinated sites of the Pt, which are typically the most active sites for PDH, entailing deep dehydrogenation and hence responsible for a major portion of the carbon formation.[2,35,36] As such, $10Al_2O_3$/Pt/MgGaAlO shows an activity similar to the Pt/MgGaAlO catalyst, while generating less carbon during the process at similar conversions. For the $40Al_2O_3$/Pt/MgGaAlO sample, the coating thickness (~4 nm) is more than the particle size itself and hence it is inevitable that activity is lost due to blocking of active sites (Table E2).

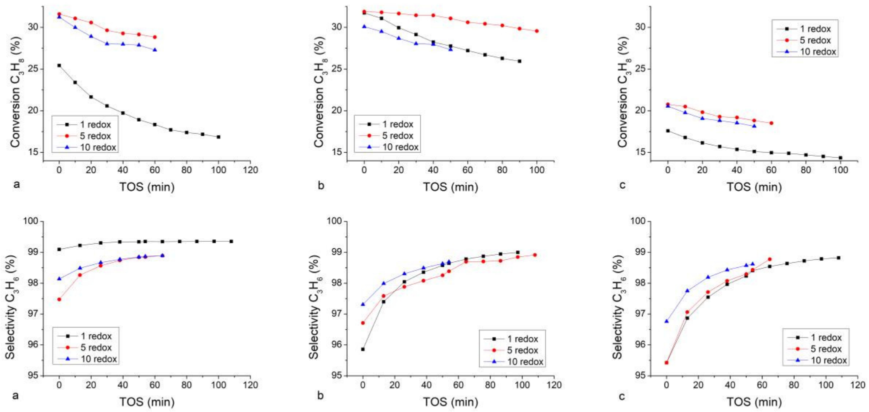

Figure 6.9: *Conversion and selectivity plots for* ***a:*** *Pt/MgGaAlO* ***b:*** *$10Al_2O_3$/Pt/MgGaAlO &* ***c:*** *$40Al_2O_3$/Pt/MgGaAlO. For STY refer to Appendix E, Figure E11. Flows : C_3H_8 = 40 Nml/min, H_2 = 40 Nml/min Ar = 120 Nml/min. Ratio C_3H_8:H_2:Ar = 1:1:3. Total flow = 200 Nml/min. Catalyst amount = 0.1 g. T =873 K. P =1.2 bar*

The selectivity towards propylene is also very slightly reduced with increasing coating thickness, despite the fact that the overall conversion of propane is much lower for the ~4 nm coated sample when compared to the ~1 nm coated sample. This is similar to what was observed for the WI samples and could have to do with the property of alumina (coating) and its slight acidic nature, which would lead to more cracking reactions.[37]

When looking at the results obtained from the activity tests for the incorporated samples and the monometallic Pt sample, it is quite evident that the presence of a promoter and coating helps to improve the activity (conversion, STY-propylene) by blocking sites of the Pt catalyst (from coating), which are responsible for C formation. This was confirmed by the C quantification for the catalysts at similar conversions (Table E2). Therefore the alumina coating, which was applied in view of reducing sintering, also had another positive effect, which is the suppression of C formation.

6.3.7 STEM results

The STEM images for fresh and extensively cycled samples (after 40 H_2/O_2 redox cycles) with their respective histograms are depicted in Figure 6.10 a-f. It is quite evident that increasing thickness of alumina coatings leads to better stability towards sintering of the NPs. The starting average NP sizes are similar for all the samples at ~1.5 nm. The average NP size after 40 redox cycles increases in the order of $40Al_2O_3$/Pt/MgGaAlO < $10Al_2O_3$/Pt/MgGaAlO < Pt/MgGaAlO (4.9 nm < 5.5 nm < 6.3 nm). The thicker the alumina coating, the lower the effect of sintering as the images confirm.

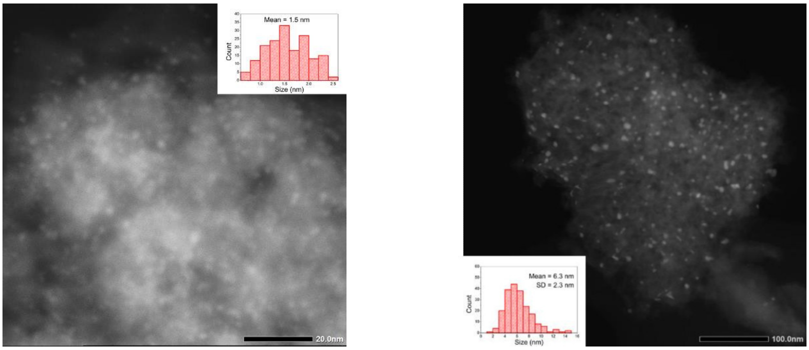

a b

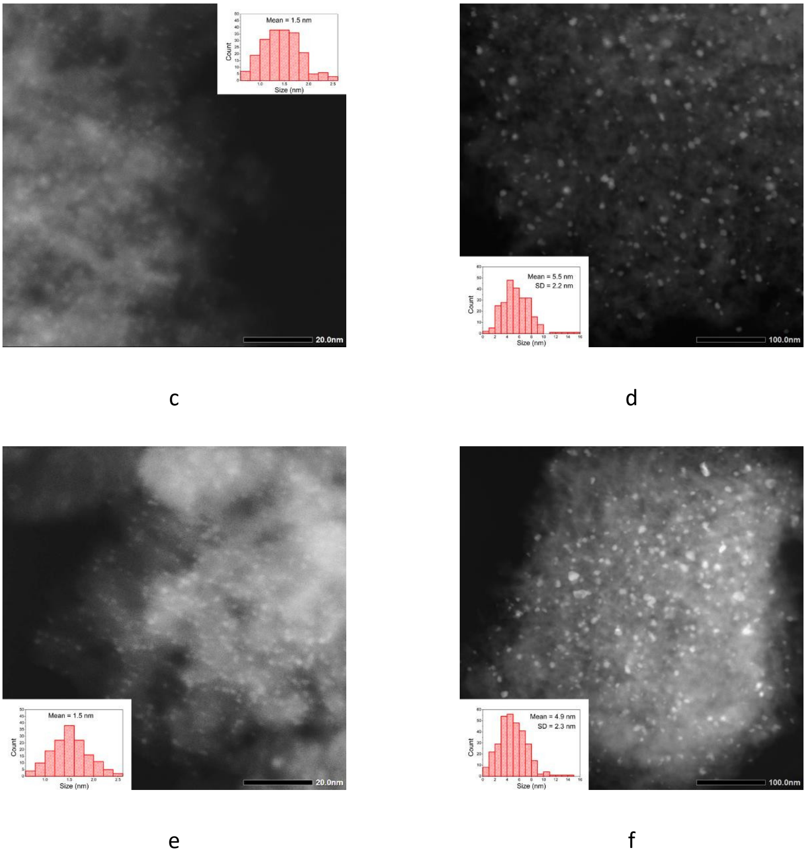

Figure 6.10: *STEM DF images of Pt/MgGaAlO, 10Al$_2$O$_3$/Pt/MgGaAlO and 40Al$_2$O$_3$/Pt/MgGaAlO; a, c & e: as prepared samples, respectively, and b, d, & f: after 40 redox cycles.*

6.4 Discussion

The application of SAXS and XAS in parallel yielded useful information as far as understanding the catalyst is concerned. SAXS provided Pt particle sizes and indicated that the catalyst didn't really sinter during the in situ measurements, comprising 5 redox cycles. The combination of SAXS and XAS allowed to conclude that the alumina coating was restricting the free mobility of the surface NPs for the WI samples (§ 6.3.4.1).

XAS data further indicated that for the coated WI samples the extent of alloying between Pt and Ga was limited, due to obstruction by the applied alumina coating of free mobility of the surface NPs required to form an alloy. Besides indirectly confirming the presence of a coating, these results indicate that it is viable to apply alumina coatings on a powder catalyst by ALD. The phenomena discussed are represented in the schematics shown in Figure 6.11.

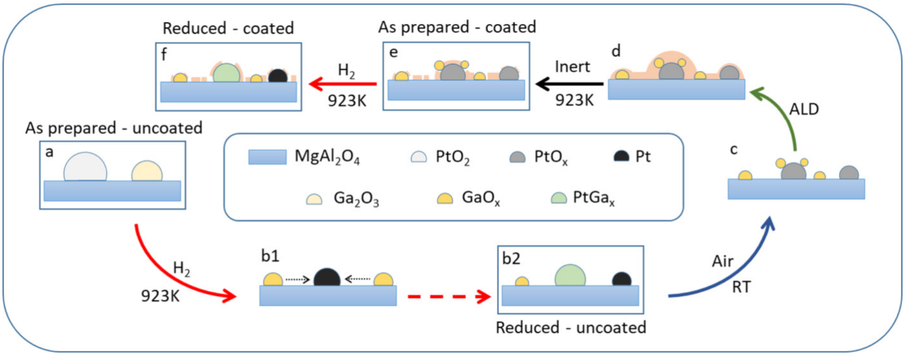

Figure 6.11: *Schematic for the coated and uncoated (1 nm coating sample) WI samples.* ***a:*** *as prepared state for uncoated sample.* ***b1:*** *reduction process for alloy formation.* ***b2:*** *reduced state for uncoated sample. Note that not all Pt and Ga participate in alloy formation.* ***c:*** *partial oxidation of Pt and Ga upon exposure to atmosphere leading to alloy segregation.* ***d:*** *coating with alumina by ALD leading to coated state.* ***e:*** *as prepared state for coated catalyst after inert calcination.* ***f:*** *reduced state for coated sample. Note: the fraction of Ga in Pt-Ga_x alloy is reduced when compared to the uncoated sample.*

The activity test results for the WI samples yielded information that the coated samples in terms of absolute conversion performed slightly worse than the uncoated samples. The activities improved upon subjecting the sample to multiple redox cycles, but the uncoated sample always performed better in terms of selectivity and conversion. These activity tests indicate that the WI samples originally do not have the optimal composition for PDH reaction, as evidenced by the improvement after multiple redox cycles, the latter due to increasing promoter/Ga content in the Pt-Ga alloy with the redox cycles. The WI method of sample preparation typically has limited control on the location of the metals on the support surface. Especially on larger surface area supports, it is possible that PtO_x and GaO_x NPs are located far apart, thereby not facilitating alloy formation. The application of multiple redox cycles will enable some migration of the NPs on the surface, thereby yielding more alloying. In light of this, the alumina coating might better be applied on the WI samples after multiple redox cycles (>5), so that a proper alloy composition is already reached. In the current conditions, where the coating was applied on a non-cycled WI sample, the coated samples always give rise to a lower selectivity towards propylene, and probably higher overall carbon formation.

The issues of the WI samples are not faced by the Ga-incorporated samples (Pt/MgGaAlO, $10Al_2O_3$/Pt/MgGaAlO, $40Al_2O_3$/Pt/MgGaAlO). This is primarily because the alloying process for such a sample does not rely on the surface location of the NPs. Instead, the Ga located in the support close to the WI Pt, will get "extracted" from the support by hydrogen spillover and form a Pt-Ga alloy. Hence, the presence of a coating should not affect the process of alloy formation. This was evidenced in the activity test results, based on the values of the selectivity achieved (>95%). Upon multiple redox treatments, the activity followed a similar pattern for all these samples. The 1nm coated sample performed slightly better than the uncoated sample in terms of overall carbon formation and deactivation over similar reaction time periods. Combining the knowledge from SAXS with the activity results, PtGa NP alloys of approximately the same size (~2.2 nm diameter) are giving slightly different activity trends, while the coated sample provided lower carbon formation. Given the thickness of the coating, it is probably not covering the entire NP, but rather certain parts at the interface between NP and support, which are responsible for carbon formation (undercoordinated sites). This hypothesis was tested by calculating the total carbon formation for the 1nm coated and uncoated sample, at the same conversions, which indeed yielded less carbon for the coated samples as discussed in § 6.3.6. A schematic of what takes place for the incorporated catalyst is shown in Figure 6.12.

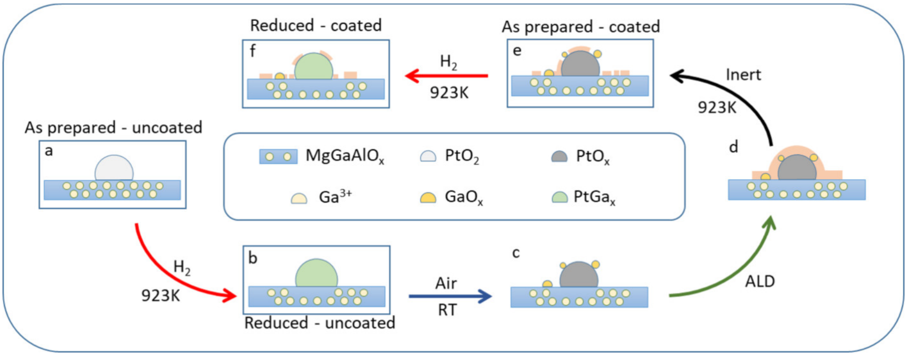

Figure 6.12: *Schematic for the coated and uncoated (1 nm coating sample) INC samples.* ***a:*** *as prepared state for uncoated sample.* ***b:*** *reduced state for uncoated sample. For this sample all the Pt participates in alloy formation.* ***c:*** *partial oxidation of Pt and Ga upon exposure to atmosphere leading to alloy segregation.* ***d:*** *coating with alumina by ALD leading to coated state.* ***e:*** *as prepared state for coated catalyst after inert calcination.* ***f:*** *reduced state for coated sample. Note: the fraction of Ga in Pt-*Ga_x *alloy is unaffected, which is unlike the WI samples. Whatever Ga is lost upon partial oxidation or because of hindrance of mobility due to coating on the surface, is regained through the support.*

Finally from STEM results it is clear that the alumina coating limits the extent of sintering of the surface NPs, and increasing thickness of the alumina coatings results in a reduced sintering effect.

6.5 Conclusions

Pt:Ga catalysts prepared by 2 different methods were investigated for the PDH reaction. These catalysts were coated with alumina by means of ALD to investigate the effect on sintering of the NPs. A combination of in situ SAXS (ASAXS) and XAS was successfully applied to investigate the effect of coating on the catalyst. The only drawback of the parallel application of SAXS and XAS was the use of a photodiode for XAS registration to accommodate SAXS acquisition, which led to data with lower signal to noise ratio. Despite this, these in situ techniques evidenced that the presence of the alumina coating hindered alloy formation between Pt and Ga in the case of the WI samples, while it did not in the case of the Ga-incorporated samples. For a limited number of in situ redox cycles, no sintering was observed. For more extensive cycling, particle size distributions from STEM do confirm sintering, though less for the coated samples.

The activity tests for the incorporated samples reflected the above findings. The coating did not prevent access of reactant molecules to the catalyst surface. It did however reduce total activity towards PDH, even more so for a thicker coating, which leads to the conclusion that access is more hindered with increasing coating thickness. However, the presence of a coating leads to lower absolute carbon formation by blocking undercoordinated sites of Pt, and slower deactivation with time on stream. Although coating leads to loss of activity compared to uncoated samples, redox cycling allows to regain some of the activity, especially for the thin alumina coating.

Finally, WI samples are more hindered by the coating application than incorporated samples, because they rely on PtO_x and GaO_x NPs proximity for alloy formation. The presence of a coating then reduces the mobility of these particles. The latter is not the case for incorporated samples, where the promotor is delivered from within the support, thus not hindering alloying. Ideally, the alumina coating for the WI sample should be applied after subjecting the catalyst to multiple redox cycles, in order to increase Ga content in the Pt-Ga alloy, since after the application of such a coating it is very difficult to increase the fraction of Ga in the Pt-Ga alloy.

Although this work uses Ga as a promoter, these findings can be extrapolated for other promoters such as Sn, Cu, etc., as the process of alloy formation would remain similar.

Appendix E: data

SAXS fits, XANES spectra for $Pt/MgAl_2O_4$, XANES spectra for redox cycling experiments, XAS spectra and modelling, activity tests in STY scale for the WI and Ga-INCorporated samples, and activity plots for monometallic Pt samples (coated and uncoated).

6.6 References

1. Filez, M. *et al.* The role of hydrogen during Pt–Ga nanocatalyst formation. *Phys. Chem. Chem. Phys.* **18**, 3234–3243 (2016).

2. Redekop, E. A. *et al.* Delivering a Modifying Element to Metal Nanoparticles via Support: Pt–Ga Alloying during the Reduction of Pt/Mg(Al,Ga)Ox Catalysts and Its Effects on Propane Dehydrogenation. *ACS Catal.* **4**, 1812–1824 (2014).

3. Detavernier, C., Dendooven, J., Pulinthanathu Sree, S., Ludwig, K. F. & Martens, J. A. Tailoring nanoporous materials by atomic layer deposition. *Chem. Soc. Rev.* **40**, 5242–5253 (2011).

4. O'Neill, B. J., Sener, C., Jackson, D. H. K., Kuech, T. F. & Dumesic, J. A. Control of Thickness and Chemical Properties of Atomic Layer Deposition Overcoats for Stabilizing Cu/γ-Al2O3 Catalysts. *ChemSusChem* **7**, 3247–3251 (2014).

5. Gong, Y. *et al.* Stabilizing Nanostructured Solid Oxide Fuel Cell Cathode with Atomic Layer Deposition. *Nano Lett.* **13**, 4340–4345 (2013).

6. Asundi, A. S., Raiford, J. A. & Bent, S. F. Opportunities for Atomic Layer Deposition in Emerging Energy Technologies. *ACS Energy Lett.* **4**, 908–925 (2019).

7. Solano, E. *et al.* In situ study of the thermal stability of supported Pt nanoparticles and their stabilization via atomic layer deposition overcoating. *Nanoscale* **12**, 11684–11693 (2020).

8. Lu, J. *et al.* Coking- and Sintering-Resistant Palladium Catalysts Achieved Through Atomic Layer Deposition. *Science (80-.).* **335**, 1205 LP – 1208 (2012).

9. Wanke, S. E. & Flynn, P. C. The Sintering of Supported Metal Catalysts. *Catal. Rev.* **12**, 93–135 (1975).

10. Rasmussen, F. B., Molenbroek, A. M., Clausen, B. S. & Feidenhans, R. Particle Size Distribution of an Ni/SiO2 Catalyst Determined by ASAXS. *J. Catal.* **190**, 205–208 (2000).

11. Binninger, T. *et al.* Particle-Support Interferences in Small-Angle X-Ray Scattering from Supported-Catalyst Materials. *Phys. Rev. Appl.* **3**, 24012 (2015).

12. Sun, P., Siddiqi, G., Chi, M. & Bell, A. T. Synthesis and characterization of a new catalyst

Pt/Mg(Ga)(Al)O for alkane dehydrogenation. *J. Catal.* **274**, 192–199 (2010).

13. Longo, A. *et al.* What Makes Fe-Modified MgAl2O4 an Active Catalyst Support? Insight from X-ray Raman Scattering. *ACS Catal.* **10**, 6613–6622 (2020).
14. Zeigarnik, A. V, Valdés-Pérez, R. E. & Myatkovskaya, O. N. C−C Bond Scission in Ethane Hydrogenolysis. *J. Phys. Chem. B* **104**, 10578–10587 (2000).
15. Sun, P., Siddiqi, G., Vining, W. C., Chi, M. & Bell, A. T. Novel Pt/Mg(In)(Al)O catalysts for ethane and propane dehydrogenation. *J. Catal.* **282**, 165–174 (2011).
16. Iglesias-juez, A. *et al.* A combined in situ time-resolved UV – Vis , Raman and high-energy resolution X-ray absorption spectroscopy study on the deactivation behavior of Pt and Pt A Sn propane dehydrogenation catalysts under industrial reaction conditions. *J. Catal.* **276**, 268–279 (2010).
17. Airaksinen, S. M. K., Bañares, M. A. & Krause, A. O. I. In situ characterisation of carbon-containing species formed on chromia/alumina during propane dehydrogenation. *J. Catal.* **230**, 507–513 (2005).
18. Nikitenko, S. *et al.* Implementation of a combined SAXS/WAXS/QEXAFS set-up for time-resolved in situ experiments. *J. Synchrotron Radiat.* **15**, 632–640 (2008).
19. Povia, M. *et al.* Combining SAXS and XAS To Study the Operando Degradation of Carbon-Supported Pt-Nanoparticle Fuel Cell Catalysts. *ACS Catal.* **8**, 7000–7015 (2018).
20. Martis, V. *et al.* A high-pressure and controlled-flow gas system for catalysis research. *J. Synchrotron Radiat.* **21**, 462–463 (2014).
21. Srinath, N. V. *et al.* In situ XAS/SAXS study of Al2O3 coated PtGa/MgAl2O4 catalysts for alkane dehydrogenation. in *2019 AIChE Annual meeting (19-AIChE)* (American Institute of Chemical Engineers (AIChE), 2019).
22. Veeraraghavan Srinath, N. *et al.* Behaviour of Platinum-Tin during CO2-assisted propane dehydrogenation: Insights from quick X-ray absorption spectroscopy. *J. Catal.* (2021). doi:https://doi.org/10.1016/j.jcat.2021.08.041
23. Klementev, K. V. Package “VIPER (visual processing in EXAFS researches) for windows”. *Nucl. Instruments Methods Phys. Res. Sect. A Accel. Spectrometers, Detect. Assoc. Equip.* **448**, 299–301 (2000).
24. Olsbye, U., Moen, O., Slagtern, Å. & Dahl, I. M. An investigation of the coking properties of fixed and fluid bed reactors during methane-to-synthesis gas reactions. *Appl. Catal. A Gen.* **228**, 289–303 (2002).
25. Froment, G. F., Bischoff, K. B. & De Wilde, J. *Chemical reactor analysis and design*. **2**, (Wiley New York, 1990).
26. Mears, D. E. Diagnostic criteria for heat transport limitations in fixed bed reactors. *J. Catal.* **20**, 127–131 (1971).
27. Ferguson, J. D., Weimer, A. W. & George, S. M. Atomic layer deposition of ultrathin and

conformal Al2O3 films on BN particles. *Thin Solid Films* **371**, 95–104 (2000).

28. Balakrishnan, K. & Schwank, J. FTIR study of bimetallic Pt-Sn/Al2O3 catalysts. *J. Catal.* **138**, 491–499 (1992).

29. Marchesini, F. A., Gutierrez, L. B., Querini, C. A. & Miró, E. E. Pt,In and Pd,In catalysts for the hydrogenation of nitrates and nitrites in water. FTIR characterization and reaction studies. *Chem. Eng. J.* **159**, 203–211 (2010).

30. Zhu, H. *et al.* Sn surface-enriched Pt-Sn bimetallic nanoparticles as a selective and stable catalyst for propane dehydrogenation. *J. Catal.* **320**, 52–62 (2014).

31. Filez, M. *et al.* Unravelling the formation of Pt-Ga alloyed nanoparticles on calcined Ga-modified hydrotalcites by in situ XAS. *Chem. Mater.* **26**, 5936–5949 (2014).

32. Filez, M., Redekop, E. A., Poelman, H., Galvita, V. V & Marin, G. B. Advanced Elemental Characterization during Pt–In Catalyst Formation by Wavelet Transformed X-ray Absorption Spectroscopy. *Anal. Chem.* **87**, 3520–3526 (2015).

33. Srinath, N. V., Poelman, H., Reyniers, M.-F., Dendooven, J. & Galvita, V. Redox evolution of Pt-Sn alloys studied by time-resolved XAS. in *14th European congress on Catalysis (EuropaCat 2019): Catalysis without borders* (2019).

34. Frenkel, A. I., Hills, C. W. & Nuzzo, R. G. A View from the Inside: Complexity in the Atomic Scale Ordering of Supported Metal Nanoparticles. *J. Phys. Chem. B* **105**, 12689–12703 (2001).

35. Lu, Z. *et al.* Atomic Layer Deposition Overcoating Improves Catalyst Selectivity and Longevity in Propane Dehydrogenation. *ACS Catal.* **10**, 13957–13967 (2020).

36. Aly, M., Fornero, E. L., Leon-Garzon, A. R., Galvita, V. V & Saeys, M. Effect of Boron Promotion on Coke Formation during Propane Dehydrogenation over Pt/γ-Al2O3 Catalysts. *ACS Catal.* **10**, 5208–5216 (2020).

37. Zhang, Y. *et al.* Comparative study of bimetallic Pt-Sn catalysts supported on different supports for propane dehydrogenation. *J. Mol. Catal. A Chem.* **381**, 138–147 (2014).

Chapter 7

Conclusions and perspectives

7.1 Conclusions

Throughout this thesis, numerous factors pertaining to the propane dehydrogenation reaction (PDH) were examined. The continuously increasing global demands for propylene make PDH an important process for propylene production, as the existing processes for its production (steam cracking and FCC) cannot keep up due to their dependency on the feedstock and operating conditions. Moreover, propylene is just a by-product of steam cracking and FCC.

One of the major factors explored in this thesis is the viability of adding CO_2 to the feed, to make a form of CO_2-assisted PDH for Pt-based bimetallic catalysts. The utilization of CO_2 in this period of time, is of primordial importance due to the elevated concerns of global warming that is caused by the significant increase in atmospheric concentrations of CO_2, which is a greenhouse gas. While the consumption of CO_2 in CO_2-assisted PDH is limited, its co-feeding could have benefits such as higher propane conversions through the equilibrium shift caused by consumption of product H_2 by the fed CO_2, reduced carbon formation through the reverse Boudouard reaction, and increased propylene yields by desorption of propylene facilitated through RWGS reaction. The main objective is to bring an improvement to PDH. However, the addition of CO_2 modifies many other variables through its capability to change the thermodynamics of the reaction and to interact with the bimetallic catalyst with potential to oxidise the promoter element.

To explore the effects of CO_2 addition, a detailed analysis of a Pt:Sn catalyst (3 wt% Pt, 0.4 wt% Sn, 3:1 atomic ratio), supported on a lower and higher surface area $MgAl_2O_4$ support (LSA & HSA), was performed for CO_2-assisted PDH. The technique of use for detailed analysis of dynamic changes occurring to the catalyst, in presence of both reductive (H_2) and oxidising (CO_2) atmospheres, is in situ XAS. Measurements were performed at both Pt L_{III}-edge and Sn K-edges, and extensive data analysis was carried out in both the XANES and EXAFS regions. As part of the data analysis, the big data technique, multivariate curve resolution with alternating least squares (MCR-ALS), was used to determine the exact contents of Pt and Sn that were participating in alloy formation. The other aspects investigated were: 1. Nanoparticle (NP) size effects on the ease of Pt-Sn alloy formation, 2. effect of CO_2 on the alloy, 3. effect of H_2/O_2 redox cycles on alloy integrity and 4. determination of the average phase of the alloy.

The use of different surface areas led to variation in NP sizes present on the support surface, whereby a lower surface area entailed a larger NP size and vice-versa. Through fingerprint analysis of the XANES region of the Pt L_{III}-edge during H_2-TPR, smaller NPs were found to more readily form a Pt-Sn alloy than larger NPs. For the latter, PtO_2 was first reduced to Pt before alloy formation began, while for smaller NPs, Pt immediately formed alloy with Sn as soon as it was reduced.

Oxidation of Sn to SnO and subsequently to SnO_2 by CO_2 was confirmed, but the oxidation to SnO occurs more readily than oxidation to SnO_2. This oxidation of Sn leads to loss of the Pt-Sn alloy phase. The average Pt-Sn alloy phase formed was determined to be Pt_3Sn. This determination was performed by means of successful use of MCR-ALS as big data technique, allowing quantification of the exact amount of Sn and Pt present in the sample that formed an Pt-Sn alloy. For HSA, it was quantified that only 42% of the Sn present in the sample went into the Pt-Sn alloy phase after one H_2-reduction step. This value increased to 72% upon subjecting the sample to 10 H_2/CO_2 redox cycles. As for the LSA support, 92% of the Sn present got incorporated into the alloy after one H_2-reduction step, due to the closer proximity of impregnated Pt and Sn present in the sample, which facilitated more Sn incorporation into the Pt-Sn alloy.

Subsequently, the Pt:Sn/HSA catalyst was tested for PDH, CO_2-PDH at different CO_2:C_3H_8 ratios, for alternate cycling experiments of CO_2 and C_3H_8 to figure out the potential applicability of CO_2 as a regenerative gas.

The PDH tests confirmed the findings from XAS, in that with increasing redox cycles the content of Sn in the Pt-Sn alloy increases. This was evidenced via an increase in selectivity towards propylene through PDH, when testing the catalyst after several H_2/O_2 redox steps. The CO_2:C_3H_8 ratio studies showed that lower ratios showed better activity. The reasoning for this is that when the ratio increases, the amount of CO_2 in the system rises, which can assist towards segregating the Pt-Sn alloy through oxidation of Sn to SnO and subsequently to SnO_2. Once the alloy is segregated the activity drops. The presence of H_2 in the system, formed through PDH, is therefore critical to maintain the integrity of the alloy. Based on the activity tests, it is recommended to dynamically adjust the CO_2 feed rate based upon the propane conversion. When the catalyst is deactivating due to inevitable carbon formation from PDH, the absolute amounts of H_2 formed and entering the system also decrease, which thereby dynamically changes the CO_2:H_2 ratio for a constant CO_2 feed. This would lead to an increasing rate at which the Sn gets oxidised to SnO and subsequently SnO_2.

Through qualitative assessment it was found that it is possible to reduce the SnO_2 with carbon. However, whether reduction leads to SnO or Sn could not be determined. CO_2 is able to react with the carbon by means of the reverse Boudouard reaction, but only for the carbon that is present on the active sites. The RWGS reaction takes place parallel to CO_2-PDH, thereby helping to improve activity by shifting the equilibrium towards the products.

Two catalysts (Pt:Sn – 3 wt% Pt & 3 wt% Sn, Pt:In – 3 wt% Pt & 3 wt% In, atomic ratio = 1:1.5) were then characterized in detail through in situ QXAS, where the main aim was to find how these catalysts behave under a CO_2 atmosphere and in presence of both H_2 and CO_2 as these are the components in CO_2-PDH that affect the alloy stability. The reasoning behind using these two catalysts was that the data for Pt:Sn can form a comparative basis for the findings in chapter 3 (3:1 Pt:Sn atomic ratio sample, Pt:Sn/HSA), and they can both be used for comparison as they are both known to be viable catalysts for PDH. Moreover, an additional reason is that In and Sn have a quite different potential for oxidation by CO_2.

Through XANES analysis, it was confirmed that oxidation of In and Sn by a pure CO_2 atmosphere is possible and the oxidation of In occurred more readily. This was concluded based on isothermal CO_2-oxidation experiments that were conducted at 873 K. CO_2-TPO showed that the oxidation of both In and Sn began occurring at low temperatures (< 500 K), and once oxidation of the promoter began, a change in the white line (WL) intensity of the Pt edge was also recorded, implying loss of alloy.

Several in situ experiments with co-feeding of H_2 and CO_2 were conducted, through which it was determined that the Pt-In and Pt-Sn alloys did not segregate with increasing CO_2:H_2 ratio. A slight increase in the WL was recorded, which implied a larger quantity of surface species participating in the reaction. This was confirmed through modulation excitation experiments (ME), where a reversible process of alloying/de-alloying was observed. MCR-ALS for these samples (Pt:Sn & Pt:In with 1:1.5 atomic ratio) did not prove to be as fruitful as it did for the Pt:Sn/HSA sample. The reason for this is that when the content of Sn in the Pt-Sn alloy increases, it tends to behave more like a bulk sample. Thermodynamic calculations indicate that theoretically it should not be feasible to oxidise In, Sn or Ga by CO_2. However, this oxidation is observed in practice for the samples analysed, showing that these calculations are typical for bulk metals and not for nanoparticles. Due to increased “bulk-like” behaviour at a Pt:promoter atomic ratio of 1:1.5, the alloying/de-alloying process becomes much slower, as the kinetics of change of the promoters decreases. However, the changes occurring to the Pt:In sample were much more substantial than for Pt:Sn. The actual fraction of Pt participating in this process was estimated to be about 11 atoms out of 100 for the Pt:In catalyst. Pt:Sn showed a much lower fraction: 1 atom out of 100. The latter was ascribed to the two feed compositions used for the ME experiment with insufficient difference to induce surface changes to the alloy. Employing more distinct conditions should lead to more Pt engagement in the oscillation experiments.

EXAFS modelling was conducted for the spectra measured at RT subsequent to various experiments. The modelling revealed that the composition of In in the Pt-In alloy did not change through multiple H_2/O_2 redox cycles, remaining quasi-constant. One change that did occur to the sample was to the NP size, in that it sintered to form larger NPs upon high temperature (873 K) redox treatments. This sintering is enhanced by the high volatility of In, which led to a loss of 24% of the total In present in the sample through the in situ experiments, and by the surface rearrangement of the Pt-In alloy during reaction at 873 K. The main alloy phase identified for Pt:In was $Pt_{13}In_9$, mostly present at the surface and as such the active phase, with a complementary Pt_3In phase in the bulk.

As was concluded for the Pt:Sn/HSA sample, increased redox treatments (H_2/O_2) led to increased Sn content in the Pt-Sn alloy for the Pt:Sn sample. The average alloy phase is Pt_3Sn which gradually shifted to Pt_1Sn_1 with increased redox steps. No changes to the NP size were found, remaining quasi-constant.

The Pt:In and Pt:Sn catalysts were tested for PDH, CO_2-PDH and RWGS. A monometallic Pt (3 wt% Pt) and a Pt:Ga (3 wt% Pt, 1.1 wt% Ga – atomic ratio = 1:1.2) catalyst were added to the set to make a comparative study. All catalysts showed an improved performance upon CO_2

addition to the feed. Equilibrium conversions for RWGS were achieved during CO_2-PDH, which led to a thermodynamic shift that thereby induced an increased conversion of propane. The other reason for improved performance with CO_2 addition was attributed to suppressed carbon formation through the reverse Boudouard reaction.

Lower CO_2:C_3H_8 ratios (0.125:1) gave better results for CO_2-PDH for all catalysts. The reasoning is the same as mentioned earlier for the Pt:Sn/HSA sample, wherein the higher ratios can lead to increased alloy segregation and thereby blocking of active sites by the Sn, In or Ga oxides. Since RWGS and reverse Boudouard reactions take place, increasing CO_2:C_3H_8 ratios would lead to increased competition for adsorption sites between CO_2 and C_3H_8 on the catalyst, which is another reason for reduced activity towards CO_2-PDH.

Similar to Pt:Sn, Pt:Ga showed increased promoter content with increased H_2/O_2 redox cycles. The latter led to a drop in propane conversion during CO_2-PDH. This is attributed to two reasons: 1. because the higher promoter content makes the alloy more prone to promoter extraction from the alloy by the presence of CO_2, leading to Pt site blocking, and 2. the loss of number of available Pt sites on the surface of the NP with increased promoter content, which inherently leads to lower activity as the Pt sites are responsible for dehydrogenation. Pt:In also showed a loss in activity with increased redox cycle treatments but the reason for that lies in NP sintering, as was concluded from XAS.

All 3 catalysts were tested for PDH and showed similar performance. Through this result it is concluded that the activity differences observed for CO_2-PDH are due to the presence of CO_2, and not to inherent activity differences between the catalysts.

Addition of a promoter led to lower overall carbon formation during CO_2-PDH when compared to the monometallic Pt counterpart. The total carbon amount formed was in the order: Pt > Pt:Ga > Pt:In > Pt:Sn.

Therefore, dehydrogenation of propane over Pt is improved through both promoter addition and CO_2 addition as a co-feed. Amongst the promoters investigated, Sn showed the best performance as the Pt-Sn alloy is more stable than Pt-In and Pt-Ga alloys. Pt:Sn also forms less carbon than Pt:Ga and Pt:In, which extends its performance. The main factors to control in order to actually gain process improvement with a CO_2 co-feed (CO_2-PDH), are the alloy composition, i.e. the promoter content, and the feed ratio CO_2:C_3H_8, which depends on the bimetallic catalyst being employed.

Adding CO_2 to the feed is not the only potential way to improve the PDH process. The other possibility that was investigated in this thesis was addition of an alumina coating through atomic layer deposition (ALD) to Pt:Ga catalysts.

Alumina coated Pt:Ga catalysts prepared through 2 different methods of preparation were investigated. The investigation was undertaken through the combined use of in situ SAXS (ASAXS) and XAS. The drawback of such a parallel application lies in the substitution of the typical ionisation chamber with a photodiode for XAS registration to accommodate SAXS acquisition, leading to lower signal-to-noise ratios. However, in spite of this, through the combined use of these techniques, it was found that the presence of the coating hindered the process of alloy formation between Pt and Ga in the case of wet impregnated (WI) samples. This was not the case for the Ga-incorporated samples. Sintering was not observed for the limited number of redox cycles performed in the in situ experiments, but extensive cycling did confirm sintering (through PSD from STEM images). The extent of sintering was however reduced for the coated samples.

Activity tests for the incorporated samples for PDH reflected the findings from XAS/SAXS. The presence of a coating did not prevent access of reactant molecules to the catalyst surface, but it did reduce the total PDH activity with increased thickness of coating. The presence of the coating, however, reduced the total amount of carbon formed through blocking of the undercoordinated sites of Pt, which are typically held responsible for carbon formation. Slower deactivation with time-on-stream was recorded. Although coating leads to loss of activity compared to uncoated samples, redox cycling allows to regain some of the activity, especially for the thin alumina coating.

The WI samples were more hindered by the coating application than the incorporated samples, as they rely on the proximity of PtO_x and GaO_x for alloy formation. The presence of a coating reduced the mobility of the particles and thereby the extent of alloy formation. This was not the case for the Ga-incorporated samples, where Ga was delivered from within the support, and therefore the coating did not hinder alloy formation. Hence, the application of an alumina coating for the WI sample should be applied after subjecting the catalyst to a few redox cycles, to increase the Ga content in the Pt-Ga alloy.

Although the analysis of coating application is performed for Pt:Ga samples, the findings can be extrapolated towards other promoters, such as Sn, Cu, Ge, etc., as the alloy formation process would be similar. However, it can likely not be extrapolated to In, as its behaviour is atypical compared to other promoters, due to its volatility.

7.2 Perspectives

The multiple conclusions from this work can be translated into some recommendations and suggestions for future work.

1. The use of the big data technique MCR-ALS, as it was applied in this thesis, is not possible in every scenario. Through MCR-ALS analysis, it was possible to determine the exact amount of Pt and Sn that was participating in the alloy formation. This was however only feasible as the content of Sn present in that sample, relative to Pt, was low. As mentioned earlier, a higher Sn content would mean that the promoter oxidation by CO_2 would be slower due to more "bulk-like" behaviour.

2. ME analysis in this work was successful despite the absence of numerous alloy references. This was because for Pt:In and Pt:Sn, through the use of different samples/treatments, the promoter content in the alloy was altered, so that these could be used as "different" alloy references. A similar ME analysis as performed in this work can theoretically be applied to other bimetallic systems, but care must be taken to ensure the availability of references or to design the experiments in a fashion such that the experimental data can be used as potential reference for the analysis.

3. The choice of promoter for CO_2-PDH should be based upon its CO_2-oxidation and H_2-reduction potential. Pt:Sn proved to be a good catalyst, therefore any promoter that is chosen has to be one with lower potential for oxidation by CO_2 than Sn, can form an alloy with Pt and should form less carbon than Pt:Sn. Although in this work a combination of LH and MvK mechanism is proposed for CO_2-PDH, the former is the dominant reaction pathway.

4. In is not recommended to be used as a promoter for Pt-based or other catalysts, where the reaction is expected to occur at temperatures above 780 K. This is the case for metallic In and not for In oxide as the oxide is stable. But if there is a suspicion of formation of metallic In, then it is better to not use it altogether.

5. Through application of H_2/O_2 redox cycles, it was found that the promoter content in the Pt-M alloy for Pt:Ga and Pt:Sn samples increased and this led to a decrease in CO_2-PDH activity. The presence of a coating for a WI sample led to hindrance of alloy formation. Therefore, a viable option could be to subject the Pt:Sn catalyst (WI catalyst with Sn excess) to about 3 redox cycles, culminating with a H_2 reduction step, following which a coating can be applied. Then, the promoter content should remain relatively stable through regeneration steps and therefore the activity for CO_2-PDH would be maintained.

6. Care has to be taken when using a hydrotalcite-type support. In this work, the benefit of the Ga-incorporated support was shown if a coating is applied for such a sample. However, such sample has to be maintained at a high temperature on a continuous basis. The reason for this is that "storage" at room temperature for extended periods of time will lead to re-formation of a layered structure through hydration. Upon subsequent high temperature treatment, this structure will collapse again, rendering the applied coating meaningless as the initial application was for a "different" lattice configuration.

7. The amount of promoter (loading) to be added in a hydrotalcite-type support has to be chosen with caution. If the promoter content is high relative to the present Pt, then through regeneration/redox cycles, the content of the promoter in the Pt-M alloy will continuously increase. The presence of a coating would not change this and therefore, there is a possibility that upon subjecting the sample to multiple redox cycles, no difference between the coated and uncoated samples would remain. For this reason, the strategy of preparing a WI bimetallic sample that is subjected to a few redox cycles (3 to 5), culminating with a H_2-reduction followed by a coating application, is more promising for long-term application. The concern of sample storage, that is present for hydrotalcite-type support, would be rendered obsolete for the coated WI sample. This is of course provided that care is taken to run the appropriate pre-treatments prior to the coating application for the WI sample.

8. Another possibility would be to prepare a phase-pure sample through colloidal synthesis followed by the coating application. This would be challenging, as preparing a bimetallic alloy through colloidal synthesis is not an easy task. It would however, be interesting to investigate to see the potential benefits of such a monodisperse sample.

Appendix A

The step response set up consists of a fixed bed reactor and can be used for catalytic and gas-solid reactions. The advantage of the setup is that it allows the users to choose between a variety of feeds, consisting of various gases or liquids, that will be vaporized, and an inert flow through the reactor. Thus, it provides flexibility to perform reactions under various feed specifications without changing the reactor conditions of temperature and pressure. In addition, switching between different feed mixtures is possible through a fast switching valve. This enables the users to simulate a “step–response” or “alternate pulse” experiment in the desired feed conditions, instead of a slow gradient in the feed composition and hence it is called step response reactor. The reactor effluent can be analysed using an online GC and MS. Typically a catalyst/material mass of 0.01-1g can be loaded in the reactor.

The setup can be broadly divided into three sections namely Feed, Reactor and Analysis. The flow diagram is shown in Figure A1. The various parameters in these sections such as flow, temperature and pressure are PLC (programmable logic controller) enabled.

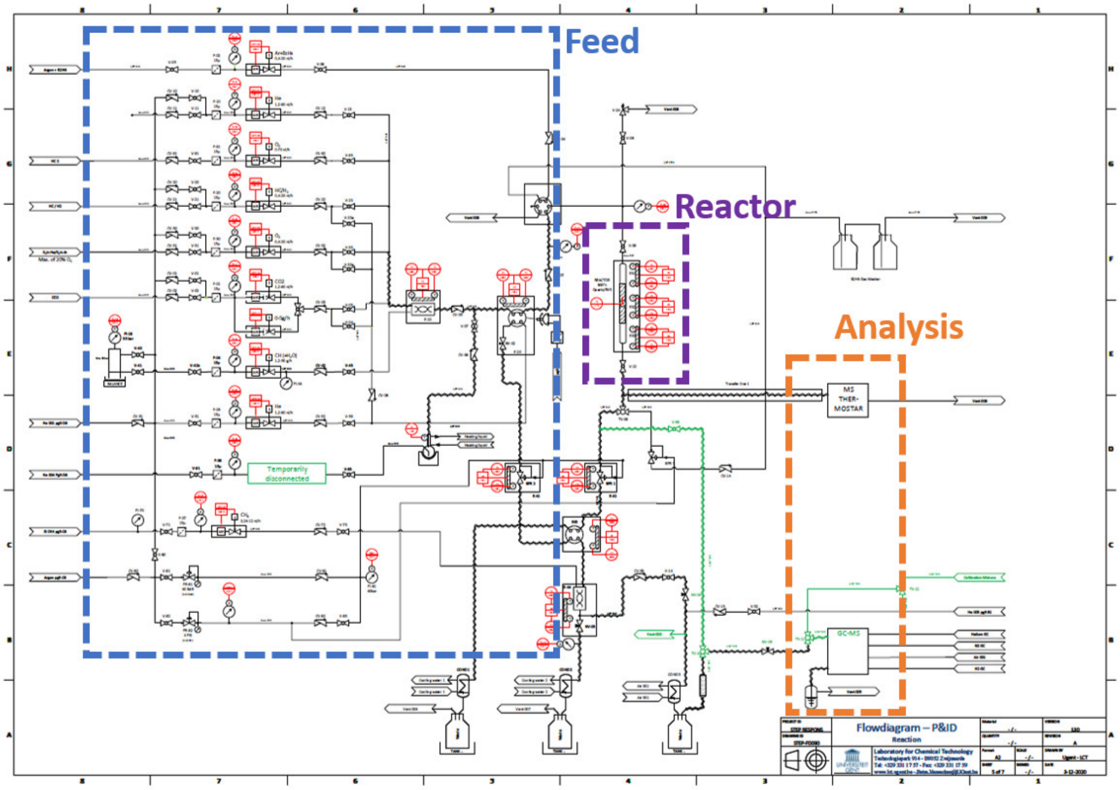

Figure A1: *The flow diagram of the step response setup at Laboratory for Chemical Technology (LCT), Ghent University, with feed, reactor and analysis sections.*

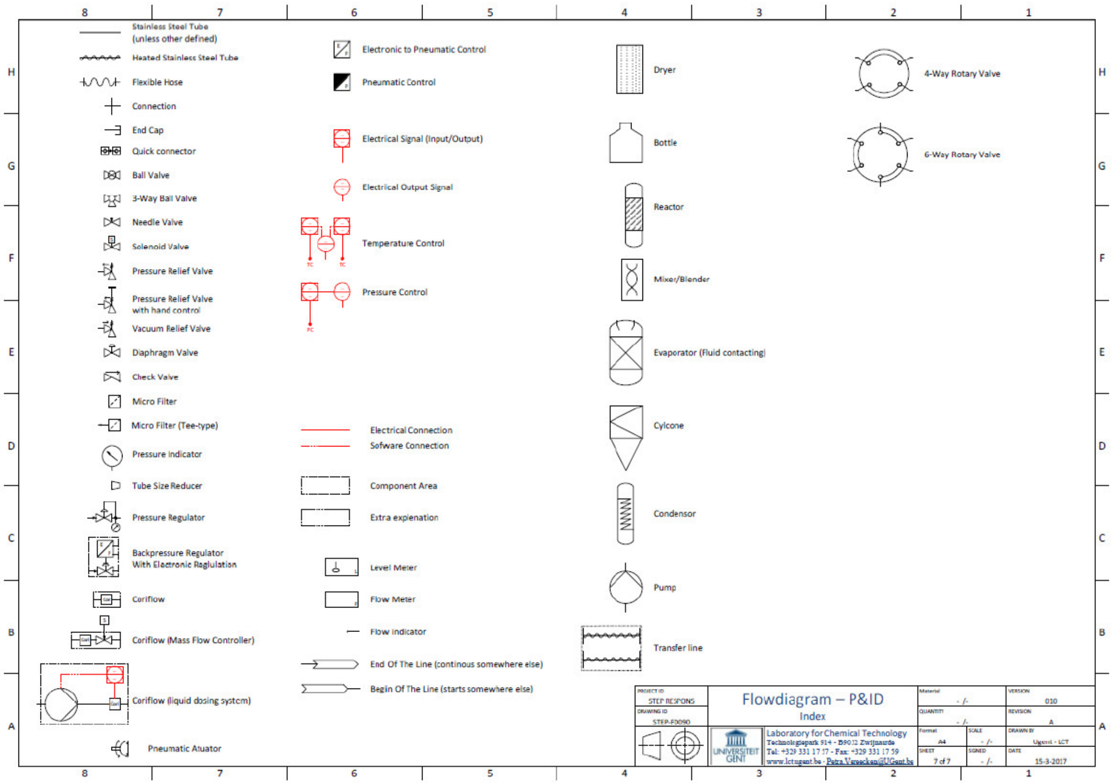

***Figure A2:** List of symbols for the flow diagram (Piping & Instrumentation Diagram - P&ID) in Figure A1.*

Appendix B

Supporting information for Chapter 3

B-1. Pt L_{III}-XANES spectra

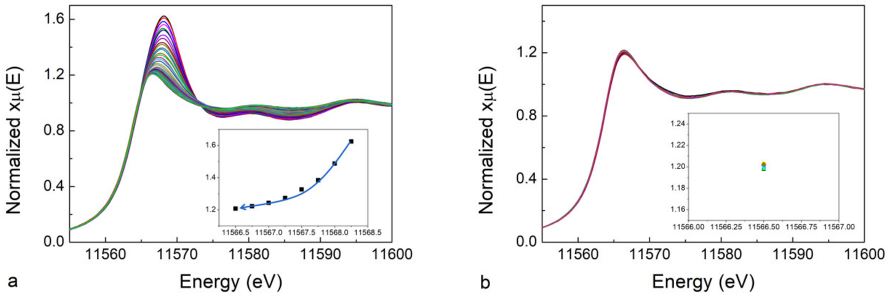

Figure B1: *XANES spectra at Pt L_{III}-edge during* ***a:*** *H_2-TPR from room temperature to 923 K under a flow of 2 ml/min H_2 mixed with 5 ml/min Ar (total flow 7 ml/min) and* ***b:*** *CO_2-TPO (RT to 923 K) at a flow rate of 2 ml/min of CO_2 mixed with 5 ml/min of Ar (7 ml/min total flow) for monometallic Pt/LSA. The insets for the two plots show the maximum WL intensity values taken as average of the data points present at each energy position. The arrows within the inset graphs provide a guide-to the-eye as to how the maxima positions shift with temperature and time.*

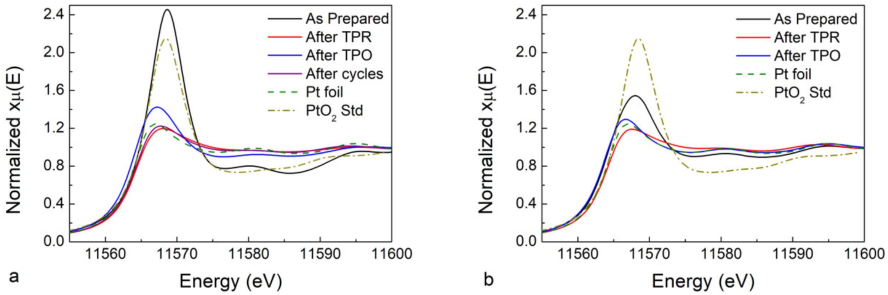

Figure B2: *All RT XANES spectra collected at the Pt L_{III}-edge subsequent to each treatment (H_2-TPR, CO_2-TPO, CO_2/O_2 REDOX cycles) for Pt:Sn supported on* ***a:*** *HSA and* ***b:*** *LSA. The plot also contains the Pt foil and PtO_2 XANES spectra.*

B-2. Sn K-edge XANES spectra

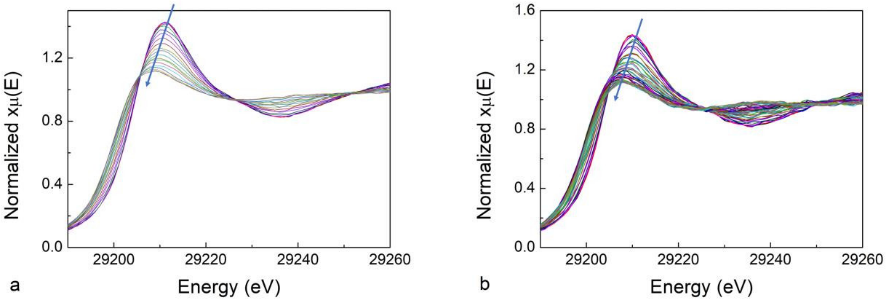

Figure B3: *XANES spectra at Sn K-edge during H_2-TPR from room temperature to 923 K under a flow of 2 ml/min H_2 mixed with 5 ml/min Ar (total flow 7 ml/min), for Pt:Sn samples supported on* ***a:*** *HSA and* ***b:*** *LSA. The arrows provide a guide towards the trend followed during reduction.*

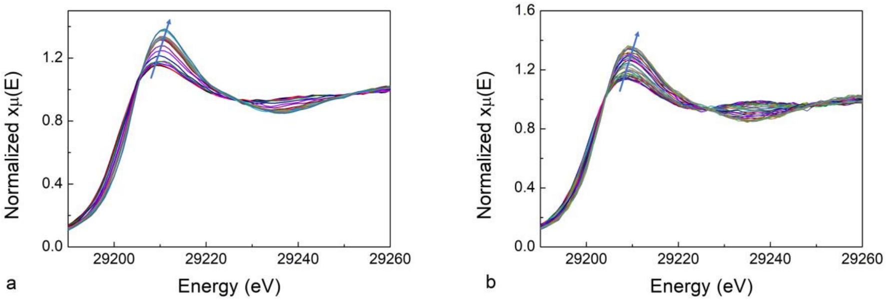

Figure B4: *XANES spectra at Sn K-edge during CO_2-TPO from room temperature to 923 K under a flow of 2 ml/min CO_2 mixed with 5 ml/min Ar (total flow 7 ml/min), for Pt:Sn samples supported on* ***a:*** *HSA and* ***b:*** *LSA. The arrows provide a guide towards the trend followed during oxidation.*

B-3. Pt L_{III}-edge EXAFS fits

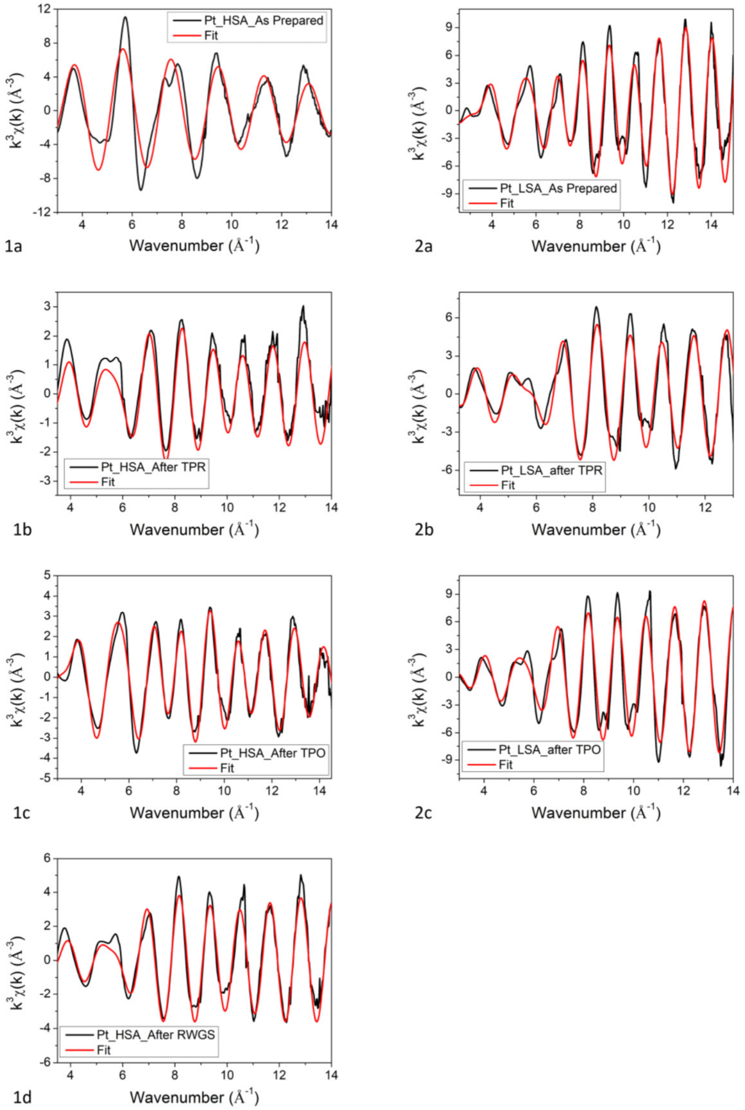

Figure B5: *All k-space signals at the Pt L_{III}-edge for the Pt:Sn/HSA* ***(1)*** *and Pt:Sn/LSA* ***(2)*** *catalysts.* ***a:*** *As prepared state,* ***b:*** *After TPR,* ***c:*** *After TPO and* ***d:*** *After RWGS. All black lines are the original k-space signals, while the red lines are the fits.*

Table B1: *EXAFS fitting results at the Pt L_{III}-edge for Pt:Sn/LSA subsequent to each treatment. Bold values in brackets are Pt cluster sizes when assuming hemispherical nanoparticle shapes.*

	Fresh	**Reduced**	**Oxidised**
$N_{Pt\text{-}O}$	1.7 ± 0.3		9.5 ± 0.4
$R_{Pt\text{-}O}$ (Å)	2.00 ± 0.01		2.76 ± 0.01
$\sigma^2_{Pt\text{-}O}$ (10^{-3} * Å^2)	3.4 ± 1.7		6 ± 0.2
$N_{Pt\text{-}Pt}$	7.3 ± 0.5	8.2 ± 1.4 **(~6 nm)**	
$R_{Pt\text{-}Pt}$ (Å)	2.76 ± 0.01	2.77 ± 0.01	
$\sigma^2_{Pt\text{-}Pt}$ (10^{-3} * Å^2)	5 ± 0.3	6.5 ± 1	
$N_{Pt\text{-}Sn}$		2.5 ± 1.4	
$R_{Pt\text{-}Sn}$ (Å)		2.75 ± 0.01	
$\sigma^2_{Pt\text{-}Sn}$ (10^{-3} * Å^2)		10 ± 2	
ΔE_0 (eV)	4.7 ± 0.7	3.6 ± 1.5	5.1 ± 0.5
R factor	0.04	0.03	0.02

B-4. Sn K-edge EXAFS fits

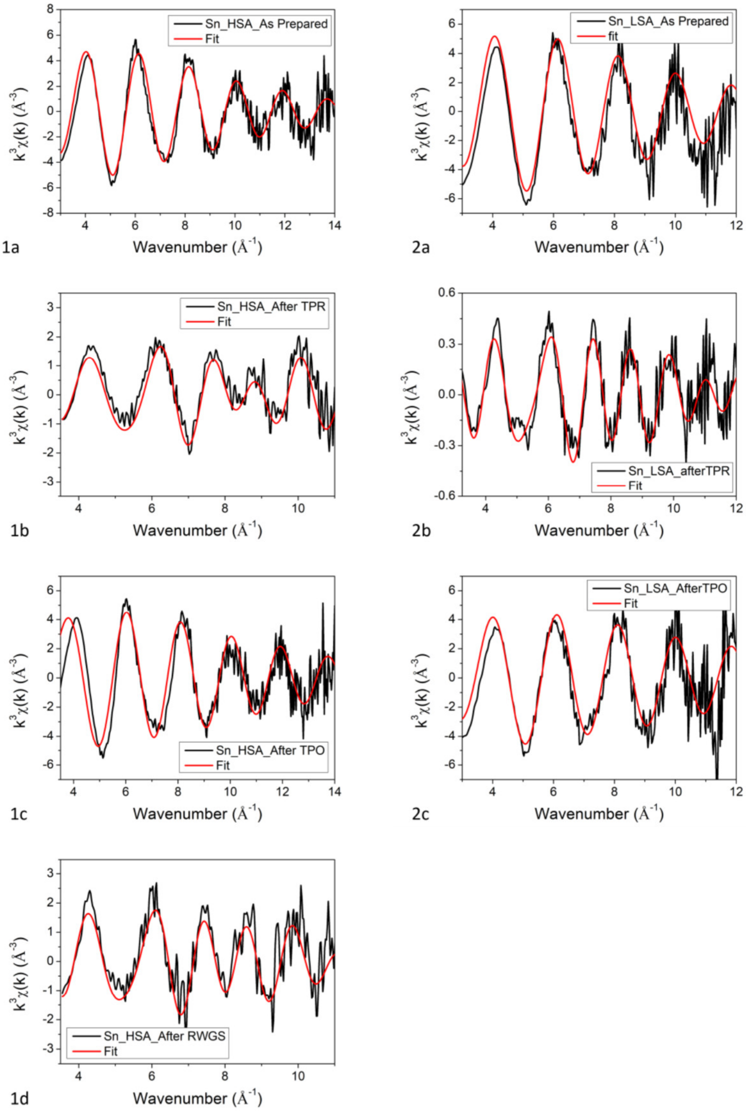

Figure B6: *All k-space signals at the Sn K-edge for the Pt:Sn/HSA* ***(1)*** *and Pt:Sn/LSA* ***(2)*** *catalysts.* ***a:*** *As prepared state,* ***b:*** *After TPR,* ***c:*** *After TPO and* ***d:*** *After RWGS. All black lines are the original k-space signals, while the red lines are the fits.*

Table B2: *EXAFS fitting results at the Sn K-edge for Pt:Sn/LSA subsequent to each treatment.*

	Fresh	**Reduced**	**Oxidised**
N_{Sn-O}	5.8 ± 0.3	0.4 ± 0.1	4.6 ± 0.5
R_{Sn-O} (Å)	2.05 ± 0.01	2.03 ± 0.04	2.04 ± 0.01
σ^2_{Sn-O} (10^{-3} * Å^2)	5.3 ± 0.6	3 ± 2	3.8 ± 0.9
N_{Sn-Pt}		7.6 ± 1.2	
R_{Sn-Pt} (Å)		2.74 ± 0.01	
σ^2_{Sn-Pt} (10^{-3} * Å^2)		10 ± 1.6	
ΔE_0 (eV)	1.6 ± 0.5	0.5 ± 1.6	-6.5 ± 1.6
R factor	0.08	0.07	0.08

B-5. XANES during RWGS reaction

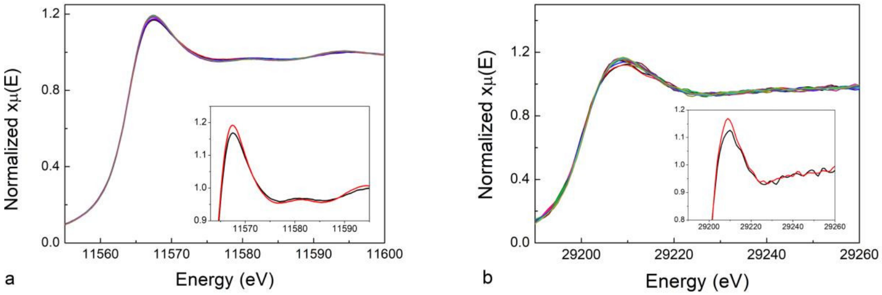

Figure B7: *XANES spectra collected at* ***a:*** *Pt L_{III}-edge and* ***b:*** *Sn K-edge during RWGS reaction at 923 K with 2 ml/min H_2, 2 ml/min CO_2 and 3 ml/min Ar flows for Pt:Sn/HSA sample. Inset of* ***(a&b)*** *shows the first (black) and last (red) spectrum during RWGS.*

B-6. MCR-ALS Results

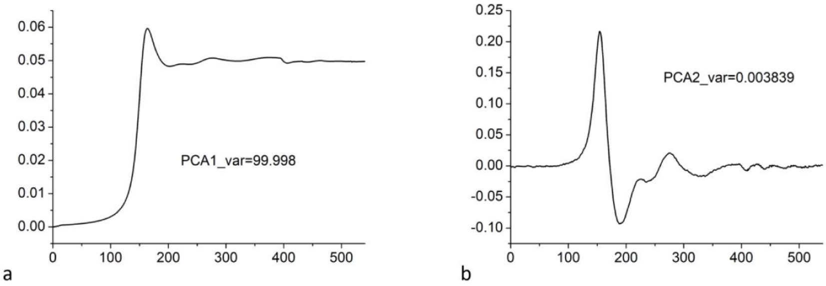

Figure B8: *MCR-ALS determination* ***a & b:*** *main principal components and their respective variances shown in the graph (main graphs Figure 3.5).*

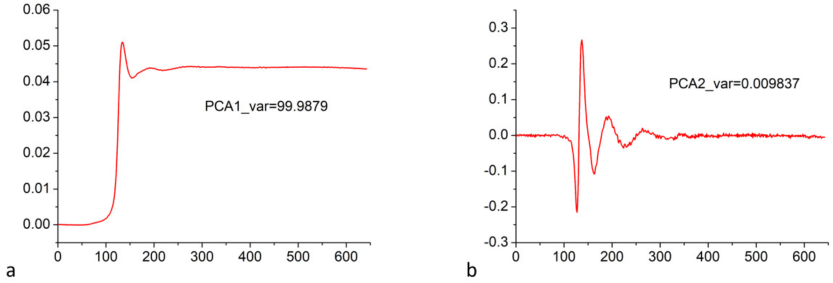

Figure B9: *MCR-ALS determination* ***a & b:*** *main principal components and their respective variances shown in the graph (main graphs Figure 3.7).*

B-7. Pt:Sn Phase diagram

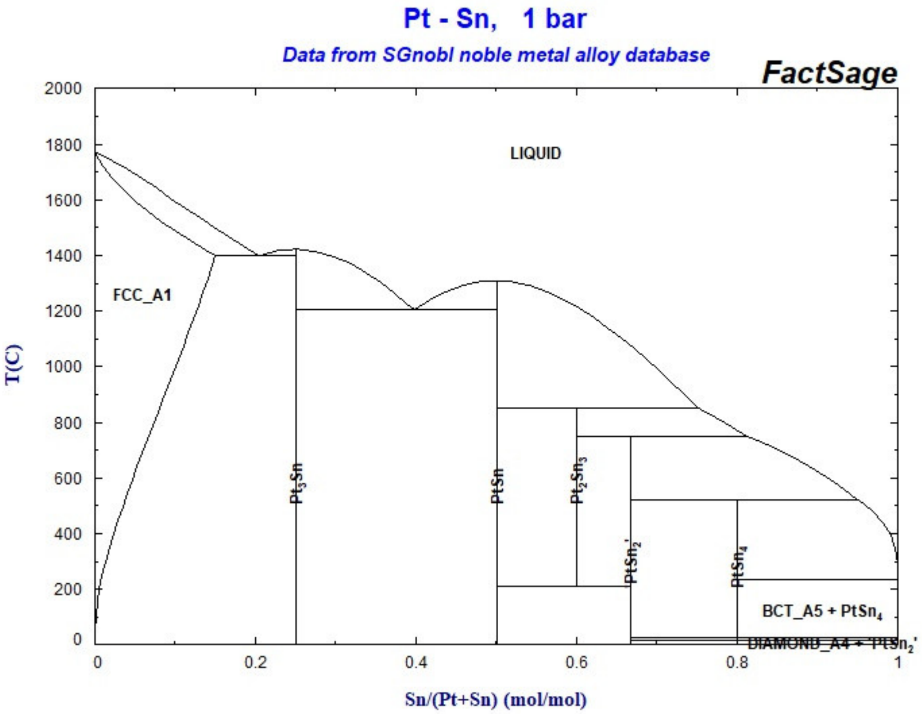

Figure B10: *Pt-Sn phase diagram.*

B-8. PDH activity test results

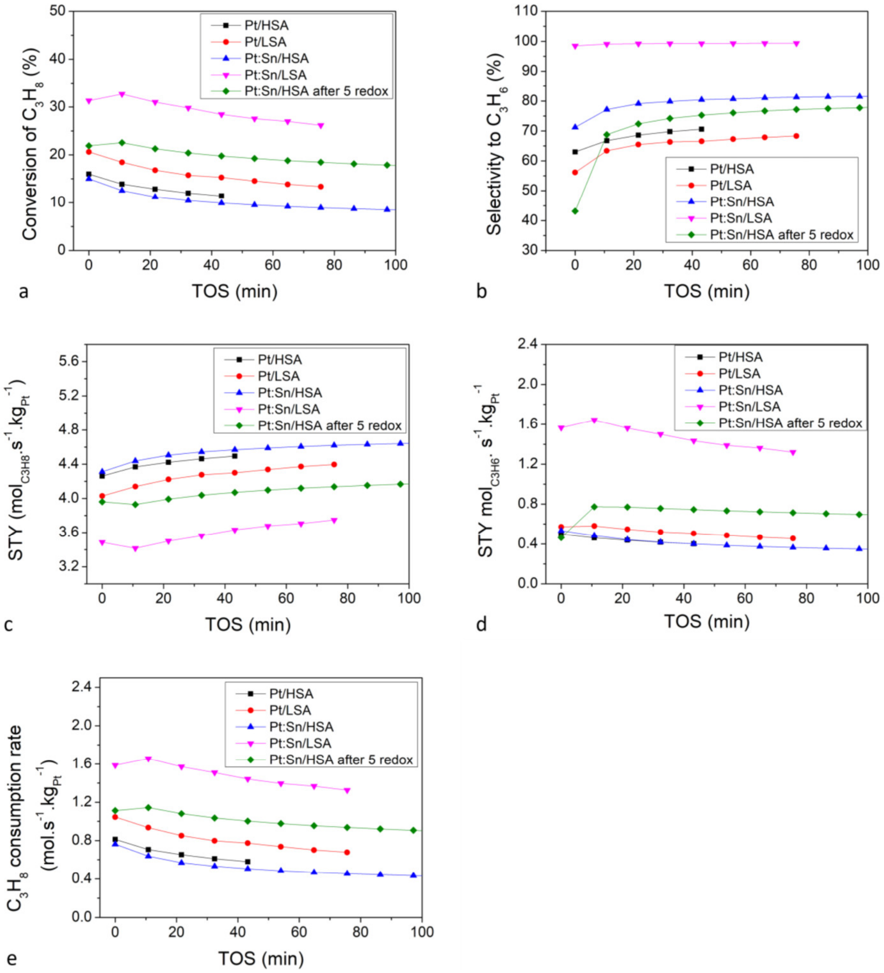

Figure B11: *PDH activity test results for the 4 catalysts (Pt/HSA, Pt/LSA, Pt:Sn/HSA (after 1 reduction step and also after 5 redox cycles), and Pt:Sn/LSA) performed at 873 K and 1.2 bar, with a feed flow of C_3H_8:H_2:Ar at a ratio of 1:1:3 and a total flow rate of 200 Nml/min.* ***a:*** *conversion,* ***b:*** *selectivity to C_3H_6,* ***c:*** *STY of C_3H_8,* ***d:*** *STY of C_3H_6,* ***e:*** *C_3H_8 consumption rate.*

B-9. CO_2-assisted PDH, C_3H_8/O_2 cycles, and RWGS experiments

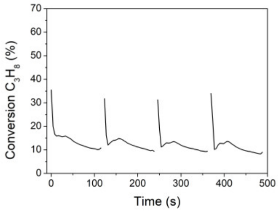

Figure B12: *C_3H_8/O_2 alternating flow results at 873 K. Propane was flown (40 Nml/min) over the catalyst for 2 mins after which O_2 was fed (10 Nml/min) for 2 mins. The oxygen flow is not shown in the plot, but it was in between the slight increases of activity observed.*

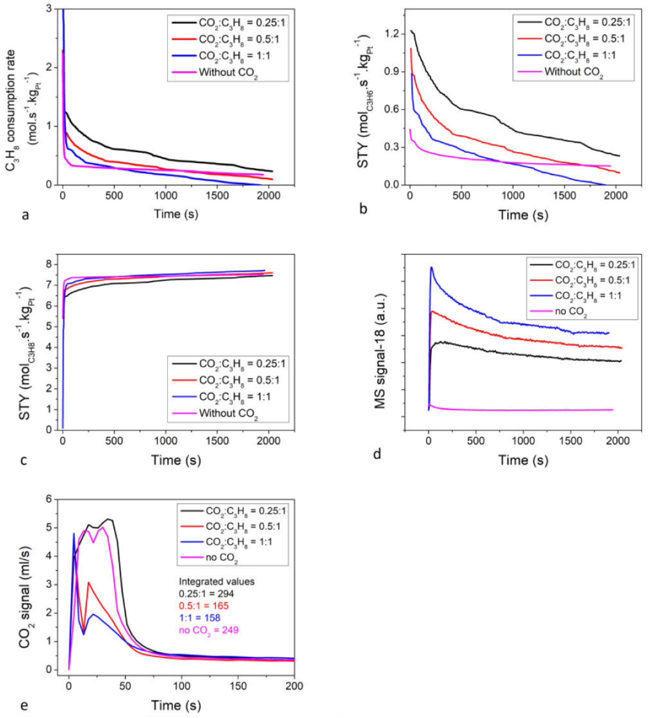

Figure B13: a: *Propane consumption rates for the CO_2-assisted PDH experiment.* ***b & c:*** *STY for propylene and propane, respectively. Reactions performed at 873 K over the Pt:Sn/HSA catalyst.* ***d:*** *Signal at m/z=18 (H_2O) during the reaction.* ***e:*** *signal at m/z = 44 (CO_2) when flowing 100 ml/min of 10% O_2/Ar at 873 K subsequent to the CO_2-PDH reactions. Integrated values of areas are shown within the graph.*

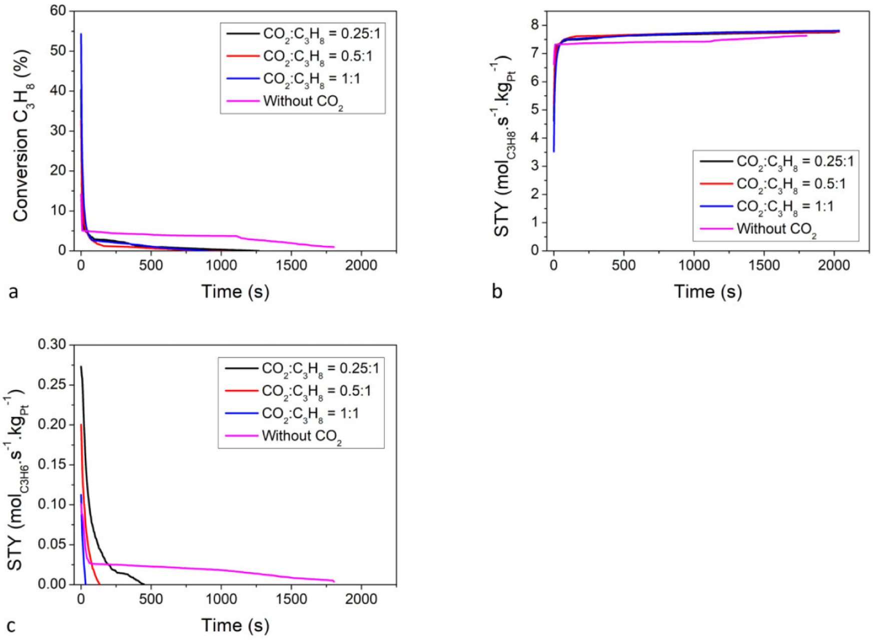

Figure B14: ***a & b:*** *STY for propylene and propane, respectively.* ***c:*** *conversion of propane. Reactions performed at 873 K for the monometallic Pt/HSA catalyst.*

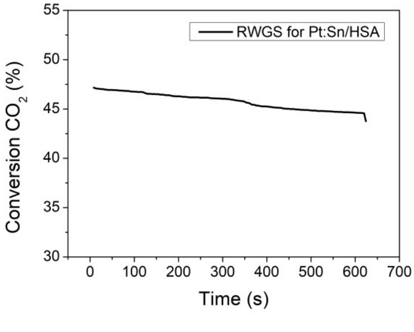

Figure B15: *RWGS at 873 K for the Pt:Sn/HSA catalyst with flows of C_3H_8 = 20 Nml/min, CO_2 = 20 Nml/min and Ar = 160 Nml/min.*

Appendix C

Supporting information for Chapter 4

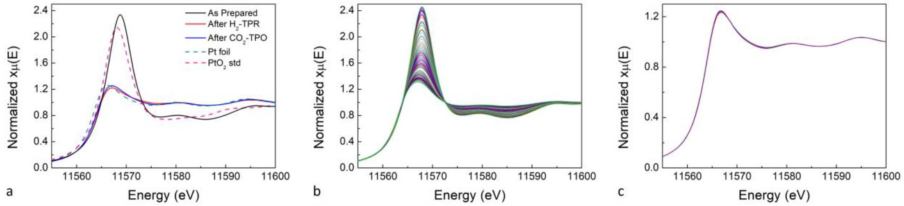

Figure C1: *XAS data at the Pt L_{III}-edge for the monometallic $Pt/MgAl_2O_4$ sample.* ***a:*** *XANES spectra at RT subsequent to the treatments.* ***b:*** *XANES during H_2-TPR up to 873 K. Final WL position reached was 11567.2 eV.* ***c:*** *XANES spectra during CO_2-TPO up to 873 K.*

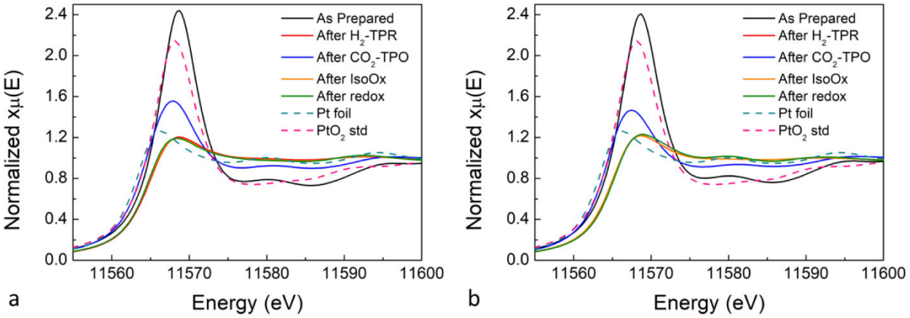

Figure C2: *All RT XANES spectra collected at the Pt L_{III}-edge subsequent to each treatment (H_2-TPR, CO_2-TPO, Isothermal CO_2-oxidation, H_2/O_2 & H_2/CO_2 redox cycles, maximum temperature 873 K) for* ***a:*** *Pt:In and* ***b:*** *Pt:Sn. The plots also contain the reference spectra of Pt foil and PtO_2 (dashed lines).*

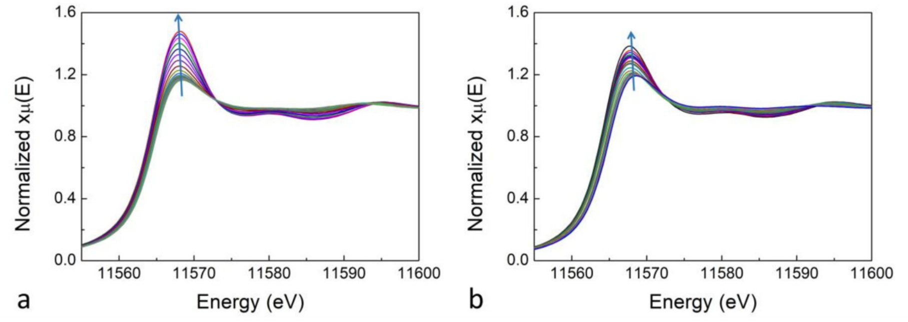

Figure C3: *XANES CO_2-TPO profiles up to 873 K at the Pt L_{III}-edge for* ***a:*** *Pt:In and* ***b:*** *Pt:Sn. CO_2 = 5 Nml/min, He = 5 Nml/min (total flow = 10 Nml/min). The arrows show the direction of change.*

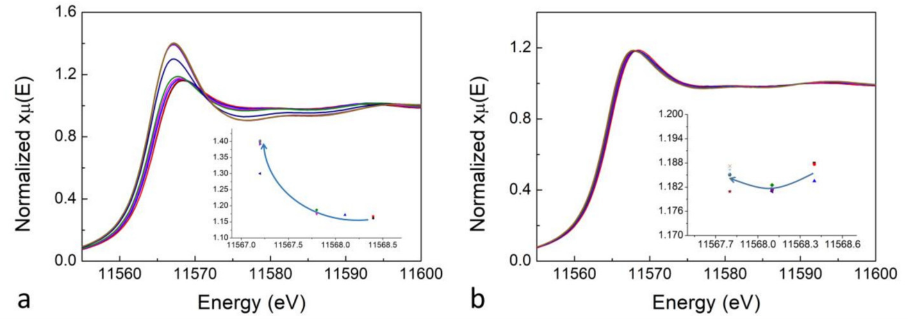

Figure C4: *XANES profiles during Isothermal CO_2-oxidation at 873 K at the Pt L_{III}-edge for* ***a:*** *Pt:In and* ***b:*** *Pt:Sn. The insets of the graphs show the evolution of the WL maxima during the isothermal oxidation. CO_2 = 5 Nml/min, He = 5 Nml/min (total flow = 10 Nml/min).*

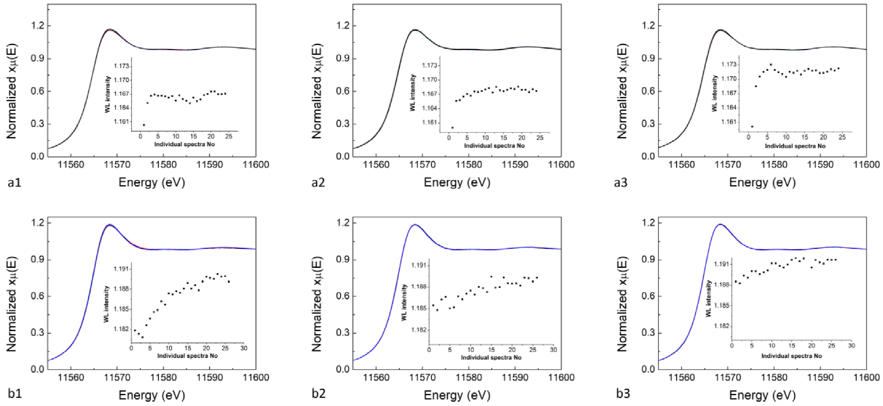

Figure C5: *RWGS measurements at 873 K at the Pt L_{III}-edge for **a:** Pt:In, **b:** Pt:Sn. **1:** 1:1 H_2:CO_2 (H_2 = 1 Nml/min, CO_2 = 1 Nml/min, He = 8 Nml/min), **2:** 1:3 H_2:CO_2 (H_2 = 1 Nml/min, CO_2 = 3 Nml/min, He = 6 Nml/min), **3:** 1:5 H_2:CO_2 (H_2 = 1 Nml/min, CO_2 = 5 Nml/min, He = 4 Nml/min). Insets of the graphs show the evolution of WL intensity.*

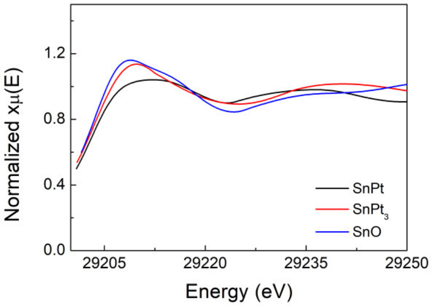

Figure C6: *Theoretical XANES spectra at the Sn K-edge for 3 different standard crystals: Pt_3Sn, PtSn, SnO.*

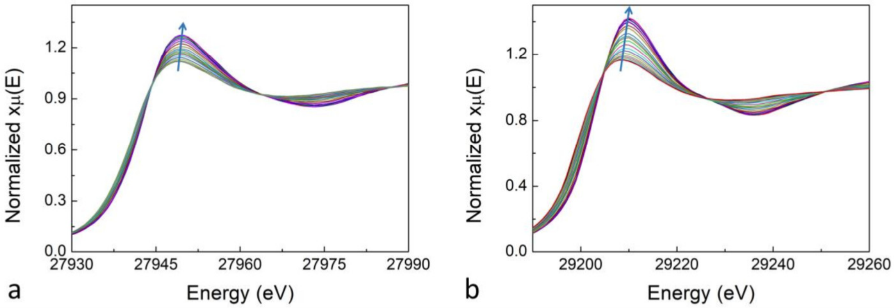

Figure C7: *XANES profiles during CO_2-TPO up to 873 K for* ***a:*** *Pt:In (In K-edge) and* ***b:*** *Pt:Sn (Sn K-edge). CO_2 = 5 Nml/min, He = 5 Nml/min (total flow = 10 Nml/min).*

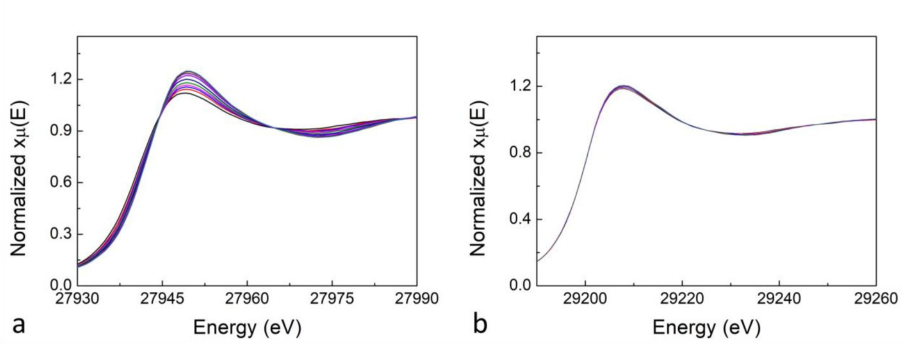

Figure C8: *XANES profiles during isothermal CO_2-oxidation at 873 K for* ***a:*** *Pt:In (In K-edge) and* ***b:*** *Pt:Sn (Sn K-edge). CO_2 = 1 Nml/min, He = 9 Nml/min (total flow = 10 Nml/min).*

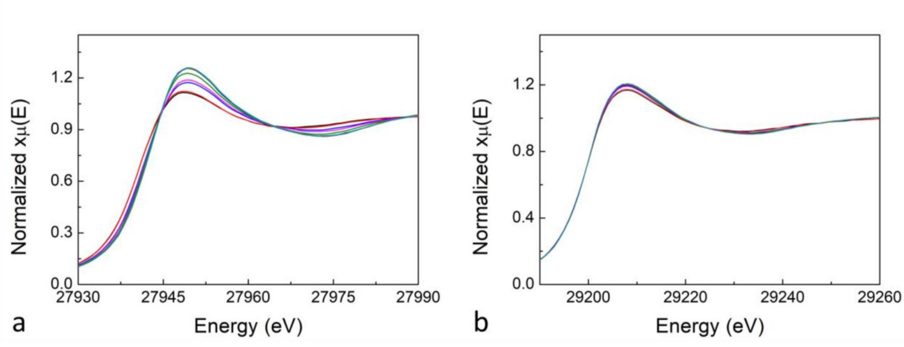

Figure C9: *XANES profiles during isothermal CO_2-oxidation at 873 K for* ***a:*** *Pt:In (In K-edge) and* ***b:*** *Pt:Sn (Sn K-edge). CO_2 = 5 Nml/min, He = 5 Nml/min (total flow = 10 Nml/min).*

XANES analysis for Pt:In/$MgAl_2O_4$ with 6wt% In. This shall henceforth be named as Pt:In6.

Experiments for Pt:In6 were performed similar to the experiments done for Pt:In and Pt:Sn. The only difference in terms of experiments performed being that, no modulation excitation experiments were conducted for this catalyst. A few but not all of the results are shown and discussed below.

All the XANES spectra are presented in the figure C10. The final WL position subsequent to the H_2-TPR was found to be located at 11569 eV, which is 0.6 eV higher than for the Pt:In sample. This indicates that a Pt-In alloy phase with more In than for Pt:In was formed for Pt:In6. Pt underwent complete reduction, while In underwent partial reduction.

During CO_2-TPO up to 873 K (figure C10-3), just like for the Pt:In sample, In oxidized back completely, leading to a change in the Pt WL.

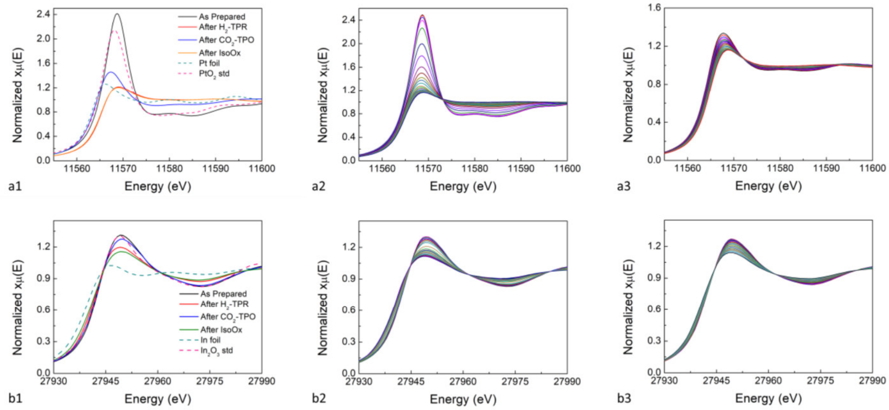

Figure C10: *XANES spectra for Pt:In6 at the* ***a:*** *Pt L_{III}-edge and* ***b:*** *In K-edge.* ***1:*** *All RT XANES spectra subsequent to experiments,* ***2:*** *H_2-TPR XANES profiles up to 873 K and* ***3:*** *CO_2-TPO profiles up to 873 K.*

EXAFS results

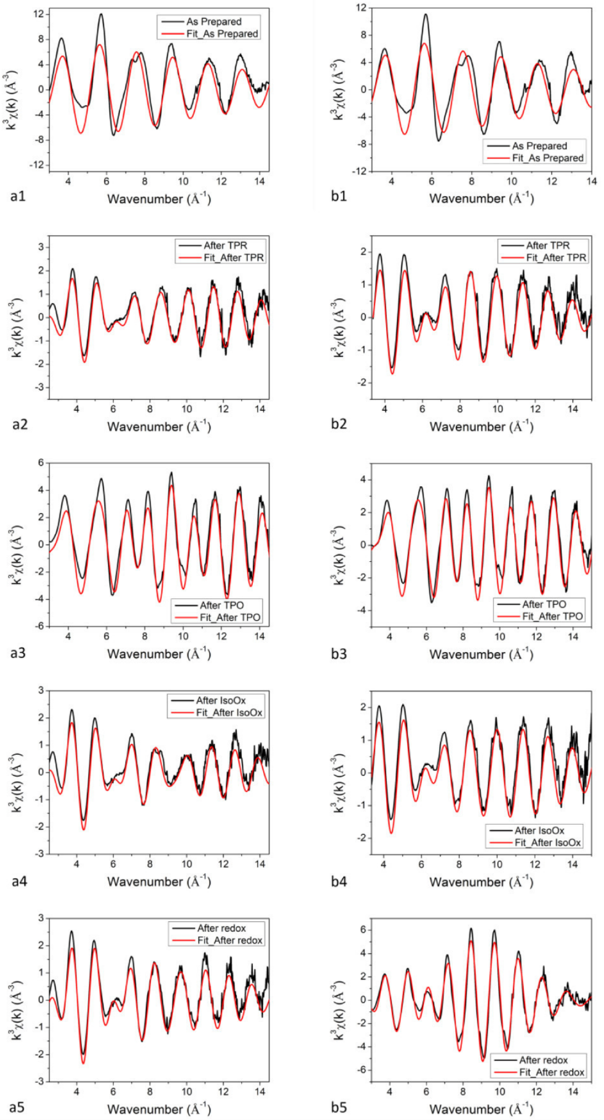

Figure C11: *All k-space signals at the Pt L_{III}-edge for the* ***(a)*** *Pt:In and* ***(b)*** *Pt:Sn catalysts.* ***1:*** *As prepared state,* ***2:*** *After H_2-TPR,* ***3:*** *After CO_2-TPO,* ***4:*** *After IsoOx,* ***5:*** *After redox. All black lines are the original k-space signals, while the red lines are the fits.*

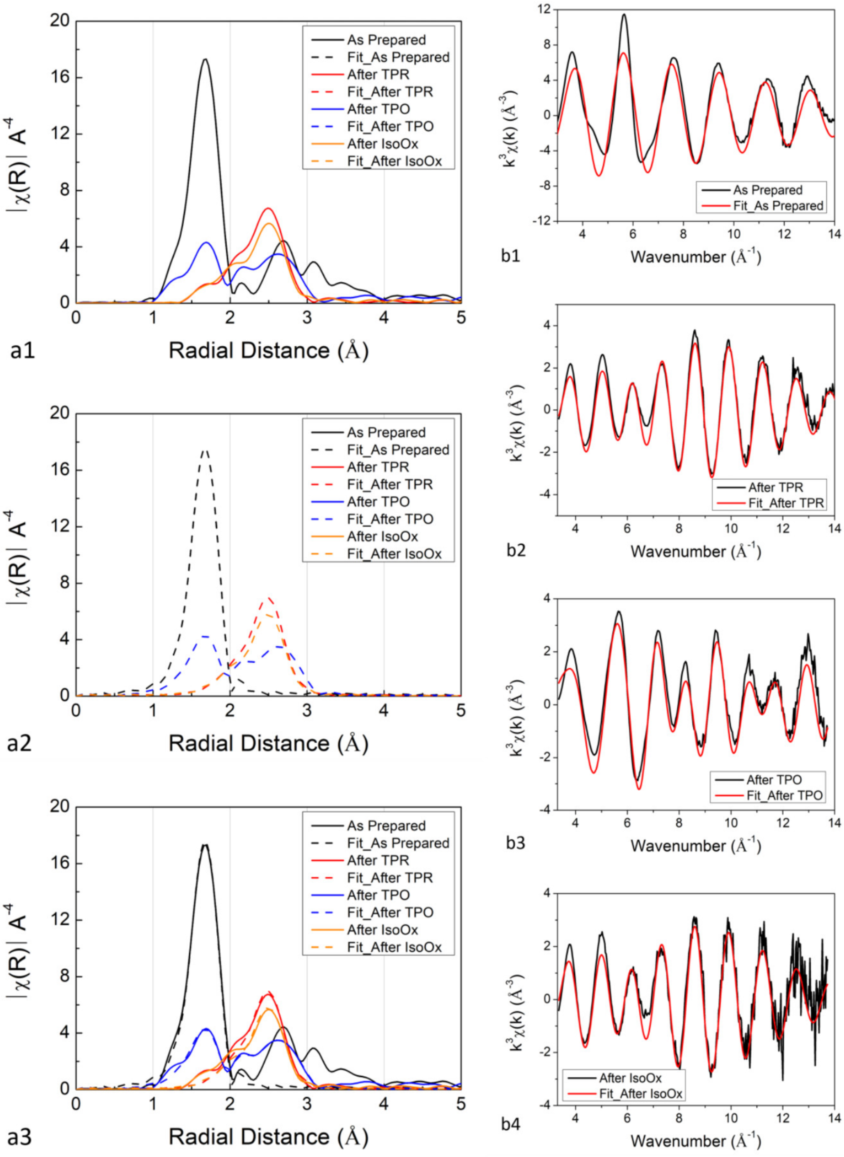

***Figure C12:** EXAFS spectra at Pt L_{III} for PtIn6. **a1:** Fourier transformed R-space spectra at RT, subsequent to each treatment, **a2:** Fit of R-space spectra, **a3:** Merged graph including data and fit together. **b:** k-space signals at the Pt L_{III}-edge for **1:** As prepared state, **2:** After TPR, **3:** After TPO, **4:** After IsoOx.*

***Table C1:** EXAFS fitting results at the Pt L_{III}-edge for the Pt:In6 catalyst at RT, subsequent to each experiment.*

	Fresh	**AfterTPR**	**AfterTPO**	**After IsoOx**
N_{Pt-O}	6.3 ± 0.3		2.1 ± 0.4	
R_{Pt-O} (Å)	2.01 ± 0.01		2.02 ± 0.01	
σ_{Pt-O} (10^{-3}*Å^2)	3.2 ± 0.3		6 ± 2	
N_{Pt-In}		4.5 ± 0.4		4.3 ± 0.7
R_{Pt-In} (Å)		2.68 ± 0.01		2.67 ± 0.006
σ_{Pt-In} (10^{-3}*Å^2)		9.7 ± 0.5		10 ± 1
N_{Pt-Pt}			5.2 ± 1.4	
R_{Pt-Pt} (Å)			2.73 ± 0.01	
σ_{Pt-Pt} (10^{-3}*Å^2)			10 ± 2	
ΔE_0 (eV)	7.1 ± 0.6	1.0 ± 0.9	6.5 ± 2.5	-0.6 ± 1.3
R factor	0.04	0.06	0.05	0.04

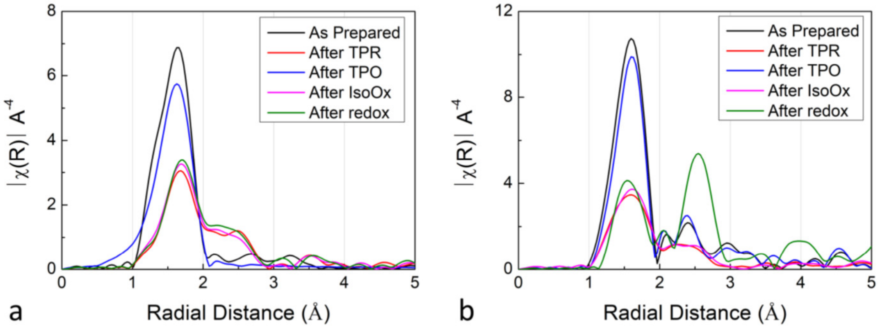

***Figure C13:** R-space spectra resulting from the RT EXAFS after each treatment, at the **a:** In K-edge (for Pt:In) and **b:** Sn K-edge (for Pt:Sn).*

***Table C2:** EXAFS fitting results at the In K-edge for the Pt:In catalyst subsequent to each experiment.*

	As prepared	**After TPO**
N_{In-O}	6.3 ± 0.8	5.7 ± 0.6
R_{In-O} (Å)	2.11 ± 0.8	2.11 ± 0.01
σ^2_{In-O} (10^{-3}*Å^2)	8.6 ± 1.3	9.9 ± 1.2
ΔE_0 (eV)	-2.6 ± 1.4	-0.18 ± 1.4
R factor	0.07	0.07

Table C3: *EXAFS fitting results at the Sn K-edge for the Pt:Sn catalyst subsequent to each experiment.*

	Fresh	**After TPO**	**After redox**
N_{Sn-O}	6.0 ± 0.9	5.3 ± 0.6	2.14 ± 0.24
R_{Sn-O} (Å)	2.03 ± 0.01	2.03 ± 0.01	2.06 ± 0.01
σ^2_{Sn-O} (10^{-3}*Å^2)	4.9 ± 1.1	4.8 ± 0.9	6.8 ± 1.1
N_{Sn-Pt}			2.8 ± 0.5
R_{Sn-Pt} (Å)			2.71 ± 0.01
σ^2_{Sn-Pt}(10^{-3}*Å^2)			6.4 ± 0.9
ΔE_0 (eV)	-0.88 ± 2.3	0.3 ± 1.7	5.2 ± 2.1
R factor	0.06	0.07	0.05

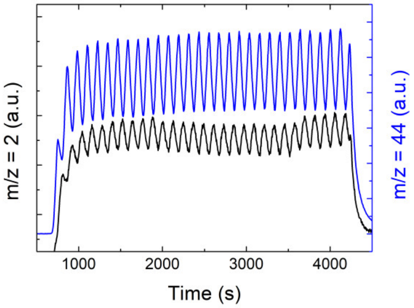

Figure C14: *MS signals for H_2 (m/z = 2) and CO_2 (m/z = 44).*

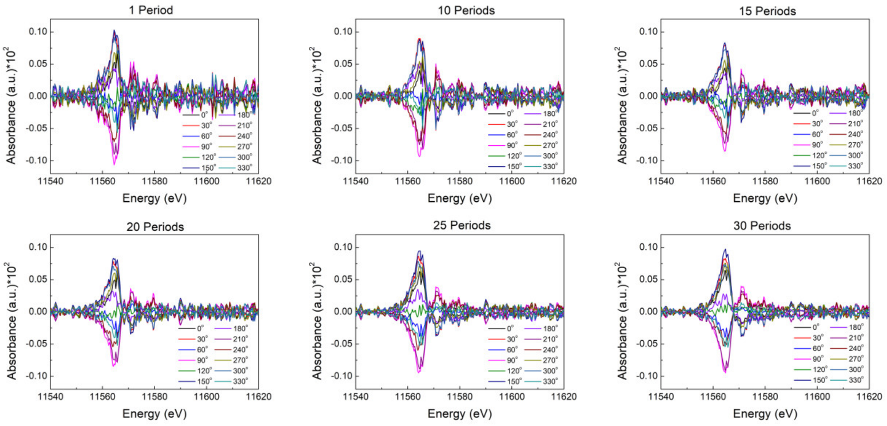

Figure C15: *Demodulated Pt L_{III} spectra for Pt:Sn consisting of 24 spectra each averaged over 1, 10, 15, 20, 25 & 30 periods. ME spectra acquired at 873 K during H_2:CO_2 cycling.*

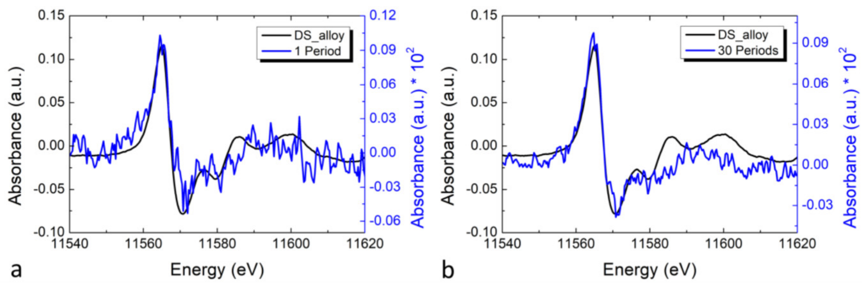

Figure C16: *Demodulated Pt L_{III} spectra averaged over* ***a:*** *1 period****,*** ***b:*** *30 periods, comparison with DS generated from the "After TPR" and "After redox" states for the Pt:Sn sample.*

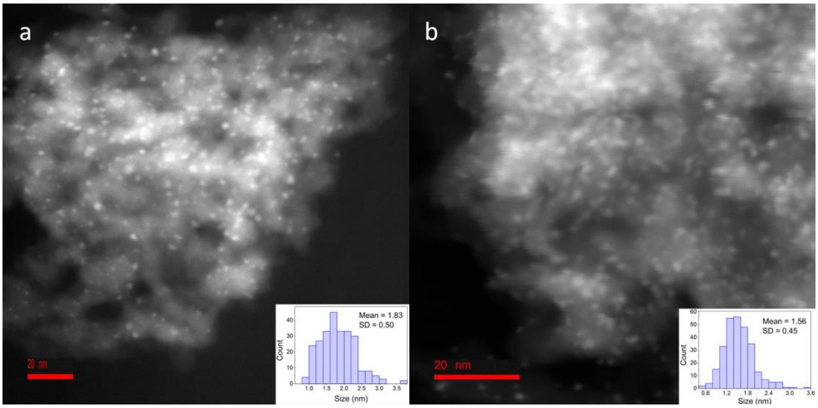

Figure C17: *DF-STEM images and their particle size distributions of* ***a:*** *Pt:In and* ***b:*** *Pt:Sn subsequent to all the XAS measurements.*

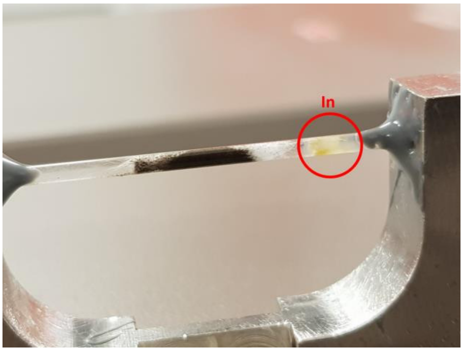

Figure C18: *Picture of the capillary after the in situ XAS experiments for the Pt:In sample. The yellow colouration of the inner wall of the capillary stems from In that was lost from the catalyst.*

Appendix D:

Supporting information for Chapter 5

D-1. Ellingham diagrams

The Ellingham diagrams are plotted for Ga, In and Sn under O_2, CO_2 and H_2 atmospheres (Figure D1). The calculations were performed based on values of constants and other thermodynamic data from thermochemical data available in literature[1]. From the O_2 Ellingham diagram, it can be seen that the 3 elements prefer to stay in an oxidised state throughout the applied conditions. They will only reduce when O_2 partial pressures fall below the respective Ellingham lines for each of the elements. Under CO_2 atmosphere none of the 3 elements should oxidise to their respective oxides, based on the calculations. This however is applicable to bulk systems and it can be different for nanoparticles, which has been shown for other systems[2,3]. The properties of the 3 gases, O_2, CO_2 and H_2, were obtained through the NIST database.

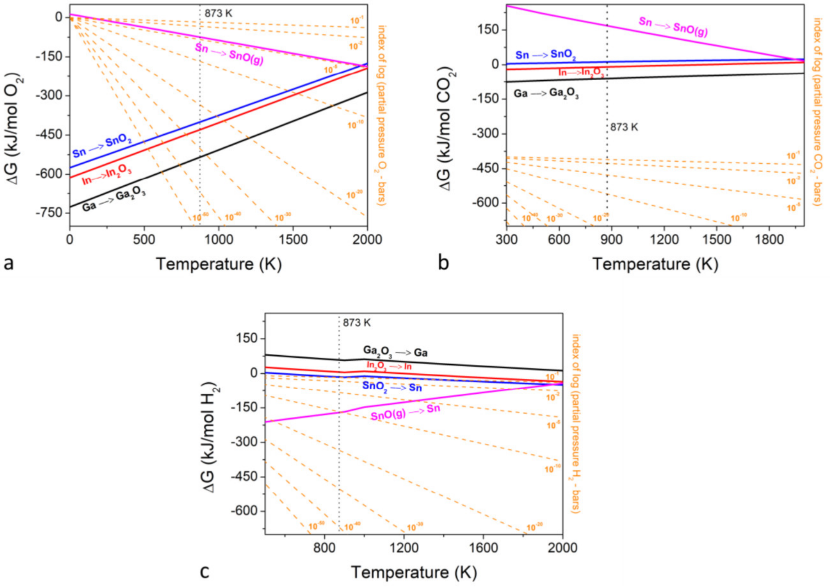

Figure D1: *Ellingham diagrams for Ga, In and Sn under* ***a:*** *O_2,* ***b:*** *CO_2 and* ***c:*** *H_2 atmospheres.*

The formulas used for plotting of the Ellingham diagrams are listed in the Table D1.

Table D1: *List of equations used for calculation of values depicted in the Ellingham diagrams. The properties of O_2, CO_2, H_2, CO and H_2O were obtained from the NIST database.*

	Ga	**In**	**Sn**
O_2	$(4/3)Ga + O_2 \rightarrow (2/3)\ Ga_2O_3$	$(4/3)In + O_2 \rightarrow (2/3)\ In_2O_3$	$Sn + O_2 \rightarrow SnO_2$
CO_2	$(2/3)Ga + CO_2 \rightarrow (1/3)\ Ga_2O_3 + CO$	$(2/3)In + CO_2 \rightarrow (1/3)\ In_2O_3 + CO$	$(1/2)Sn + CO_2 \rightarrow (1/2)SnO_2 + CO$
H_2	$(1/3)Ga_2O_3 + H_2 \rightarrow (2/3)Ga + H_2O$	$(1/3)In_2O_3 + H_2 \rightarrow (2/3)In + H_2O$	$(1/2)SnO_2 + H_2 \rightarrow (1/2)Sn + H_2O$

D-2. Catalyst characterizations

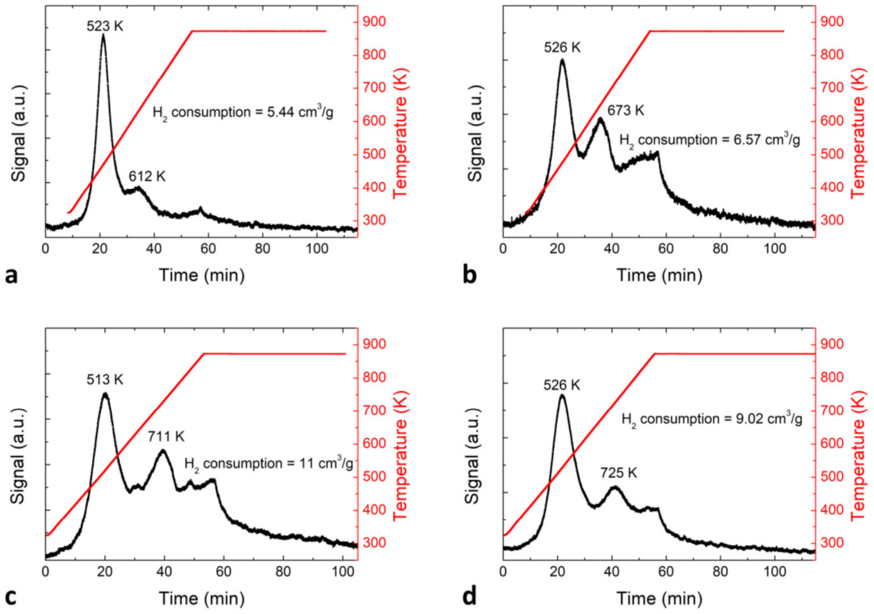

Figure D2: *H_2-TPR signal for* ***a:*** *Pt/$MgAl_2O_4$,* ***b:*** *Pt:Ga/$MgAl_2O_4$,* ***c:*** *Pt:In/$MgAl_2O_4$,* ***d:*** *Pt:Sn/$MgAl_2O_4$. One main peak appears for the monometallic sample, two major peaks are observed for all three bimetallic samples.*

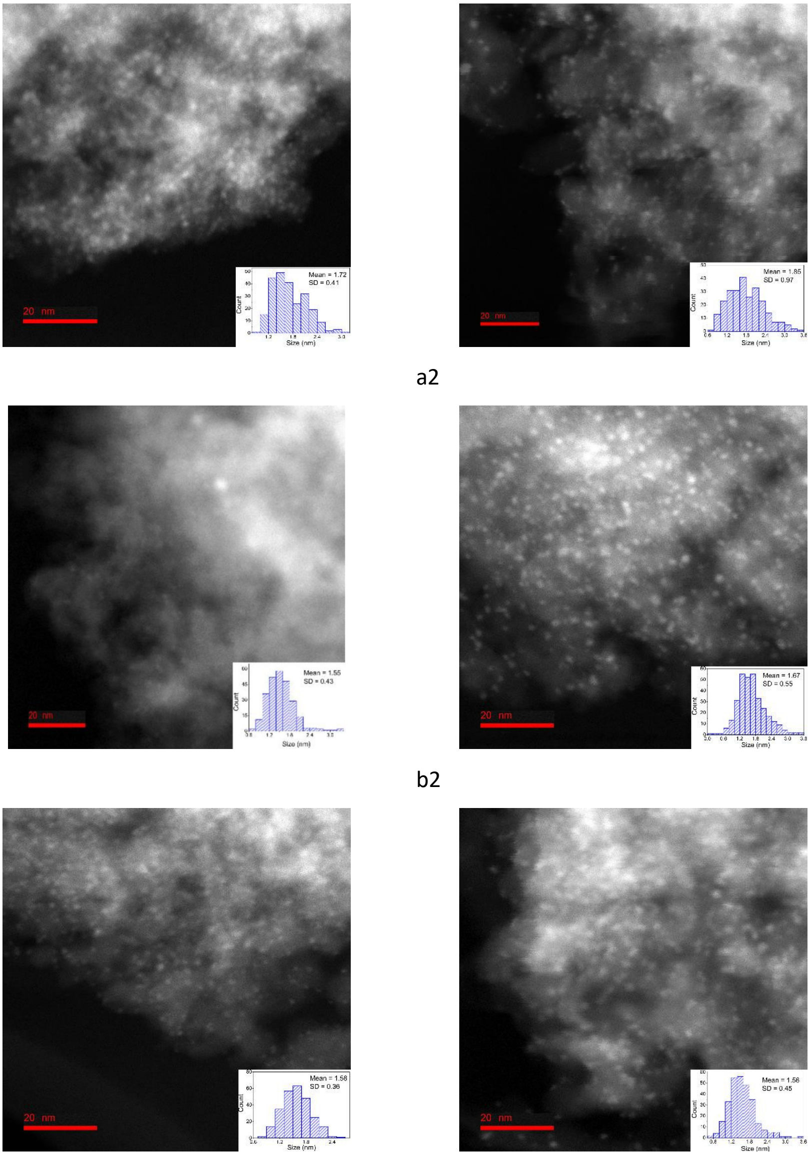

a1 a2

b1 b2

c1 c2

Figure D3: *DF STEM images for the bimetallic catalysts.* ***a1:*** *Pt:Ga/$MgAl_2O_4$ reduced,* ***a2:*** *Pt:Ga/$MgAl_2O_4$ after 20 redox cycles/spent,* ***b1:*** *Pt:In/$MgAl_2O_4$ reduced,* ***b2:*** *Pt:In/$MgAl_2O_4$ after 20 redox cycles/spent,* ***c1:*** *Pt:Sn/$MgAl_2O_4$ reduced and* ***c2:*** *Pt:Sn/$MgAl_2O_4$ after 20 redox cycles/spent.*

D-3 Activity test results

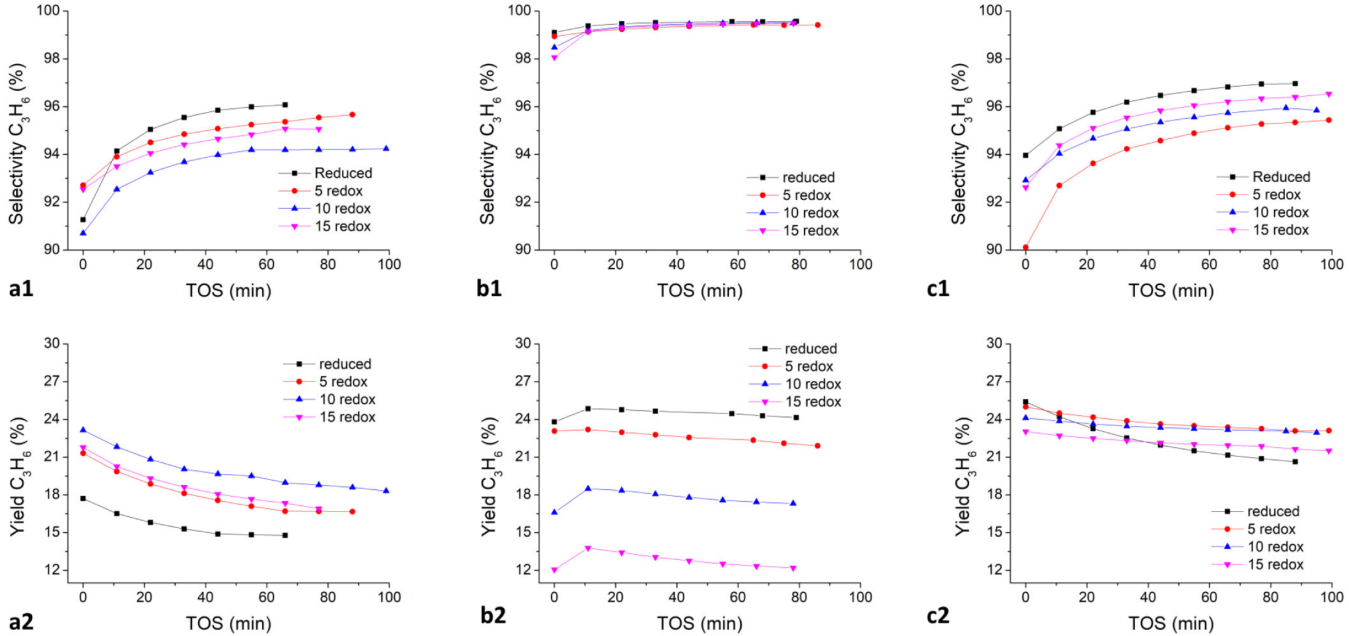

Figure D4: *Activity plots during PDH for* ***a:*** *Pt:Ga,* ***b:*** *Pt:In and* ***c:*** *Pt:Sn.* ***1:*** *Propylene selectivity &* ***2:*** *propylene yield. Flows for PDH: C_3H_8 = 40 Nml/min, H_2 = 40 Nml/min, Ar = 70 Nml/min. Total flow = 150 Nml/min. Catalyst amount = 0.1 g. T = 873 K. P = 1.2 bar.*

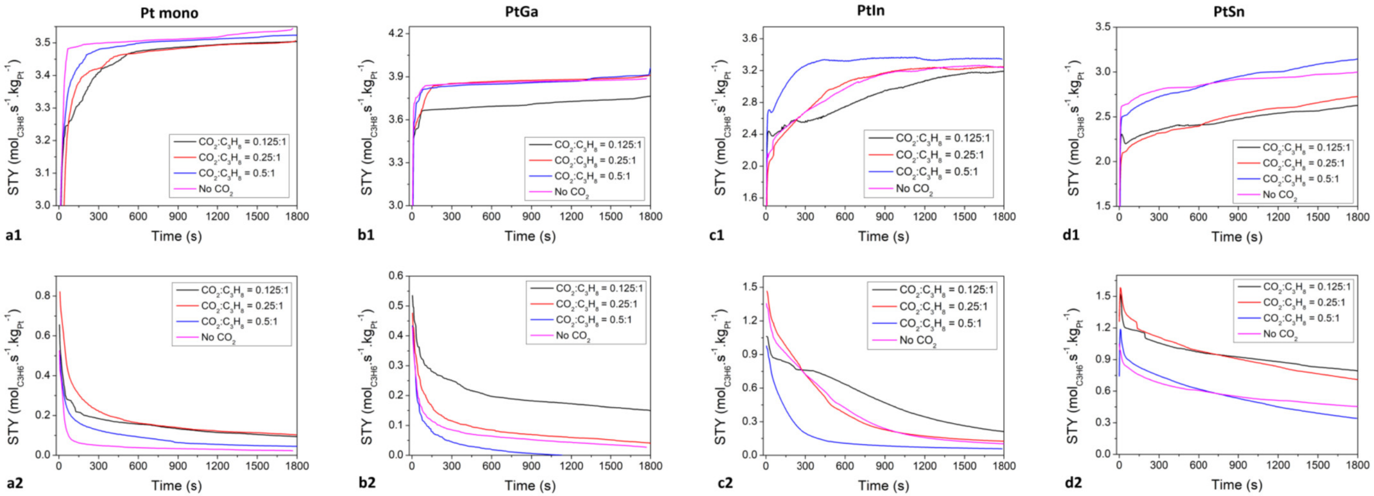
Pt mono
PtGa
PtIn
PtSn
STY (mol$_{C3H8}$.s^{-1}.kg$_{Pt}$$^{-1}$)
STY (mol$_{C3H6}$.s^{-1}.kg$_{Pt}$$^{-1}$)
Time (s)
CO_2:C_3H_8 = 0.125:1
CO_2:C_3H_8 = 0.25:1
CO_2:C_3H_8 = 0.5:1
No CO_2
a1
b1
c1
d1
a2
b2
c2
d2
0
300
600
900
1200
1500
1800

-

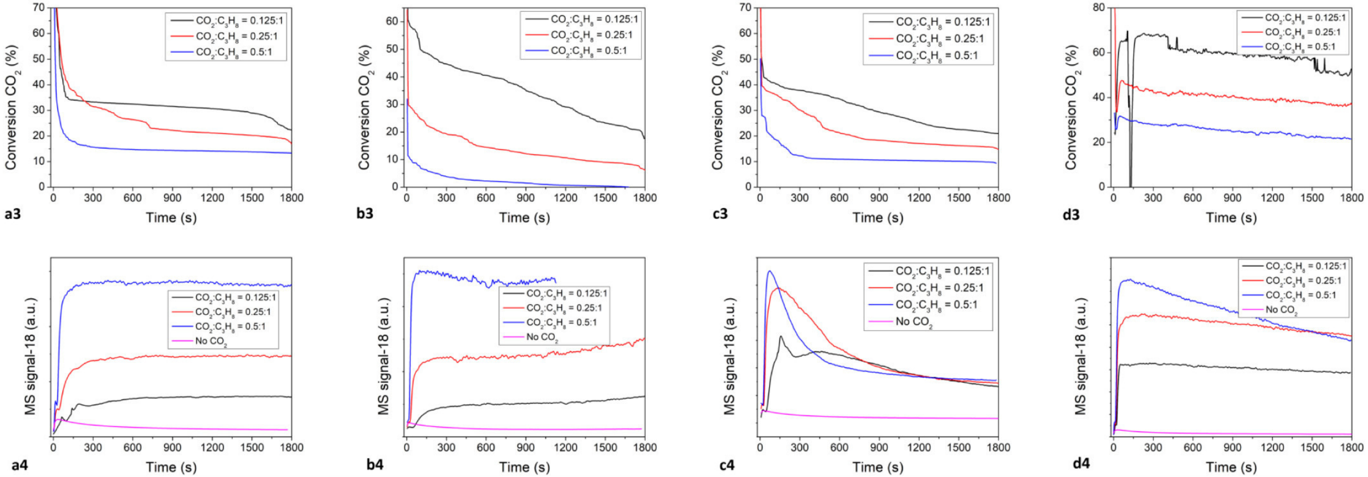

Figure D5: *All activity plots for ratio studies for CO_2-PDH for* ***a:*** *Pt/$MgAl_2O_4$,* ***b:*** *Pt:Ga,* ***c:*** *Pt:In and* ***d:*** *Pt:Sn.* ***1:*** *Space time yield (STY) C_3H_6,* ***2:*** *STY C_3H_8,* ***3:*** *CO_2 conversion,* ***4:*** *m/z = 18 signal (for H_2O outlet). For information on flow rates please refer to §5.2.3 in chapter 5.*

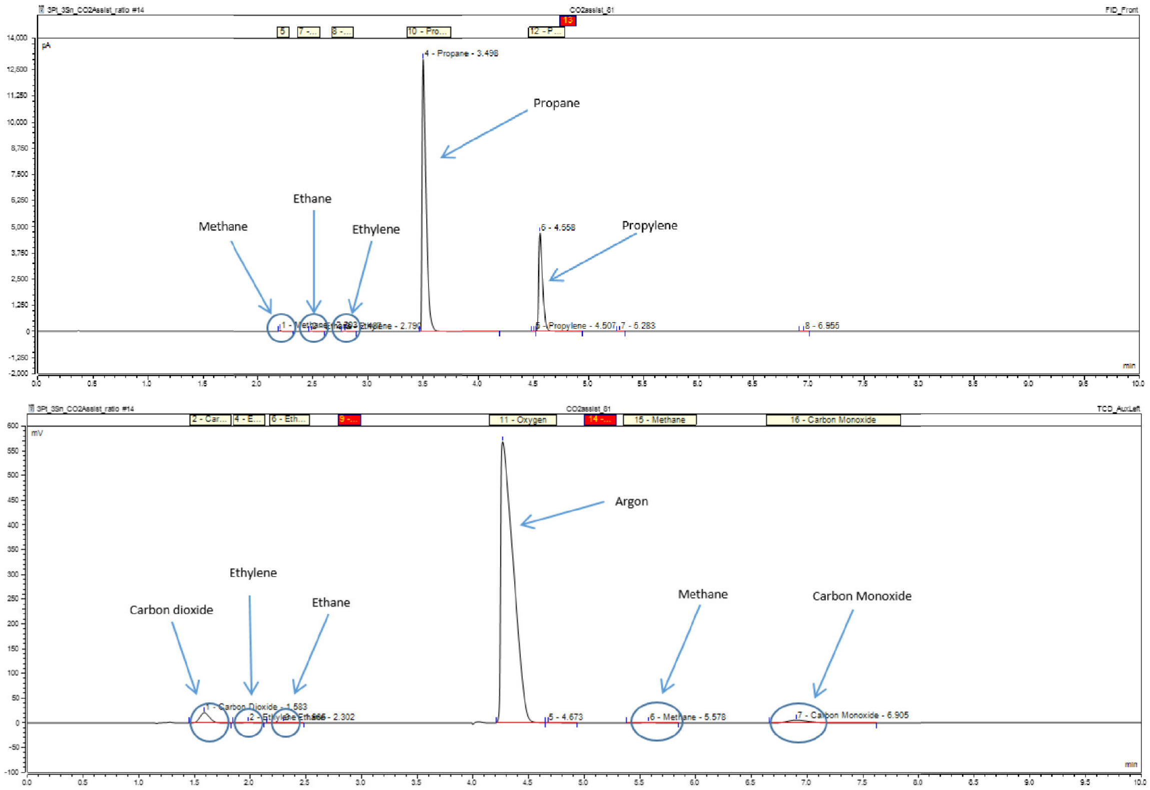

Figure D6: *Chromatogram obtained for the Pt:Sn catalyst during CO_2-PDH at 0.125:1 - CO_2:C_3H_8 ratio flow.* ***Top:*** *from FID showing CH_4, C_2H_6, C_2H_4, C_3H_8 and C_3H_6 peaks.* ***Bottom:*** *TCD showing CO_2, C_2H_6, C_2H_4, Ar, CO and CH_4 peaks.*

Appendix D:

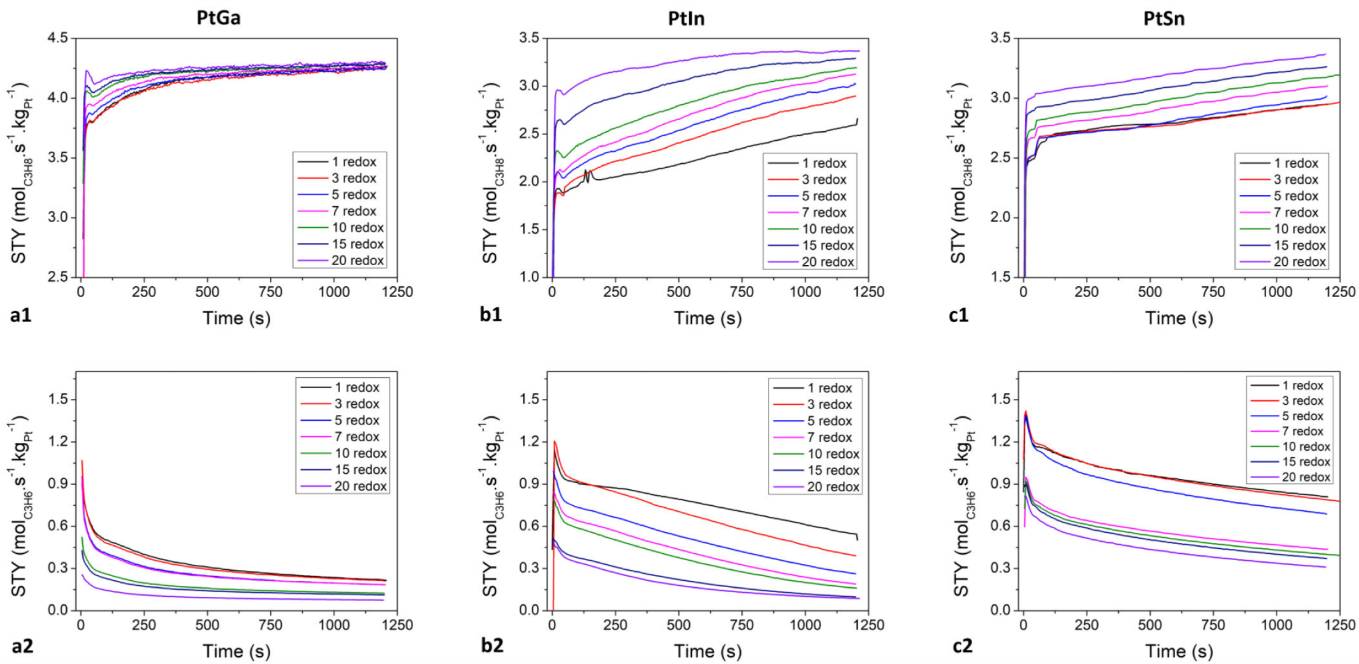
PtGa
PtIn
PtSn
STY (mol$_{C3H8}$.s^{-1}.kg$_{Pt}$$^{-1}$)
STY (mol$_{C3H6}$.s^{-1}.kg$_{Pt}$$^{-1}$)
Time (s)
1 redox
3 redox
5 redox
7 redox
10 redox
15 redox
20 redox
a1
b1
c1
a2
b2
c2
0
250
500
750
1000
1250
2.5
3.0
3.5
4.0
4.5
1.0
1.5
2.0
0.0
0.3
0.6
0.9
1.2

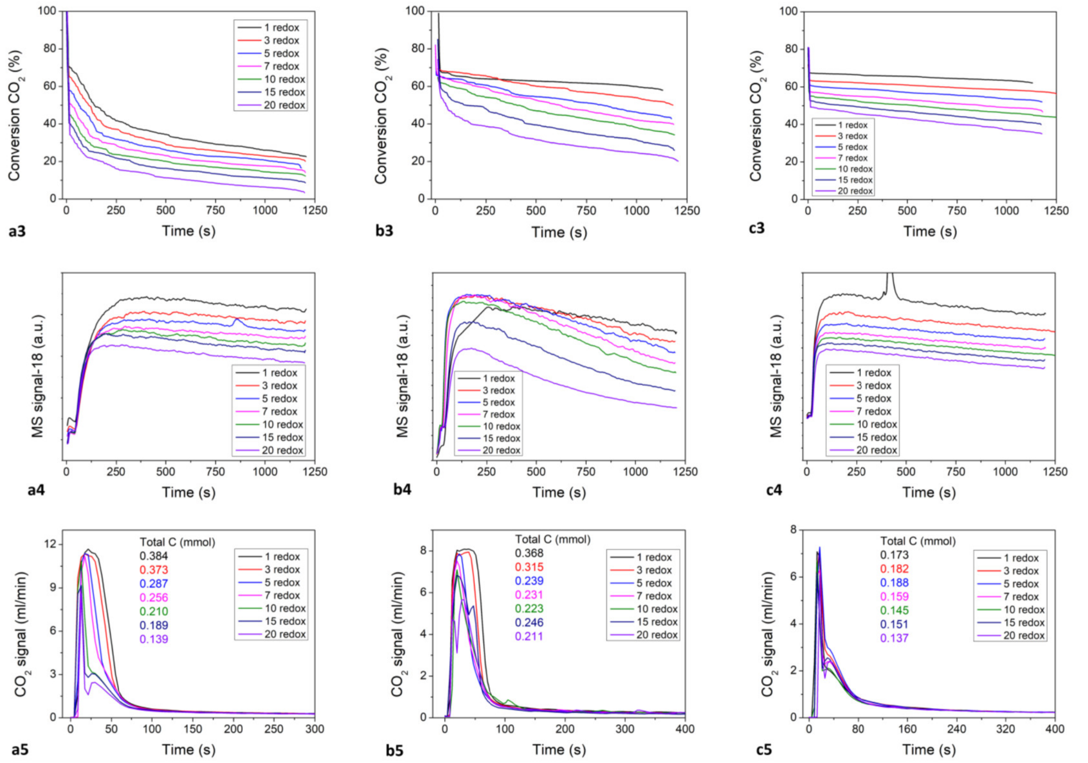

Figure D7: *All activity plots CO_2-PDH after redox activation for* ***a:*** *Pt:Ga,* ***b:*** *Pt:In and* ***c:*** *Pt:Sn.* ***1:*** *Space time yield (STY) of C_3H_6,* ***2:*** *STY for C_3H_8,* ***3:*** *CO_2 conversion,* ***4:*** *m/z = 18 signal (for H_2O outlet),* ***5:*** *m/z = 44 signal during O_2 flow after each reaction step to quantify outlet CO_2 and thereby the carbon formed during reaction (integrated values show total CO_2). For information on flow rates please refer to §5.2.3 in chapter 5.*

Appendix D:

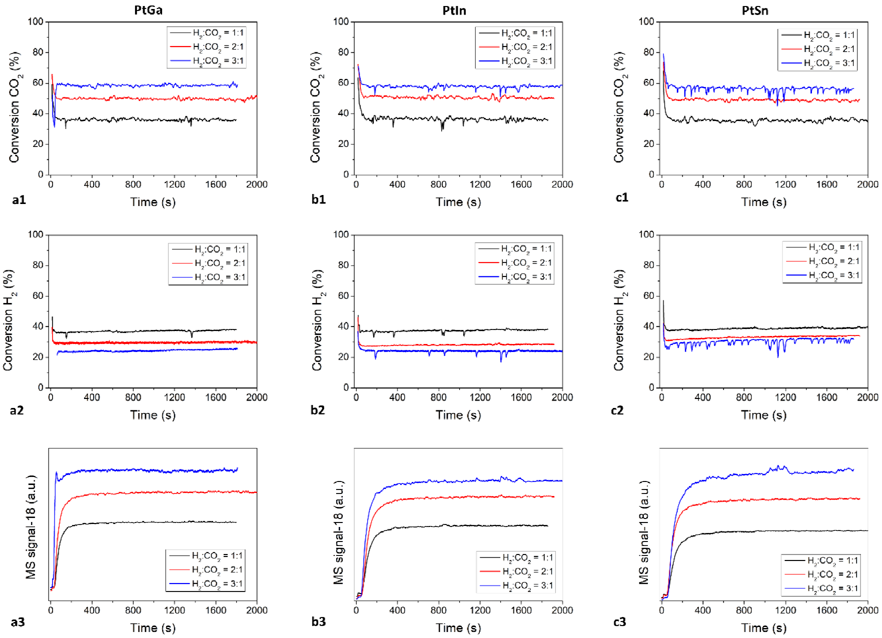

Figure D8: *Activity plots for RWGS experiments at 3 different ratios of H_2:CO_2 for* ***a:*** *Pt:Ga,* ***b:*** *Pt:In and* ***c:*** *Pt:Sn.* ***1:*** *CO_2 conversion,* ***2:*** *H_2 conversion, 3: m/z = 18 signal (H_2O outlet). Flows: CO_2 = 10 Nml/min, H_2 = 10-30 Nml/min, Ar = 110-130 Nml/min, Total flow = 150 Nml/min. Mass of catalyst = 0.1 g.*

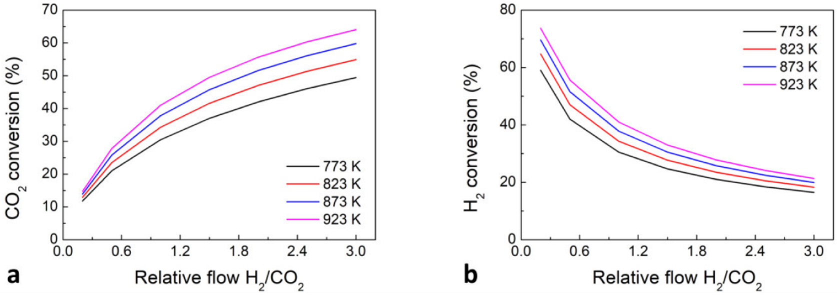

Figure D9: *Thermodynamic calculation of the equilibrium conversion of* ***a:*** *CO_2 &* ***b:*** *H_2 with respect to relative flow of H_2 to CO_2 at different temperatures.*

References

1. Knacke, O. & Hesselmann, K. *Thermochemical properties of inorganic substances*. (Springer, 1991).

2. Navrotsky, A., Ma, C., Lilova, K. & Birkner, N. Nanophase Transition Metal Oxides Show Large Thermodynamically Driven Shifts in Oxidation-Reduction Equilibria. *Science (80-.).* **330**, 199 LP – 201 (2010).

3. Navrotsky, A., Mazeina, L. & Majzlan, J. Size-Driven Structural and Thermodynamic Complexity in Iron Oxides. *Science (80-.).* **319**, 1635 LP – 1638 (2008).

Appendix D:

Appendix E:

Supporting information for Chapter 6

SAXS data

WI samples

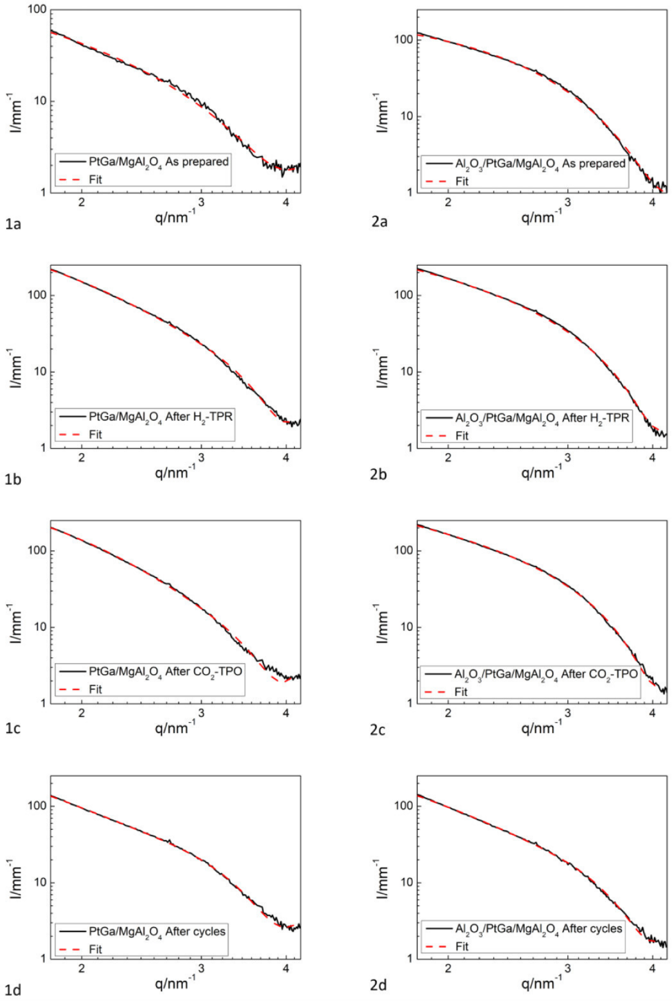

Figure E1: *All SAXS fits for the Pt:Ga/ $MgAl_2O_4$* ***(1)*** *and $10Al_2O_3$/Pt:Ga/$MgAl_2O_4$* ***(2)*** *catalysts.* ***a:*** *As prepared state,* ***b:*** *After TPR,* ***c:*** *After TPO and* ***d:*** *After H_2/O_2 cycles. All black lines are the original SAXS signals (not normalized), while the dashed red lines are the fits.*

Appendix E:

Ga-INC samples

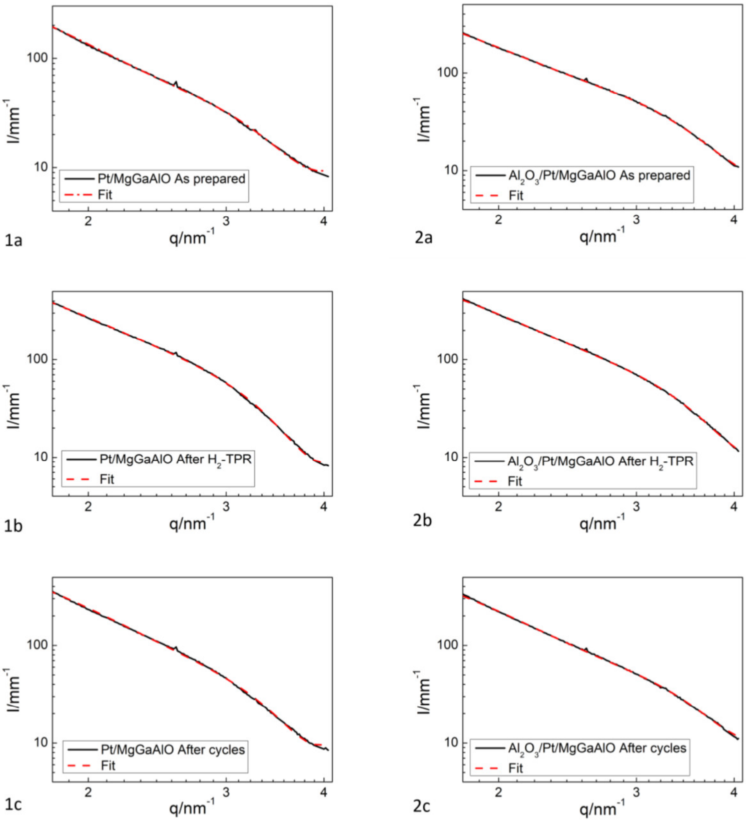

Figure E2: *All SAXS fits for the Pt/ MgGaAlO **(1)** and 10Al_2O_3/Pt/MgGaAlO **(2)** catalysts.* ***a:*** *As prepared state,* ***b:*** *After TPR,* ***c:*** *After H_2/O_2 cycles. All black lines are the original SAXS signals (not normalized), while the dashed red lines are the fits.*

XAS data

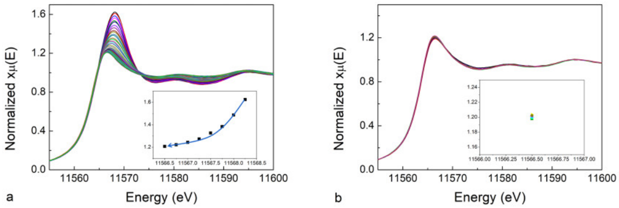

Figure E3: *XANES spectra for monometallic Pt/MgAl$_2$O$_4$ at Pt L$_{III}$-edge during **a:** H$_2$-TPR from room temperature (RT to 923 K) under a flow of 2 ml/min H$_2$ mixed with 5 ml/min Ar (total flow 7 ml/min) and **b:** CO$_2$-TPO (RT to 923 K) at a flow rate of 2 ml/min of CO$_2$ mixed with 5 ml/min of Ar (7 ml/min total flow). **The insets for the two plots show the WL maximum at each energy position**. The arrows within the inset graphs provide a guide-to the-eye as to how the maxima positions shift with temperature and time[1].*

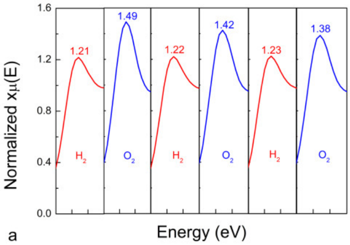

Figure E4: *Pt:Ga/MgAl$_2$O$_4$. Values within the graphs depict the WL height reached at the end of a 20 min half-cycle. Each half-cycle of (—) H$_2$-cycle for 20 min (5 ml/min of 5%H$_2$/He) and (—) O$_2$ cycle for 20min (2 ml/min 20% O$_2$/He+3 ml/min He). 5 total H$_2$/O$_2$ cycles were performed finishing with a H$_2$ half-cycle at the end (not all half-cycles shown).*

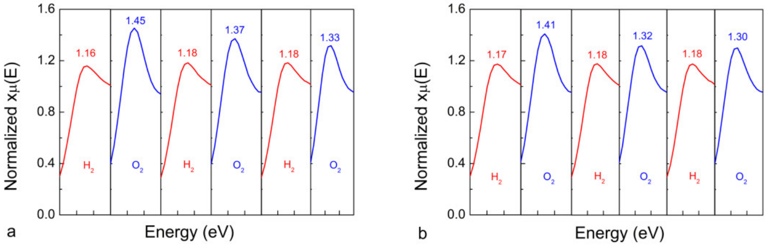

Figure E5: a: *Pt/MgGaAlO, **b:** 10Al$_2$O$_3$/Pt/MgGaAlO. Values within the graphs depict the WL height reached at the end of a 20 min half-cycle. Each half-cycle of (—) H$_2$-cycle for 20 min (5 ml/min of 5% H$_2$/He) and (—) O$_2$ cycle for 20 min (2 ml/min 20% O$_2$/He+3 ml/min He). 5 total H$_2$/O$_2$ cycles were performed finishing with a H$_2$ half-cycle at the end (not all half-cycles shown).*

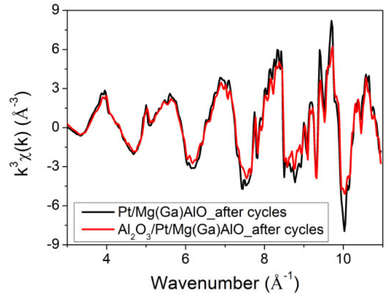

Figure E6: *k^3-weighted k-space EXAFS signal for (—) Pt/MgGaAlO and (—) $10Al_2O_3$/Pt/MgGaAlO samples after 5 O_2/H_2 redox cycles with last H_2 exposure.*

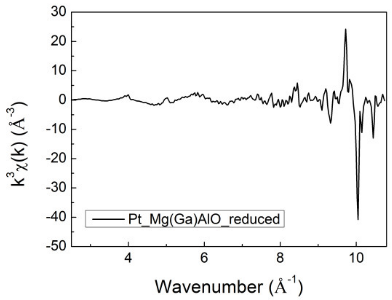

Figure E7: *k^3-weighted k-space EXAFS signal for Pt/MgGaAlO reduced state. The signal has very low S/N ratio and is difficult to treat for EXAFS modelling adequately.*

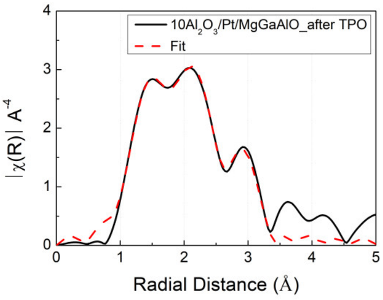

Figure E8: *Experimental k^3-weighted Fourier transformed EXAFS signal and fit at RT at the Pt L_{III}-edge for $10Al_2O_3$/Pt/MgGaAlO after CO_2-TPO.*

***Table E1:** EXAFS fitting results at the Pt L_{III}-edge for $10Al_2O_3$/Pt/MgGaAlO catalyst for the "after CO_2-TPO state".*

$N_{Pt\text{-}O}$	*2.03 ± 0.37*
$R_{Pt\text{-}O}$	*1.91 ± 0.012*
$\sigma^2_{Pt\text{-}O}$ (10^{-3}*Å^2)	*0.011 ± 0.0026*
$N_{Pt\text{-}Pt}$	*9.15 ± 1.26*
$R_{Pt\text{-}Pt}$	*2.68 ± 0.007*
$\sigma^2_{Pt\text{-}Pt}$ (10^{-3}*Å^2)	*0.014 ± 0.0013*
ΔE_0	*-4.8 ± 1.7*
R factor	*0.05*

Activity Tests

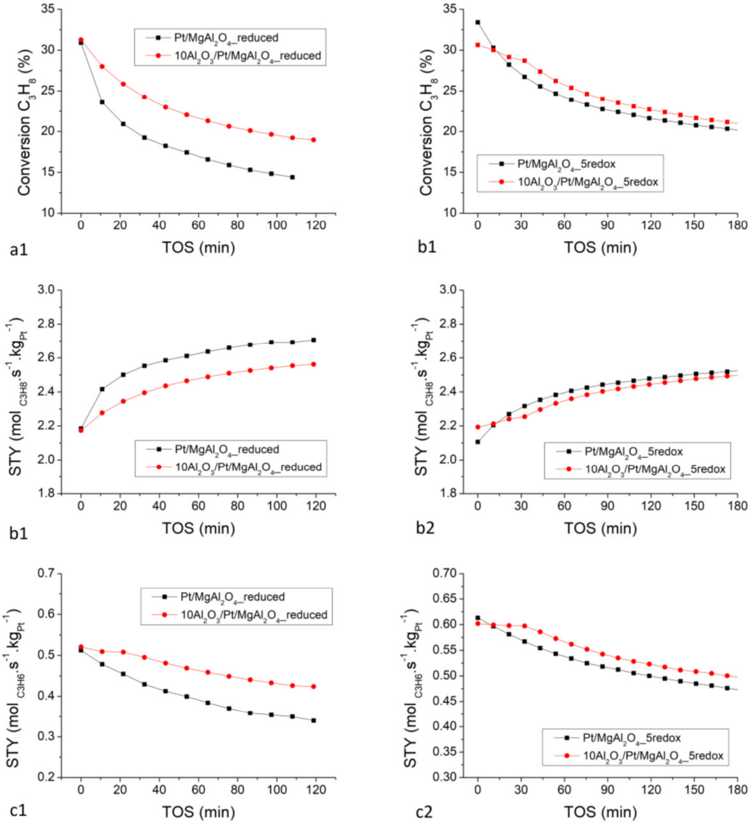

***Figure E9:** Activity results for **Pt/MgAl$_2$O$_4$ (black)** and **10Al$_2$O$_3$/Pt/MgAl$_2$O$_4$ (red)**. **a1:** C_3H_8 conversion for samples after 1 reduction step at 873 K for 30 min, **a2:** C_3H_8 conversion after 5 H_2/O_2 redox treatments with a H_2 reduction as the last step.; **b1:** STY C_3H_8 for reduced state, **b2:** STY C_3H_8 for cycled state, **c1:** STY C_3H_6 reduced state, **c2:** STY C_3H_6 for cycled state. Flows : C_3H_8 = 40 Nml/min, H_2 = 40 Nml/min Ar = 120 Nml/min. Ratio C_3H_8:H_2:Ar = 1:1:3, total flow = 200 Nml/min, catalyst amount = 0.1 g, T =873 K, P =1.2 bar.*

Appendix E:

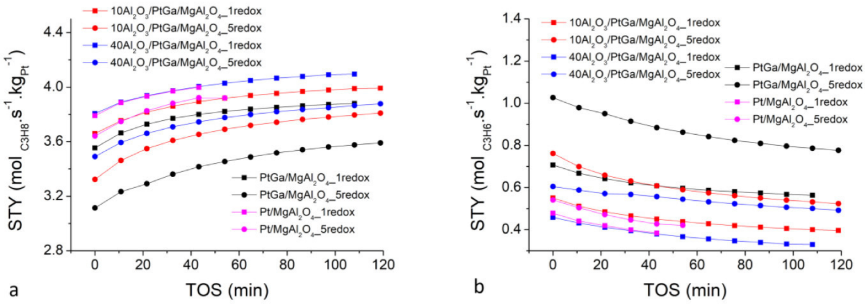

Figure E10: *Activity test results for the coated and uncoated Pt:Ga WI catalysts.* ***a:*** *STY C_3H_8,* ***b***: *STY C_3H_6. Flows : C_3H_8 = 40 Nml/min, H_2 = 40 Nml/min Ar = 120 Nml/min. Ratio C_3H_8:H_2:Ar = 1:1:3, total flow = 200 Nml/min, catalyst amount = 0.1 g, T =873 K, P =1.2 bar.*

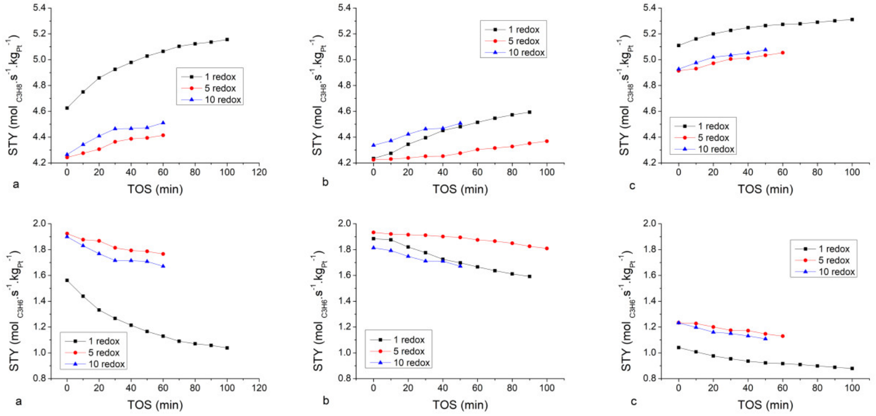

Figure E11: *All reaction plots for* ***a:*** *Pt/MgGaAlO* ***b:*** *10Al_2O_3/Pt/MgGaAlO* ***c:*** *40Al_2O_3/Pt/MgGaAlO. Flows : C_3H_8 = 40 Nml/min, H_2 = 40 Nml/min Ar = 120 Nml/min. Ratio C_3H_8:H_2:Ar = 1:1:3, total flow = 200 Nml/min, catalyst amount = 0.1 g, T =873 K, P =1.2 bar.*

Table E2: *Reaction data values for the coated and uncoated incorporated samples, with data for total carbon generated after each of the reaction steps. Graphs are presented in Figure E11.*

Pt/MgGaAlO						***10Al$_2$O$_3$/Pt/MgGaAlO***						***40Al$_2$O$_3$/Pt/MgGaAlO***					
Time (h)	***Redox cycles***	***Conversion values (%)***		***Δ (%)***	***mmol C***	***Time (h)***	***Redox cycles***	***Conversion values (%)***		***Δ (%)***	***mmol C***	***Time (h)***	***Redox cycles***	***Conversion values (%)***		***Δ (%)***	***mmol C***
2	*1*	*Initial*	*25.41*	***8.56***	***0.76711***	*2*	*1*	*Initial*	*31.71*	***5.78***	***0.932***	*2*	*1*	*Initial*	*17.59*	***3.24***	***0.3063***
		Final	*16.85*					*Final*	*25.93*					*Final*	*14.35*		
1	*5*	*Initial*	*31.58*	***2.76***	***1.00446***	*2*	*5*	*Initial*	*31.87*	***2.32***	***1.058***	*1*	*5*	*Initial*	*20.75*	***2.25***	***0.4638***
		Final	*28.82*					*Final*	*29.55*					*Final*	*18.5*		
1	*10*	*Initial*	*31.22*	***3.95***	***1.25346***	*1*	*10*	*Initial*	*30.07*	***2.75***	***0.728***	*1*	*10*	*Initial*	*20.54*	***2.4***	***0.5779***
		Final	*27.27*					*Final*	*27.32*					*Final*	*18.14*		

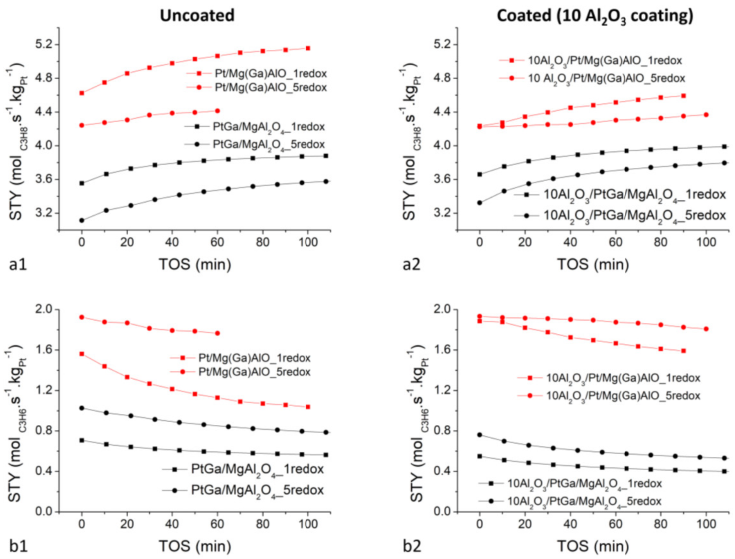

Figure E12: *Comparison of STY for Pt:Ga/$MgAl_2O_4$ (wet impregnated) and Pt/MgGaAlO (Ga- incorporated) samples for* ***a:*** *propane and* ***b:*** *propylene.* ***1:*** *uncoated and* ***2:*** *coated samples. STY was calculated based on the Pt Wt% obtained from ICP. Flows : C_3H_8 = 40 Nml/min, H_2 = 40 Nml/min Ar = 120 Nml/min. Ratio C_3H_8:H_2:Ar = 1:1:3, total flow = 200 Nml/min, catalyst amount = 0.1 g, T =873 K, P =1.2 bar.*

References

1. Veeraraghavan Srinath, N. *et al.* Behaviour of Platinum-Tin during CO2-assisted propane dehydrogenation: Insights from quick X-ray absorption spectroscopy. *J. Catal.* (2021). doi:https://doi.org/10.1016/j.jcat.2021.08.041

Appendix F

List of Publications

Thesis publications	
Chapter 3	J.Cat., (2021) In press doi:https://doi.org/10.1016/j.jcat.2021.08. 041.
Chapter 6	ACS Catal., (2021) 11320-11335 doi:10.1021/acscatal.1c03146.
Submitted work	
Chapter 4	J. Cat, Submitted
Chapter 5	J. Cat, Submitted
Other publications	
Catal. Sci. Technol., 10 (2020), 6987-7001	
ACS Catal., 10 (2020), 6613-6622	
Appl. Catal., B, 300 (2022), 120720	
J. Phys. Chem. C., 126 (2022), 1426-1438	
Oral Presentations	
Redox evolution of Pt-Sn alloys studied by time-resolved XAS	14th European Congress on Catalysis (EuropaCat 2019), 2019, Aachen, Germany,
Alumina coated PtGa based catalysts for propane dehydrogenation	Chemical Research in Flanders, 2nd Symposium (CRF-2), 2019, Blankenberge, Belgium
In situ XAS/SAXS study of Al_2O_3 coated PtGa/$MgAl_2O_4$ catalysts for alkane dehydrogenation	American Institute of Chemical Engineers Annual Meeting (AIChE 2019), Orlando, USA

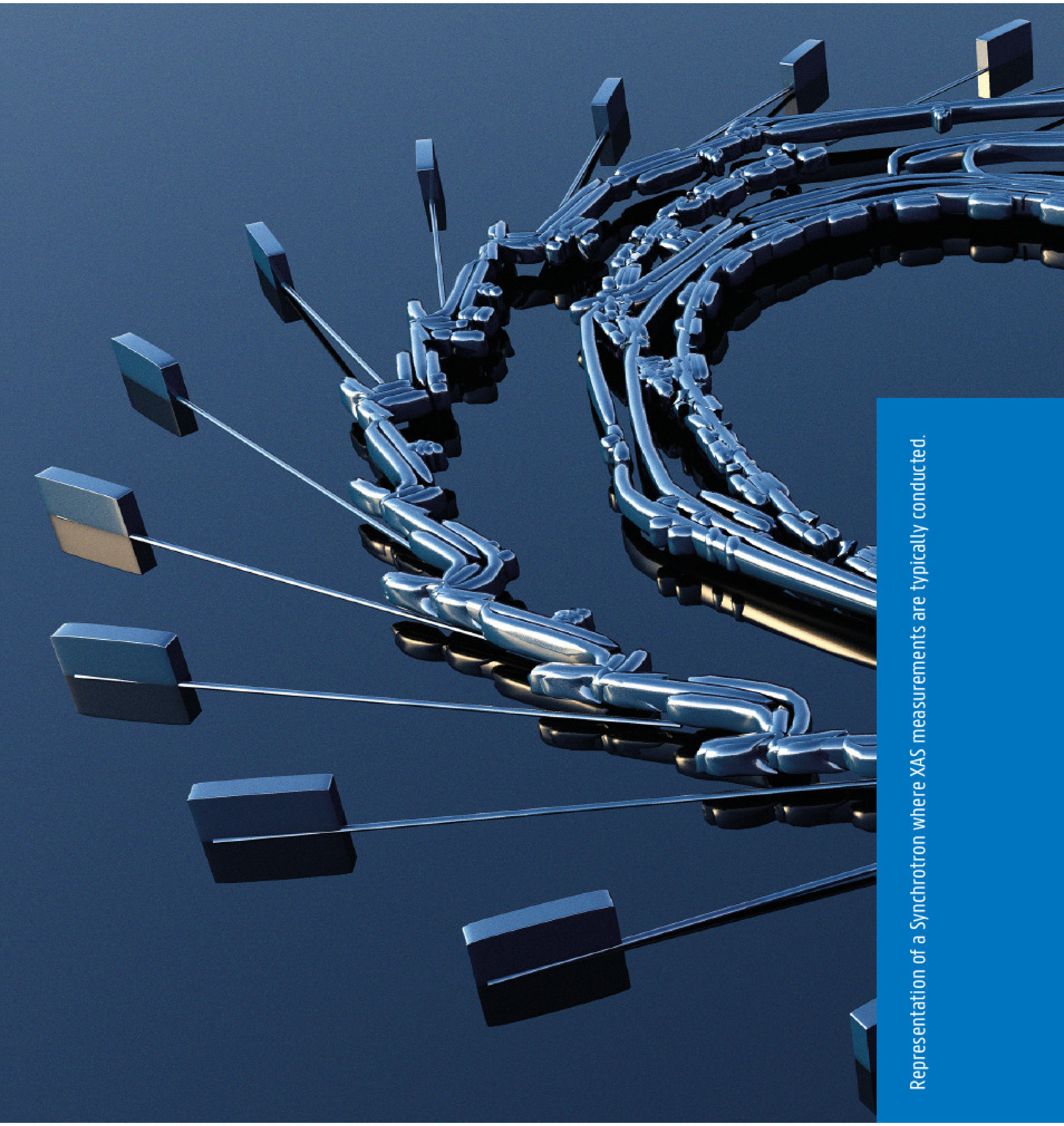

Representation of a Synchrotron where XAS measurements are typically conducted.